Analogue quantum simulating a bilayer Hubbard system or a monolayer Hubbard system with reservoir - thermodynamics, entropy and spin correlations

Dissertation
zur
Erlangung des Doktorgrades (Dr. rer. nat.)
der
Mathematisch-Naturwissenschaftlichen Fakultät
der
Rheinischen Friedrich-Wilhelms-Universität Bonn

vorgelegt von
Jens Samland
aus
Berlin-Neukölln

Bonn 2022

Angefertigt mit Genehmigung der Mathematisch-Naturwissenschaftlichen Fakultät
der Rheinischen Friedrich-Wilhelms-Universität Bonn

1. Gutachter: Prof. Dr. Michael Köhl
2. Gutachter: Prof. Dr. Martin Weitz

Tag der Promotion: 19.10.2022
Erscheinungsjahr: 2022

gewidmet
Miriam Machill
Italien, Portugal, Rumänien, Indien, Ukraine.
Analysis auf Mannigfaltigkeiten, theoretische Quantenfeldtheorie,
experimentelle Quanten-Vielteilchenphysik.
Göttingen, Rostock, München, Amsterdam, Bonn.
Ein Zuhause. Diese Arbeit ist für Dich.

Ich danke Laura Nagelschmidt, René Heyse, Roxanne Pretzsch, meinen Freunden in Göttingen, Karlsruhe und Berlin und meinem Vater und meiner Mutter.

Abstract

The high controllability of analogue quantum simulators using ultracold atoms in optical lattices pushes forward the frontiers in the experimental investigation of the fermionic Hubbard model. The bilayer Hubbard model is a step beyond the two-dimensional Hubbard model that extends the latter by incorporating a coupling between two two-dimensional Hubbard systems. This is also a step forward in the idea of analogue quantum simulate real materials such as the copper oxide high temperature superconductors which possess a coupled layer structure. This thesis is dedicated to the experimental implementation of an analogue quantum simulator for a bilayer Hubbard system with cold atoms in optical mono- and bi-chromatic lattices.

The measurement of competing magnetic order in the bilayer Hubbard system is a result of the work during the course of this thesis. This measurement requires a high controllability of the system which goes along with a precise calibration and fundamental characterisation of the implemented bilayer Hubbard system. Here, the calibration of the interaction strength by means of a comparison between data and theoretical predictions becomes possible through one major outcome of this thesis. This is a method to compute interacting Wannier functions in an optical superlattice. A further major outcome of this thesis is the measurement of thermodynamics, density fluctuations and entropy in the bilayer system considered as a monolayer Hubbard system with reservoir. Further outcomes of this thesis for a fundamental characterisation of the bilayer Hubbard system are:

1. The characterisation of the Hubbard band insulator.
2. The computation of the potential map for an optical bi-chromatic superlattice.
3. The calibration of the optical bi-chromatic superlattice by comparing experimental data to theoretical predictions. Here, the band projection position operator method to compute non-interacting Wannier functions in a superlattice was successfully implemented in this thesis. The latter are the starting point for the newly developed method to compute interacting Wannier functions.

Acknowledgement

I thank Prof. Dr. Michael Köhl that he gave me the great opportunity to work on this quantum gas experiment. The high complexity of the experiment which is the result of about 15 years of work originates from the physics and the amount of information to continuously operate and extend the experiment. From my point of view, this experiment therefore represents a transition experiment where a single person might just still operate and extend the experiment for a certain time but not efficiently. The high complexity furthermore revealed the different talents of each person which are usually covered in the everyday life. Finally, my experimental work on a real strongly correlated quantum many body system gave me a deep insight into the fundamentals of quantum mechanics. Vielen Dank.

I thank Dr. Marcel Gall that he took his time to show me the experiment and gave me a profound introduction into it. He was the contact person when I was still in Amsterdam at the end of my Master's thesis.

I thank Dr. Nicola Wurz that she explained me the experiment and important theoretical background.

I thank Dr. Chun Fai Chan that he explained me the DQMC calculations and code.

I thank Janek Fleper for his explanations to the DMD. His work on setting up a profound basis for data analysis in *python* facilitated the work.

I thank Nick Klemmer that he invited me to sports when I arrived in Bonn. A first step to find a place in Bonn after the move from Amsterdam.

Furthermore, I thank Prof. Dr. Reinhard Kienberger and Prof. Dr. Florian Schreck for their support during the Master's thesis.

Contents

1 Introduction 1
1.1 Analogue quantum simulations . . . 1
1.2 Analogue quantum simulating the Hubbard model . . . 3

2 Theory 7
2.1 Hubbard model . . . 7
2.1.1 Introduction . . . 7
2.1.2 Phase diagram of the Hubbard model . . . 10
2.1.3 Bilayer Hubbard model . . . 16
2.2 Wannier functions in a superlattice . . . 17
2.2.1 Superlattice potential and band structure . . . 18
2.2.2 Non-interacting, maximally-localised Wannier functions . . . 23
2.2.3 Derivation of Hubbard parameters using Wannier functions . . . 28
2.2.4 Interacting Wannier functions . . . 30

3 Experimental setup 33
3.1 Cooling to quantum degeneracy . . . 34
3.1.1 Laser system . . . 34
3.1.2 Magneto optical trap, transport and Ioffe-Pritchard trap . . . 37
3.1.3 Dipole trap . . . 40
3.2 Imaging . . . 42
3.2.1 z-imaging . . . 42
3.2.2 x- and y-imaging . . . 45
3.3 Lattices . . . 45
3.3.1 Bi-chromatic, vertical z-superlattice . . . 45
3.3.2 Bi-chromatic, in-plane x-superlattice . . . 49
3.3.3 Monochromatic, in-plane y-lattice . . . 54
3.4 Feshbach resonances and coils . . . 54
3.4.1 Feshbach resonances in potassium ^{40}K . . . 54
3.4.2 Feshbach coil system . . . 55
3.5 Density and spin discrimination in a single two-dimensional lattice plane . . 58
3.5.1 Zeeman splitting . . . 58
3.5.2 Radio frequency swaps . . . 58
3.5.3 Tomography . . . 58
3.5.4 Singly/Doubly site occupation discrimination . . . 60
3.5.5 Spin state discrimination . . . 62
3.5.6 Microwave shelving and imaging . . . 62
3.6 Digital mirror device . . . 63

4 Results and discussion 67
4.1 Calibrating the superlattice and bilayer Hubbard parameter . . . 67
4.1.1 Superlattice depth calibration . . . 67
4.1.2 Superlattice symmetry point calibration . . . 69

4.1.3 Superlattice phase calibration 71
4.1.4 Superlattice phase stability 75
4.1.5 Calibration of the Hubbard tunnelling parameter t 75
4.1.6 Second plane emptying 75
4.1.7 Calibration of the Hubbard interaction strength U 77
4.2 Implementing an analogue quantum simulator for a bilayer Hubbard system 79
4.2.1 An interacting, 50:50 spin mixtured atomic gas in two dimensions . 79
4.2.2 Loading the gas in a two-dimensional, in-plane optical lattice 83
4.2.3 Producing a Hubbard band insulator in the two-dimensional lattice . 90
4.2.4 Splitting the Hubbard band insulator to obtain a quantum simulator for a coupled bilayer Hubbard system 94
4.2.5 The underlying potential across the quantum simulator 98
4.2.6 Singly and doubly occupancies in both planes of the bilayer system . 101
4.2.7 Determinant quantum Monte Carlo simulations 104
4.2.8 Compressibility of the bilayer Hubbard system 104
4.3 Spin correlations in the bilayer system 105
4.3.1 Intralayer spin correlations 105
4.3.2 Interlayer spin correlations 111
4.3.3 Spin correlations for varying ratios U/t 114
4.4 Thermodynamics in the bilayer Hubbard system considered as monolayer Hubbard system with reservoir 115
4.4.1 A bilayer as a monolayer Hubbard system with reservoir 115
4.4.2 Equation of state, compressibility and the bilayer system temperature 115
4.4.3 Local and thermodynamic density fluctuations 118
4.4.4 Pressure and entropy 120

5 Outlook **123**
5.1 Bilayer Hubbard model 123
5.1.1 First-order correlation function in a bilayer Hubbard system 123
5.1.2 Particle-hole symmetry and pair correlations in a bilayer system . . 124
5.2 Implementation of the Rice-Mele model 124
5.2.1 Depth-, tunnelling- and interaction strength calibration in the x superlattice 126
5.2.2 Outlook: Floquet systems and edge state detection 130

Bibliography **133**

List of Figures **145**

CHAPTER 1

Introduction

1.1 Analogue quantum simulations

Analogue quantum simulation is the approach to simulate real, complex many body quantum systems like a solid with a more controllable real (analogue) quantum system [147] in order to gain insight and to understand the properties and behaviour of the former. This concept is attributed to Richard Feynman who discussed it in his seminal lecture "Simulating Physics with Computers" in 1982 [52]. Analogue quantum simulation of many body quantum systems offers two fundamental advantages compared to the simulation with a classical computer. First, the dimension of the Hilbert space of a many body quantum system increases exponentially with the number N of particles d^N where d is the single particle Hilbert space. Thus, classical computation of such systems is very limited. Second, the classical computation of *fermionic* many body quantum systems suffers from the sign problem which hinders the calculation at decreasing temperatures and increasing particle numbers [45]. In contrast, the analogue quantum simulation offers the possibility to experimentally observe fundamental, quantum mechanical principles and to investigate complex, strongly correlated bosonic and fermionic many body quantum systems. Analogue quantum simulators have been built in the last decades on several experimental platforms. This includes ions in magnetic traps [17][109], Rydberg atoms [151] [112], photonic systems, cold molecules [16] and cold, neutral atoms [18].

The analogue quantum simulation with cold, neutral atoms bases on the principle of light-matter interaction. In the presence of (laser) light, the electronic structure in the atoms is modified which is referred to as light shift of the electronic energy levels. In the framework of a two level system this light shift is given by [86]

$$V_{\mathrm{LS}} = \pm \frac{\hbar\Gamma^2}{8\Delta}\frac{I(r)}{I_{\mathrm{sat}}}, \tag{1.1}$$

where, $\hbar$, Γ, Δ, I and I_{sat} are the reduced Planck constant, the decay rate of the upper level, the detuning of the laser light from the atomic resonance, the light's intensity and the saturation intensity, respectively. Furthermore, the "+"-sign in Eq. 1.1 captures the light shift of the ground state energy level while the "-"-sign describes the light shift of the excited state. Thus, neutral atoms feel a potential in the presence of light which is referred to as dipole potential. In turn, a light intensity gradient $\nabla I(r)$ acts as a dipole force whose sign depends of the detuning Δ and on the atom's internal state, i.e. if the atom is in the ground or in an excited state.[1] In cold atom experiments, the atoms are typically prepared in the ground state. Hence, exposed to far red-detuned laser light ($\Delta < 0$ and $|\Delta| \gg \Omega_R$[2]), atoms are attracted to the highest intensity while in the presence of blue-detuned laser light ($\Delta > 0$ with $\Delta \gg \Omega_R$) they are expelled from the laser light. As an example, for potassium atoms with a main transition wavelength of 766 nm between the $4s^2S_{1/2}$ and the $4s^2P_{3/2}$ state, laser beams at 1064 nm and 532 nm produces attractive and repulsive potentials for the atoms, respectively. Besides this, the used laser beams have typically a Gaussian profile and therefore exhibit an intensity gradient in radial direction. Thus, in a red-detuned Gaussian beam where the intensity is highest along the beam axis, atoms are trapped in radial direction in the beam center. Moreover, in longitudinal direction, an intensity gradient can be created by focussing the laser beam. So the atoms are confined in all directions in the beam focus.

A periodic potential for atoms can be produced by an optical standing wave which is referred to as *optical lattice*. Such an optical standing wave is commonly generated by e.g. retro-reflecting a Gaussian laser beam. In the case of a red-detuned optical lattice, the atoms thus arrange periodically at the light intensity maxima of the standing wave. The periodic arrangement of the atoms in the optical lattice leads to the name "optical crystal"due to the similarity between the periodic optical lattice potential for atoms and the periodic lattice potential for electrons from the atomic nuclei in a solid. In this regard, analogue quantum simulation with cold, neutral atoms in optical lattices can be used to simulate solids.

The success of neutral atom analogue quantum simulators in the last two decades bases strongly on the creation of such optical crystals. Nowadays, temperatures and kinetic behaviour of the atomic ensemble in the optical crystal can be adjusted, two-particle interaction strengths can be tuned over a wide range employing Feshbach resonances and one, two or three dimensional optical crystal potentials can be created and almost arbitrarily shaped. Moreover, the system's behaviour can be observed on a single lattice site level and the occupation of a lattice site with a single or two atoms can be distinguished. All this allows for precisely determining the dependence of individual system properties on single parameters. In real solids, the most prominent example of correlated fermionic systems in a periodic potential, such precise determination is often hindered by impurities in the material and high costs for the production of several probes with different parameter settings. The investigation of the behaviour of *correlated electrons in solids* can therefore be endorsed by neutral atom analogue quantum simulators.

---

[1] This is in contrast to the scattering force which light exerts on atoms when its frequency is close to the resonance of the atomic transition, i.e. $\Delta \approx 0$. This scattering force saturates for strong intensity and decreases with $1/\Delta^2$ while the dipole force does not saturate and only decreases with $1/\Delta$.

[2] Here, Ω_R is the Rabi frequency in the two level picture.

1.2 Analogue quantum simulating the Hubbard model

In fact, the creation of optical crystals realises the paradigmatic Hubbard model for solids in an analogue quantum simulator (Fig. 2.1 left). The Hubbard model was introduced by John Hubbard [76] in 1964. Transition metal monoxides like FeO, NiO, CoO were first linked to this model [121] since both, the materials and the model, exhibit an antiferromagnetic ordered Mott insulating (AFM) phase (Fig. 1.1, AFM). In subsequent decades, the Hubbard model in two dimensions (Fig. 2.1 left) was employed for copper oxide compounds which consist out of separated CuO_2 layers (cf. upper plane in Fig. 2.1 right). Additionally to a Mott insulating- and an antiferromagnetic ordered phase [72], these compounds exhibit a high temperature superconducting (SC) phase (Fig. 1.1, SC) [11]. Here, initiated by Anderson, the hope has been that the rather simple Hubbard model also contains the essential features needed for high temperature superconductivity. To date, the emergence of this phase is not yet fully understood [2] and it is only believed that super exchange interactions are responsible for high temperature superconductivity in doped materials like the cuprates (Fig. 2.1 right) [3][92].[3] In contrast, it is known, that in conventional or s-wave (S=0, l=0) superconductors, superconductivity arises due to the phonon intermediated electron-electron interactions.[4]

Various phases in the Hubbard model (Fig. 1.1) were already created and investigated with cold atoms in optical lattices. At half-filling and sufficient low temperatures an antiferromagnetic, Mott-insulating (AFM) state which remains stable even for small doping forms. This phase was observed for example in [30][66]. However, at larger doping and high temperatures the system crosses over into a normal metallic state. This cross-over into a metallic state was likewise observed in [30][66]. By lowering the temperature, the metallic state crosses over into a so-called strange metal and, at even lower temperatures, a pseudo gap regime opens up. This regime is characterized by a suppression of the spectral weight [43].[5] The pseudo gap was experimentally confirmed in [43]. Below the critical superconducting temperature, the phase diagram exhibits two regions ("doms") of superconducting states. One is on the hole doped and one on the electron doped side. D-wave pairing, a possible mechanism for d-wave superconductivity on the hole doped side [33], was theoretically analysed for a two-layer Hubbard model in [23] and theoretically studied in the context of cold fermions in an optical lattice in [75][116][118]. In an experiment, however, the required low temperature for these phases could not be reached so far.

In the last decade, the creation and investigation of different phases in the Hubbard model with cold atoms in optical lattices went also along with the experimental implementation of extensions of the simple Hubbard model and of different underlying geometries. For example, a honeycomb lattice geometry as in layered graphene was realized with cold atoms e.g. in [94][119]. A triangular lattice which exhibits a frustrated antiferromagnetic phase was realised for example in [130][155]. A so-called Lieb lattice is important due to

---

[3] High temperature superconductivity is also referred to as unconventional or d-wave (S=0,l=2) superconductivity and was likewise observed in other layered materials like CoO_2 [145].

[4] Typical elements which exhibit a conventional or s-wave superconducting phase are Al, Nb and Pb [41]. Copper, cobalt and nickel oxides in contrast possess an unconventional or d-wave superconducting phases [145]. p-wave (S=1,l=1) superconductivity occurs for example in Sr2RuO4 [98].

[5] The spectral weight is the integrated induced conductivity over a range of applied frequencies [106].

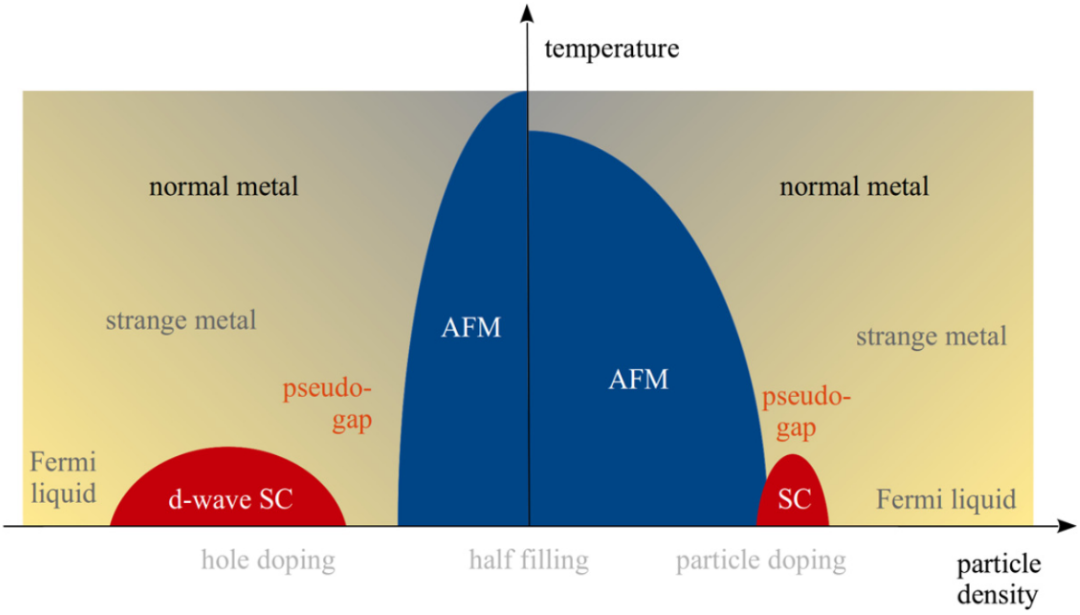

Figure 1.1: Schematic phase diagram for cuprates. At half-filling and low temperatures the ground state is antiferromagnetic (AFM). This state persists for small hole and electron doping. For higher doping, however, at high temperatures the AFM state crosses over into a metallic state. For decreasing temperatures, the metal becomes a strange metal before a pseudo gap opens. At even lower temperatures, a superconducting region (”dome”) arises on the hole- as well as on the electron-doped side. While the superconducting state is of d-wave type on the hole doped side, the electron doped side reveals a s-wave superconducting phase. The figure is taken from [146].

its similarity to the CuO_2 planes in high temperature superconductors. In this model, in addition to a common square Hubbard model (Fig. 2.1 left), lattice sites are added to the middle of each link between two sites of the square model. These sites thus represent the oxygen atoms in the CuO_2 planes (Fig. 2.1 right). The Lieb lattice was investigated with cold atoms in optical lattices for example in [61][53]. Beside the geometry, extensions to the simple Hubbard model were investigated. One of them is the Periodic Anderson Model (PAM) that includes more than one energy band [124]. Moreover, non-local interactions [148] or next-nearest neighbour tunnelling [102] was taken into account to explain measurements on analogue quantum simulators with cold atoms. Considerably, if next-nearest neighbour tunnelling (along the diagonals) in a square Hubbard model is included, the particle-hole symmetry breaks. This is especially also the case for the high temperature superconducting cuprates which can be directly seen from the asymmetry of the phase diagram (Fig. 1.1) [134].

This work describes the first implementation of a bilayer square Hubbard model with cold atoms in optical lattices. The bilayer model extends the simple two-dimensional Hubbard model by coupling two Hubbard planes to each other (Fig. 2.4 left). This is a step towards a more realistic analogue quantum simulation of real copper oxides in which neighbouring CuO_2 are also coupled to each other (Fig. 2.1). The bilayer Hubbard model was theoretically studied in [80][129][63]. A bilayer Hubbard system was simultaneously to this work implemented in [85].

Thesis structure

In this thesis, I detail the experimental implementation of our bilayer Hubbard system and two main measurements on it, namely spin correlations and thermodynamics in the bilayer Hubbard system. I structured the thesis in five chapters:

After the introduction in this chapter, I first introduce the mono- and bilayer Hubbard model in chapter 2. Its characteristics and the current state of the art in building analogue quantum simulators for this model is the precondition to be able to built an analogue quantum simulator for the bilayer Hubbard system. Second, I detail the computation of non-interacting Wannier functions employing the band projection position operator method and elaborate the method to compute interacting Wannier functions which was developed during this thesis. This is required in order to be able to quantify if the implemented bilayer Hubbard system behaves as theoretically expected.

In chapter 3, I describe the experimental setup which we used to implement the analogue quantum simulator for the bilayer system. During the course of this thesis, we extended this setup by one vertical and one horizontal optical, bi-chromatic superlattice. The vertical superlattice was used for the implementation of the bilayer system.

Chapter 4 presents all measurements: first (chapter 4.1), on the calibration of the vertical superlattice. Here, the theory of Wannier functions from chapter 2 is employed. Second (4.2), on the implementation and characterisation of the bilayer system. Third (4.3), on the first main result, namely spin correlation measurements in the bilayer Hubbard system. And finally (4.4), the second main result, thermodynamics in the bilayer Hubbard system.

Chapter 5 gives the outlook which also summaries the main calibration results of the horizontal optical superlattice. This lattice will be used in the future to implement the Rice-Mele model.

List of publications

During the course of this thesis, the article

- **Competing magnetic orders in a bilayer Hubbard model with ultracold atoms** M. Gall*, N. Wurz*, J. Samland, C. F. Chan and M. Köhl, Nature 589, 40-43 (2021). https://doi.org/10.1038/s41586-020-03058-x.

was published (*These authors contributed equally).

The following two articles are in preparation

- **Thermodynamics, density fluctuations and entropy in a bilayer Hubbard system using cold atoms** J. Samland, N. Wurz, M. Gall and M. Köhl

- **Interacting Wannier functions in superlattices - comparing predictions from a new recipe to measurements in two independent optical superlattices** J. Samland and M. Köhl

CHAPTER 2

Theory

The last chapter gave an introduction to the concept of analogue quantum simulators. Chapter three will describe the experimental setup with which an analogue quantum simulator for a bilayer Hubbard system was implemented during this thesis. This chapter details, on the one hand, the fundamentals of the mono- and bilayer Hubbard model, especially their phase diagrams. A precise knowledge of the monolayer Hubbard model phase diagram is required as it provides the general, partly subtle properties and features of the Hubbard model which were exploited during the implementation of the bilayer Hubbard system. For example, how is the interaction strength to be set to create a Hubbard Mott insulator. Moreover, the phase diagram of the bilayer Hubbard model is described since it was partially measured during this thesis for the first time. On the other hand, the second main section elaborates the theory of Wannier functions in superlattices which is important to calibrate the optical superlattice used to create the bilayer Hubbard system. A method to compute interacting Wannier functions was developed in the course of this thesis and is discussed. This enables to validate the measured interaction strength with theory. The theory of Wannier functions in this chapter is used in chapter four where the calibration and implementation of the bilayer Hubbard system is described.

2.1 Hubbard model

This chapter introduces first to the monolayer Hubbard model, refers to the development of analogue quantum simulators for the Hubbard model in the last two decades and elucidates the monolayer Hubbard model phase diagram. Next, the bilayer Hubbard model and its phase diagram are introduced.

2.1.1 Introduction

The Hubbard model describes interacting quantum particles on a lattice (Fig. 2.1 left). Its Hamiltonian in second quantisation reads [76][121][58]

$$H_{\mathrm{Hub}} = -t \sum_{\langle i,j,\rangle,\sigma} (\hat{c}^{\dagger}_{i,\sigma}\hat{c}_{j,\sigma} + \mathrm{h.c.}) + U \sum_{i} \tilde{n}_{i,\uparrow}\tilde{n}_{i,\downarrow} - \sum_{i} \mu_{i,\sigma}\tilde{n}_{i,\sigma}. \tag{2.1}$$

The first term of the right hand side is governed by the tunnelling amplitude t. Furthermore, it contains the annihilation operator $\hat{c}_{i,\sigma}$ and its complex conjugated, the creation operator, $\hat{c}^{\dagger}_{i,\sigma}$. The annihilation operator destroys a particle on lattice site i with spin σ while the creation operator creates one. The consecutive application of $\hat{c}^{\dagger}_{i,\sigma}\hat{c}_{j,\sigma}$ onto a state thus describes a particle being destroyed at j and created at i which is interpreted as tunnelling or "hopping" of the particle from j to i. The tunnelling strength is given by the overlap integral $t_{ij} = \int w^{\dagger}_{i}(z)[-\hbar^2\nabla^2/(2m)]w_j(z)\ \mathrm{dz}$. Here, $w_i(z)$ and $w_j(z)$ describe the Wannier functions (cf. Fig. 2.9) of localised particles at site i and j, respectively. For a homogenous system, $t_{ij} = t$ is site-independent. The angled brackets $\langle i, j, \rangle$ in Eq. 2.1 indicate that the sum runs only over pairs of lattice indices i, j with $i = j \pm 1$, so nearest neighbour lattice sites. The Hamiltonian is hence a good approximation for systems where the overlap between Wannier functions from next nearest neighbour sites is negligible. By describing the tunnelling of particles between adjacent lattice sites, the first term in Eq. 2.1 takes the role of the kinetic energy in the Hamiltonian. Its negative sign indicates that an increase of the tunnelling strength t and, hence, delocalisation of the particles, leads to a reduction of the total energy.

The second term in Eq. 2.1 represents the interaction energy of particles on the lattice. Beside the on-site interaction parameter U, it contains the number operator $\tilde{n}_{i,\sigma} = \hat{c}^{\dagger}_{i,\sigma}\hat{c}_{i,\sigma} - 1/2$ which counts the number of particles of the respective spin σ on lattice site i. For fermions $\tilde{n}_{i,\sigma} + 1/2 = 0, 1$ for each spin due to Pauli's exclusion principle. The consecutive application of the number operators for each spin $\tilde{n}_{i,\uparrow}\tilde{n}_{i,\downarrow}$ in Eq. 2.1 is non-zero only if two particles with different spin occupy the same lattice site i. Then, the interaction energy is increased by the amount of the interaction strength U. In the pseudo potential approximation [18] $U = g \int |w(z)|^4 \mathrm{dz}$ with $g = 4\pi\hbar^2 a_s/m$. Here, $w(z)$ is again the Wannier function and a_s and m denote the scattering length and the particle mass, respectively [86]. Summing over all lattice sites i yields the total interaction energy that contributes to Eq. 2.1. In the simplest version of the Hubbard model the interaction between two particles is fully on-site meaning that only particles which occupy the *same* lattice site interact with each other. This is reflected by the same index i in the term $\hat{n}_{i,\uparrow}\hat{n}_{i,\downarrow}$. The model can be extended to nearest-neighbour interactions [5] yielding $U_{ij} = g \int w_i(z)^2 w_j(z)^2 \mathrm{dz}$ [148].

The third term in Eq. 2.1 accounts for a possible varying potential energy between different sites in the lattice. Here, $\mu_{i,\sigma}$ is the local chemical potential and $\hat{n}_{i,\sigma}$ the number operator for site i and spin σ. In general, $\mu_{i,\sigma}$ is spin dependent indicated by its index σ. When realising the Hubbard model with cold atoms in optical lattices, the underlying potential is, however, spin independent ($\mu_{i,\sigma} = \mu_i$). But, it has a underlying Gaussian energy landscape due to the Gaussian lattice laser beams (Fig. 4.12 right).[1] Thus, the local chemical potential μ_i is site-dependent and determined by the Gaussian potential

---

[1] Magnetic field gradients across the optical lattice can be additionally used in order to evoke a spin dependent potential.

which can be approximated by an harmonic potential close to the beam center. This yields $\mu_i = \mu_0 - V_{\text{harm}}(r)$ [86] employing the local density approximation (LDA).
In general, the parameters t and U have to be on the same order of magnitude and both have to be smaller than the temperature of the system $t, U < T$. Otherwise higher bands become populated (PAM model, see introduction) and the single band Hubbard approximation becomes inaccurate. The Hubbard model serves for modelling single copper oxide layers in copper oxide compounds that exhibit high temperature superconductivity (cf. Fig. 2.1 left and right).

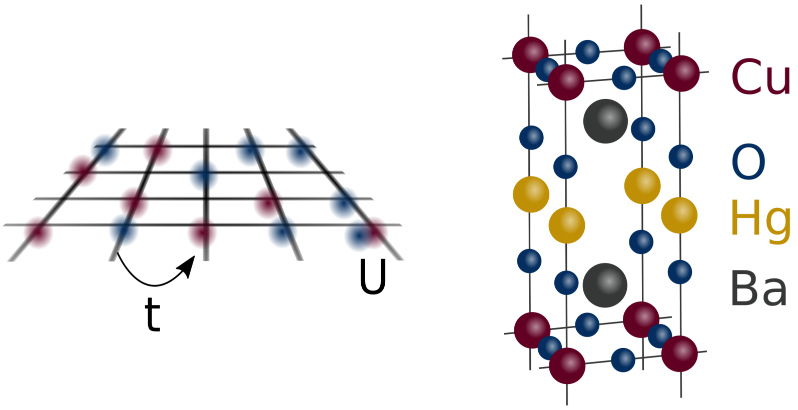

Figure 2.1: Left Monolayer Hubbard model. Fermionic particles in two different spin states (red and blue) are confined to a lattice structure. Tunnelling between neighbouring lattice sites is governed by the tunnelling amplitude t. Due to Pauli's exclusion principle each site can only be occupied by one fermion of each spin. Two fermions of different spins interact with each other with strength U if they are on the same lattice site. **Right** $HgBa_2CuO_{4+\delta}$ high temperature superconducting material. Two copper oxide layers are separated but coupled across a layer with Ba and Hg. Each individual CuO_2 layer has a square lattice structure similar to the square Hubbard model. Due to the oxygen atoms on the links between two respective Cu atoms in the CuO_2 planes, however, the Lieb lattice better reflects the actual structure of the CuO_2 planes than a simple squared Hubbard model. The bilayer Hubbard model takes into account the coupling between the two CuO_2 layers. The figure is taken from [8].

Experimental realisation of the Hubbard model with cold atoms

First experimental realisations of the *Bose*-Hubbard model with cold bosons in optical lattices [78] were made in three dimensions [67] and one dimension [143]. Realisations of the three dimensional Fermi-Hubbard model were achieved a little later [136] due to more intricate cooling of fermions caused by Pauli blocking.[2] With the successful implementation of quantum gas microscopes for bosons, the two-dimensional Bose-Hubbard model on a single site level could be investigated [7][139][6]. The study of the two-dimensional Fermi-Hubbard model on a single lattice site level using quantum gas microscopes followed

---

[2] Pauli blocking was experimentally observed in a cold atom experiment with optical lattices in [117].

again a few years later [29][70][120]. These experiments, however, suffered from parity projection. During fluorescence imaging of the fermionic atoms in the optical lattices light assisted collisions occurred and atoms on doubly occupied lattice sites were lost. Thus, only the parity of the occupation could be detected. The parity projection could be circumvented later in [117]. Other analogous quantum simulators were able to distinguish between empty, singly and doubly occupied sites or spin up and spin down states earlier, but had an imaging resolution slightly below the point spread function of a single lattice site [39]. For the simulation of the Fermi-Hubbard model the light element ^{6}Li and relatively heavy element ^{40}K were mostly in use. While the dynamics with ^{6}Li atoms are much faster and due to easier cooling the Hubbard regime $t, U < T$ can be reached easier, ^{40}K exhibits a richer hyperfine structure in the ground state for implementing spin-dependent potentials and spin-orbit coupling [30].

The experimental realisations of the Hubbard model were also achieved using optical tweezers. While optical lattices provide hundreds of lattice sites where atoms are loaded in, optical tweezers, in contrast, were employed to follow a bottom-up approach [9]. Here, single lattice sites can be subsequently connected to each other one by one enabling to form a large number of possible distinct, one and two-dimensional structures. By combining these optical tweezers with quantum gas microscopes the behaviour in two [114] to tens of lattice sites can be studied accurately [141].

2.1.2 Phase diagram of the Hubbard model

The properties of a fermionic gas in a lattice described by the Fermi-Hubbard model (Eq. 2.1) are determined by the parameters t, U and μ as well as by the temperature of the gas T. Depending on the parameter, the gas exhibits distinct phases which cross over in each other or undergo a phase transition when changing the parameters (Fig. 2.2).

2.1.2.1 Atomic and non-interacting limit

In the two limiting cases $t \rightarrow 0$ (atomic limit) and $U \rightarrow 0$ (non-interacting), the Hubbard Hamiltonian in Eq. 2.1 can be solved and studied analytically for a homogenous system, i.e. $\mu = 0$ and the third term in Eq. 2.1 becomes zero.

Atomic limit

In the atomic limit, $t = 0$ and $\mu = 0$, Eq. 2.1 reduces to the second term on the right hand side and the total energy equals the interaction energy. Then, in the Fock basis, the Hamiltonian is diagonal. Fock states with occupation numbers $0, 1$, e.g. $|1, 1, 1, 1, 1, ...\rangle$, have a total energy of $E = 0$. In contrast, Fock states with double occupations, e.g. $|1, 2, 1, 1, 1, ...\rangle$ possess energies of $E = U$. Here, a double occupation refers to an occupation of a lattice site with a spin up and a spin down particle and Pauli's exclusion principle forbids an occupation of a lattice site with more than two fermions. The state with double occupation is separated in energy from the state without double occupation by U. This

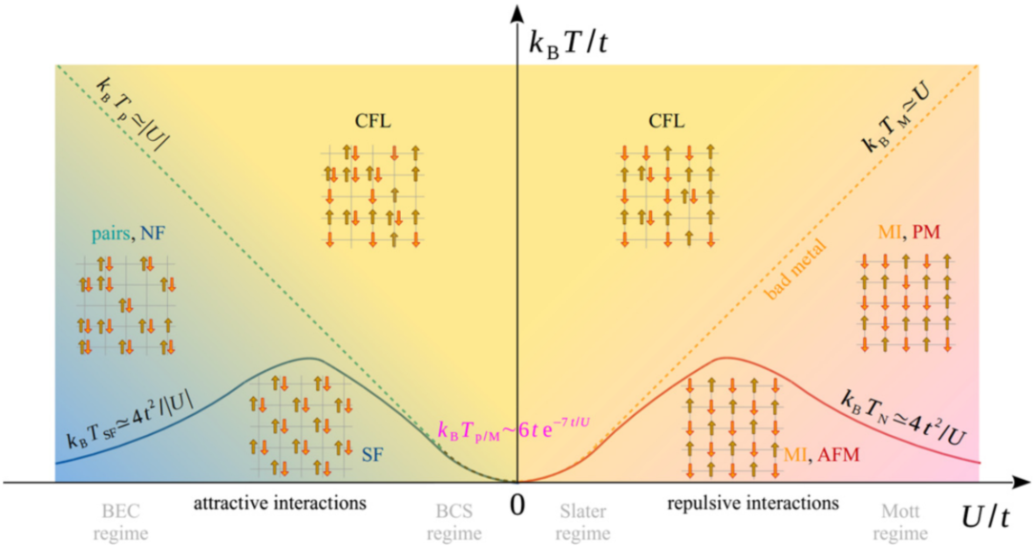

Figure 2.2: Schematic phase diagram of the Hubbard model as a function of temperature and interaction strength. For high temperatures a metallic state (correlated Fermi liquid CFL) is present. For increasingly strong repulsive interactions a smooth cross over from the metallic to a paramagnetic Mott insulating (MI,PM) state happens. For temperatures below the super exchange energy, a second order phase transition from the Mott insulator to an antiferromagnetic phase (AFM) with long range spin correlation in three dimensions exists. On the attractive side, the metallic state crosses over to a state with preformed pairs (normal fluid NF) for increasing attractive interactions. At temperatures below the super exchange energy a second order phase transition occurs. If the interaction are strongly attractive in this case, the preformed pairs form a Bose-Einstein condensate (BEC) of repulsively interacting hardcore bosons. For smaller attraction, the BEC crosses over in BCS pairs. This figure is taken from [146].

leads to two Hubbard bands, a lower and upper one (Fig. 2.3 left).[3]

In the atomic limit and for strong, repulsive interaction, $U \to \infty$, (Fig. 2.2, right side) states with double occupation lie in the upper Hubbard band and are energetically unfavourable for temperatures $k_B T < U$. Then, at half filling, i.e. with *in average* one fermion per lattice site $n = 1$, the ground state of the system tends to become a Mott insulator (MI) (cf. Fig. 2.2). In an *ideal* Mott insulator each lattice site is exactly occupied by one particle and reads in the Fock basis $|1, 1, 1, ...\rangle$. This Mott state is insulating since the transport of a conducting particle implicates double occupation when tunnelling to an already occupied site. This in turn would require an additional amount of energy U to occupy a state in the upper Hubbard band. Nickel oxide is a Mott insulator [111]. In cold atom experiments first Mott insulators were induced with bosonic atoms in three [67], two [6] and one [143] dimension. With fermionic atoms, Mott insulators were produced a

---

[3] For finite t, the band width of each Hubbard band in one spatial dimension is given by the dispersion relation $\epsilon_q = -2t\cos(aq)$ yielding a band width of $W = 4t$.

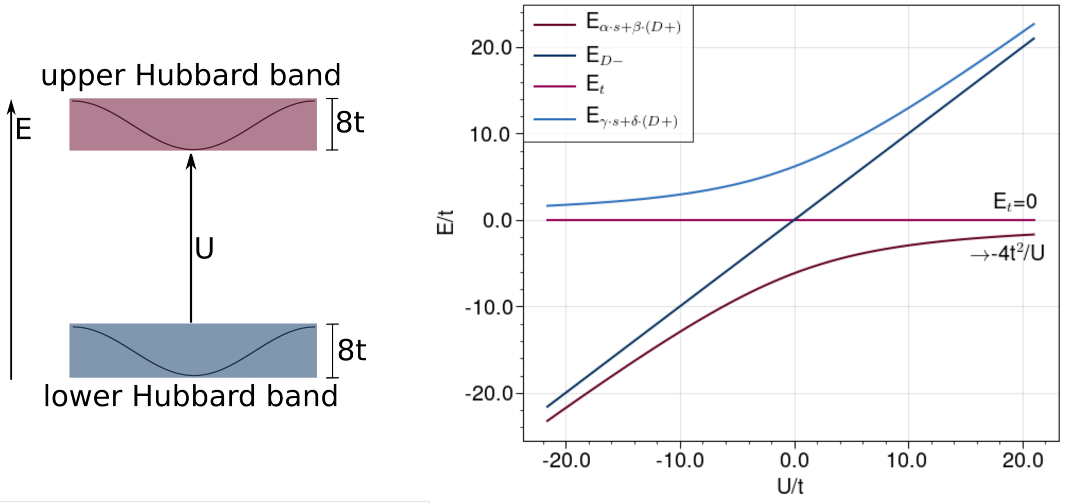

Figure 2.3: Left The upper and lower Hubbard band. Both are separated by the interaction strength U. For finite t, the bandwidth in one dimension is $4t$ and in two dimensions $8t$ where t is the tunnelling amplitude. **Right** Eigenenergies of the singlet, triplet and the $D_{+/-}$ state as a function of the ratio U/t. The spacing between the singlet and triplet state corresponds to the super exchange energy.

little later in three [136] and two [39] dimensions. The observation of a two-dimensional Mott insulator on a single lattice site level was achieved for example in [66][30]. A key feature of the Mott insulator is a vanishing compressibility κ [49]. The compressibility was measured in [39] and a vanishing $\kappa = 0$ was observed for strong interactions $U/t \approx 12$. For intermediate interactions, $U/t \approx 8$, the compressibility is strongly reduced. Another feature of a Mott insulator is a Mott gap in the spectral function where excitations are hindered due to the interaction strength U.

In the atomic limit and for strong, *attractive* interactions, $U \rightarrow -\infty$, (Fig. 2.2, left side) double occupation becomes favourable for temperatures $k_B T < |U|$. In this case preformed pairs form [146]. They consist of two fermions with one fermion in the spin up and one in the spin down state. Hence, the pair's total spin is zero and the pairs behave like hardcore bosons with nearest-neighbour repulsive interaction among each other [107]. This leads to charge density waves (CDW) in the regime of strong attractive interactions [73].

Non-interacting limit

The non-interacting (tight-binding) limit, $U = 0$ and $\mu = 0$ in Eq. 2.1, corresponds to the center of the phase diagram (Fig. 2.2). In this case, double occupancies in the lattice are energetically equivalent to single occupations or to empty sites. This leads to an equal probability of all occupations. Moreover, since $U = 0$, there is only a single Hubbard band. For unity filling (2 particles per site) the system enters a band insulating state where all energy states in the single Hubbard band are occupied and tunnelling between sites is suppressed by Pauli blocking. For smaller filling, however, the Hubbard band is only partially filled and tunnelling between sites is not hindered. This leads to

a metallic state which is compressible and exhibits a gapless excitation spectrum [66] in contrast to the Mott and band insulator. The Hubbard Hamiltonian in Eq. 2.1 in the non-interacting limit is analytically solvable like its counterpart in the atomic limit $t = 0$. Considering a homogenous system with $\mu = 0$, the second and third term on the right hand side of Eq. 2.1 drop out. In real space the resulting kinetic Hamiltonian is not diagonal due to the c_i and c_j referring to different lattice sites. By Fourier transforming $c^\dagger_{i,\sigma} \xrightarrow{\mathcal{F}} 1/\sqrt{N}\sum_l e^{iql} c^\dagger_{i,\sigma} =: c^\dagger_{q,\sigma}$, however, H_{Hub} can be diagonalised resulting in $H_{\text{Hub}} = -2t\sum_{q,\sigma}\cos(aq)\hat{n}_{q,\sigma}$ in momentum space in one dimension. Here, q, a are the quasi momentum and lattice constant, respectively. The dispersion relation of the Hubbard Hamiltonian $\epsilon_q = -2t\text{cos}(aq)$ thus corresponds to the ground band in a band structure calculation from the time-independent Schrödinger equation with a periodic potential (Fig. 2.6 left). The Hubbard Hamiltonian therefore reflects a single band approximation which remains valid as long as the Hubbard parameter are smaller than the band gap between the ground and first excited Bloch band, i.e. $t, U, k_{\text{B}}T < E_{\text{band2}} - E_{\text{band1}}$. Otherwise corrections have to be made to account for atoms in higher bands (PAM model) [107].
For a square lattice in two dimensions, the dispersion relation can be simply expanded because both dimensions are independent from each other. Hence, $\epsilon_q = -2t[\cos(aq_x) + \cos(aq_y)]$ in two dimensions [134]. The shape of the Fermi surface in two dimensions thus changes from circular (low filling) over diamond (half filling) to square (unity filling) when increasing the filling in the two-dimensional lattice. In the half filled case, the Fermi surface is perfectly nested with the nesting vector $Q = (\pi, \pi)$. Experimentally, the Fermi surface was measured in a three dimensional optical lattice [87].

2.1.2.2 Between the limiting cases, repulsive side

Between the limiting cases $U \to 0$ and $t \to 0$, for $U > 0$, (Fig. 2.2), a smooth cross over from the metallic state or Fermi liquid to a Mott insulating state occurs with increasing repulsive interaction strength. In this regime, the Hamiltonian H_{Hub} (Eq. 2.1) is not analytically solvable even in the homogeneous system, i.e. $\mu = 0$. High temperature series expansions and determinant quantum Monte Carlo methods can be employed in this case as done for this thesis (Fig. 4.14). Experiments with cold atoms in optical lattices elucidated this cross over experimentally for bosons and fermions in three [6][136], two [139][30][66] and one [143] dimension. Even if the behaviour for a large system is analytically intractable in this regime, important insights can be gained by analytically solving Eq. 2.1 for only two sites. Thus, the effect of tunnelling as well as on-site interactions can be taken into account. The matrix representation of H_{Hub} for two sites reads [42]

$$H^{\text{2sites}}_{\text{Hub}} = \begin{pmatrix} 0 & 0 & 0 & 0 \\ 0 & U & 0 & -2t \\ 0 & 0 & U & 0 \\ 0 & -2t & 0 & 0 \end{pmatrix} \tag{2.2}$$

within the basis which comprises a singlet and triplet state $s/t = 1/\sqrt{2}(|\uparrow,\downarrow\rangle \mp |\downarrow,\uparrow\rangle)$ as well as two states with doubly occupation $D_{+/-} = 1/\sqrt{2}(|\uparrow\downarrow, 0\rangle \pm |0, \downarrow\uparrow\rangle)$. Here, the triplet state with energy $E_{\text{triplet}} = 0$ and the D_- state with energy $E_{D-} = U$ are eigenstates.

The other two eigenstates are linear combinations of the singlet and D_+ state. For strong repulsive interactions, the energy of the ground state is approximated by $-4t^2/U$ (Fig. 2.3 right). The energy of the second lowest lying triplet state is 0 [121]. The energy difference between both states therefore amounts to $J = -4t^2/U$. This quantity is called the super exchange energy. In cold atom experiments it could be precisely determined and controlled in [148] and in a Floquet system in [42]. Furthermore and essentially, due to the dominant singlet part in the ground state, the latter is anti-ferromagnetic ordered contrarily to the higher lying triplet state. This implicates that a system which is cooled from a temperature $k_BT > 4t^2/U$ to $k_BT < 4t^2/U$ passes a second order phase transition in the spin sector from the paramagnetic Mott insulator discussed above to an anti-ferromagnetically ordered Mott insulator on the repulsive side of the phase diagram (Fig. 2.2). Experimentally, the two site Hubbard model was studied using cold atoms in optical tweezers [114][12]. A dimerised two-dimensional lattice which is effectively the realisation of many separated two site Hubbard models was furthermore studied in [65]. In these systems short range correlations between two spins on two adjacent sites were detected. Short range correlations in a common two-dimensional square lattice were studied in [37].

Likewise as in the two site Hubbard model, a phase transition from a paramagnetic Mott insulator to an anti-ferromagnetic ordered Mott insulator occurs in a lattice at temperatures $k_BT < 4t^2/U$. According to the Mermin-Wagner-Hohenberg theorem, this second order phase transition reveals anti-ferromagnetically long range order below the critical temperature. In three dimensions this critical Néel temperature is finite with a maximum at $T_N = 0.36t$ whereas in two dimensions the second order phase transition occurs only at zero temperature where quantum fluctuations diminish [146]. In the low temperature regime, mean-field theory, high temperature series expansions (HTSE) and determinant quantum Monte Carlo (DQMC) methods can be employed to compare theoretical predictions with experimental results from analogue quantum simulators. With DQMC, quantum states on 4×4, 8×8 or 16×16-site square lattice structures are commonly computed [26]. At very low temperatures, however, computational simulations of fermionic lattice models away from half-filling fail due to the sign problem [146]. In cold atom experiments with fermions in optical lattices, anti-ferromagnetic correlations were observed in two dimensions [47]. The observation of an anti-ferromagnet with singe site resolution using a quantum gas microscope was achieved in [72][28][120][101][21]. Anti-ferromagnetic correlations in Hubbard chains were detected in [19].

Heisenberg spin model

For strong repulsive interactions where tunnelling is strongly suppressed, the Hubbard model is simplified to the Heisenberg spin model $H_{\mathrm{Hei}} = J \sum_{\langle i,j \rangle} \vec{S}_i \vec{S}_j$ which, in turn, simplifies to the Ising model $H_{\mathrm{Ising}} = J \sum_{\langle i,j \rangle} S_i^z S_j^z$ when considering only one direction [125]. These models describe individual spins on a lattice with nearest neighbour spin-spin coupling where the parameter J denotes the coupling strength. For $J > 0$ the ground state is anti-ferromagnetically ordered and for $J < 0$ ferromagnetically. An important connection to the Hubbard model can be made by comparing the energy states of both models: The two site Heisenberg model has one lowest singlet state with energy $-3J/4$ and a degenerated triplet state with energy $J/4$. The two site Hubbard model has two levels with energies $-4t^2/U$ and 0. Thus, $J = -4t^2/U$ which is just the super exchange energy [121].

In cold atom experiments, Ising spin chains were studied with spinless bosons in a tilted optical lattice in [140]. The computational simulation of spins on more than two sites is usually performed using the method of Young tableaux [131] which was done for four sites in [153].

2.1.2.3 Between the limiting cases, attractive side

On the attractive side of the phase diagram (Fig. 2.2) and for finite t, the ground state is increasingly dominated by doubly occupancies for increasing attractive interactions. In a lattice, above the critical temperature $k_BT > 4t^2/U$ and for temperatures $k_BT < U$, preformed pairs form an incoherent normal fluid phase which is referred to as pseudo-gap regime [146]. This regime exhibits a reduced density of states at the Fermi energy [22]. By reducing the temperature to below $k_BT < 4t^2/U$ at strong attractive interactions, a quantum phase transition in three dimensions to a Bose Einstein condensate (BEC) of strongly bound fermionic pairs occurs. This condensation was observed with cold atoms in a three dimensional trap in [79][157]. In a three dimensional optical lattice, Bose Einstein condensation of fermionic pairs was seen by detecting interference peaks [33]. These peaks signal long range order which, in turn, indicates superfluidity. Furthermore, transport and expansion of fermions in three dimensional optical lattices as a function of the attractive interaction strength were studied in [144][137] and [69], respectively.

For decreasing attractive interactions below the critical temperature $k_BT < 4t^2/U$ the pairing energy decreases and a cross over from a BEC type to a Bardeen Cooper Schrieffer (BCS) type superfluid at small attractive interactions occurs [126]. Experimentally, this pairing energy was measured in a three dimensional trap without an optical lattice for different interaction strengths by radio frequency spectroscopy [31]. Here, the observation of an energy gap in the low energy excitation spectrum revealed the superfluid regime at sufficient low temperatures. The low energy excitation spectrum was likewise investigated in [142] establishing photoemission spectroscopy in cold atom experiments. With the improvement to angle-resolved photoemission spectroscopy (APRES) within a quantum gas microscope the single particle spectrum for attractively interacting fermions in a two-dimensional lattice could be experimentally measured [22]. APRES is widely used in solid state physics. Theoretically, the two-dimensional case was studied in [133][110][118]. [4] Moreover, the second order pair correlation function was examined in [25] to study the pairing behaviour as a function of the interaction strength and of the filling.

2.1.2.4 Particle-hole symmetry

The Hubbard model exhibits the important so-called particle hole symmetry (PHS) [134]. To discuss this, the third term of Eq. 2.1 is first rewritten as [58]

---

[4] In two dimensions, a Berezinskii–Kosterlitz–Thouless (BKT) transition from a normal to a superfluid phase occurs at finite temperatures only away from half-filling.

$$\sum_{i,\sigma} \mu_{i,\sigma} \tilde{n}_{i,\sigma} = \mu \sum_{i,\sigma} \tilde{n}_{i,\sigma} + h \sum_{i} (\tilde{n}_{i,\uparrow} - \tilde{n}_{i,\downarrow}). \tag{2.3}$$

This equation emphasizes two contributions to the Hubbard Hamiltonian. The first term on the right hand side accounts for a variation in the total density which is adjusted by the chemical potential μ. Here, $\mu_{i,\sigma} = \mu$ is assumed to be site and spin independent. The second term accounts for a spin-imbalance between the spin up $\tilde{n}_{i,\uparrow}$ and spin down $\tilde{n}_{i,\downarrow}$ populations which is adjusted by the effective (magnetic) Zeeman potential h.

Furthermore, the particle hole *transformation* is given by

$$c_{i,\uparrow} \rightarrow c_{i,\uparrow} \tag{2.4}$$

$$c_{i,\downarrow} \rightarrow (-1)^{(i_x+i_y)} c^{\dagger}_{i,\downarrow}. \tag{2.5}$$

It transforms the Hubbard Hamiltonian (Eq. 2.1) by swapping the sign of the interaction strength $U \rightarrow -U$ and exchanging the parameters $\mu \leftrightarrow h$ in Eq. 2.3. Thus, due to $U \rightarrow -U$, the attractive and repulsive side of the phase diagram (Fig. 2.2) are related to each other by this transformation. The exchange of $\mu \leftrightarrow h$, however, causes that a doping away from half-filling translates to a spin-imbalance on the other side of the phase diagram. So, at half-filling and in a spin-balanced system for example, the transformation translates a Mott insulator (anti-ferromagnetically order state) on the repulsive side of the phase diagram to preformed pairs (charge density wave) on the attractive side [73]. For theoretical calculations the particle hole transformation can be employed in order to simulate the Hubbard model on the attractive side and deduce its behaviour on the repulsive side where the sign problem hinders the computation in the low temperature regime [22]. In cold atom experiments the particle hole transformation was experimentally verified in [58]. As mentioned, the cuprates does not exhibit the particle-hole symmetry as reflected in their non-symmetric phase diagram (Fig. 1.1). To account for this in cold atoms gas experiments, the Lieb lattice can be employed or next-nearest neighbour tunnelling can be included.

2.1.3 Bilayer Hubbard model

The bilayer Hubbard model extends the monolayer Hubbard model by a second layer which is coupled to the first one (Fig. 2.4 left). Its Hamiltonian reads [135][20]

$$\begin{aligned} \hat{H}_{\text{biHub}} = & -t \sum_{\langle i,j, \rangle, l, \sigma} (\hat{c}^{\dagger}_{i,l,\sigma} \hat{c}_{j,l,\sigma} + \hat{c}^{\dagger}_{j,l,\sigma} \hat{c}_{i,l,\sigma}) \\ & - t_{\perp} \sum_{i,\sigma} (\hat{c}^{\dagger}_{i,1,\sigma} \hat{c}_{i,2,\sigma} + \hat{c}^{\dagger}_{i,2,\sigma} \hat{c}_{i,1,\sigma}) \\ & + U \sum_{i,l} \tilde{n}_{i,l,\uparrow} \tilde{n}_{i,l,\downarrow} - \sum_{i,l,\sigma} \mu_l \tilde{n}_{i,l,\sigma}. \end{aligned} \tag{2.6}$$

As in the monolayer Hubbard Hamiltonian (Eq. 2.1), t, U, μ denote the intra-plane tunnelling amplitude, the on-site interaction strength and the chemical potential, respectively. The new quantity is the inter-plane tunnelling amplitude $t_\perp$ governs the second term on the right hand side of Eq. 2.6. It describes the tunnelling strength across the two planes of the bilayer system. The index $l = 1, 2$ denotes the respective plane. The chemical potential μ_l is plane dependent such that the filling of each plane can be adjusted separately. The meaning of the other variables is described for Eq. 2.1.

In the non-interacting limit, $U = 0$, and for $\mu_l = 0$ the last two terms in Eq. 2.6 vanish. In this case the dispersion relation reads

$$\epsilon_\pm(q_x, q_y) = \pm t_\perp + 2t[\cos(q_x) + \cos(q_y)]. \tag{2.7}$$

For $t_\perp = 0$, this reduces to the dispersion relation of the two-dimensional Hubbard model. For $t_\perp \neq 0$, however, a bonding (-) and an anti-bonding (+) band exist with a band width of $8t$ each (cf. Fig. 2.3 left). Thus, a metallic state constitutes between $t_\perp = 0 - 4t$ where both bands still overlap. In contrast, above $t_\perp = 4t$ a band insulating state forms due to a completely filled lower bonding band which is separated from the anti-bonding band. At half-filling both bands are perfectly nested by the vector $Q = (\pi, \pi)$.
For infinite, repulsive interactions $U \to \infty$ the bilayer Hubbard model reduces to the bilayer Heisenberg model. The latter exhibits a quantum phase transition at $t_\perp = 1.588t$ from an intra-plane anti-ferromagnetically ordered state in both planes at small $t_\perp$ to a band insulating state of inter-layer singlet bonds at high $t_\perp$ [132].
In order to study the phase diagram of the bilayer Hubbard model (Fig. 2.4 right) including repulsive interactions and varying $t_\perp/t$, different theoretical methods where employed, e.g. cluster dynamical mean field theory [80] or determinant Quantum Monte Carlo methods [63][129]. While [80] predicted a large metallic phase for small to intermediate U, the phase diagram of [63] exhibits a metallic phase only in the non-interacting limit and in [129] a metallic phase does not arise at all.

The cross-over between an intra-plane anti-ferromagnetically ordered state in both planes at low ratios $t_\perp/t$ and a band insulating state of inter-layer singlet bonds at high $t_\perp/t$ was measured during this thesis for the first time for different interaction strengths (Fig. 4.27 right).

2.2 Wannier functions in a superlattice

The realization of the bilayer Hubbard model (Sec. 2.1.3), with cold atoms using two mono- and one bi-chromatic optical lattice as described in this thesis requires a precise calibration of the lattices. The calibration methods which were used throughout this thesis base in general on the comparison between measurements and theoretical predictions of atoms in the optical lattice system.
In this chapter the theory of localized particles in a mono- or bichromatic lattice potential is elucidated enabling for the theoretical predictions. In Sec. 2.2.1 the general

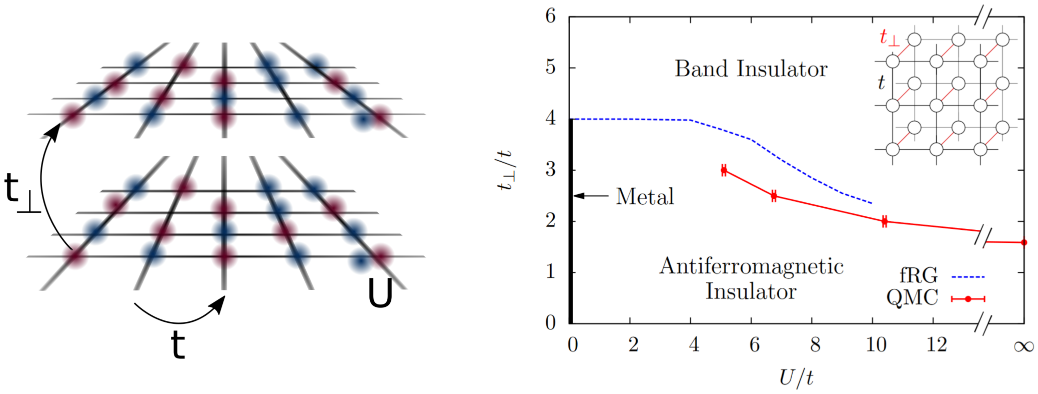

Figure 2.4: Left Bilayer Hubbard model (cf. Fig. 2.1 for the monolayer Hubbard model). The additional tunnelling parameter $t_\perp$ couples the upper and lower plane. **Right** Phase diagram of the bilayer Hubbard model as a function of $t_\perp/t$ (y-axis) and U/t (x-axis). At strong inter-plane coupling $t_\perp/t \gg 1$, a band insulating (BI) state is present with individual singlet bonds between the layers. In contrast, at small inter-plane coupling, intra-layer antiferromagnetic (AFM) spin correlations reveal. A metallic state persists only in the non-interacting case. There, at values $t_\perp/t < 4$, the two Hubbard bands with width $W = 8\,\mathrm{t}$ (cf. Fig. 2.3 left) overlap which give rise to a metallic state. The cross over between the BI and AFM is smooth. In the limit of strong repulsive interactions, the Hubbard model reduces to the Heisenberg model where a phase transition from a BI to an AFM happens at $t_\perp/t = 1.588$. The figure is taken from [63].

superlattice potential is discussed. Subsequently, the computation of Wannier functions in this potential is presented (Sec. 2.2.2). The Wannier functions are employed thereafter to calculate the Hubbard parameters t, $t_\perp$ and U (Sec. 2.2.3). Finally, in Sec. 2.2.4, the discussion is extended from non-interacting Wannier functions to interacting Wannier functions. This enables to match experimental measurements of the interactions strength in the superlattice with theoretical expectations.

2.2.1 Superlattice potential and band structure

A general superlattice potential in one spatial dimension can be written as [84]

$$V_{sl}(z) = -V_l \cos^2(k_l z - \phi) + V_s \cos^2(k_s z). \tag{2.8}$$

Here, V_l and V_s are the lattice depths of the “long” and “short” lattice with wavelength λ_l and λ_s, respectively. In the following, for explanation and plotting purposes, the wavelengths are chosen to be $\lambda_l = 1064\,\mathrm{nm}$ and $\lambda_s = 532\,\mathrm{nm}$. Furthermore, V_l and V_s are given by the light shift (Eq. 1.1). The long lattice has a wave number of $k_l = 2\pi/\lambda_l$ and the short lattice of $k_s = 2\pi/\lambda_s$. The phase ϕ shifts the long lattice with respect to the short lattice. The sign -/+ of the individual potentials arises due to the red-/ blue-detuning of the 1064 nm / 532 nm lattice laser with respect to the main optical resonance at 766 nm in potassium.

The parameters V_l, V_s and ϕ affects the depth and shape of the superlattice (Fig. 2.5). For $V_s = 0$, the superlattice turns into a monochromatic lattice potential. A change of the long lattice depth V_l then changes the height of this monochromatic lattice (Fig. 2.5 left). A change in the phase ϕ moves the monochromatic potential along the spatial x-axis. Such a monochromatic lattice is used as two-dimensional, lattice in the experimental setup (Fig.3.10).

In a *superlattice* configuration ($V_l \neq 0$, $V_s \neq 0$) with $\phi = 0$, an increasing short lattice depth V_s leads to a change in the barrier height (Fig. 2.5 center). For larger short lattice depths the double well center barrier increases. Simultaneously, the two potential minima move outwards with respect to the center barrier. A configuration with $\phi = 0$ as shown in Fig. 2.5 is called "symmetric superlattice configuration" or "superlattice at the symmetry point". An increase of the long lattice depth V_l (not shown in Fig. 2.5) increases the depth of the whole lattice. In this case, the potential minima move inwards, i.e. towards the center barrier.

The superlattice phase ϕ induces a tilt between two adjacent sites in the superlattice (Fig. 2.5 right). The phase period is $\pi/2$, meaning that the symmetric superlattice configuration reveals periodically for $\phi \in z \cdot \pi/2$ with $z \in \mathbb{Z}$. The potential minima, however, shift continuously along the spatial x-axis if the superlattice phase is varied from one to another symmetric configuration. The latter effect only occurs when the phase ϕ goes into the long lattice potential in Eq. 2.8, i.e. $k_l \cdot z - \phi$. Contrarily, if the phase goes into the short lattice potential, the potential minima do not shift. A so-called Thouless pump makes use of this continuous shift [96]. The configuration at $\phi = \pi/4$ is called antisymmetric.

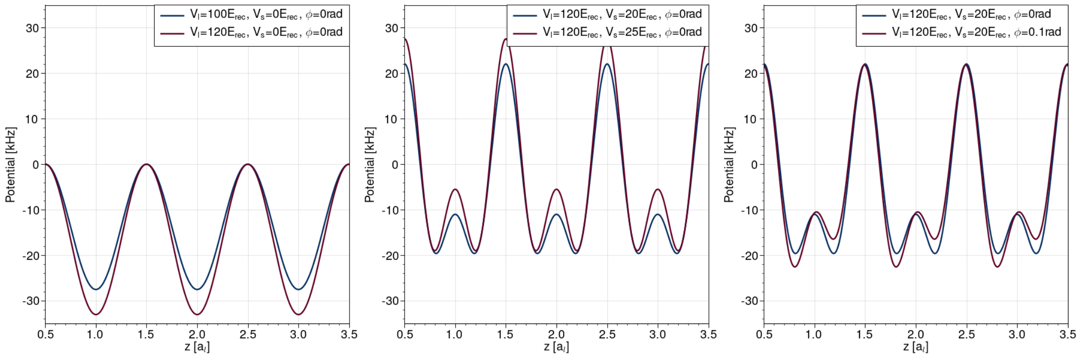

Figure 2.5: Superlattice potential. **Left** For vanishing short lattice potential, the superlattice turns into a monochromatic optical lattice whose depth depends on the amplitude V_l. **Center** An increase of the short lattice amplitude V_s in a symmetric superlattice configuration $\phi = 0$ leads to a higher barrier. The double well center barrier height changes while the potential minima moves with respect to the center barrier. **Right** A change in the superlattice phase tilts the superlattice potential. The symmetric configuration reveals for $\phi \in z \cdot \pi/2$ with $z \in \mathbb{Z}$ but with a spatial displacement of the entire lattice along the x-axis.

Eigenenergies and eigenfunctions in the superlattice

In the superlattice potential, eigenenergies and eigenfunctions for non-interacting, massful particles are computed from the superlattice Hamiltonian

$$\hat{H}_{sl} = \hat{H}_{sl}^{kin} + \hat{H}_{sl}^{pot} = -\frac{\hbar^2}{2m}\partial_z^2 + V_{sl}, \tag{2.9}$$

where m is the particle mass, $\hbar$ is the reduced Planck's constant and ∂_z^2 is the second spatial derivative with respect to the coordinate z. As in the case of a monochromatic lattice [86], the superlattice potential breaks the continuous translational symmetry but preserves a discrete one which is, in real space, the translation of the potential by the long lattice constant a_l. In Fourier space, according to Bloch's theorem, the discrete translational symmetry manifests such that only plane waves that differ by the reciprocal lattice vector $G = 2\pi/a_l$ contribute to individual eigenfunctions of $\hat{H}_{sl}$. The eigenfunctions which are referred to as Bloch functions can therefore be written as

$$\psi_q(z) = \sum_l u_q^l(z) \cdot e^{i(q+Gl)z}. \tag{2.10}$$

Here, q is the lattice momentum which is the conserved quantity according to Noether's theorem and the functions $u_q^l(z)$ have the same spatial period as the superlattice. The determination of the eigenfunctions $\psi_q(z)$ of $\hat{H}_{sl}$ thus reduces to the computation of the elements $u_q^l(z)$. The latter can be interpreted as weights of the plane waves with wave number $q + lG$ which contribute to the Bloch wave $\psi_q(z)$. In order to obtain $u_q^l(z)$, the matrix elements $\exp(i(q+Gl)z)^*\hat{H}_{sl}\exp(i(q'+Gl')z)$ are calculated and the resulting matrix[5] [84]

$$\hat{H}^{ll'} = \left(2V_s - \frac{V_l}{2}\right)\cdot \mathbb{1} + \begin{pmatrix} \ddots & & & & & & \\ & (q-4)^2 & -\frac{V_l}{4}e^{2i\phi} & V_s & 0 & 0 & \\ & -\frac{V_l}{4}e^{-2i\phi} & (q-2)^2 & -\frac{V_l}{4}e^{2i\phi} & V_s & 0 & \\ & V_s & -\frac{V_l}{4}e^{-2i\phi} & q^2 & -\frac{V_l}{4}e^{2i\phi} & V_s & \\ & 0 & V_s & -\frac{V_l}{4}e^{-2i\phi} & (q+2)^2 & -\frac{V_l}{4}e^{2i\phi} & \\ & 0 & 0 & V_s & -\frac{V_l}{4}e^{-2i\phi} & (q+4)^2 & \\ & & & & & & \ddots \end{pmatrix} \tag{2.11}$$

is diagonalized. The lattice depths V_l and V_s are given in units of the recoil energy $E_{\text{rec}} = \frac{\hbar^2 k^2}{2m}$. Due to the discrete translational symmetry, the lattice momentum q is restricted to values

$$q \in \left[\frac{\pi}{a_l}\left(-1 + \frac{2}{L}\right) + k \cdot \frac{2\pi}{a_l L}, \frac{\pi}{a_l}\right] \tag{2.12}$$

---

[5] In order to compute the matrix elements, Euler's formular to rewrite the superlattice potential $V_{sl}(z)$ in terms of exp-functions as well as the equality $\int \mathrm{dz}\, \exp(i(n-m)z) = \delta_{nm}$ is employed.

with $k = 0, 1 \dots$. Here, L represents the number of double wells in the superlattice [14]. The diagonalization of $\hat{H}^{ll'}$ and computation of its eigenvectors $u_q(z)$ and eigenvalues v_q^E is numerically performed in this thesis with the python method *eigh* from the scipy.linalg library for $q \pm 2m$ with $m \in [-10, 10]$. The eigenvalues are also referred to as eigenenergies.

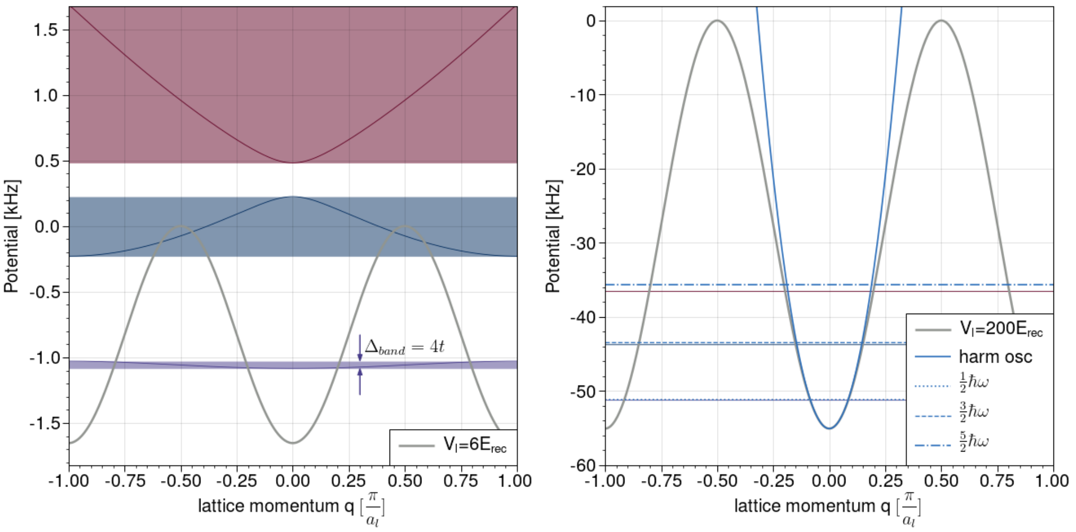

Figure 2.6: Bandstructure in a monochromatic lattice. **Left** Band structure of the first three bands in a shallow lattice with depth of $V_l = 6\,\mathrm{E}_{\mathrm{rec}}$ and lattice constant a_l. This lattice configuration is used to create a two-dimensional Hubbard system (Sec. 4.2.2). The band energy depends strongly on the lattice momentum q. The width of the first band is given by four times the tunnelling amplitude. **Right** Band structure of a deep lattice. Such lattice configurations are used e.g. to freeze the motion in a lattice or calibrate the lattice depth. The bands are flattened and each well can be approximated by the harmonic oscillator potential. The first three harmonic oscillator levels are depicted for comparison.

For a shallow, monochromatic lattice with depth of $V_l = 6\,\mathrm{E}_{\mathrm{rec}}$ and lattice constant a_l, as it is used for the two-dimensional lattice in the experimental setup (Fig.3.10), the eigenenergies strongly depend on the lattice momentum q (Fig. 2.6 left). This leads to so-called energy bands (Fig. 2.6 left, shaded regions) which together form the band structure. The bands are separated due to the periodic potential and a transition between two of them can only occur if the lattice momentum q is conserved. This results from the calculation of the matrix elements $\hat{H}^{ll'}$. Throughout this thesis, the bands are numbered starting from the 0^{th} band which is the ground band. The first excited band is called 1^{st} band etc.. The band width of the ground band is given by $\Delta_{\mathrm{band}} = 4t$ which is equivalent to the band width in the non-interacting Hubbard model (Fig. 2.3 left).

In contrast, for a deep, monochromatic lattice with depth of $200\,\mathrm{E}_{\mathrm{rec}}$ and lattice constant a_l, the bands are flattened and the gaps between the bands are increased compared to the shallow lattice (Fig. 2.6 right). The deep lattice can be approximated by a harmonic oscillator potential with [86]

$$V_{\mathrm{harO}}(z) = \frac{m}{2}\omega_{\mathrm{harO}}^2 z^2 \qquad \text{with} \qquad \omega_{\mathrm{harO}} = 2\sqrt{V_l}\frac{E_{\mathrm{rec}}^{\mathrm{z1064}}}{\hbar}. \tag{2.13}$$

Here, m, ω_{harO}, V_l and E_{rec}^{z1064} are the mass of the particle in the harmonic potential, the angular harmonic oscillator frequency and the lattice depth in units of its recoil energies $E_{\mathrm{rec}}^{\mathrm{z1064}}$, respectively. The eigenenergies of the harmonic oscillator potential are given by $E_n = \hbar\omega(n + 1/2)$ (Fig. 2.6 right). For higher bands the discrepancy between the eigenenergies of the harmonic oscillator potential and the monochromatic lattice potential increases. The band structure of a monochromatic lattice will be compared to experimental data at a later point in order to calibrate the lattice depth of each lattice via lattice modulation spectroscopy (Sec. 4.1.1).

In contrast to the band structure of the monochromatic lattice, the band structure in a superlattice consists of pairs of bands (Fig. 2.7 left). Again, for large lattice depths of $V_l = 120\,\mathrm{E}_{\mathrm{rec}}$ and $V_s = 20\,\mathrm{E}_{\mathrm{rec}}$ in the symmetric configuration, the bands are flattened out. The formation of pairs of bands in the band structure becomes clearer by considering the band energy as a function of the short lattice depth (Fig. 2.7 center). By increasing the latter, the bands that belong to a pair approximate each other. In the limit for large, short lattice depths, the superlattice transforms into a monochromatic lattice and the two bands of each pair transform to a single band. This cross over from two into a single band can also be understood in terms of the Brioullin zone. The Brioullin zone is the primitive cell of the reciprocal lattice and, hence, in one dimension for a monochromatic lattice with short lattice constant a_s, it contains lattice momenta $q \in [-\pi/a_s, \pi/a_s]$. Contrarily, in a superlattice, the Brioullin zone contains lattice momenta $q \in [-\pi/a_l, \pi/a_l]$ (Eq. 2.12) where the long lattice constant $a_l = 2 \cdot a_s$. Thus, the Brioullin zone of the superlattice has a width half of the Brioullin zone of the monochromatic lattice with short lattice constant a_s. In the limit when the superlattice transforms to a monochromatic lattice for an increasing short lattice depth, the picture of unfolding the Brioullin zone of the superlattice to the Brioullin zone of the monochromatic lattice can be stressed. Conversely, starting from a monochromatic lattice with short lattice constant a_s and turning on the second lattice with long lattice constant a_l such that a superlattice forms, the picture of folding the larger Brioullin zone of the monochromatic lattice into the Brioullin zone of the superlattice can be drawn. This can be seen as the origin of the two bands of one pair arising from folding the band at the edge of the superlattice Brioullin zone where $q = \pi/a_l$.

The phenomenon of "avoided crossing" of energy bands in a superlattice becomes visible when considering the band energy as a function of the superlattice phase ϕ (Fig. 2.7 right). The energy gap between the ground and first excited band first increases as a function of ϕ up to 0.16. The band energy of the 2^{nd} excited band, however, decreases in this range. This would lead to a crossing of the energy bands of the first and second excited band. In order to avoid this crossing, however, the energies start to de- and increase again for phases $\phi > 0.16$. The same happens at higher phases with the 2^{nd} and 3^{rd} as well as with the 3^{rd} and 4^{th} band.

With the definitions of the superlattice potential as in Eq. 2.8 and the phase factor in

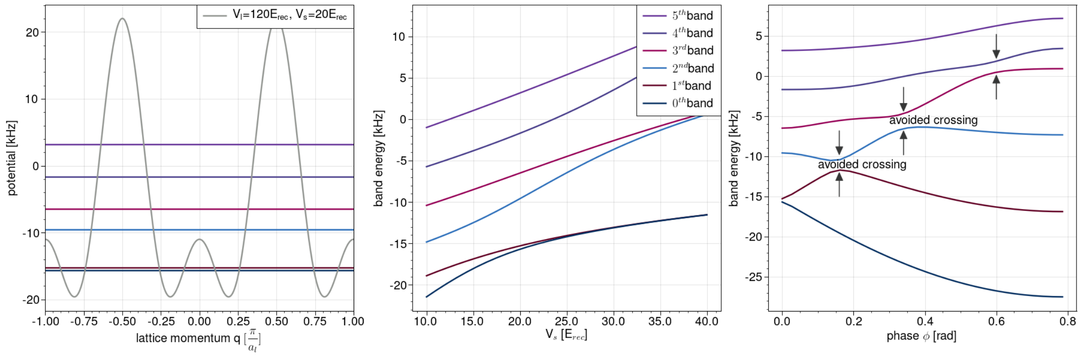

Figure 2.7: Bandstructure in a bi-chromatic lattice. **Left** First six energy bands in a deep, symmetric superlattice with $V_l = 120\,\mathrm{E_{rec}}$ and $V_s = 20\,\mathrm{E_{rec}}$. The energy bands are flat and arises as pairs. **Center** For increasing short lattice depths V_s, the two energy bands within one pair approximate each other. In the limit of high V_s, the superlattice approaches a monochromatic lattice the two bands goes over into a single band. **Right** Avoided crossing of energy bands as a function of the superlattice phase.

the Hamiltonian Eq. 2.11 the superlattice's periodicity in phase matches the periodicity of the band structure.

2.2.2 Non-interacting, maximally-localised Wannier functions

Bloch waves $\psi_q^n(z)$ in band n and with lattice momentum q given by Eq. 2.10 extend over the whole lattice. Numerically, they are computed by inserting the eigenvectors $u_q(z)$ from $\hat{H}^{ll'}$ in Eq. 2.10. In order to gain a more intuitive understanding of physical processes of particles in a super- or monochromatic lattice, however, it is convenient to work with functions localized to individual lattice sites. One possibility to achieve this is to Fourier transform the set of orthonormal Bloch functions to a complete, orthonormal set of so-called Wannier functions $w^n(z - a_l l)$. Here, n is the band index and l is the index of the l^{th} well of the lattice or l^{th} double well in case of a superlattice. Therefore,

$$w_l^n(z - a_l l) = \frac{1}{\sqrt{L}} \sum_{q=-\pi/a_l}^{\pi/a_l} e^{-iqa_l l} \psi_q^n(z). \tag{2.14}$$

This set of localized Wannier functions, however, is not unique. Multiplying the set of Bloch functions by a complex phase factor $\psi_q^n(z) \rightarrow e^{i\phi(n,q)} \cdot \psi_q^n(z)$ gives a different, complete set of Bloch functions and, hence, a different set of Wannier functions. The chosen gauge of $\phi(n, q)$ of the Bloch waves determines thereby the spread of the resulting individual Wannier functions while keeping their center modulo the lattice site index unchanged [99]. Thus, in order to define a unique set of Wannier functions an additional condition (a gauge) to the Wannier functions is required. One plausible gauge is the one which leads to the Wannier functions with *minimum* spatial spread or, in other words, maximally-localized Wannier functions. The idea of how the spread of Wannier functions can be minimized by the correct gauge is pictorially described in [14]: Considering a Wannier function localized at lattice site l, then, its spread is minimized by choosing the phase $\phi(n,q)$ of the Bloch functions in band n such that all Bloch functions for different q constructively interfere at site l. A straightforward ansatz to compute the set of maximally localized Wannier functions is the band projection position operator (BPPO) method [82]. The equivalence between the Wannier functions resulting from this BPPO ansatz and the Wannier functions with minimum spread due to the correct gauge from the definition in Eq. 2.14 was demonstrated in [99]. The BPPO ansatz was applied to a superlattice in [108].

The BPPO approach employs the projection operator $\hat{P}_n = \sum_q |n,q\rangle \langle n,q|$ onto band n. Here, $|n,q\rangle$ is the Dirac notation for the Bloch function $\psi_q^n(z)$ and its complex conjugated is denoted as $\langle n,q|$. The projected *position* operator follows as $\hat{x}_n^{\mathrm{proj}} = \hat{P}_n \hat{x}_n \hat{P}_n$ [82]. The maximally localized Wannier functions $|n,l\rangle$ in band n at lattice site l are defined as eigenstates of this band projected position operator $\hat{x}_n^{\mathrm{proj}} |n,l\rangle = l \cdot a_l |n,l\rangle$. In order to explicitly compute the Wannier functions, the matrix elements $\chi_{qq'}^{nn'} = \langle n,q| \hat{x}_n^{\mathrm{proj}} |n',q'\rangle$ are first calculated. They read for two involved bands n and n' [14]

$$\begin{aligned}\chi_{qq'}^{nn'} = a_l e^{\frac{i\cdot a_l}{2}(q-q')} \\ \cdot \Bigg[\delta_{qq'} \cdot \left(\frac{L-1}{2} + (-1)^{m-m'} \frac{i}{2\pi(m-m')} \right) (u_q^n)^* \cdot u_{q'}^{n'} \\ + (1-\delta_{qq'}) \cdot \frac{i}{a_l(q-q')} (u_q^n)^* \cdot u_{q'}^{n'} \\ + (1-\delta_{qq'}-\delta_{mm'}) \cdot (-1)^{m-m'} \cdot \frac{i}{2\pi(m-m') + a_l(q-q')} (u_q^n)^* \cdot u_{q'}^{n'} \Bigg],\end{aligned} \tag{2.15}$$

Here, the u_q^n's are the eigenvectors of the matrix $\hat{H}^{ll'}$ (Eq. 2.11), the index m takes values $m \in [-10, 10]$ throughout this thesis to limit the needed computation time for diagonalization[6] and the lattice momentum $q \in [\pi/a_l(-1+2/L) + k \cdot \frac{2\pi}{a_l L}, \pi/a_l]$ with $k = 0, 1, \ldots$. Again, the number L corresponds to the number of double wells in the considered superlattice [14]. The diagonalization of the resulting matrix with elements given by Eq. 2.15 leads to a basis transformation from $n, q \rightarrow l, m$. The new index m represents the m^{th} localized state within the l^{th} double well. This localized state is constructed by

$$b_{lm}(z) = \sum_{n,q} \chi_{l,m}^{n,q} \cdot \psi_q^n(z). \tag{2.16}$$

---

[6] Theoretically, all bands form a complete basis set of orthonormal function which are needed to compute Wannier function with *minimum* spread. The restriction to $m \in [-10, 10]$ and, thus, 21 bands is, however, sufficient here to calculate the Hubbard parameters and compare them with experimental measurements.

Hence, the elements of the eigenvectors $\chi_{l,m}^{n,q}$ for fixed l, m represents the weights for the corresponding Bloch functions with lattice momentum q in band n.
For two bands, i.e. $n, n' \in \{1, 2\}$ in Eq. 2.15, the resulting matrix 2.15 is a two-by-two block matrix and has dimensions of $(2 \times \mathrm{N}_q) \times (2 \times \mathrm{N}_q)$ where N_q denotes the number of possible q states in the superlattice. Here, N_q is given by the width of the interval $[\pi/a_l(-1+2/L), \pi/a_l]$ divided by the spacing $2\pi/(a_l L)$. Consequently, the basis transformation $n, q \to l, m$ leads to two localized states with index $m \in \{1, 2\}$ per each of the eleven double wells. Thus, there is one localised state in the left and one in the right well (Fig. 2.8 left). The offset of both states is here set to the ground state energy in the superlattice where the bands are considered to be flat.[7]
For four bands, i.e. $\{1, 2, 3, 4\}$ in Eq. 2.15, it yields a four-by-four block matrix and, consequently, four localized states arises with index $m = 1, .., 4$. Their offset is set to the energy of the 1st excited, flat band in the superlattice (Fig. 2.8 left). The four eigenvectors of these four localized states (Eq. 2.16) have four corresponding eigenvalues (Fig. 2.8 center, inset). These eigenvalues correspond to the center of mass of the corresponding localized states [14]. Thus, two eigenvalues are located in the left and two in the right well of the corresponding double well.
All eigenvalues of the diagonalized matrix in Eq. 2.15 together appear in eleven groups since the superlattice is formed by $L = 11$ double wells (Fig. 2.8 center).

Taking more than two bands into account in Eq. 2.16 in order to compute localized states, has to be treated with caution. If the superlattice phase is for example set to $\phi = 0.2\,\mathrm{rad}$, mixing of the two lowest bands leads to two localized states in the lower well of the double well which are both, however, not centred in the well (Fig. 2.8 right). The reason for that can be understood considering the band structure of the superlattice (Fig. 2.7 right). In the symmetric configuration, i.e. $\phi = 0$, the two lowest energy levels arises as a pair. Here, both levels have a similar energy. Consequently, mixing of these bands is suitable and leads to well localized states (Fig. 2.8 center). For a phase of $\phi = 0.2\,\mathrm{rad}$, however, the 1st and 2nd excited band are close to each other while the ground band has a much lower energy (Fig. 2.7 right). Thus, in order to obtain localized states, the lowest band needs to be treated alone while the 1st and 2nd excited band are mixed. In this thesis, the calculations for the calibration of the superlattice was restricted to a single or two bands. The mixing of more bands as discussed in this section for four bands is primarily performed in order to demonstrate the construction of higher band Wannier functions. The latter is needed e.g. in the context of the lattice depth calibration via lattice modulation spectroscopy (Sec. 4.1.1). Here, excitations from the ground to e.g. the second excited state are enforced and matrix transition elements can be computed by using the ground state and second excited state Wannier functions.

The localized states from Eq. 2.16 are used to finally construct Wannier functions. The Wannier functions in the left/right well of the l^{th} double well are given by a weighted

---

[7] Considering only a single band $n = n'$ in Eq. 2.15 leads to a single localized state with $m = 1$ in each double well. This state is spread over the entire double well and therefore inappropriate to describe physical processes between the two wells of one double well at least in the symmetric superlattice configuration.

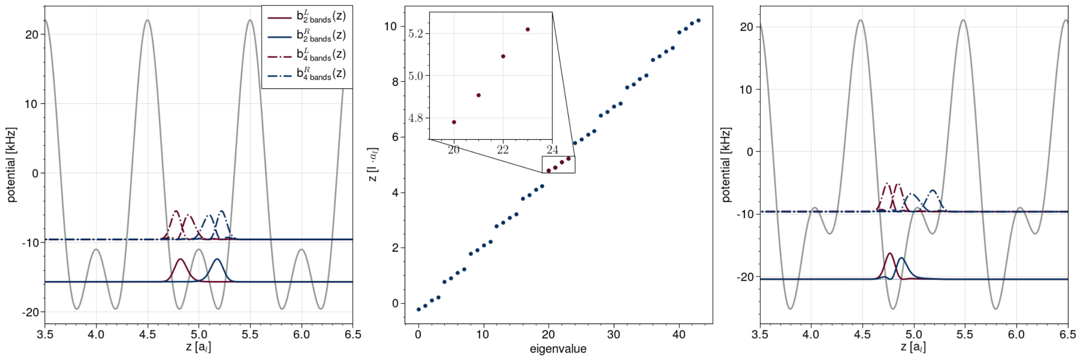

Figure 2.8: Eigenfunctions/-values of the band projected position operator $\hat{x}_n^{proj}$. **Left** Localized states constructed by Eq. 2.16 with two (lower two localized states) and four (upper four states) bands i.e. $n, n' = 1, 2$ or $1, 2, 3, 4$ in Eq. 2.15. **Center** Eigenvalues of the diagonalized matrix with entries $\chi_{qq'}^{nn'}$ for $L = 11$ double wells in the superlattice and four bands. They form eleven groups with four elements each. Each eigenvalue corresponds to the center of mass of the corresponding localized state. **Right** Localized states in a tilted superlattice. Taking two bands into account leads to two non-centred localized states in the lower band. In the upper band the third localized state from the left cannot be assigned to one of the two wells since it is centred around the double well's barrier.

superposition of the $m/2$ left/right localized states $b_{lm}(z)$. The weight for each localized state is determined by the eigenvector element $\eta_{mm'}$ of the projected Hamiltonian [84]

$$H^{L/R}_{mm'} = \sum_{n,q} \epsilon_q^n (\chi_{l,m}^{n,q})^* \chi_{l,m}^{n,q}. \tag{2.17}$$

The Hamiltonian $H^{L/R}$ projects the localised states onto the left and right well, respectively, setting $m, m' \in [1, .., N/2]$ for the left and $m, m' \in (N/2, .., N]$ for the right well. Here, N is the number of mixed bands.

The Wannier functions are then computed by [84]

$$W_{L/R}(z - a_l l) = \sum_{n,q} \sum_{mm'} \eta_{mm'} \chi_{lm}^{nq} \psi_q^n(z). \tag{2.18}$$

If the superlattice is in symmetric configuration, two band can be taken into account in Eq. 2.15. Consequently, the left/right ground state Wannier function corresponds to the left/right localized state $b_{lm}(z)$, respectively (Fig. 2.9 left). Furthermore, the left/right 1^{st} excited Wannier functions arise using four bands and are superimposed from the two localized states $b_{lm}(z)$ in each well respectively (Fig. 2.9 left). The latter have weights from Eq. 2.17.

In a tilted superlattice with a phase of $\phi = 0.2\,\text{rad}$, the ground band is well separated from

the 1st and 2nd excited band (Fig. 2.9 center, lower dashed line). Moreover, in contrast to the symmetric case, the ground band energy is much lower than the potential energy of the upper, right well. A strongly localized, centred, ground energy Wannier function in the lower well constitutes therefore by considering only the ground band. Mixing the 1st and 2nd excited band in Eq. 2.16, whose energies are both above the potential energy of the upper, right well minimum, leads to a localized Wannier function in the left and right well, respectively (Fig. 2.9 center). Here, the energy offset of the two latter Wannier functions is set to be the average of the energy levels of the 1st and 2nd band.
In the antisymmetric superlattice configuration, i.e. $\phi = \pi/4$, the energy levels are well separated (cf. Fig. 2.7 right). Thus, the first three Wannier functions are constructed using only the first, second and third band, respectively (Fig. 2.9 right). Furthermore, due to the deep lattice, the Wannier functions can be approximated by harmonic oscillator wave functions (Fig. 2.9 right) since the deep potential well can be regarded as a harmonic oscillator potential. The offset of the harmonic oscillator wave functions is here set to the respective oscillator level.

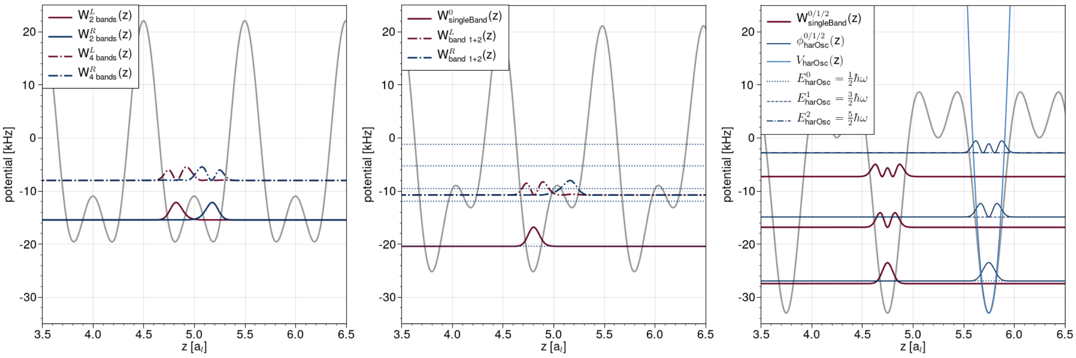

Figure 2.9: Wannier functions. **Left** Ground and 1st excited state Wannier functions in the left and right well in a symmetric superlattice. The two ground state Wannier functions are computed using two bands whereas the 1st excited state Wannier functions are computed using four bands. **Center** The ground state Wannier function in the tilted superlattice is computed using a single band since the ground state energy is lower than the potential energy of the upper well. The 1st excited state Wannier functions are computed by mixing the 1st and 2nd band. **Right** Wannier functions in the antisymmetric configuration. Each computed from the single corresponding band. For comparison the harmonic oscillator potential and its wave functions are computed.

The restriction to a finite number of considered bands in order to obtain localized Wannier functions does not allow to obtain maximally localized Wannier functions which reveal from the full basis set of localized functions $b_{lm}(z)$ in Eq. 2.16. The intricacy of mixing the correct bands and due to an increasing computation time when taking higher bands into account, however, prompt to restrict the calculations throughout this thesis to one or two bands. It will be shown in chapter four and five that quantities basing on these single or two band Wannier functions well match with the experimental data.

2.2.3 Derivation of Hubbard parameters using Wannier functions

The numerical determination of Wannier functions in each well of a double well from Eq. 2.18 (Fig. 2.9) opens the possibility to determine secondary quantities like the Hubbard parameters, namely the tunnelling amplitude t, interaction strength U and on-site energy E.

The on-site energy E of a particle in one well of the double well is intuitively given in terms of Wannier functions in the left or right well $W^{L/R}$ and simultaneously expressed by the BPPO eigenfunctions respectively as [64][84]

$$E_{\text{onsite}}^{L/R} = \int W_{L/R}^{*}(z) \cdot V_{sl}(z) \cdot W_{L/R}(z) \mathrm{d}z = \sum_{n,q} \sum_{mm'} \eta_m^{*} \eta_{m'} \epsilon_q^n (\chi_{lm}^{nq})^{*} \chi_{lm'}^{nq}. \tag{2.19}$$

Here, $V_{sl}(z)$ is the superlattice potential, $m, m' \in [1, ..., N_b/2]$ to compute the on-site energy of the left and $m, m' \in (N_b/2, ..., N_b]$ to compute the on-site energy of the right well of the double well and ϵ_q^n is the band energy of the corresponding band n with lattice momentum q. Furthermore, the χ_{lm}^{nq} are the eigenvector elements from Eq. 2.15 and the $\eta_{m'}$ are the eigenvector elements of the projected Hamiltonian.

The tunnelling amplitude t is determined by the overlap between the two ground state Wannier functions in neighbouring wells. Hence,

$$t^{\text{in/out}} = \int W_{\mathbf{L/R}}^{*}(z) \left[\frac{-\hbar^2}{2m} \nabla^2 + V_{sl}(z) \right] W_{\mathbf{R/L}}(z) \mathrm{d}z = \sum_{n,q} \sum_{mm'} \eta_m^{*} \eta_{m'} \epsilon_q^n (\chi_{lm}^{nq})^{*} \chi_{lm'}^{nq}. \tag{2.20}$$

In contrast to the computation of the on-site energy in terms of the BPPO eigenfunctions, for the tunnelling between two wells m is in $[1, ..., N_b/2]$ while m' is in $(N_b/2, ..., N_b]$. Thus, m runs over the localized states in the left and m' over the localized states in the right well. In order to compute the tunnelling out of a double well m and m' change their role.

The interaction strength U between two particles on the same site is given by

$$U^{L/R} = \frac{4\pi\hbar^2 a_{sc}}{m} \int |W_{L/R}(z)|^4 \mathrm{d}z. \tag{2.21}$$

Here, a_{sc} is the scattering length between two particles which is given in [24] for one, two and three dimension.

The superlattice configuration affects the Wannier functions and, hence, the deduced Hubbard parameter (Fig. 2.10). For example, at a constant long lattice depth of $V_l = 120\,\mathrm{E}_{\text{rec}}$, an increasing short lattice depth leads to an increasing barrier height. This causes steeper slopes in the potential (Fig. 2.5 center) and the Wannier functions become compressed

(Fig. 2.10 left, inset). In turn, the overlap between the two Wannier functions at neighbouring sites is diminished and the tunnelling amplitude decreases exponentially (Fig. 2.10 left, blue curve and lower x-axis). Contrarily, for increasing long and constant short lattice depth, the two wells in the double well slowly approximate each other and the tunnelling amplitude therefore increases (Fig. 2.10 left, red curve and upper x-axis).

The on-site energy behaves opposite (Fig. 2.10 center). For constant long and an increasing short lattice depth the ground state energy increases due to the anti-confinement of this lattice (blue curve). Here, the anti-confinement manifests in the "+" sign of V_s in the superlattice potential (Eq. 2.8). In contrast, an increasing long lattice depth at constant short lattice depth leads to a decreasing on-site energy to larger negative values due to a stronger confinement.

Finally, in the exemplary case of attractive interactions, i.e. that the scattering length $a_{sc} < 0$, an increasing short lattice depth increases the center barrier and compresses the Wannier functions which, in turn, increases the absolute value of the interaction energy (Fig. 2.10 right). An increasing long lattice depth at constant short lattice depth in contrast reduces the compressional effect of the center barrier leading to broadened Wannier function and, hence, to a smaller interaction energy.[8]

The affects on the Hubbard parameters is here discussed for a symmetric superlattice, the argumentation, however, remains valid also for superlattice configurations away from the symmetry point.

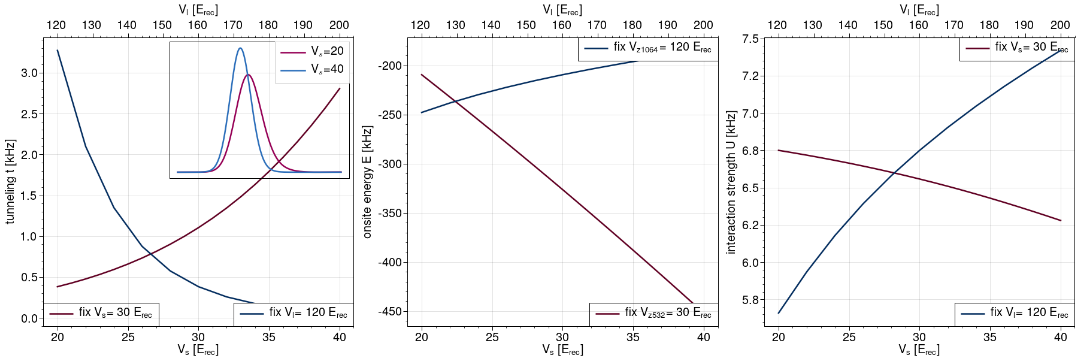

Figure 2.10: Effect of the two lattice depths of the long and short lattice on the Hubbard parameters and on the Wannier functions. **Left inset** An increase of the short lattice depth leads to compressed Wannier functions. **Left** Tunnelling amplitude as function of the long (red curve, upper x-axis) and short (blue curve, lower x-axis) lattice depth. **Center** On-site energy as function of the long (red curve, upper x-axis) and short (blue curve, lower x-axis) lattice depth. **Right** Interactions energy as function of the long (red curve, upper x-axis) and short (blue curve, lower x-axis) lattice depth for attractive interaction with scattering length smaller zero.

---

[8] In the symmetric superlattice, two particles in the double well would split for repulsive interactions such that both particle occupy the left and right well. This would lead to a vanishing on-site interaction energy.

2.2.4 Interacting Wannier functions

The derivation of maximally localized Wannier functions from the BPPO bases on a Hamiltonian for non-interacting single particles in a superlattice (Sec. 2.2.2). The resulting Wannier functions therefore describe non-interacting particles. Eq. 2.21 in turn employs these Wannier functions in order to compute the on-site interaction energy between them. The on-site interactions, however, modify the Wannier functions which then in turn changes the on-site interaction energy. Qualitative speaking, repulsive interaction broaden the Wannier functions while attractive interaction narrow them. The reason behind is that for example for repulsive interaction, the scattering length is positive and, hence, the interaction strength U greater than zero. Consequently, a broadened Wannier function reduces the interaction strength. The effect of interactions on Wannier functions was studied in [93][89][156]. A self-consistent approach was used in [156] in order to compute interacting Wannier functions in a Bose-Hubbard model. The self-consistent equation is here deduced from a variational approach by which the single-band ground state energy of the Wannier function is minimized. In the Mott-insulating regime the ground state reads $|n_0, n_0, ..., n_0\rangle$ with n_0 being the number of particles per site. The self-consistent equation is then simplified to [156]

$$\sum_j \frac{\mu_j}{N_0} W(z - z_j) = H_0 W(z) + g_0(n_0 - 1)|W(z)|^2 W(z) + 2g_0 n_0 \sum_{r_j \neq 0} |W(z - z_j)|^2 W(z) \tag{2.22}$$

Furthermore, in [156], the Wannier function is expanded in terms of single particle Wannier functions as

$$W(z - z_j) = \sum_{n=1}^{M} (c_n w_n(z - z_{j-1}) + b_n w_n(z - z_j) + c_n w_n(z - z_{j+1}). \tag{2.23}$$

In this thesis simplification are made to Eq. 2.22 in order to compute interacting Wannier functions for fermions in a superlattice. For bosons in the deep Mott-insulating regime each lattice site is occupied by an integer number of bosons. For fermions in the band insulating regime each lattice site is likewise occupied by an integer number with $|n_0, n_0, ..., n_0\rangle$ where $n_0 = 2$. Moreover, for deep lattices, the Wannier functions are well localized to one lattice site. This simplifies Eq. 2.22 in two ways: While the sum on the left side of 2.22 reduces to a single term, namely the Wannier function at site j, the third term on the right side of Eq. 2.22 vanishes. Thus, the simplified equation reads

$$\frac{\mu_j}{N_0} W(z - z_j) = H_0 W(z) + g_0(n_0 - 1)|W(z)|^2 W(z). \tag{2.24}$$

The considered Wannier function in Eq. 2.23 is also simplified. On the one hand, for deep lattices it is again suitable to restrict to localized Wannier functions such that in Eq. 2.23 the terms $c_n = 0$. On the other hand, by using only the ground band Wannier function the sum on the right hand side in Eq. 2.23 reduces to a single Wannier function. Thus, $W(z-z_i) = b_n w(z-z_i)$ and $w(z-z_i)$ is chosen to be the non-interacting Wannier function from Eq. 2.18 (Fig. 2.9).

Following the idea that the total energy $E_{\text{tot}} = E_{\text{kin}} + E_{\text{onsite}} + U$ is minimum for the correct interacting Wannier function at a given interaction strength, the on-site energy (Eq. 2.19), the interaction energy (Eq. 2.21) and the kinetic energy

$$E_{\text{kin}} = \int W^*(z) \left[-\frac{\hbar^2}{2m} \partial_z^2 \right] W(z) \mathrm{d}z \tag{2.25}$$

are computed in a first loop cycle for the non-interacting Wannier function. The total energy is then determined as the sum of these three values. In a second cycle, the non-interacting Wannier function is inserted into the simplified Eq. 2.24 leading to a perturbation of the initial non-interacting Wannier function in terms of the interaction strength g_0. The total energy for this perturbed function is subsequently determined and the perturbed function is inserted into Eq. 2.24. By repeating this self-consistent approach, the Wannier function with minimum total energy can be constructed giving the final interacting Wannier function. The parameters E_{kin}, U, E_{onsite} as a function of the iteration shows the expected behaviour recalling that for attractive interactions, the Wannier function is expected to become compressed compared to the initial, non-interacting Wannier function and that for repulsive interactions the Wannier function is expected to be broadened. Concretely, on the one hand for attractive interactions (red curves, left y-axis), a more and more compressed Wannier function throughout the iterations reduces its on-site energy stepwise because the potential energy is minimum in the center of the well (Fig. 2.11 left). The negative interaction energy deceases likewise (Fig. 2.11 center). In contrast, the kinetic energy increases due to a stronger curvature of the compressed Wannier function (Fig. 2.11 right) and holds up against the implosion of the Wannier function. On the other hand, for repulsive interactions (blue curves, right y-axis), the step-by-step broadening of the initial, non-interaction Wannier function throughout the iterations leads to an increasing on-site energy (Fig. 2.11 left), while the interaction energy as well as the kinetic energy decreases (Fig. 2.11 center/right).

As a result of counter-interacting effects of the kinetic, interaction and on-site energy, the total energy $E_{\text{tot}} = E_{\text{kin}} + E_{\text{onsite}} + U$ exhibits a minimum in the attractive and repulsive case (Fig. 2.12 left, attractive (red curve, left y-axis) / repulsive (blue curve, right y-axis)). As intuitively expected, the final repulsively interacting Wannier function with minimum total energy (Fig. 2.12 center) is broadened while the attractively interacting Wannier function (Fig. 2.12 right) is narrowed compared to the initial non-interacting Wannier function.

Experimental interaction strength measurements between two particles in a superlattice can thus be compared to theoretical prediction using either non-interacting or interacting Wannier functions. The theoretical calculations, however, bases on one dimensional Wannier functions. In order to account for this difference, the scattering length is adapted

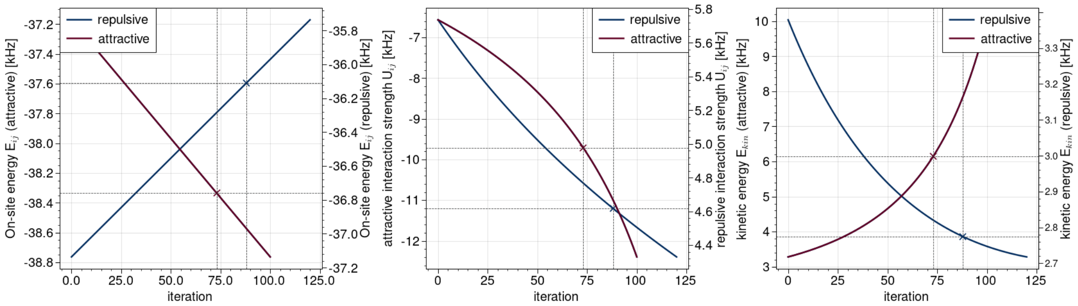

Figure 2.11: Left on-site, **center** interaction and **right** kinetic energy of the ground band Wannier functions with attractive (red curves, left y-axis) and repulsive (blue curves, right y-axis) interactions as a function of the iteration step. The Wannier functions are iteratively modified using Eq. 2.22 in order to find the interacting Wannier function.

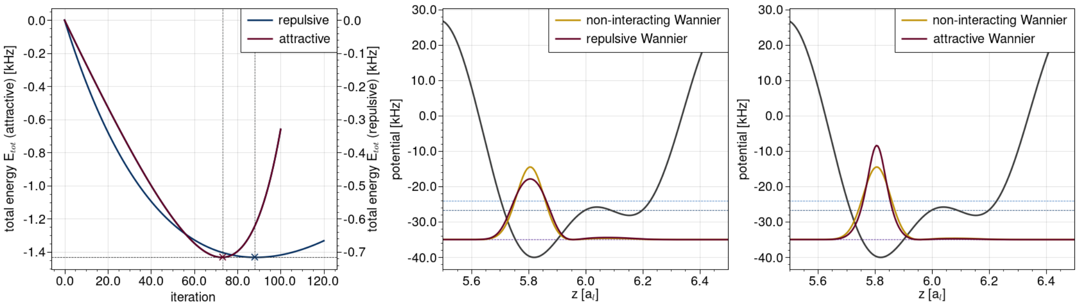

Figure 2.12: Left total energy of the ground band Wannier functions with attractive (red curves, left y-axis) and repulsive (blue curves, right y-axis) interactions as a function of the iteration step.**Center** Non-interacting and broadened Wannier function due to repulsive interactions. **Right** Non-interacting and narrowed Wannier function due to attractive interactions.

according to [24].

CHAPTER 3

Experimental setup

The concept of highly controllable analogue quantum simulators to simulate complex quantum many body systems, e.g. copper oxide compounds, was presented in chapter one. Subsequent, the monolayer Hubbard model as a minimum model for copper oxide layers in such compounds was reviewed in chapter two and the discussion was extended to the bilayer Hubbard model for two coupled layers. In this chapter the experimental setup is described which was used and extended to build an analogue quantum simulator for a bilayer Hubbard system. The characterisation of this bilayer Hubbard system is presented in the beginning of the following chapter four “Results”.

The structure of the current chapter orients towards the experimental cycle which typically ended by absorption imaging of the atoms in various optical lattice settings. The typical cycle started with the generation of a quantum degenerated Fermi gas of fermionic potassium atoms in a magneto-optical trap (MOT) and in a subsequent Ioffe-Pritchard trap. Both are detailed in this chapter. Then, the atoms were commonly loaded into different optical lattices whose setups are likewise presented here. Furthermore, high intensity absorption imaging of the trapped atoms is elucidated and the setup for the generation of magnetic Feshbach fields as well as for tomography, radio frequency spectroscopy and the digital mirror device are discussed.

In total, the experimental setup to implement a quantum simulator for a bilayer Hubbard system comprised three separated optical tables, ten laser systems, four computers for controlling and simultaneous data evaluation as well as electronics for the generation of radio frequency and microwave pulses. Furthermore, a water cooling facility for coils, temperature monitoring and air conditioning were supervised.
From the three optical tables one was intended for the setup of all laser systems. It is referred to as “laser table”. The second accommodated the actual experiment and is therefore referred to as “experiment table”. The third, smaller optical table was used for additional laser systems for which the main laser table did not offer enough room. The laser systems included the lasers itself as well as optical setups for laser frequency

stabilisation, offset locking and laser intensity control. The light was guided to the experiment table via optical fibres, where the actual experiment with the magneto optical trap, transport stage, Ioffe-Pritchard trap, Feshbach coils, glass cell and magnetic shielding were located. Moreover, the beam path setups for two dipole traps, five optical lattice beams, one digital mirror device as well as three cameras were positioned on this table.
Furthermore, the experiment was controlled with an *iRobo industrial* PC from IPC2U. This computer comprised two digital (*PCI-DIO64* from Viewport) and two analogue cards whose output could be set by a software on the so called "control PC". The digital cards were needed for binary operations like switching on/off a shutter or a Mosfet. In contrast, analogue operations like the setting of a laser beam intensity required an analogue card output. The industrial PC was synchronized to a 10 MHz DDS clock which, in turn, received its clock signal from GPS. Beside the control of the main experiment cycle which usually took 60 s, the control of individual devices via *python* scripts and home built software was required. This comprised the generation and control of radio frequency and microwave pulses and sweeps as well as real-time feedback loops and temperature monitoring. Other main tasks were real-time image reading and further image evaluation.

3.1 Cooling to quantum degeneracy

In the experiment the fermionic potassium ^{40}K was used. ^{40}K exhibits a versatile hyperfine structure in the ground state in contrast to fermionic lithium ^{6}Li. Moreover, the heavier mass of potassium compared to lithium causes slower dynamics in optical lattices [30]. ^{40}K has a natural abundance of 0.0117% and is stable compared to experimental relevant time scales. The vapour pressure at a temperature $T = 293\,\mathrm{K}$ amounts to $p_{\mathrm{vap}} = 1.3 \times 10^{-8}$ mbar. The enriched ^{40}K potassium source was vapoured into the chamber of the magneto optical trap (Sec. 3.1.2). The electronic structure of potassium reads $1s^2 2s^2 p^6 3s^2 p^6 4s^1$. The D2 line in bosonic ^{39}K (Fig. 3.1, left) and in fermionic ^{40}K (Fig. 3.1, right) was mainly employed for example for imaging. The wavelength of this transition is $\lambda_{\mathrm{D2}} \approx 766\,\mathrm{nm}$ which corresponds to a frequency of $\nu_{\mathrm{D2}} \approx 391\,\mathrm{THz}$. The life time of the $^2P_{3/2}$ state is 26(5) ns with a natural linewidth of 6.035(11) MHz. The Doppler temperature of the D2 line is $T_{\mathrm{Dop}} = 145\,\mu\mathrm{K}$. The saturation intensity is $I_{\mathrm{sat}} = 1.75\,\mathrm{mWcm}^{-2}$ [100]. Bosonic ^{39}K potassium was used for spectroscopy locking due to its high natural abundance of about 93%.

3.1.1 Laser system

The laser system (Fig. 3.2) used for the magneto-optical trap, absorption imaging and optical pumping consisted of two lasers. A cooling laser which is referred to as "cooler" and a repumping laser referred to as "repumper" . Both lasers were employed in order to trap and efficiently cool the ^{40}K atoms in the magneto optical trap (MOT) and prepare them for the mechanical transport from the MOT to the subsequent Ioffe-Pritchard trap (Sec. 3.1.2). The cooler was used for absorption imaging (Sec. 3.2).

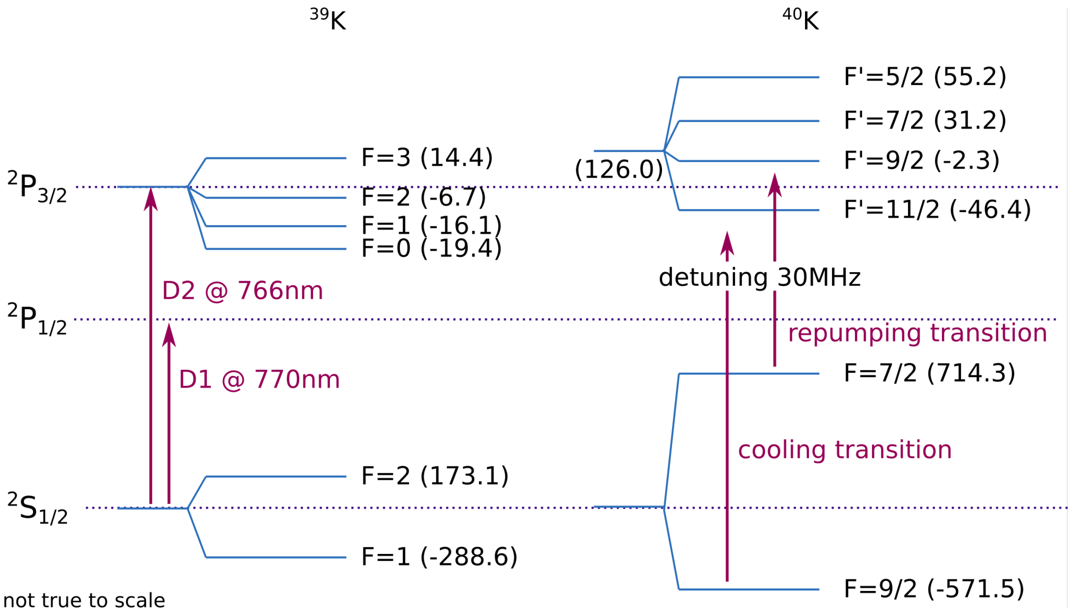

Figure 3.1: Hyperfine structure in potassium ^{39}K (left) and ^{40}K (right). The level scheme of the $^2P_{1/2}$ state is not depicted. The $^2S_{1/2} \leftrightarrow {}^2P_{3/2}$ D2 transition was used throughout this thesis. In the experiment, the fermionic ^{40}K was used. Moreover, repumping and cooling laser transition used for the magneto optical (MOT) trap and imaging. For the MOT both lasers were red-detuned from the respective resonance by $-30\,$MHz.

Repumper

The repumper was a *DLC DLpro* from *Toptica* which is an external cavity diode laser (Fig. 3.2). Its output laser frequency was adjusted to drive the $4^2S_{1/2}, F = 7/2$ to $4^2P_{3/2}, F = 9/2$ transition in the fermionic potassium isotope ^{40}K (Fig. 3.1 right). Thus, atoms that cycled in the cooling transition and fell into the dark $4^2S_{1/2}, F = 7/2$ state were recycled with the repumper to the cooling cycle by driving these atoms back to the $4^2P_{3/2}, F = 9/2$ state from where they fell to the $4^2S_{1/2}, F = 9/2$ state. The repumping laser had a linear output polarisation which was adjusted with a $\lambda/2$ wave plate to match the input polarisation of the subsequent tapered amplifier (TA). The output power of the latter was 1.1 W. An optical isolator after the TA protected the TA from back reflections of the high power laser light at the following optical elements. After the isolator, the repumper light was split. One arm was used for optical pumping and the second one to stabilize its frequency. For frequency stabilisation a Doppler free saturation spectroscopy lock method was employed [55]. Since the bosonic potassium isotope ^{39}K was used for spectroscopy in the cell (high natural abundance) the output laser frequency of the repumper had to be shifted to the D2-line in ^{39}K instead of driving the $4^2S_{1/2}, F = 7/2$ to $4^2P_{3/2}, F = 9/2$ transition in ^{40}K as in the experiment for the MOT (cf. Fig. 3.1 left/right). An acoustic optical modulator (AOM) in double pass configuration was employed for this purpose after the cube. Passing twice through the $\lambda/4$ wave plate in the double pass configuration led to a total rotation of the light's polarisation by

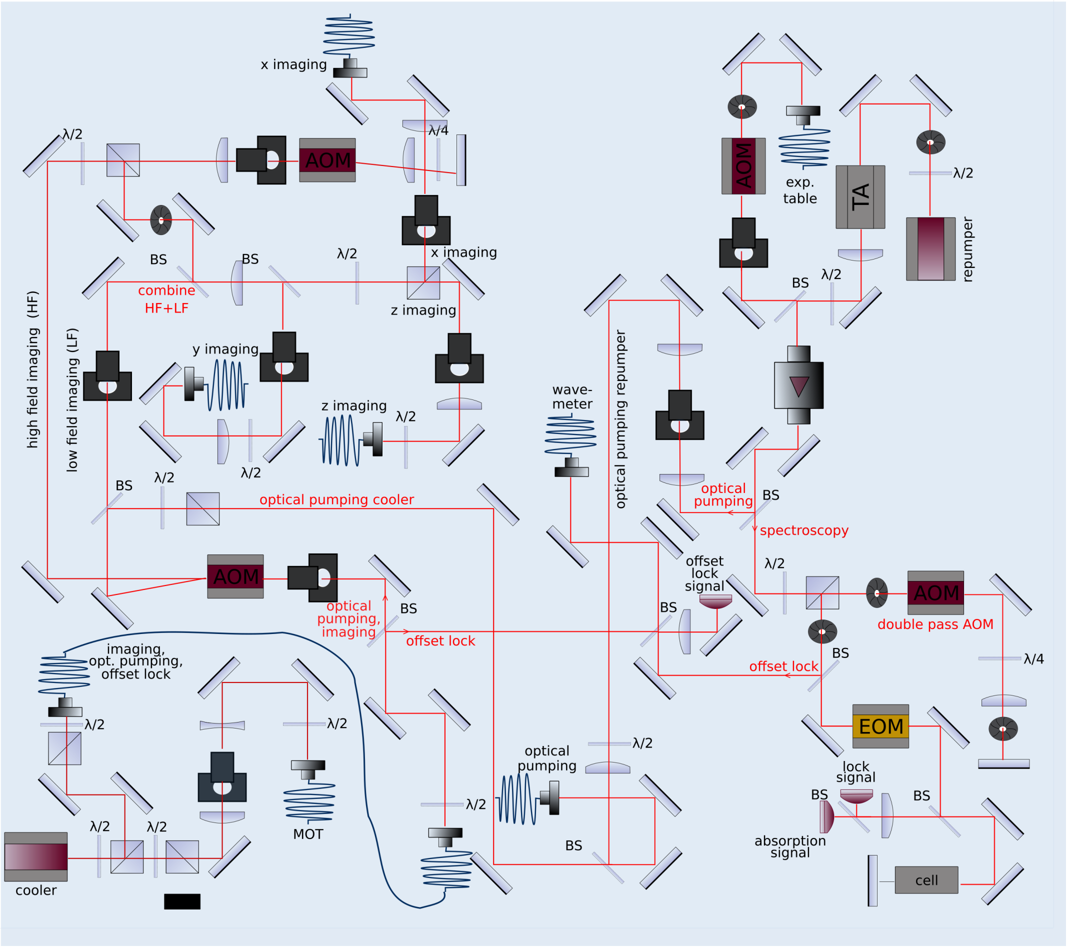

Figure 3.2: Laser table. The optical setups for the repumping and cooling laser to drive the repumping and cooling transitions in ^{40}K (cf. Fig. 3.1). The setup comprised optical paths for Doppler free spectroscopy locking, offset locking, the magneto optical trap, optical pumping and imaging.

90 °. Thus, on the return path the light was reflected at the cube towards the electro-optical modulator (EOM). The latter produced side bands before the light passed twice the spectroscopy cell. Finally, the light was sent onto a photodiode. The latter routed the converted electronic signal to the lock box. The produced Pound-Drewer-Hall signal [15] served to lock the repumping laser frequency onto the D2-line in ^{39}K. In the optical paths used for the experiment, the repumper frequency, however, was therefore stabilized at the $4^2\mathrm{S}_{1/2}, F = 7/2 \leftrightarrow 4^2\mathrm{P}_{3/2}, F = 9/2$ transition in ^{40}K.

Cooler

The cooler comprised a *Verdi V10* laser and a *MBR 110 Ti:Sapphire system* (TiSa) both from Coherent. The Verdi pumped the TiSa laser at a wavelength of 532 nm. The Ti:Sapphire crystal in the TiSa laser ring resonator subsequently down converted this light to around 766 nm. The output frequency of the Ti:Sa was fine adjusted with the etalon. The cooler was employed in order to drive the $4^2\mathrm{S}_{1/2}, F = 9/2 \leftrightarrow 4^2\mathrm{P}_{3/2}, F = 11/2$ transition in ^{40}K at a wavelength of around 766 nm (Fig. 3.1 right). The output power of the Ti:Sa was about 1 W. Most of this power was sent through an optical fibre to the MOT while about 100 mW were used for optical pumping, absorption imaging and the offset lock with which the cooler was frequency locked to the frequency stabilised repumper (Fig. 3.2). In this optical path, after the fibre output coupler, the weak cooler beam was first partitioned with a beam splitting plate. The part for the offset lock was then overlapped with a weak repumper beam yielding a beat note. An offset lock photodiode converted the beat note to an electronic signal which was mixed with an adjustable set frequency from a local oscillator. A similar offset locking scheme as in [138] was used. Furthermore, the locked cooler frequency could be controlled via the experimental control sequence by adjusting the set frequency of the local oscillator. This control was necessary for changing the cooler light's frequency in order to either trap atoms in the MOT or performing absorption imaging of the atoms in the science cell at different magnetic field strengths.

3.1.2 Magneto optical trap, transport and Ioffe-Pritchard trap

The magneto optical trap (MOT) bases on the principle of the scattering force of near-resonant laser light onto particles in a trapping magnetic quadrupole field [55]. The trapping field was produced by a pair of coils in anti Helmholtz configuration. A power supply *EA PS 3016-20B* delivered the power. Water cooling of the coils was not needed. The cooling and repumping laser beams were first overlapped and then split into three pairs of opposite travelling beams and directed onto the MOT center. Respective circular polarisation was achieved using quarter wave plates. In order to capture the potassium atoms in the trap center at around room temperature both lasers were blue detuned by 30 MHz to the cooling $4^2\mathrm{S}_{1/2}, F = 9/2 \leftrightarrow 4^2\mathrm{P}_{3/2}, F = 11/2$ and repumping $4^2\mathrm{S}_{1/2}, F = 7/2 \leftrightarrow 4^2\mathrm{P}_{3/2}, F = 9/2$ transition in ^{40}K, respectively (Fig. 3.1 right). Driving the cooling transition with the cooler led to a population of the dark $4^2\mathrm{S}_{1/2}, F = 7/2$ state with atoms. In order to not loose these atoms from the MOT, the repumper drove them back to the $4^2\mathrm{P}_{3/2}, F = 9/2$ state from which they fell again into the cooling cycle. A colder atomic sample in the MOT was obtained by creating a so called dark MOT [81]. The dark MOT was temporary and not spatially as in [81]. Using only little repumping light caused that atoms remained longer in the dark $4^2\mathrm{S}_{1/2}, F = 7/2$ state and, thus, could not be heated by the strong cooling light and many transition cycles. After loading this dark MOT, the repumper was switched off and the power of the cooling light was shortly increased. This compressed the atomic sample in the MOT due to an increased "restoring force" and prepare the atoms for the transport from the MOT cell to the science cell through the thin differential pumping tube. 1×10^8 atoms at a temperature of about 600 µK were roughly trapped after loading.

The transport of the atoms in the magnetic field minimum in the trap center of the transport coils required that the atoms occupy low-field seeking m_F states. During the MOT phase, however, low and high field seeking states were occupied. Thus, atoms in high field seeking states with $m_F < 0$ would have escaped from the magnetic field minimum in the trap center. To avoid this the compressing MOT light and quadrupole magnetic field at the end of the MOT phase were rapidly turned off and a homogenous magnetic field was ramped up simultaneously. This defined a quantisation axis. Cooler and repumper light were subsequently employed to optically pump (cf. 3.2 for opt. path) the atoms into the low field seeking states with $m_F > 0$. After preparing most of the atoms in the upper $m_F > 0$ states of the $F = 9/2$ manifold the homogenous field was switched off again. A magnetic field with a gradient of 80 G/cm was ramped up in 500 µs at the same time by discharging three large capacitors of 4.7 mF through the transport coils. This fastness was needed to prevent atoms to escape from the trap center. A power supply *EA-PS 9040-510* then increased this gradient to 300 G/cm and the atoms were transported to the science cell through the differential pumping tube (Fig. 3.3, box in the center). There, the current through the transport coils was diminished and the atoms were loaded from the trap of the transport coils into the Ioffe-Pritchard trap (Fig. 3.3).[1] The pressure in the science cell was about 10×10^{-11} mbar such that collisions with background atoms were kept rare with respect to the trapping time.

The Ioffe-Pritchard trap consisted of the Ioffe bars as well as of the Pinch and compensation coils. The Ioffe bars induced a radially quadrupole field with increasing magnetic field strength in radial direction and zero field along the x-axis. Atoms in low field seeking $m_F > 0$ states were therefore trapped in the center. Due to the absence of a finite field along x, however, these atoms could spontaneously undergo transitions to high field seeking m_F-states and escape from the trap (Majorana losses). To circumvent this, the Pinch coils induced a finite field with quadratic shape along this axis [55] where the atoms were trapped in the minimum. The current through the Ioffe bars were driven by a *6690A* power supply from Agilent. For the pinch and offset coils a *EA-PS 9040-510* from Lambda was used. The coils were water cooled (Sec. 3.4.2).
In order to cool the atoms in the Ioffe trap after the transport, magnetic evaporation was performed. The principle of every evaporative cooling technique bases on removing the hottest atoms in a trap. Then, after thermalisation the remaining atoms have lower temperature. For *magnetic* evaporative cooling the magnetic field dependence of the Zeeman splitting in the electronic structure of atoms is employed to address and remove the hottest atoms. Since the magnetic field in the Pritchard trap increases with radius, the Zeeman splitting likewise does (Fig. 3.4 left). Furthermore, the hottest atoms have highest kinetic energy and are therefore predominately located in outer regions of the trap. In contrast, colder atoms do not possess enough kinetic energy to reach these regions. Thus, hotter and colder atoms can be discriminated by the Zeeman splitting and independently addressed and removed using radio- or microwaves.

In the experiment, the potassium atoms in the Ioffe trap occupied the low-field seeking states with $m_F > 0$ in the lowest $4^2\mathrm{S}_{1/2} F = 9/2$ manifold. Radio frequencies as well as microwaves could be used to transfer the atoms either to a $m_F < 0$ state in the lowest $F = 9/2$ manifold (radio frequencies) or to the $m_F > 0$ states in the $F = 7/2$ manifold

---

[1] More information can be found in [57][51].

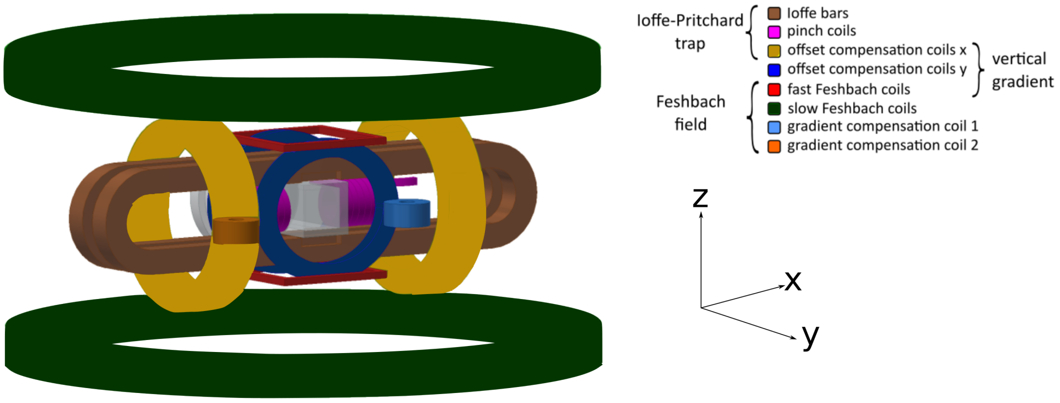

Figure 3.3: Ioffe-Pritchard trap, Feshbach coils, offset coils around the science cell. The coordinate system defines the lab system. Atoms are transported from the magneto optical trap to the science cell where they are trapped in a Ioffe-Pritchard trap. After cooling by magnetic evaporation they are loaded into the dipole trap. The Feshbach coils generate the magnetic field for controlling the scattering length between two atoms (Sec. 3.4). The compensation coils were used to compensate an in-plane magnetic field gradient evoked by the fast Feshbach coils. This illustration is taken from [38].

(microwave frequencies). All these states are high field seeking states such that atoms in these states escape from the trap. Microwaves were used. Therefore, it had to be taken into account that the $F = 7/2$ manifold has a negative Landé g-factor and is, hence, ordered inversely. This means that, in a magnetic field and in contrast to the $F = 9/2$ manifold, the $m_F > 0$ states have lower energy than the $m_F < 0$ states in the $F = 7/2$ manifold (Fig. 3.4 left). The difference between the positive m_F states of the $F = 9/2$ and positive m_F states of the $F = 7/2$ manifold thus decreases with increasing field strength in the outer regions. For addressing hot atoms an initial low frequency microwave at 1.2 GHz was therefore used and its frequency was slowly increased to 1.27 GHz to address and remove colder atoms (Fig. 3.4 right).
The microwave was generated by a direct digital synthesiser (DDS) board which could be controlled over an interface at the experiment control computer. A 100 W amplifier was used to amplify the generated microwave. The evaporation takes 17 s. In the end stage of this evaporation, however, microwaves were not suitable any more to further reduce the temperature. Due to the offset field of the Ioffe trap along x the order of the internal states changed [57]. Thus, the coldest atoms were suddenly addressed by the microwave. To circumvent this, radio frequencies were used instead of microwaves to swap the internal state of the hottest atoms in the $F = 9/2$ manifold to high field seeking $m_F < 0$ states.

After evaporation the atoms were imaged via x-imaging (Sec. 3.2.2), and the atom number as well as the temperature were extracted. It usually resulted in about 10^7 atoms at a temperature of about 3 µK.[2]

---

[2] More information can be found in [57].

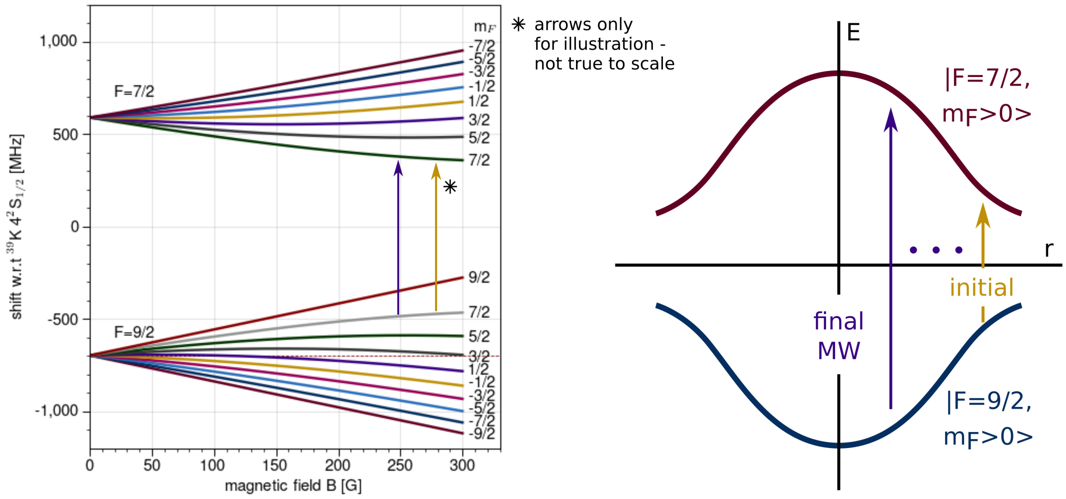

Figure 3.4: Left Zeeman splitting of the $4^2\mathrm{S}_{1/2} F = 9/2$ and $F = 7/2$ manifold in fermionic ^{40}K potassium (cf. Fig. 3.1). The $F = 7/2$ state has a negative Landé-g factor. The four lowest Zeeman levels of the $F = 9/2$ were used in order to create spin mixtures (Sec. 4.2.1.1), for tomography and for singles/doubles discrimination (Fig. 3.15). **Right** Magnetic evaporation scheme. The Zeeman splitting depends on the magnetic field strength which becomes stronger further away from the center of the Ioffe-Pritchard trap. Hence, the Zeeman splitting is reduced there due to a negative Landé-g-factor of the $F = 7/2$ state. Starting with low microwave frequencies to change the internal state of hot atoms in the outer region of the trap from a low $F = 9/2, m_F > 0$ a to high $F = 7/2, m_F > 0$ field seeking state evaporates the hottest atoms. Increasing the microwave frequency slowly evaporates colder atoms closer to the trap center.

3.1.3 Dipole trap

In order to reach the quantum regime the fermionic potassium atoms were loaded from the magnetic Ioffe-Pritchard trap into a dipole trap after magnetic evaporation. A seed laser with a distributed feedback (DFB) diode provided linearly polarized light with an output power of about 20 mW after a polarising maintaining output fibre. This light was sent to a noise generator which broadened the linewidth[59]. A broad linewidth going along with a small coherence length of the laser light was preferable in order to avoid any interferences in the glass cell at the location of the atoms.[3] After passing the noise generator the light was amplified by a *Koheras Boostik* 10 W *fibre laser amplifier* from NKT photonics. The output of the amplifier was split into two beams with a power of roughly 2 W each (Fig. 3.5 left). The two beams for two separated dipole traps were necessary in order to let the dipole beams cross roughly perpendicularly at the location of the atoms and, thus, setting up a trap with sufficient confinement in all directions. The horizontal dipole trap

---

[3] Such interferences can arise when the dipole trap light with sufficient coherence length reflects at the inner, non-coated side of the glass cell.

is referred to as Dth while the second dipole trap as “dimple”.[4] After splitting the output, both beams were sent through a respective acoustic optical modulator (AOM) and coupled into a fibre. The coupled light was then sent to the experimental table. The AOMs served to control the power of the respective beam. In order to achieve power control, two photodiodes on the experimental table were installed. They measured some residual light in the optical path from each respective dipole beam and sent a corresponding converted voltage to an respective PID control unit. The PID, in turn, compared the received voltage with a control voltage which could be set by the experimental control sequence and feedbacked the error signal to the AOM controller which regularised the AOM by adjusting the radio frequency power.[5][6]
In the Dth optical path on the experimental table, a cylindrical telescope strongly widened the vertical Dth beam radius (Fig. 3.10). This enabled to focus the beam with the f=250 mm lens just before the glass cell down to a waist of $\mathrm{w}_z^{\mathrm{Dth}} \approx 20\,\mu\mathrm{m}$ in z direction at the location of the atoms. The resulting strong confinement for the atoms in z direction was needed in order to hold the atoms in the trap against gravity. The waist in y direction was $\mathrm{w}_y^{\mathrm{Dth}} = 143\,\mu\mathrm{m}$. The vertical Rayleigh range in x direction was $x_{R,z}^{\mathrm{Dth}} = 1.2\,\mathrm{cm}$ owing to the small waist in z direction. The Dth beam at the location of the atoms could be imaged with the Baseler camera (Fig. 3.10). The Dth was shown onto the atoms under a small horizontal angle with respect to the x-axis. This prevented interferences due to back reflections. The Dth was likewise detuned with respect to the x lattice to avoid interferences.

The Dth beam was aligned onto the atoms manually using a mirror mount with Piezo adjusters in the optical path (Fig. 3.10). The voltage for the Piezo electric elements was provided by a Piezo controller from Thorlabs. In the vertical direction the Dth position was additionally stabilised using a feedback loop. The feedback relied on an error signal which was obtained from the discrepancy of the vertical set position of the Dth and the measured vertical position using the Baseler camera (Fig. 3.10) in each experiment cycle. The optimum vertical position resulted from a thermometry measurement in the dipole trap after evaporative cooling (Sec. 4.2.1.2). The measured temperature depended on the relative position of the Dth with respect to the center of the Ioffe-Pritchard trap. Setting the Dth slightly below the Ioffe trap center yielded the lowest temperatures.

The second dipole trap, the dimple, had, in contrast to the Dth, a nearly round shape with waists of about $(\mathrm{w}_x,\mathrm{w}_y)=(119\,\mu\mathrm{m}, 148\,\mu\mathrm{m})$. It was shown onto the atoms under an angle of 45° with respect to the z axis and perpendicular to the Dth (Fig. 3.7). This confined the atoms tightly in the x direction along which the DTh had its long Rayleigh range. Evaporative cooling in the crossed dipole trap was performed by lowering the dipole beam power (Sec. 4.2.1.2).

---

[4] For the strongly focussed dipole traps with waists of about $20 - 200\,\mu\mathrm{m}$ and Rayleigh ranges of several milli- up to centimetres, atoms are usually only weakly confined along the beam axis. To confine them in all directions a second dipole trap is therefore needed which shines perpendicularly to the first dipole trap beam onto the atoms.

[5] The set voltage in the experimental control sequence was calibrated by measuring the power of each beam for different set voltages with a power meter.

[6] A new AOM controller box was installed during this thesis.

3.2 Imaging

The atoms could be imaged in all three directions, i.e. x,y and z (Fig. 3.3) using three different cameras. Cooler light was used as imaging light for all cameras. The optical path setup on the laser table for providing imaging light is depicted in Fig. 3.2. Here, an AOM was inserted into the optical path after splitting some cooler light for the offset lock after the cooler output fibre. With this AOM, light could be sent either in the low field (LF) or high field (HF) imaging path by switching on/off the AOM. While the low field path was sent to the combining beam splitter directly (Fig. 3.2), the high field path comprised a second AOM in double pass configuration. With this AOM the imaging light frequency could be changed while preserving the beam direction. This was needed if the light's frequency had to be adapted to the D2 resonance which depended on the magnetic (high) field. The optical paths of low and high field imaging were recombined at the beam splitter and sent to the x-,y- and z-imaging polarisation maintaining optical fibre respectively (Fig. 3.2).

Since absorption imaging required very short imaging light pulses a special, house build AOM controller was employed for x,y, and z-imaging respectively. This digital laser intensity control (DLIC) unit enabled to regulate the AOM on a 10 µs scale.

3.2.1 z-imaging

Imaging setup

The z-imaging setup (Fig. 3.5 right) allowed for high-resolution *in-situ* absorption imaging of the atoms. The collimated, polarisation cleaned imaging beam after the fibre output coupler was first enlarged using a telescope. With a quarter wave plate circular polarisation of the light was achieved in order to drive the σ^- transition during absorption imaging. Then, by a combination of a f=350 mm achromatic doublet lens and a f=8 mm aspherical lens the atoms were illuminated by a collimated beam. The aspherical lens had a high numerical aperture of NA=0.5. It was held by a non-magnetic mount on the inner side of the cell. After the atom plane in the center of the glass cell, a second equivalent aspherical lens was likewise attached to the upper, inner cell wall. Using a doublet lens with focal length of f=200 mm thereafter led to a theoretical magnification of $\mathrm{M}_{\mathrm{theo}} = 25$. In the focus of the f=200 mm lens closer to the z-camera a fast kinetic mask was installed. It was used to operate the camera in the fast kinetic mode. A quarter wave plate changed the polarisation of the imaging light again and, hence, prevented that reflected light from the CCD chip interact with the atoms [105]. Finally, a retarder shifted the image onto the CCD chip which was protected from stray light and DMD light by a D2 transition line filter at 767 nm.

The z-imaging CCD camera was an *iXon+ Ultra888* from Andor with a quantum efficiency of 94%. Its pixel size was 13 µm. In the experiment the fast kinetic mode was enabled and the whole CCD chip was divided into three parts each of size 1024×512. This allowed for taking three images in a fast sequence. While the first and second image were taken to image the atoms, e.g. to separately image singly and doubly occupied sites or spin up/spin down singles in the optical lattice, the third image was taken as a “bright” image with only the light on but without any atoms. Additionally, “dark” images with no light

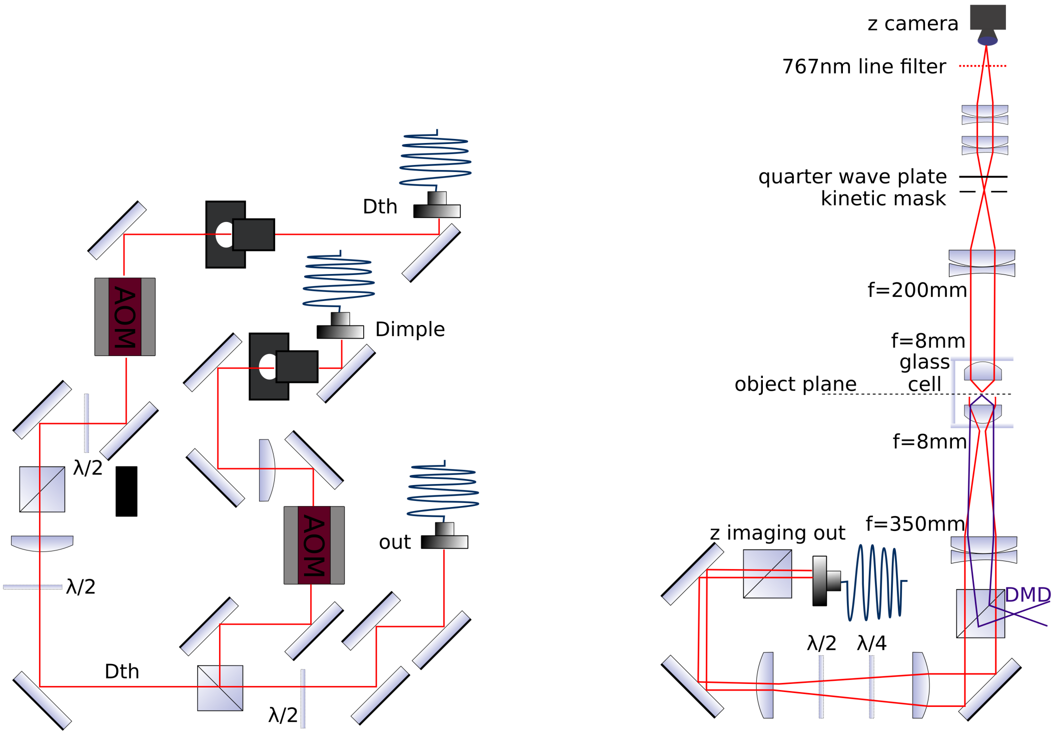

Figure 3.5: Left. Optical setup of the two dipole traps, Dth and dimple. The intensity of the beams was controlled with acoustic optical modulators. Each beam was fibre coupled and guided to the experimental table. **Right**. Optical setup of the vertical z-imaging path which allowed for in-situ, high-resolution imaging (see Fig. 3.3 and Fig. 3.10 for lab coordinate system).

were taken separately once in a while in a run of 1000 images. The averaged dark image thereby measured the noise from e.g. stray light and electronic noise and was subtracted from each of the other three images respectively.

Imaged densities

The optical densities were calculated from the three images after subtracting the averaged dark image. In general, the optical density of the atomic ensemble is connected to the recorded intensity distribution on the CCD camera chip by the high intensity corrected Lambert-Beer law[48]

$$\mathrm{OD(x,y)} = \sigma(I) \cdot \mathrm{n(x,y)} = -\alpha \cdot \ln\left(\frac{I_{\mathrm{aft}}\mathrm{(x,y)}}{I_{\mathrm{bef}}\mathrm{(x,y)}}\right) + \frac{I_{\mathrm{bef}}\mathrm{(x,y)} - I_{\mathrm{aft}}\mathrm{(x,y)}}{I_{\mathrm{sat}}}. \qquad (3.1)$$

Here, I_{bef} and I_{aft} are the intensities before and after the atomic ensemble, $n(x, y)$ is the integrated column density over the line of sight which is the z direction for z-imaging and $\sigma(I)$ is the cross section for the D2 transition in ^{40}K. This cross section is intensity dependent which becomes relevant for high imaging intensities

$$\sigma(I) = \frac{\sigma_0}{I + \left(\frac{2\Delta}{\Gamma}\right)^2 + I/I_{\text{sat}}}. \tag{3.2}$$

Here, $\sigma_0 = 3\lambda^2/(2\pi)$ is the resonant cross section, Δ is the detuning from resonance and $I_{sat} = \hbar\omega_0\Gamma/(2\sigma_0)$ is the saturation intensity for this transition. The intensity before the atoms I_{bef} could not be measured in the experiment. Instead the bright image with no atoms was employed for this purpose. The factor $\alpha = I_{\text{sat}}^{\text{eff}}/I_{\text{sat}}$ was a high intensity correction factor that resulted from the experimentally determined cross section and saturation intensity. The measured intensity on each camera pixel was related to the number of electronic counts in this pixel by the quantum efficiency of the camera. The quantum efficiency was experimentally determined in [48]. Here, further information about the calibration of the $iXon$ camera are described.

z-camera focussing

For focusing the z-camera onto the atoms in the object plane (Fig. 3.5 right), the modulation transfer function (MTF) was computed by measuring density fluctuations in in-situ images of a single atom plane[38].[7] In Fourier space, the observed density fluctuations yielded from the product of the density fluctuations in real space in the atom (object) plane times the Fourier transformed point spread function

$$\delta n_{\text{image}}(\vec{k}) \approx \delta n_{\text{atomPlane}}(\vec{k}) \cdot \mathcal{F}(\text{PSF}). \tag{3.3}$$

Then, the MTF yielded from

$$\text{MTF}(k) \approx \text{const.} \cdot \sqrt{\langle|\delta n_{\text{image}}(\vec{k})|^2\rangle}. \tag{3.4}$$

A correlated atomic ensemble was here ensured by heating the atoms in the two-dimensional lattice so that the spectrum of the density fluctuations becomes constant. uation simplifies. The MTF was nearly constant in a disk around the zero frequency component in the correct image plane, see [38], while away from the focussed position of the $iXon$ z-camera inhomogeneities revealed. The point spread function could be deduced from the measured MTF yielding a FWHM of the PSF of about 2.6 µm.[8]

z-camera magnification

The magnification of the z-imaging could be determined experimentally via density density correlations (Eq. 4.12 and Fig. 4.11). In that section, the procedure to infer the absolute and relative angles of the two in-plane lattices from the measurement of density density correlations is elucidated. In addition, the magnification of the imaging system could be

---

[7] In principle, one would use the point spread function (PSF) from a point like object in the object plane to focus onto the object plane. The PSF, however, is directly accessible only in a quantum gas microscope with single site resolution. Therefore, the MTF was employed here.

[8] More information can be found in [38].

deduced considering the distance between the measured dips d_{dip} in the autocorrelation function. The observed distance depends on the time of flight t_{TOF} and the length of one CCD pixel on the camera chip. Here, the length in the image plane is $l^{\mathrm{CCDpx}} \hat{=} l^{\mathrm{CCDpx}}_{\mathrm{imagePlane}} = 13\,\mu\mathrm{m}$ and in the object plane (Fig. 3.5 right) it is $l^{\mathrm{CCDpx}}_{\mathrm{objPlane}}$. The distance is then

$$d_{\mathrm{dip}} = \frac{1}{l^{\mathrm{CCDpx}}_{\mathrm{objPlane}}} \cdot \frac{2\pi\hbar t_{\mathrm{TOF}}}{ma}. \tag{3.5}$$

Here, m is the atomic mass of potassium and a is the lattice spacing. The magnification is then just the ratio between the pixel size in the image and in the object plane. It yielded $\mathrm{M}_{\mathrm{meas}} = l^{\mathrm{CCDpx}}_{\mathrm{imPlane}} / l^{\mathrm{CCDpx}}_{\mathrm{objPlane}} \approx 23$. This is a little smaller than the theoretically expected magnification of $\mathrm{M}_{\mathrm{theo}} = 25$. A rigorous derivation can be found in [38].

3.2.2 x- and y-imaging

x-imaging
The x-camera (Fig. 3.10) was mainly used to image the atoms in the Ioffe-Pritchard trap and determine the atom number as well as the temperature. An *Apogee U-Series* camera was installed for this purpose. The numerical aperture of the imaging lens was only NA=0.03. The resolution was 16 µm due to limiting optical access. This forbid to resolve the atomic density distribution in-situ where the size of the atom cloud was on the order of tens of micrometer. To extract information though the Ioffe-Pritchard trap was switched off and the atoms were imaged after time of flight. From the imaged momentum distribution the atom number and temperature could be inferred. The fast kinetic mode of the camera was used to avoid low variations in the imaging light between the atom and the bright images. More information are provided in [57].

y-imaging
The y-camera (Fig. 3.10) was an Andor *iXon 897 Ultra*. It was mainly employed to determine the number and temperature of the atoms in the dipole trap after evaporative cooling (cf. thermometry in Sec. 4.2.1.2). A better optical access than in the x direction enabled a resolution of about 6 µm. The magnification was about 2.6. In-situ imaging, however, was not feasible. The desired information was inferred from the momentum distribution after time of flight as in x-imaging. As for the two other cameras the fast kinetic mode was used.

3.3 Lattices

3.3.1 Bi-chromatic, vertical z-superlattice

The vertical optical z superlattice included an infrared and a green monochromatic optical lattice with wavelengths of 1064 nm and 532 nm, respectively.
For the 1064 nm lattice, two different laser sources were employed. One of them which is referred to as “small Mephisto” was used for an antisymmetric superlattice configuration in which initially only every second plane in the vertical 532 nm lattice was loaded (Sec.

4.2.1.3). The other source is referred to as "big Mephisto" and was used in the bilayer configuration. There, superlattice phases around the symmetric configuration were needed. Using a single laser source for the 1064 nm lattice was not feasible due to a limited range of the offset lock of the vertical superlattice. This prevented to tune the superlattice phase between the symmetric and antisymmetric configuration. The names "small" and "big" Mephisto originates from their respective laser source. While the big Mephisto refers to a 20 W version of the diode-pumped, solid-state Nd:YAG *Mephisto* laser from Coherent, the small Mephisto refers to a 0.5 W version.

Setup laser table
The big Mephisto laser beam was first sent through an optical isolator and subsequently beam shaped (Fig. 3.6). The power was then split. One arm guided the light to the y lattice fibre, before which a tiny portion was branched off for the offset lock. The y lattice branch included a shutter and an AOM for intensity control. The second arm guided the light to the z1064 lattice fibre. On a beam splitting cube, the light from the big Mephisto was combined with the light from the small Mephisto to enable to switch between symmetric and antisymmetric superlattice configurations as described above. The light intensity of both beams could thereafter be controlled via a shared AOM. The linear polarisation of both beams, however, was perpendicular to each other due to the polarising beam splitting cube. In order to align both polarisations for fibre coupling into the same polarisation maintaining fibre a $\lambda/2$ wave plate was employed. It was mounted on a shutter and inserted into the beam path when the small Mephisto laser was on but taken off when the big Mephisto's light was on. Thus, it turned only the small Mephisto beam's polarisation by 90° aligning it parallel to the polarisation of the big Mephisto laser beam. The optical fibre guided the light to the experimental table.
The 532 nm laser was a diode-pumped, solid-state Neodymium Vanadate laser *Verdi V10* from Coherent (Fig. 3.6). After branching off light for the offset lock, the high power laser beam was sent to the experimental table through a corresponding optical high power fibre.

Setup experiment table
On the experimental table (Fig. 3.7) the linear polarisation of the outgoing 532 nm laser beam was first rotated with a $\lambda/2$ wave plate such that the two beams after the polarising beam splitting cube had a balanced power. Then, a second $\lambda/2$ wave plate in the lower beam path rotated the linear polarisation of the lower beam by 90° in order to align it in parallel to the polarisation of the upper beam. Hence, interference of both beams at the coincidence spot in the glass cell became possible and an optical lattice formed there. By independently adjusting the upper and lower mirror behind the cube and, thus, changing the direction of the respective beam the coincidence spot could be manually set. This enabled the alignment of the lattice onto the place where the atoms were held in the combined (Dth plus dimple) dipole trap. While turning the mirrors had an impact onto the coincidence spot in the xy plane its z position remained unchanged. The angle by which the upper and lower beam encounter the atom plane was $\Theta_z = 14.5°$. This yielded a lattice spacing for the green z lattice of [38]

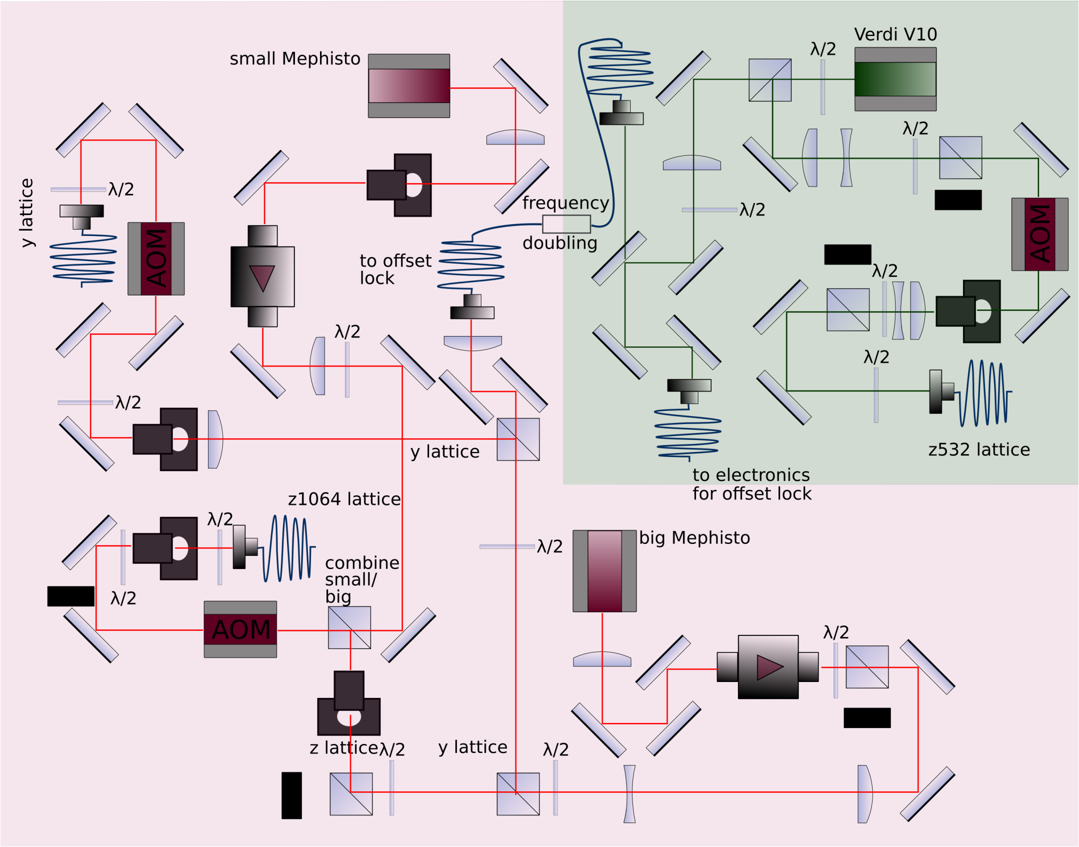

Figure 3.6: Laser setup for the vertical z superlattice and the y lattice. The z1064 lattice comprised two lasers, the "small" and "big" Mephisto. The green z532 laser was locked onto the big Mephisto via a frequency offset lock.

$$a_{z532} = \frac{\lambda_z}{2\sin(\Theta_z)} = 1.06(1)\,\mu\text{m} \tag{3.6}$$

The waist of the 532 nm laser at the coincidence spot was about 115 µm.

The 1064 nm infrared lattice was combined with the 532 nm beam at the beam splitting cube. With two Piezo controlled mirrors before the cube, the two 1064 nm beams after the cube could be aligned in parallel to the two 532 nm beams. The lattice constant of the resulting z1064 lattice was $a_{z1064} = 2a_{z532}$. It formed at the same spot as the 532 nm lattice. The glass plate in the upper beam path induced a different optical path length for the upper 1064 nm and 532 nm beam. This, in turn, introduced a phase difference between both lattices at the coincidence spot. By rotating this glass plate the light path through the glass could be varied and, hence, the relative phase between the lattices roughly adjusted.

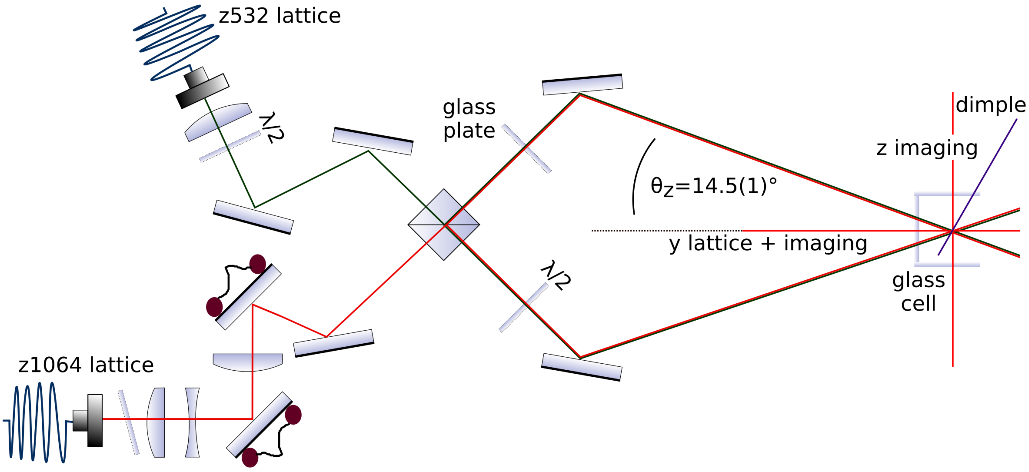

Figure 3.7: Z superlattice setup on the experimental table. At the beam splitting cube the z532 and z1064 monochromatic laser beams were combined. Moreover, each individual beam was first split and subsequently superimposed at the location of the atoms in the science glass cell (cf. Fig. 3.3 and Fig. 3.10). This way, both beams form each a monochromatic optical lattice at the coincidence spot of the atoms, respectively. Together they form a superlattice whose phase can roughly be adjusted with the glass plate.

Offsetlock

In order to build the superlattice with a precisely adjustable superlattice phase the vertical green lattice was locked onto the infrared lattice via an offset lock (Fig. 3.8). By locking the Verdi onto the big Mephisto laser the high stability performance of the latter with a spectral line width of about 1 kHz and a frequency stability of 1 MHz/min could be exploited. In contrast, the Verdi laser possessed a linewidth of less than 5 MHz. For the offset lock, fibre coupled light from the big Mephisto was sent into a periodically poled lithium niobate (PPLN) crystal. There, its frequency was doubled by non-linear up-conversion which yielded 532 nm laser light (Fig. 3.6). The latter was then guided to the Verdi laser table. After the output coupler it was combined with branched 532 nm light from the Verdi laser on a beam splitter. The superimposed beam was finally directed onto an ultrafast photodiode (PD) *DXM30AF* from Thorlabs (Fig. 3.8). This photodiode converted the optical into an electronic beat note and sent it to a *HMC 264* mixer from analog. The second (LO) port of the mixer was connected to a voltage controlled oscillator (VCO) *HMC 733* from analog. This VCO could be tuned in a range of $10-20$ GHz providing a supply voltage $\mathrm{V}^{\mathrm{ctr}}_{\mathrm{zlock}}$ of $0-10$ V. The mixer amplified the VCO signal and frequency-doubled it before mixing it with the electrical beat note. The resulting sum frequency was cut with a following 780 MHz low pass filter. The difference frequency which was in the MHz rather than in the GHz regime was subsequently amplified with a low-noise and a high-gain amplifier.[9] The signal was then split into two arms. One

---

[9] In order to tune the superlattice phase of the z superlattice over a sufficient tuning range, high frequency

arm was delayed and both were recombined in a second mixer which provided the typical error signal of the offset lock [138]. This error signal was finally input into a PID lock box after an additional high pass filter. The proportional and the integrated error signal were used for feedback to two independently Piezo controlled mirrors in the cavity of the Verdi laser. In this way, a mode jump free range of up to 7 GHz could be achieved by optimising the temperature and current of the big Mephisto as well as of the Verdi laser. The ramp speed of about 155 MHz/ms was optimized for long sweeps. Detailed information about the offset lock can be found in [59].

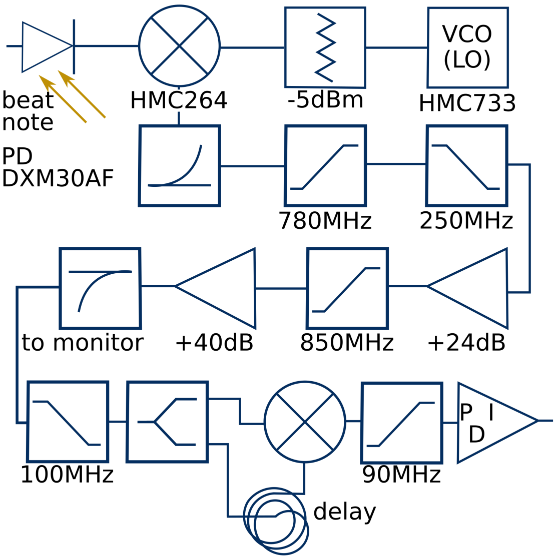

Figure 3.8: Offset lock electronic setup to stabilise the relative phase between the z532 and z1064 monochromatic optical lattice. The beat note of the two lasers was mixed with the signal of the local oscillator (LO), filtered and split into two arms. One arm was delayed and by recombining them thereafter, an error signal for locking could be generated.

The depth of each monochromatic, vertical lattice was calibrated (Sec. 4.1.1) as well as the superlattice phase (Sec. 4.1.3).

3.3.2 Bi-chromatic, in-plane x-superlattice

Like the z superlattice, the x superlattice consisted of an infrared and a green monochromatic optical lattice with wavelengths of 1064 nm and 532 nm, respectively. The lattice spacing $a_{\mathrm{x1064/x532}} = \lambda_{\mathrm{x1064/x532}}/2$, however, amounted to half of the respective wavelength in contrast to the lattice spacing of the two vertical z lattices whose spacing is given by Eq. 3.6. The superlattice was partially rebuilt during this thesis. A first setup is described in [84]. The setup was modified thereafter in order to implement Floquet

---

components in the Gigahertz range were needed due to the large vertical lattice spacing (Eq. 3.6).

systems.

Setup laser table

The 532 nm light was produced by frequency doubling 1064 nm light. A *Mephisto Mopa* 55 W laser from Coherent provided the necessary power of 1064 nm light (Fig. 3.9). From this beam, a tiny portion was first branched off for the offset lock. Subsequently, the beam was slightly focussed by a lens with long focal length in order to match the waist to the spatial mode of the frequency doubling cavity. The latter was a monolithic bow tie cavity and set up in [83]. For a stable operation of the cavity a Hänsch-Couillaud lock was implemented [71]. Therefore, some out coupled, frequency-doubled light from the entrance mirror was circularly polarized by a quarter wave plate, split at a beam splitting cube and sent onto two photodiodes. The high power, frequency-doubled 532 nm beam at the out couple mirror of the cavity was first shaped using a telescope and then sent through an AOM for intensity regulation. A big shutter with high heat capacity was employed in the beam path. Overheating of this shutter due to the intense laser light could thus be avoided. The fibre guided the light to the experimental table.
A *Koheras ADJUSTIK Y10 fibre laser and amplifier* from NKT photonics provided the 1064 nm light for the x1064 lattice (Fig. 3.9, amplifier out). About 4 W were used. Again, as for the frequency doubled 1064 nm light from the *Mephisto MOPA*, a tiny portion of light was first branched off for the offset lock, while the high power beam was sent into an AOM in double pass configuration. This enabled to change the frequency of the laser light very rapidly by changing the driving frequency of the AOM. The beam direction, however, was not effected by this and the subsequent fibre coupling efficiency remained constant. To improve the fibre coupling efficiency a lens with long focal length focussed the beam onto the polarisation maintaining fibre and matched the spatial mode of beam and fibre.

Setup experiment table

The infrared x1064 beam on the experimental table after out coupling from the fibre was shaped with a telescope, polarisation cleaned and sent through an optical isolator (Fig. 3.10). The isolator was important since by retro-reflecting the laser beam on the other side of the science cell to form an optical lattice the back reflected beam had high power. Without the isolator this high power beam could have passed the optical fibre back into the fibre amplifier and would have destroyed the latter. After the optical isolator a tiny portion of light was branched off to be shown onto a calibrated photodiode for intensity stabilisation. This was achieved by a PID loop that generated an error signal comparing the photodiode signal with a set voltage from the experimental control and fed it back to the AOM controller of the double pass AOM (Fig. 3.9). The x1064 lattice beam then passed three optics which were used to combine it with the other beams on the path to the glass cell, i.e. the Dth, x532 and x-imaging beam. First, the x1064 beam path was overlapped with the Dth beam path on a polarising beam splitting cube. Second, the x532 beam path was combined to the former with a dichroic mirror. While this mirror was reflecting 1064 nm light, 532 nm light was transmitted. Another dichroic mirror was finally used to overlap the imaging light path for x-imaging light at a wavelength of 766 nm onto the three other optical paths. Just before the science cell, a 250 mm lens then focussed

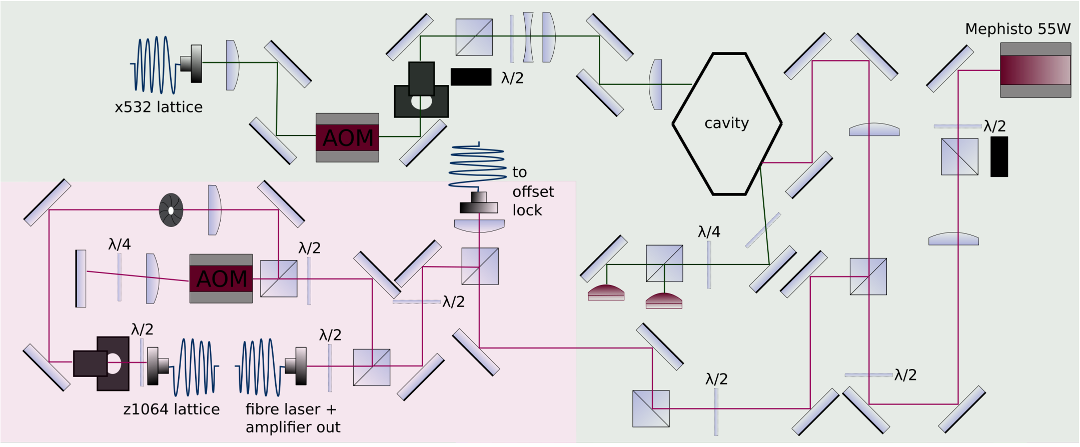

Figure 3.9: Laser setup of the horizontal x superlattice. 532 nm light was generated by frequency-doubling 1064 nm light from a 55 W laser in a bow tie cavity. A fibre laser provided likewise 1064 nm light and was locked onto the 55 W laser via a frequency offset lock. Both, the frequency doubled 532 nm light after the cavity and the 1064 nm light from the stabilised fibre laser were used to implement a frequency stabilised superlattice in x direction.

the Dth and lattice beams to the spot of the atoms in the cell. A second 250 mm lens on the other side of the cell collimated the beams. The imaging light was separated from the three other beams by a dichroic mirror. However, little light from these three beams passed the dichroic mirror and all beams could be observed on the Baseler camera (Fig. 3.10). A retro-reflecting mirror was installed to create the optical lattices at 1064 nm and 532 nm by inducing a standing wave. Since the Dth beam formed a small angle with respect to the lattice beams, the Dth light was not retro reflected at the retro mirror, thus preventing the formation of a standing wave.

The setup of the x532 beam path after out coupling comprised the same important optical elements as the path of the x1064 beam, i.e. an isolator, photodiode for intensity stabilisation and a telescope for beam shaping (Fig. 3.10). The telescope consisted of a cylindrical and a round telescope such that the horizontal and vertical beam waist could be adjusted independently. On the one hand a strongly focussed beam enabled to obtain higher 532 nm lattice depths while on the other hand, a tight focussing went along with a strong curvature of the underlying potential. The x532 beam waists were chosen such that lattice depths of up to 25 E_{rec} could be set. Simultaneously, the waist of the x532 beam in y direction was closely matched to the waist of the round 1064 nm lattice beam yielding about $w_y^{x532} \approx w_y^{x1064} \approx 140\,\mu m$.

Setup offset lock

For the offset lock of both x lattice lasers, the two 1064 nm laser beams were overlapped on a beam splitter and sent onto a photodiode (Fig. 3.9 and Fig. 3.11 left). It converted the optical into an electronic beat note. The beat note was subsequently mixed with the signal from a local oscillator (LO) in a mixer *ZX05-10H-S+*. A direct digital synthesiser

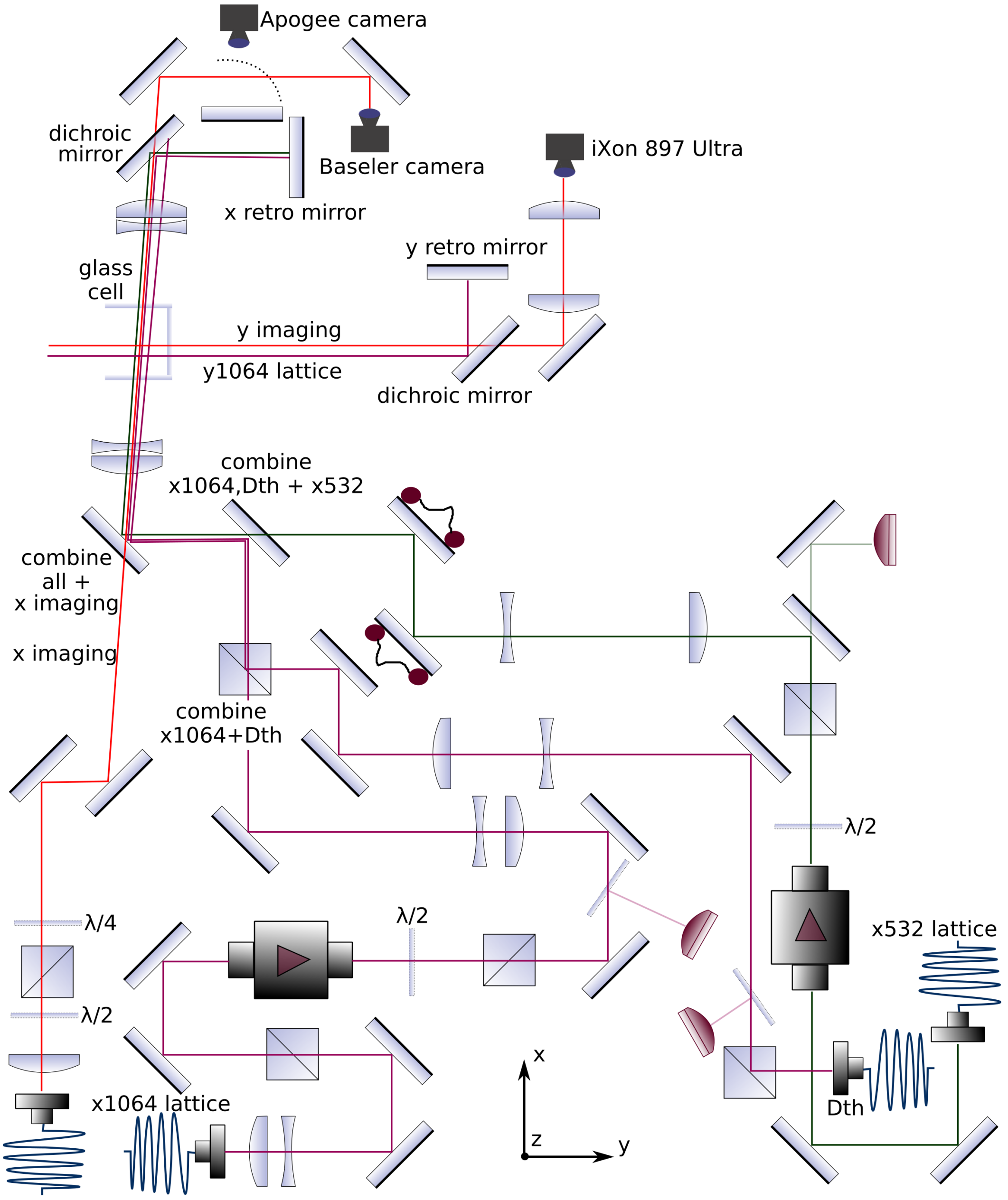

Figure 3.10: Optical setup on the experimental table for the horizontal dipole trap, all in-plane lattices and x- and y-imaging (cf. Fig. 3.3 lab coordinates). For the vertical lattices, z-imaging and the dimple dipole trap see Fig. 3.7.

(DDS) *AD9914* board generated the LO signal. It was connected to a Rasberry Pi which, in turn, read frequency settings from the experimental control PC via a *python* script. An upper and lower frequency could be set this way. Moreover, frequency ramps between the two set frequencies were adjustable and could be triggered via a 5 V signal. After mixing, the high frequency component of the combined signal was cut with a low pass filter (Fig. 3.11 left). Then, the signal was split into two arms. Using a short radio frequency cable in the second arm the signal there was phase delayed and both arms were recombined again in a mixer. The delay line produced a phase difference between the signals in both arms. This, after recombining the two lines, resulted in a voltage whose amplitude depended on the phase difference and, furthermore, on the DDS set frequency. Hence, by scanning the DDS set frequency, an error signal with a cosine shape with several zero crossings could be produced [138]. The error signal was finally sent into a PID lock box and the integration (I) part was fed back into the fast wavelength modulation port of the Koheras ADJUSTIK Y10 fibre laser from NKT photonics.

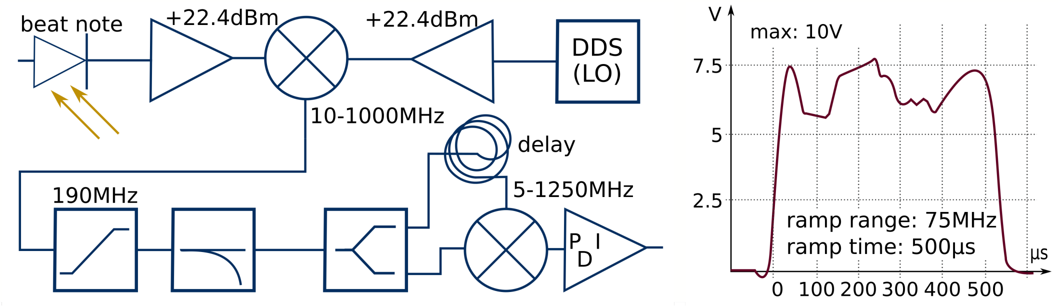

Figure 3.11: Left Offset lock electronic setup to stabilise the relative phase between the x532 and x1064 monochromatic optical lattice. **Right** PID Error signal when sweeping the DDS frequency (see right figure) by 75 MHz in 500 µs. This fast ramp was required to induce non-adiabatic transitions e.g. in the measurement of Rabi oscillations.

A change in the offset lock DDS frequency $\Delta\nu$ evoked a change in the superlattice phase ϕ by $\Delta\phi = 2\pi\Delta\nu L/c$. Here, L is the spatial distance between the science cell and the retro reflecting mirror which was estimated to be 50 cm (Fig. 3.10). Therefore, in order to be able to sweep between the symmetric and antisymmetric superlattice configuration corresponding to $\Delta\phi = \pi/4$, an offset lock frequency range of about 75 MHz was required. A sweep over this range could be achieved without a delock of the laser down to a sweep time of 500 µs (Fig. 3.11 right, error signal). This was required in order to induce non-adiabatic Landau-Zener sweeps between the antisymmetric and symmetric superlattice configuration in the horizontal x superlattice.

Superlattice phase stabilisation

The superlattice phase was stabilised against temperature, pressure and humidity fluctuations in the room. All three parameters changed the reflective index of the air between the glass cell and the retro-reflecting mirror in the x lattice optical path which, in turn, changed the optical path lengths for both x lattices differently. Thus, the relative phase between the x1064 and x532 lattice became unstable. In order to limit the resulting phase fluctuations, a sensor close to the retro reflecting mirror recorded the three parameters. The noticed change in each parameter was then converted to a required change in the DDS set frequency to maintain the current superlattice phase with the offset lock. This way, a phase stability of ±1 MHz over several days could be reached. In [150], the same three parameters were considered when stabilising the superlattice phase there.

Lattice alignment
The alignment of both monochromatic, optical x lattices were performed independently. The forward beams could be aligned roughly using the Baseler camera. Fine adjustment was achieved by observing the atomic cloud in the red- and blue- detuned potential respectively. While the blue-detuned 532 nm beam cut a passage though the atom cloud, the 1064 nm beam attracted the atom cloud such that the beam center coincided with the center of the atom cloud. This could be used to center the beam to the z-camera frame. The two retro-reflected beams were aligned by maximising the ellipticity of the atom cloud. The calibration of the lattice depth was similar to the depth calibration of the z superlattice (Sec. 4.1.1).

3.3.3 Monochromatic, in-plane y-lattice

The power for the monochromatic 1064 nm y lattice was provided by the big 20 W Mephisto (Fig. 3.6). The intensity was regulated via an AOM. A fibre coupling efficiency up to more than 90% could be reached. After guiding the light to the experimental table, the y lattice was induced by retro-reflection (Fig. 3.10). Due to the relative long distance between the aligning mirrors and the location of the atoms, the y lattice was the most unstable compared to the other lattices. The linear polarisation of the y lattice light was perpendicular to the x lattice light in order to avoid interferences.

The angle between both lattices was inferred from density-density correlations in time of flight (Fig. 4.11 right). The alignment of the y lattice beam with respect to the z-camera was achieved by observing the in-situ density profile of the atoms which were attracted to the center of the red-detuned y lattice beam. The retro reflected beam was aligned by measuring the waist and ellipticity of the atom cloud in the trap. For best alignment, the cloud size in x direction became smallest when the forward and reflected beams overlapped perfectly.

3.4 Feshbach resonances and coils

3.4.1 Feshbach resonances in potassium ^{40}K

Interactions between two fermionic atoms in cold atom experiments are described in terms of Feshbach resonances in a two channel picture (Fig. 3.12 left). The two channels, each describing a van-der-Waals potential, have discrete possible energy levels. The open channel lies energetically below the closed channel. For $r \to \infty$, both atoms are in the continuum of the open channel with energy $E = 0$. Here, the closed channel with energy $E > 0$ is inaccessible. By approaching each other the continuum of the open channel has a finite energy splitting δ_{FB} to a discrete energy level of the closed channel and the latter is, hence, still inaccessible. The splitting, however, can be tuned by a magnetic field such that $\delta_{\mathrm{FB}} = 0$ becomes zero. Then the levels of both channels coincide which leads to the resonant formation of bound states in the closed channel between atoms with different magnetic moments at the center of the Feshbach resonance.[10] Furthermore, at magnetic fields around the Feshbach resonance, the kind of interaction in the bound state depends on the magnetic field strength with respect to the resonance field. Considering the two channel picture, if the level of the closed channel lies above (below) the level of the open channel, the two atoms interact repulsively (attractively) with each other. Thus, in conclusion, by changing a magnetic Feshbach field across a resonance, the interactions in cold atom experiments can be tuned between repulsive and attractive [32][18][123].

A general Feshbach resonance in terms of the s-wave scattering amplitude a_{sc}[11] can be described by

$$a_{\mathrm{sc}}(B) = a_{\mathrm{sc}}^{0}\left(1 - \frac{\delta_{\mathrm{FB}}}{B - B_0}\right). \tag{3.7}$$

Here, B is the magnetic field, a_{sc}^{0} is the background scattering length which corresponds to the energy level of the last bound energy level in the open channel, B_0 is the magnetic field at which the scattering length diverges, i.e. the location of the center of the Feshbach resonance, and δ_{FB} is the width of the resonance [32]. In the presence of two Feshbach resonances, an analytical model for overlapping Feshbach resonances was deployed in [77].

The Feshbach resonances for potassium mixtures of $|F = 9/2, m_F = -9/2 \leftrightarrow -7/2\rangle$ and $|F = 9/2, m_F = -9/2 \leftrightarrow -5/2\rangle$ in the $4^2\mathrm{S}_{1/2}$ ground state lies around 200 G (Fig. 3.12 right). Furthermore, the two resonances $|m_F = -7/2 \leftrightarrow -5/2\rangle$, $|m_F = -7/2 \leftrightarrow -3/2\rangle$ and $|m_F = -5/2 \leftrightarrow -3/2\rangle$ in the $F = 9/2$ manifold were employed in order to set the interaction strength between two atoms in the dipole trap and in the optical lattice as well as for tomography (Sec. 3.5.3) and single doubles discrimination (Sec. 3.5.4).
The interaction strength U between two cold atoms was computed following Eq. 2.21 where the scattering length a_{sc} from Eq. 3.7 was inserted.

3.4.2 Feshbach coil system

The experimental setup to induce a Feshbach magnetic field comprised two pairs of coils (Fig. 3.3). The two large, green coils with a radius of 17.5 cm are referred to as slow Feshbach coils, whereas the rectangular red coil pair is referred to as fast Feshbach coils. The name originated from their respective inductances. The slow Feshbach coils have a relatively large inductance of 2.3 mH per coil. Thus, the induced magnetic field can only be ramped and changed slowly. This Helmholtz coil pair was used for large, homogeneous magnetic offset fields around the $|F = 9/2, m_F = -9/2\rangle \leftrightarrow |F = 9/2, m_F = -7/2\rangle$ Feshbach resonance at 202 G. A power supply from Delta provided the voltage and current for the slow Feshbach coils. In contrast, the fast Feshbach coils have an inductance of about

---

[10] The energy of bound states was experimentally measured in [35]. A coherent coupling between separated atoms and molecules using a Feshbach resonance was studied in [44].

[11] In cold atom experiments, only s-wave scattering is relevant.

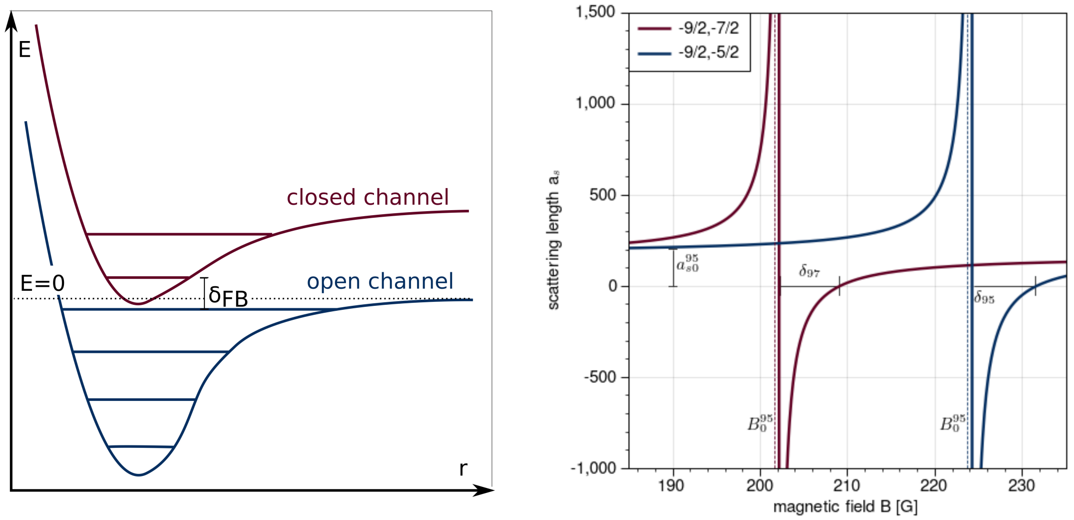

Figure 3.12: Left. Channel picture of low-energy, two body collisions. The energy difference δ_{FB} between levels of the open and closed channel can be tuned via a magnetic Feshbach field. Depending on the magnetic field with respect to the resonance field, attractive and repulsive interactions between two particles can be adjusted. **Right** The $m_F = -9/2 \leftrightarrow -7/2$ and $m_F = -9/2 \leftrightarrow -5/2$ Feshbach resonances in potassium ^{40}K.

40 µH per coil [57]. They were employed to rapidly change the magnetic field (Sec. 4.2.4).

Water cooling circuit

The coils of the Ioffe-Pritchard trap as well as the slow Feshbach coils were water cooled in the inner which was necessary due to the high currents of up to 300 A. 6 °C house water was used for the primary circuit (Fig. 3.13). *A Pentair Multi Evo 3-40M* water pump increased the pressure in the house water pipe just before it entered the 10 kW heat exchanger *Neslab System 1* from ThermoFisher. The closed, secondary water circuit was connected to this heat exchanger on the other side. It conducted the water through the coils. A second *Pentair Multi Evo 3-40M* pump increased the pressure in the secondary water circuit. Additional filters in this circuit were installed to clean the water from dust particles before entering the coils. Thus, impurities did not settle inside them. In contrast to the other coils the fast Feshbach coils were not water cooled. This limited the electric current through the coils as well as the time duration for holding a magnetic field with this coil pair. In order to protect all coils against overheating, temperature sensors were installed. With the use of an interlock system which compared the measured temperatures to given set values the respective power supplies could be shut down if a coil pair started to overheat.

Current stabilisation

A current stabilisation scheme for the slow Feshbach coils was required in order to minimize noise in the induced large, homogenous magnetic offset field. The setup is illustrated in [38]. The current stabilisation scheme comprised two feedback loops for slow and fast

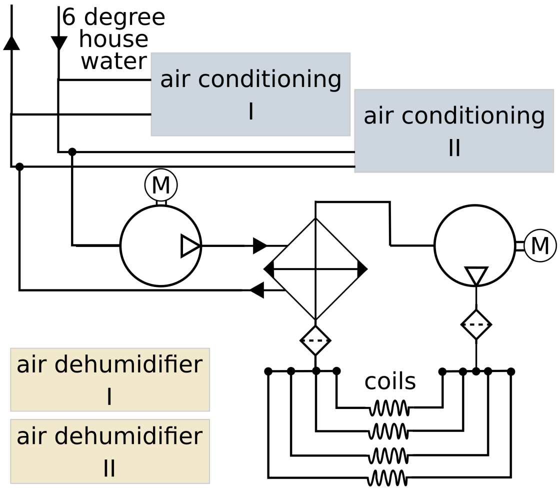

Figure 3.13: Water cooling circuit for the coil system (Fig. 3.3). 6 ° house water served as primary circuit in a heat exchanger. Water in the secondary circuit cooled the coils. Air dehumidifier stabilise the humidity level in the room.

field changes respectively.

The slow regulation was achieved by a PID control loop onto the *Delta* power supply for the slow Feshbach coils. A current transducer measured the current through the coils after an on/off switching Mosfet and provided a process voltage for comparison to a set voltage. Here, the set voltage could be adjusted by the experimental control and the resulting error signal was sent to a PID that passed it back to the power supply [57]. With this regulation loop, however, 50 Hz noise from the main power line could not be diminished. This was especially hindering single plane resolution (Sec. 3.5.3).

To overcome this drawback, a fast regulation based on an active load instead of a PID feedback loop was additionally installed. Here, a small portion from the current for the slow Feshbach coils was branched off and sent through the active load. Furthermore, a second current transducer measured the current directly before the coils and sent the process voltage to the active load as control signal. Depending on this control signal, the resistance of the active load was changed and more/less current was bypassed around the coils to regulate the current through them. The noise with this fast regulation could be lower by a factor of about 3.5 compared to the regulation with only the slow feedback loop. Magnetic field stabilities of about 1.2×10^{-5} could be reached [38]. This, however, could still not completely suppress the 50 Hz noise enough for tomography and a synchronisation of the experiment to the power line was implemented (Sec. 3.5.3).

Besides, the current regulation, the atoms in the glass cell were shielded from magnetic stray fields in the surrounding by a μ metal box with high magnetic permeability.

3.5 Density and spin discrimination in a single two-dimensional lattice plane

3.5.1 Zeeman splitting

For radio frequency swaps, tomography of single atom planes and singles/doubles or spin-up/spin-down discrimination the four lowest m_F-states of the $|F = 9/2\rangle$ manifold were employed (Fig. 3.4 left). Their dependence on the magnetic field is given by (in units of Hz)

$$\nu_{\mathrm{Zee}} = \frac{1}{h} B_z (g_{\mathrm{J}} \mu_{\mathrm{B}} m_{\mathrm{J}} + g_{\mathrm{I}} \mu_{\mathrm{N}} m_{\mathrm{I}}) \tag{3.8}$$

Here, for potassium, $g_{\mathrm{J}} = 1 + (g_{40\mathrm{K}} - 1) \cdot (J(J+1) - L(L+1) + S(S+1)/(2J(J+1)))$ and $g_{\mathrm{I}} = \mu_{40\mathrm{K}}/(\mu_N I_{40\mathrm{K}})$ are the g-factors of the electron and the potassium nucleus, μ_{B} and $\mu_{40\mathrm{K}}$ are the Bohr magneton and magnetic moment of the nucleus and m_{J}, m_{I} are the quantum numbers of the total angular momentum and the nucleus. Furthermore, $I_{40\mathrm{K}} = 4$ and $\mu_{40\mathrm{K}} = 2.00229421$.[12]

3.5.2 Radio frequency swaps

Radio frequency (rf) swaps were used to change the internal m_F-state of all atoms in the cloud at the same time. They were used to produce a spin mixture for efficient evaporative cooling (Sec. 4.2.1.1) and change the interaction strength. Furthermore, in a sequence of rf swaps and additional sweeps, they were used for tomography (Sec. 3.5.3), singles/doubles (Sec. 3.5.4) and spin up/spin down (Sec. 3.5.5) state detection.

The radio frequency swaps were generated by a direct digital synthesiser (DDS) board. The latter was initialized by the experimental control loading a list of all frequency settings, i.e. center frequencies and sweep widths of each swap, onto the DDS board in the beginning of each experimental cycle. The individual swaps were then triggered by a second signal from the control during the cycle. Each swap had a sweep width of 175 MHz around the transition center frequency and a time duration of 2 ms. The large frequency range and relatively long sweep duration avoided non-adiabatic transitions during the Landau-Zener sweep. The transition center frequencies for the transition between adjacent m_F-states, i.e. $|m_F = -9/2 \leftrightarrow -7/2\rangle$, $|m_F = -7/2 \leftrightarrow -5/2\rangle$ and $|m_F = -5/2 \leftrightarrow -3/2\rangle$, could be computed from the Zeeman splitting (Sec. 3.5.1). Swap efficiencies of 0.9985% were reached by rounding the sharp edges of the pulse amplitude in time [38].

3.5.3 Tomography

Tomography enabled to resolve the single atom planes in the stack of six planes by employing a combination of a magnetic field gradient and a radio frequency sweep. Within the six planes (Fig. 4.10), the second plane from the right exhibited the best combination of high atom number and cold temperature (N=5000, T/t=1.6 with $t = 224$ Hz being the

---

[12] S,L and J are the spin, angular and total angular momentum of the electron.

tunnelling amplitude). The detection of a single plane enabled the direct measurement of densities within a single atom layer avoiding an integration of the density along the imaging direction (line of sight).

Magnetic field

A vertical magnetic field gradient caused a different Zeeman splitting between the internal states of the atoms in different layers in the vertical z lattice. Using a narrow rf pulse, the m_F-state of atoms in a single plane could hence be swapped without addressing atoms in other planes. The addressed, swapped plane could furthermore be imaged to obtain the densities in this layer. In order to evoke a sufficient difference in the Zeeman splitting across adjacent planes a strong magnetic field gradient was required. The fast Feshbach coils were used for this purpose. Since these coils were not water-cooled the electric current as well as the time of high gradient was strongly limited. A maximum magnetic field gradient of $B_z = 3.33(5)\,\mathrm{mG\mu m^{-1}}$ could be hold for about 40 ms. This enabled a separation between adjacent atom planes in the green vertical 532 nm lattice of about 1200 Hz. In addition to the strong vertical magnetic field gradient, a homogeneous magnetic offset field of about 213.8 G was induced using the slow Feshbach coils. At this field strength the on-site interaction shift difference equalled zero $\Delta U = U_{37} - U_{57} = 0$. Here, U_{37} is the interaction strength between two spins on the same lattice site in the two-dimensional in-plane lattice with $|\uparrow,\downarrow\rangle = |m_F = -3/2\rangle, |m_F = -7/2\rangle$. Equivalently, U_{57} is the interaction strength between two spins on the same lattice site with $|\uparrow,\downarrow\rangle = |m_F = -5/2\rangle, |m_F = -7/2\rangle$. Thus, an rf pulse can transfer singles and doubles in the same plane even-handedly due to $\Delta U = U_{37} - U_{57} = 0$ (Fig. 3.14 left). To exploit the necessary condition ($\Delta U = 0$) the initial $|m_F = -9/2, -7/2\rangle$ spin mixture was stepwise transferred to a $|m_F = -3/2, -7/2\rangle$ spin mixture (Fig. 3.15) before the rf sweep was applied.

Radio frequency sweep

The radio frequency pulse to transfer the atoms in a single plane from $|m_F = -3/2\rangle$ to $|m_F = -5/2\rangle$ (Fig. 3.15, "tomography"), had a shape [38]

$$P_{\mathrm{slic}}(t) = A_{\mathrm{slic}}(t)\sin(2\pi\nu_{\mathrm{slic}}t). \tag{3.9}$$

with

$$A_{\mathrm{slic}}(t) = A^0_{\mathrm{slic}} \sum_{n=1}^{5} s_n \sin\left(\frac{(2n-1)\pi t}{t_{\mathrm{pulse}}}\right) \tag{3.10}$$

where

$$t_{\mathrm{pulse}} = 7.5\,\mathrm{ms}, s_1 = 0.0956, s_2 = -0.091, s_3 = 0.0483, s_4 = -0.005, s_5 = 0.002$$

The amplitude $A_{\mathrm{slic}}(t)$ is time dependent (Fig. 3.14 center). Furthermore, the frequency ν_{slic} in Eq. 3.9 corresponds to the $m_F = -3/2 \leftrightarrow m_F = -5/2$ transition frequency around

52 MHz. It can be computed from Eq. 3.8. A^0_{slic} in Eq. 3.10 was calibrated such that the sweep induced a π rotation on the Bloch sphere around the u-axis [38]. An arbitrary function generator *AWG 33600A* from Keysight generated the pulse. More information can be found in [38].

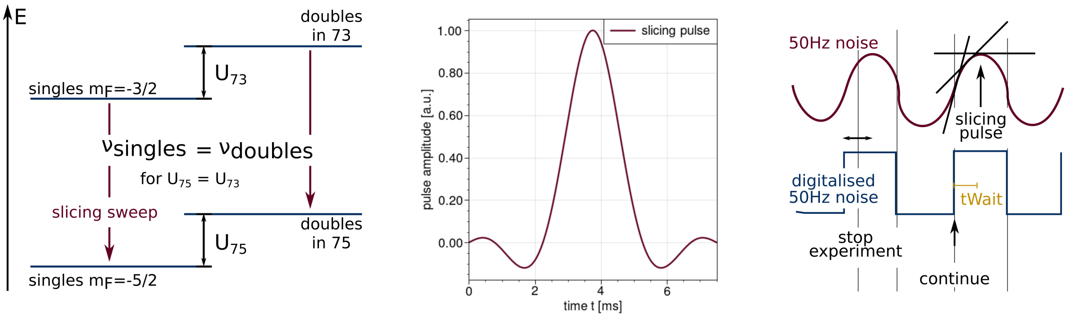

Figure 3.14: Left Necessary condition for tomography of singly *and* doubly occupied lattice sites (Fig. 3.15). Only if $U_{73} = U_{75}$, the internal state of both, singles and doubles, in a single plane can equally be changed. **Center** Tomography rf pulse which was generated with an arbitrary function generator. **Right** Synchronisation of the experiment to the power line in order to reduce magnetic field fluctuations while the tomography pulse was sent.

Synchronisation of the experiment cycle to the power line
The current stabilisation of the slow Feshbach coils (Sec. 3.4.2) did not suppress the 50 Hz noise from the power line completely. This noise on the current led to fluctuations in the magnetic offset field at a rate of 50 Hz and, therefore, in the Zeeman splitting of the internal states of the atoms. In turn, with a fixed ν_{slic} between different experimental cycles, detection noise from other planes hindered a sharp resolution of a single plane. To overcome this problem the time at which the tomography pulse was sent was synchronised to the 50 Hz noise of the power line. The experiment was therefore interrupted just before the tomography pulse by switching off the 10 MHz clock. At the following rising edge of the digitalised 50 Hz noise (Fig. 3.14 right), the experiment was continued and after an additional waiting time t_{Wait} the tomography pulse was sent. Thus, the pulse always coincided with the maximum of the sinusoidally fluctuating magnetic field at which the slope is zero and, thus, most stable. With the synchronisation to the power line and a pulse width of 500 Hz single planes could be resolved where the detected atom number in between two adjacent planes was negligible.[13]

3.5.4 Singly/Doubly site occupation discrimination

The discrimination between singly (singles) and doubly (doubles) occupied lattice sites in the two-dimensional in-plane lattice in a single shot was achieved by swapping the internal m_F-state of one of the two atoms forming a double (Fig. 3.15).

---

[13] In Fig. 4.10 each second plane was emptied before tomography such that the planes are well separated

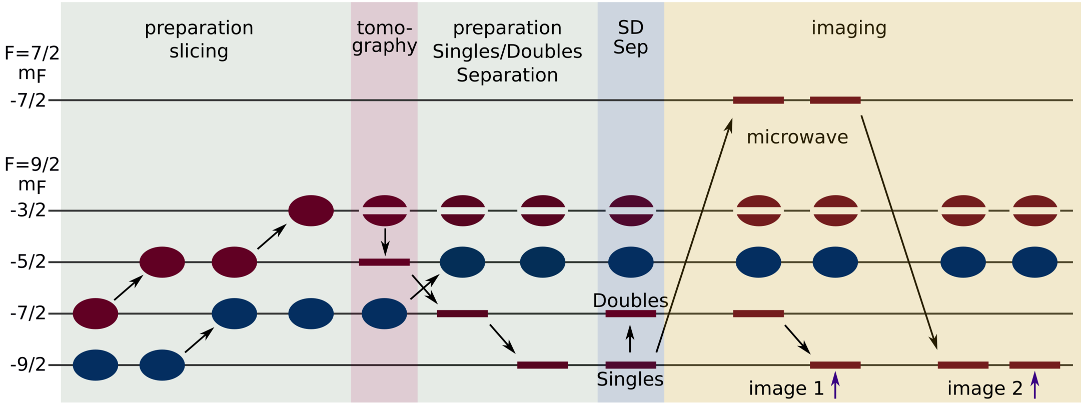

Figure 3.15: Detection scheme for singly and doubly occupied lattice sites. Microwave shelving (Sec. 3.5.6) was employed for separately imaging single and double occupations.

After the preparation for tomography (also referred to as slicing) and the tomography pulse (Fig. 3.15), the atoms were prepared for singles/doubles separation. Therefore, the atoms in the single plane which occupied the $|m_F = -5/2 >$ state after slicing were brought into the $|m_F = -9/2 >$ state while all other atoms in the $|m_F = -7/2 >$ state were transferred to the $|m_F = -5/2 >$ state. Hence, singles in the single plane occupied the $|m_F = -9/2 >$ state while doubles were in the $|\uparrow, \downarrow\rangle = |m_F = -5/2, m_F = -9/2\rangle$ state before the singles/doubles separation (SD) pulse was sent. The interaction shift was thus U_{59}. The SD pulse then transferred the "spin down" states in doubles from $|\downarrow\rangle = |m_F = -9/2\rangle$ into $|m_F = -7/2\rangle$. This changed the interaction shift to U_{57}. The absolute difference between both shifts $|U_{59} - U_{57}|/h = \nu_{\text{singlesTo7}} - \nu_{\text{doublesTo7}}$ equalled the frequency difference between transferring singles and doubles to the $|\downarrow\rangle = |m_F = -7/2\rangle$ state. At a magnetic field of about 212 G this difference was about 1.8 kHz which determined the required SD pulse width to separate doubles from singles.

SD pulse shape

The same dual channel arbitrary function generator (AWG) from Keysight which generated the tomography pulse was employed to generate the SD separation pulse. The second channel was used for this purpose. The pulse properties, i.e. amplitude, center frequency etc. were set in a python script and sent to the AWG at the beginning of each experimental cycle. The SD pulse was implemented with a time dependent amplitude $A_{\text{SD}}(t)$ and frequency $\nu_{\text{SD}} + \delta_{\text{SD}}(t)$ [38]

$$P_{\text{SD}}(t) = A_{\text{SD}}(t)\cos(2\pi t(\nu_{\text{SD}} + \delta_{\text{SD}}(t))) \tag{3.11}$$

with

---

even with a tomography pulse width of up to 1200 Hz.

$$A_{\mathrm{SD}}(t) = A^0_{\mathrm{SD}} 1/\cosh\left[5.5\left(\frac{2t}{T_{\mathrm{SD}}} - 1\right)\right] \tag{3.12}$$

and

$$\delta_{\mathrm{SD}}(t) = \frac{\delta^0_{\mathrm{SD}}}{2} \tanh\left[5.5\left(\frac{2t}{T_{\mathrm{SD}}} - 1\right)\right] \tag{3.13}$$

Here, ν_{SD} is the center frequency of the SD pulse which depended on the magnetic field and δ^0_{SD} is its width in frequency space. For a splitting between singles and doubles $\nu_{\mathrm{singlesTo7}} - \nu_{\mathrm{doublesTo7}} = 1.8\,\mathrm{kHz}$, this width was usually set to $1.2\,\mathrm{kHz}$. Furthermore, $T_{\mathrm{SD}} = 3\,\mathrm{ms}$ was the duration of the pulse whose amplitude and frequency is time dependent (Fig. 3.16). Transfer efficiencies of of 1.003(8) were reached [38].

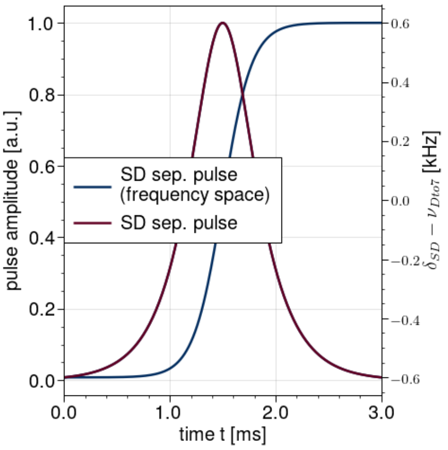

Figure 3.16: Amplitude and frequency of the singles/doubles separation pulse in time.

3.5.5 Spin state discrimination

Instead of discriminating between singles and doubles (Sec. 3.5.4), the detection scheme could be modified in order to discriminate between a spin up and a spin down state (Fig. 3.17)

During this sequence, atoms were swapped to the $|\uparrow,\downarrow\rangle = |m_F = -3/2, m_F = -9/2\rangle$ states and, thus, doubles were lost due to spin exchanging collisions. Moreover, the scheme comprised two tomography pulses: One to swap single atoms from $m_F = -3/2$ to $m_F = -5/2$ and one to swap singles from $m_F = -7/2$ to $m_F = -9/2$. Spin down atoms in $m_F = -9/2$ and spin up atoms in $m_F = -5/2$ could thus imaged separately (Sec. 3.5.6).

3.5.6 Microwave shelving and imaging

The separated imaging of either singles/doubles or two spin states required the intermediate transfer and storage of one spin state in the $|F = 7/2\rangle$ manifold. This was achieved

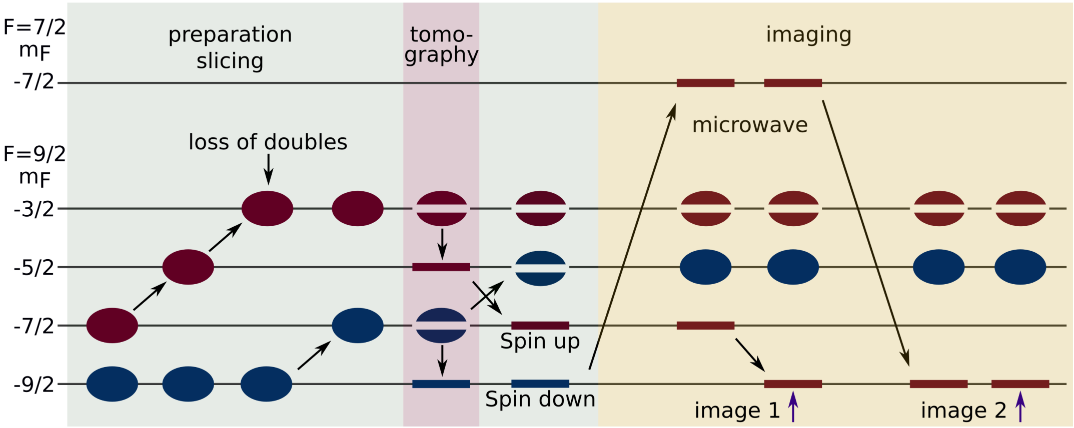

Figure 3.17: Detection scheme for "spin-up" and "spin-down" atoms in a single plane after tomography. Atoms on doubly occupied sites escaped from the optical lattice trap during "spin-up" and "spin-down" detection due to spin exchanging collisions from $|m_F = -3/2, m_F = -9/2\rangle$ to $|m_F = -5/2, m_F = -7/2\rangle$ in the preparation of tomography (slicing).

with two microwave sweeps giving this method its name "microwave shelving". Transferring one spin state of a doubly occupied site to the $|F = 7/2\rangle$ manifold, however, led to the loss of the double due to spin exchanging collisions. Therefore, atoms on singly occupied sites were brought into the $|F = 7/2, m_F = -7/2\rangle$ state instead (Fig. 3.15 or Fig. 3.17). For spin state discrimination the spin down state in $|\downarrow\rangle = |m_F = -9/2\rangle$ was microwave shelved to the $|F = 7/2, m_F = -7/2\rangle$ manifold. After this first microwave, a radio frequency swap (Sec. 3.5.2) transferred the residing atoms in the $|m_F = -7/2\rangle$ to the lowest $|m_F = -9/2\rangle$ state where they were imaged via z-imaging (Sec. 3.2.1). A second microwave subsequently transferred the atoms from the upper $|F = 7/2\rangle$ manifold back into the $|F = 9/2, m_F = -9/2\rangle$ state where a second image was taken. The storing of one spin state in the $|F = 7/2\rangle$ manifold prevented off-resonant imaging of atoms in the $|m_F = -7/2\rangle$ state.

The microwave was generated by a direct digital synthesiser (DDS) *AD9956* board and amplified before sending it to the microwave antenna close to the glass cell. The DDS board could be initialised and controlled via a Rasperry pi with a Browser interface or a *python*-script. The microwave center frequency was 1.822 GHz. The sweep width in frequency space was 2 MHz. The micro wave duration was 10 ms.

3.6 Digital mirror device

The digital mirror device (DMD) was employed to shape and/or compensate the underlying harmonic potential in the trap which was caused by the Gaussian lattice laser beams (Sec. 4.2.2.1 and Sec. 4.2.3). The DMD setup comprised a laser system, the DMD itself including a *Rasperry pi* to control the DMD and the optical path on the experimental table.

Laser system and optical setup on the experimental table

The laser system consisted out of a *Titan Sapphire ring laser Matisse C* from Sirah and a *Verdi V18* from Coherent which pumped the Ti:Sa crystal at a wavelength of 532 nm. The Matisse C ring laser was adjusted to provide light of wavelength around 735 nm. A power of up 2 W of 735 nm light was used. The output wavelength was blue-detuned with respect to the main D2 transition in potassium ^{40}K at 766 nm and, hence, this blue-detuned light could be used to compensate the red-detuned 1064 nm light from the lattice lasers. The output beam of the Matisse C ring laser was beam shaped, sent through an AOM for intensity control and fibre coupled to guide it to the experimental table (Fig. 3.18). Here, the DMD light was again shaped with a telescope and sent onto the DMD. In a 4f-setup thereafter spatial frequencies could be cut from the DMD light in the Fourier plane using an aperture. At a first cube some DMD light was then branched off and sent onto a Thorlabs camera which is referred to as “lower Thorlabs camera”. This enabled to monitor and characterise the beam before it entered the glass cell.[14] At the last beam splitting cube, the DMD light was finally combined with the z-imaging light path to conduct the light to the glass cell (cf. Fig. 3.5 right).

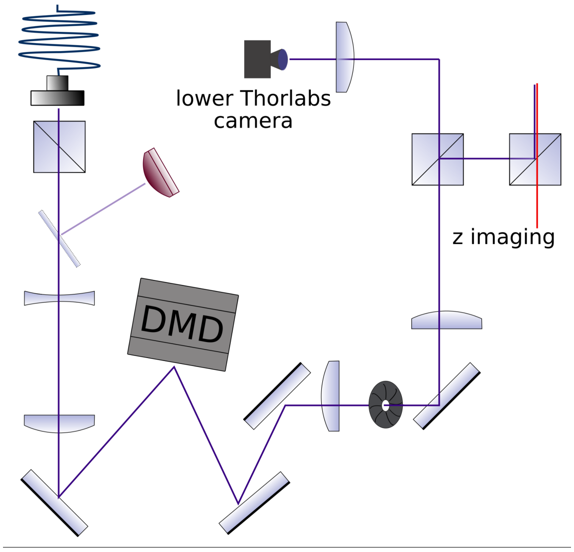

Figure 3.18: Optical setup of the DMD path. The path is combined with the z-imaging path (Fig. 3.5 right) at the beam splitting cube before the glass cell (Fig. 3.7).

Digital mirror device

The digital mirror device was a *DLP LightCrafter 6500* from Texas Instruments. It possessed an array of 1920 × 1080 micro mirrors where each of them was controllable by an on/off voltage. The size of the total array was about 14.5 × 8.2 mm. Each square mirror had a length of 7.56 µm. A *DLPC900* control board set each individual mirror voltage. In the *on*-state the voltage led to a tilt of the respective mirror by 12 ° with respect to the

---

[14] A second Thorlabs camera referred to as “upper Thorlabs camera” was installed behind the glass cell. Here, “lower” and “upper” refer to the level on the optical table.

array surface. The off-state mirrors were parallel to the surface. Hence, all mirrors in the on-state reflected the incoming Gaussian beam stemming from the Matisse C laser under a defined direction and the so “shaped” blue- detuned DMD beam was used to shape the underlying potential at the location of the atoms. Furthermore, the mirrors could be switched between on/off at a rate of up to 9500 Hz which enabled a rapid change of the mirror setting (= displayed pattern) on the DMD.[15]

The displayed patterns were loaded onto the DMD as bitmaps via a Rasperry Pi. Each pixel in the bitmap had a value 0 or 1 and corresponded to one micro mirror on the DMD, thereby setting its state to off/on, respectively. The bitmap was created with a *python* program. Exemplarily, the necessary steps to configure the DMD with the goal to compensate the underlying potential from the Gaussian lattice beams are outlined in the following. This was used for example to create a band insulator (Sec. 4.2.3).

First, the resulting potential landscape from the Gaussian lattice beams at the location of the atoms was deduced using the measured waists (Sec. 4.2.2.1) and powers (Sec. 4.1.1) of the lattice beams.

Second, the small, circular area of DMD mirrors (all and only in *on*-state) which reflects the DMD beam onto the trapping potential *center* was determined. Therefore, the atoms were held in a two-dimensional lattice (Sec. 4.2.2.2) and a thin beam out of the whole DMD beam which was created by reflection from the small, circular area of DMD mirrors in the *on*-state was shone onto the atoms. Due to the blue-detuning of the DMD light the atoms avoided the spot where the thin beam hit the cloud which produced a hole in the atomic cloud. By iteratively using other mirrors on the DMD for the circular area the one which reflects the DMD beam towards the center of the atomic cloud could be found. The latter coincided with the center of the trapping potential.

Third, after determining the “center mirror” the power of the DMD beam was calibrated using the lower Thorlabs camera. In order to do so, all DMD mirrors were set to *on* such that the whole Gaussian beam was reflected on the DMD surface into the further optical path and the light intensity was measured spatially resolved with the camera at a defined voltage in the experimental control. This yielded the calibration between light intensity and set voltage.

Forth, the thus calibrated beam intensity was converted to a resulting blue-detuned potential. By scaling up this potential such that it slightly exceeded the potential of the lattice beams everywhere the scaling factor was inferred by which the set voltage had to be multiplied to provide sufficient DMD intensity for compensation.

Fifth, the scaled intensity pattern was error diffused with an algorithm. The latter converted the scaled intensity pattern to the binary map. In this map, the algorithm set pixels to zero in order to reduce the number of reflecting DMD mirrors. Thus, the local intensity of the DMD beam was not remitted after the DMD such that the remaining local intensity pattern after the DMD equalled the necessary intensity for compensation of the Gaussian beams.

In general, this procedure allowed for arbitrary pattern generation as long as the available intensity from the Matisse C was sufficient everywhere. The point spread function of the optical path reduced the maximum achievable intensity. Furthermore, interferences due

---

[15] In [54] fast switching was employed in the attempt to implement a Floquet system.

to dust in the optical path led to disorder in the compensated potential. This disorder was analysed in [54].

CHAPTER 4

Results and discussion

The last chapter detailed the experimental setup which was used and extended to build the analogue quantum simulator for a bilayer Hubbard system. Moreover, chapter two elaborated the computation of Wannier functions used for the calculation of the bilayer Hubbard parameters, namely the tunnelling amplitude $t_\perp$ between the two atom layers in the bilayer Hubbard system and the interaction strength U in the vertical z superlattice.
In this chapter, in the first section (Sec.4.1), the calibration of the vertical z superlattice (Sec.3.3.1) and of the Hubbard parameters is presented. This calibration based on the comparison of the experimental results with theoretical predictions employing non-interacting and interacting Wannier functions. The latter are computed by the method developed in this thesis (Sec.2.2).
In the second section (4.2), the implementation steps of the bilayer Hubbard model with the experimental setup presented in chapter 3 are detailed and accompanied by a quantitative analysis. Thereby, the discussion follows the experimental control sequence steps. This implementation makes use of the calibrated Hubbard parameters from the first section of this chapter (Sec.4.1).
In Sec. 4.3, the spin correlation measurements on the bilayer Hubbard system are presented. This includes the comparison to existing theoretical predictions of spin correlations in a bilayer Hubbard system based on a Determinant Quantum Monte Carlo method.
In Sec. 4.4, results on thermodynamics are finally discussed.

4.1 Calibrating the superlattice and bilayer Hubbard parameter

4.1.1 Superlattice depth calibration

The amplitude or depth of the short z532 and long z1064 optical lattice (cf. V_s and V_l in Eq. 2.8) at the location of the atoms was calibrated employing lattice modulation spectroscopy [56][88]. Both lattice depths were calibrated separately rather than employing the lattice modulation to the superlattice as described in [97]. The method is discussed in the following for the z532 lattice. Modulation spectroscopy of the z1064 lattice, however, was performed similarly.

Starting from cold atoms in a $|-9/2, -7/2\rangle$ spin mixture confined in the dipole trap, the z532 lattice laser power was ramped up within 2 s to a finite value. This slow ramp guaranteed that the atoms were adiabatically loaded to the ground band of the one dimensional z532 lattice potential. The power of the z532 lattice laser beam was subsequently modulated for 100 ms employing the acoustic optical modulator (AOM) in the z532 lattice laser setup (Fig. 3.6).[1] The lattice modulation with amplitude $\mathrm{A}_{\mathrm{mod}}$ around V_0 (Fig. 4.1 left) can be described by

$$\mathrm{V}(t) = \mathrm{V}_0 + \mathrm{A}_{\mathrm{mod}} \cdot \cos(\nu_{\mathrm{mod}} t).$$

Here, ν_{mod} is the lattice modulation frequency. For small $\mathrm{A}_{\mathrm{mod}}$, the transition amplitude for atoms from the ground state of the optical lattice to excited states can be inferred from perturbation theory to first order as [27]

$$\mathrm{T}^{0n}_{qq'} = \delta_{qq'} \int \psi^{n}_{q'}(z)\mathrm{V}(z)\psi^{0}_{q}(z)\mathrm{d}z. \tag{4.1}$$

Here, $\delta_{qq'}$ states that the lattice momentum is preserved during the excitation. For a deep lattice, in which lattice modulation was performed, excitations to bands with index n mod $2 = 1$ are strongly suppressed due to a vanishing integral in Eq. 4.1. For example, the ratio of the transition strength between the levels $0 \leftrightarrow 1$ and $0 \leftrightarrow 2$ yielded $\mathrm{T}^{01}/\mathrm{T}^{02} = 0.0003$ (Fig. 4.1).[2] After the modulation the z532 lattice laser power was adiabatically diminished to zero within 1 ms. The adiabaticity ensured that the lattice momentum of the afore confined atoms in the ground and excited bands of the optical lattice was conservatively mapped to free space momentum[18]. Relieved from the confining potential, the atom cloud expanded in free space for a time of flight of 10 ms before absorption imaging was performed. The so-obtained, momentum-resolved optical density was plotted against the modulation frequency (Fig. 4.1 right). The theoretically predicted band transition frequencies for a specific lattice depth (Fig. 4.1 left) was then matched with the observed resonances which yielded the conversion factor between laser beam power and lattice units, i.e. recoil energies.[3] So, the lattice depth was calibrated.

For both z lattices the theoretically predicted transitions were set to the high frequency edge of the observed resonance (Fig. 4.1 right) in order to determine the conversion factor. The high frequency edge is connected to the lattice depth in the trap center where the lattice is deepest and the energy gap $\mathrm{E}_{\mathrm{ex}} - \mathrm{E}_{\mathrm{gr}}$ between excited and ground band is largest. This spatial dependence was caused by the underlying harmonic confinement of

---

[1] An arbitrary function generator *WW1071* from Tabor Electronics created the sinusoidal modulation signal and sent it to the AOM controller. The latter in turn mixed it with the 80 MHz AOM driving frequency and routed it to the AOM.

[2] This calculation bases on the Wannier functions of the three lowest energy bands (Fig. 2.9) in the antisymmetric superlattice configuration.

[3] In Fig. 4.1 the the obtained optical density is additionally momentum-resolved (x-axis) for different lattice modulation frequencies (y-axis).

the Gaussian lattice laser beams.

The increment of the modulation frequency steps of 0.25 kHz (Fig. 4.1 right, y-axis) leads to an uncertainty of the optical lattice depth. For both, the z532 and z1064 lattice the error is about 0.5% of the lattice depth. This error is propagated to the error of the Hubbard parameters t and U.

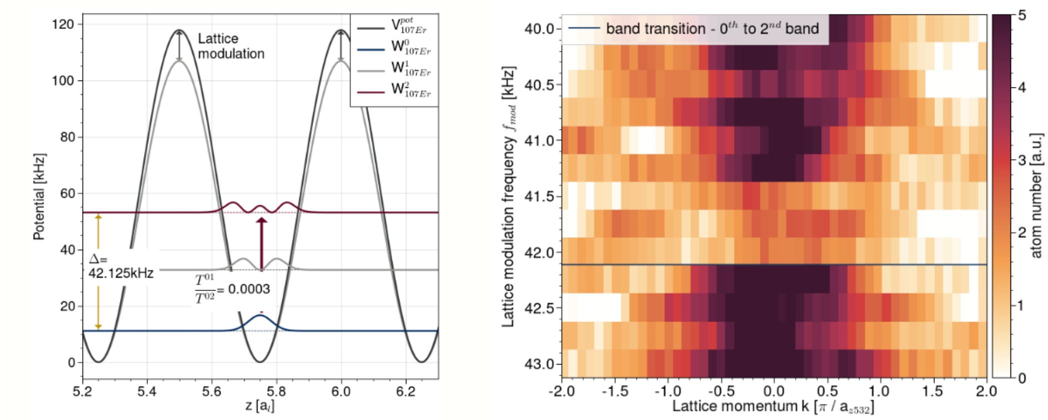

Figure 4.1: Lattice modulation spectroscopy of the z532 lattice. **Left** Lattice configuration with involved Wannier functions from the BPPO method using two bands (Sec. 2.2.2). The relative transition amplitude $T^{01}/T^{02} = 0.0003$ shows that the transition amplitude of the 0-1 transition is strongly suppressed compared to the 0-2 transition. The energy difference between the ground and second band is $\Delta = 42.125\,\text{kHz}$. This corresponds to the frequency in the right figure. **Right** Spectroscopy signal. The optical density measured with absorption imaging after time of flight as a function of the lattice modulation frequency ν_{mod} (y-axis) and of the lattice momentum k (x-axis). At resonance the atoms are excited to the second band and move rapidly out of the field of view of the z-camera during time of flight.

4.1.2 Superlattice symmetry point calibration

The symmetry point of the z superlattice was experimentally determined via a measurement of singly and doubly occupancies as a function of the z superlattice offset lock voltage $V^{\text{ctr}}_{\text{zlock}}$ in the VCO (Fig. 3.8) and, hence, the superlattice phase.

The control sequence (Fig. 4.2 left) started with a $|-9/2, -7/2\rangle$ spin mixture of atoms which was loaded into the two-dimensional in-plane lattice formed by the x1064 and y1064 lattice (Fig. 3.10). Tunnelling in z direction was frozen out setting the z532 lattice depth to $120\,\text{E}_{\text{rec}}$. Tunnelling within the plane was likewise suppressed setting both in-plane lattice depths to $30\,\text{E}_{\text{rec}}$. Subsequently, the z1064 lattice was ramped up to $200\,\text{E}_{\text{rec}}$ within 50 ms while the phase was set to the antisymmetric lattice configuration.[4] Thus, the atoms were

---

[4] As discussed in Sec. 3.3.1 the antisymmetric configuration could not be achieved with the big Mephisto for the z1064 and the z532 lattice. Here, this term refers to the most asymmetric configuration which

loaded adiabatically into the ground state of the resulting, isolated antisymmetric double wells in z direction (Fig. 4.2 left upper row). The double well barrier was then ramped down in two steps within 50 ms and 10 ms to a final varying value between $15-23\,\mathrm{E}_{\mathrm{rec}}$. In between the two ramps a radio frequency swap changed the spin mixture to $|-9/2,-5/2\rangle$ in order to induce repulsive on-site interactions at a magnetic field of 207 G. Ramping the superlattice phase subsequently in 200 ms resulted in a specific final configuration. The singly and doubly occupancies after equilibration in the double wells were then frozen by ramping up the z532 lattice again to $120\,\mathrm{E}_{\mathrm{rec}}$ and diminishing the z1064 lattice to zero within 1 ms. After performing second plane evaporation in order to empty the same well in each double well across all planes (Sec. 4.1.6), remaining singly and doubly occupancies were distinguished via singles/doubles separation (Sec. 3.5.4). Tomography was not used in this measurement leading to an integrated number of detected atoms along the line of sight in z direction.

In order to deduce the symmetry point from the number of single and double occupancies as a function of the final superlattice phase (after the 200 ms phase ramp) the obtained data were fit by the theoretical calculation of a double well system (Fig. 4.2 right). Here, the occupancies resulted from the consideration of both, a single and two fermions in a double well, respectively. The Hamiltonian for a single fermion in a double well as a function of the detuning Δ is given by Eq. 4.3. There, the off diagonals are set to the tunnelling amplitude t between the two wells. The Hamiltonian for two fermions in a doubles well is given by [12][42]

$$\mathrm{H}_{\mathrm{DW}} = \begin{pmatrix} U+2\Delta & -t & -t & 0 \\ -t & 0 & 0 & -t \\ -t & 0 & 0 & -t \\ 0 & -t & -t & U-2\Delta \end{pmatrix}, \tag{4.2}$$

where U, t and Δ are the on-site interaction strength, tunnelling amplitude and the offset between the lowest energy states in each well of the double well, respectively. The four basis states are $|\uparrow\downarrow,0\rangle$, $|\uparrow,\downarrow\rangle$, $|\downarrow,\uparrow\rangle$ and $|0,\uparrow\downarrow\rangle$. The probability of finding a double occupancy after evaporating the second well in terms of these eigenvectors is given by $p^{\mathrm{d}}_{\mathrm{DW}} = \mathrm{A}^{\mathrm{d}}|\,|\uparrow\downarrow,0\rangle\,|^2/\eta^{\mathrm{d}}$. Here, $\mathrm{A}^{\mathrm{d}}, \eta^{\mathrm{d}}$ is the amplitude and detection efficiency of doubles, respectively.[5] In contrast, a singly occupied site was measured when a double split into two singles during the phase ramp or when the double well was already initially filled by only one fermion *and* this fermion occupied the well which was not emptied during second plane evaporation. The probability for a singly occupancy was thus $p^{s}_{\mathrm{DW}} = \mathrm{A}^{\mathrm{s}}|\,|\cdot,0\rangle\,|^2 + \mathrm{A}^{2\mathrm{s}}(|\,|\uparrow,\downarrow\rangle\,|^2 + |\,|\downarrow,\uparrow\rangle\,|^2)/\eta^{\mathrm{s}}$. Here, A^{s} was the single amplitude and $|\cdot,0\rangle$ was one of the two eigenvectors describing one fermion in a double well. In order to fit the theoretical probabilities to the measured singly and doubly occupancies, three other free fit parameter were included: 1. Δ in Eq. 4.2 yielding the conversion factor

---

could be achieved employing the big Mephisto and is used in the following for shortness. Since the small Mephisto is only used for second plane evaporation any confusion is prevented.

[5] The doubles amplitude A^{d} scales the measured number of doubly occupancies to a density which can be compared to the calculations. The scaling is necessary since tomography was not used.

between $V^{\mathrm{ctr}}_{\mathrm{zlock}}$ and the detuning, 2. the interaction strength U and 3. the symmetry point.

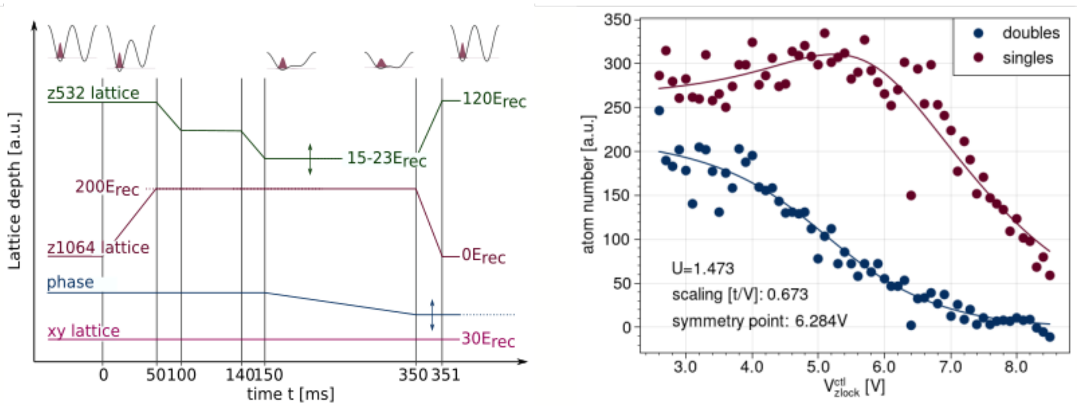

Figure 4.2: Determination of the symmetry point. **Left** Main steps of the experimental sequence. **Right** Experimental data and fit for one and/or two fermions in one well of a double well as a function of the superlattice phase.

By fitting the theory to the data, the symmetry point could routinely be found. This method, however, was not suitable to precisely determine the conversion factor between the z superlattice offset lock voltage $V^{\mathrm{ctr}}_{\mathrm{zlock}}$ and Δ in Eq. 4.2 or equivalent the superlattice phase ϕ in Eq. 2.8, due to the large number of free fit parameters, i.e. A^{s}, A^{d} etc..

4.1.3 Superlattice phase calibration

The measurement of Rabi oscillations for different z superlattice offset lock voltages $V^{\mathrm{ctr}}_{\mathrm{zlock}}$ (Sec. 3.3.1, offset lock), enabled the determination of the conversion factor between $V^{\mathrm{ctr}}_{\mathrm{zlock}}$ and Δ which describes the offset energy between the two levels in a general two level system. Therefore, the predicted dependence of the effective Rabi frequency on Δ from the two level system was fit to the measured effective Rabi frequency. In order to verify that the so obtained Δ matched the theoretical expected Δ which results from a phase $\phi \neq 0$ in the definition of the superlattice potential in Eq. 2.8, the measured effective Rabi frequencies were compared to Rabi frequencies yielded from a theoretical calculation with the BPPO method in Sec. 2.2.2.

The general two level system

A general two level system with detuning is described by the Hamiltonian [86]

$$\mathrm{H}_{2\mathrm{lev}} = \begin{pmatrix} -\Delta & \Omega_{\mathrm{R}} \\ \Omega_{\mathrm{R}} & \Delta \end{pmatrix} \tag{4.3}$$

with Ω_{R} and Δ being the common Rabi frequency and the detuning from resonance, respectively. The double well is an application of this general two level system (Fig. 4.3

left). The ansatz to solve this problem is $|\psi(t)\rangle = (C_g(t)\exp(-i\omega_g t), C_e(t)\exp(-i\omega_e t))$ in the basis $\{(1,0),(0,1)\}$. Here, $\omega_g = E_g/\hbar$ and $\omega_e = E_e/\hbar$ are the angular frequencies corresponding to the lower (E_g) and upper (E_e) energy level, respectively. Starting with a system where only the lower energy level is populated, the upper energy level can be populated by a Landau-Zener sweep. The time evolution of the population of this upper level is given by

$$|C_e(t)|^2 = \frac{\Omega_{\mathrm{R}}^2}{(\Omega_{\mathrm{R}}^{\mathrm{eff}})^2} \cdot \sin\left(\frac{\Omega_{\mathrm{R}}^{\mathrm{eff}} t}{2}\right). \tag{4.4}$$

Here, the effective Rabi frequency is defined as

$$\Omega_{\mathrm{R}}^{\mathrm{eff}} := \sqrt{\Omega_{\mathrm{R}}^2 + \Delta^2} \tag{4.5}$$

and includes the detuning $2\Delta = \hbar(\omega_e - \omega_g)$. The occupation of the lower energy level oscillates with a time shift of $\pi/2$ compared to Eq. 4.4. Eq. 4.5 states the expected dependence of the Rabi frequency on the detuning 2Δ.

Experimental sequence to induce Rabi oscillations

The experimental sequence (Fig. 4.3 right) to induce Rabi oscillations in isolated double wells along the z direction started with a polarized atomic gas in the $|m_F = -9/2\rangle$ state which was initially loaded in a two-dimensional lattice plane.[6] Tunnelling between planes was suppressed setting the vertical z532 lattice to 120 $\mathrm{E_{rec}}$. Tunnelling within each plane was frozen out setting the in-plane lattices to 30 $\mathrm{E_{rec}}$. Starting from this situation the vertical z1064 lattice was ramped up adiabatically in 50 ms to 120 $\mathrm{E_{rec}}$ while the phase was kept at a specific but constant value. This value was scanned across different measurement runs. The slow ramp up of the z1064 lattice depth of 50 ms guaranteed a loading into the ground state of each of the so formed isolated double wells. In order to induce Rabi oscillations between the lowest and first excited energy level in each double well, the first excited state was populated via a Landau-Zener sweep. The latter was performed by diabatically ramping down the z532 lattice within 100 µs to a depth between $13-20\,\mathrm{E_{rec}}$. This effectively diabatically converted two separated wells into a connected double well. The diabaticity of the ramp was fulfilled as the considered lattice configurations exhibit a maximum energy gap between the two lowest energy levels of 1.6 kHz compared to the 100 µs ramp time. For all lattice configurations the Rabi oscillation frequency was in a measurable range concerning a minimum sampling rate of 100 µs. The sampling rate was limited by the minimum length of one time step in the experimental sequence control. After a free Rabi oscillation time $t_{\mathrm{R}} \in [0...2.5\,\mathrm{ms}]$, the z1064 lattice was diminished to zero while the z532 lattice was simultaneously increased to 120 $\mathrm{E_{rec}}$ in 1 ms to freeze the motion. Each second layer was subsequently emptied using the second plane evaporation technique (Sec. 4.1.6). This enabled to make the oscillations visible as atoms were only detected - after second plane evaporation - when they were located in the not-emptied well after t_{R}.

---

[6] A similar ansatz was set up in [12].

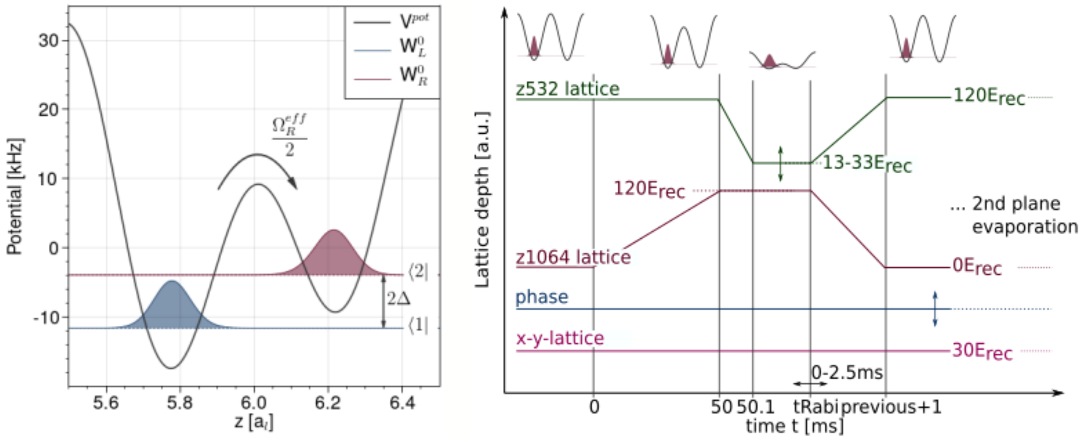

Figure 4.3: Induced Rabi oscillations in isolated double wells. **Left** A double well as application of the general two level system. **Right** The main experimental sequence steps to induce Rabi oscillations.

Analysis of the effective Rabi oscillations

The number of atoms in the not-emptied well as a function of the evolution time t_R for a symmetric superlattice configuration oscillated (Fig. 4.4 left). Determining the frequency of this oscillations from a fit to the atom number of the entire cloud, however, led to an imprecise result for the Rabi frequency. The underlying potential of the Gaussian shaped lattice laser beams led to an increase of the lattice depth and barrier height of each double well towards the trap center and, in turn, to a decrease of the Rabi oscillation frequency there. An evaluation of the entire image therefore averaged over different frequencies. In order to avoid this, all images of one measurement were sectioned and the time evolution of the atom number in each section were fit using a damped sinusoidal function

$$f_\mathrm{dampSine}(t) = \mathrm{A} \cdot e^{-t/\tau} \cos\left(\pi \nu t + \phi\right) + \mathrm{const.}$$

Here, $\mathrm{A}, \tau, \nu, \phi$ and const. are the amplitude, decay time, frequency, phase and offset, respectively.

One reason for the decay of the bare oscillations was the averaging over several planes during absorption imaging. Performing radio frequency tomography in order to select a single plane would not necessarily have led to an improvement due to atom number fluctuations. However, the decay was small and 5 oscillations were clearly visible (Fig. 4.4 left).

Subsequently, the z superlattice offset lock voltage $\mathrm{V}_\mathrm{zlock}^\mathrm{ctr}$ and, hence, the superlattice phase was scanned around the symmetry point and the Rabi oscillation measurement was performed for each phase. The extracted oscillation frequency was then plotted versus the phase in units of $\mathrm{V}_\mathrm{zlock}^\mathrm{ctr}$ (Fig. 4.4 right). The data points were fitted using the theoretical predicted dependence of the effective Rabi frequency on the detuning from the two level system (Eq. 4.5). The extracted fit parameter exemplary for the lattice depth of $\mathrm{V}_{z532} = 13\,\mathrm{E}_\mathrm{rec}$ were $\Omega_\mathrm{R} = 1692(2)\,\mathrm{Hz}$ and $\Delta = 384(6)\,\mathrm{Hz/V}$. The angular point of the parabola is at 5.89(2) V. T

Theoretically expected effective Rabi frequencies

In the experiment, the superlattice phase can be tuned in units of the offset lock voltage. In order to compare the experimentally determined effective Rabi frequency with theoretical calculations, the conversion factor from $V^{\mathrm{ctr}}_{\mathrm{zlock}}$ in units of Volts to superlattice phase in radians is needed (Fig. 4.4 right, cf. upper and lower x-axis). This factor was obtained as follows:
First, the parabola with $\Omega_{\mathrm{R}} = 1692(2)\,\mathrm{Hz}$ and $\Delta = 384(6)\,\mathrm{Hz/V}$ was plotted versus the $V^{\mathrm{ctr}}_{\mathrm{zlock}}$ in units of Volts.
Second, the function $\Omega^{\mathrm{eff}}_{\mathrm{R}} = (\Omega^2_{\mathrm{R}} + (c_{\mathrm{VToPh}} \cdot \Delta)^2)^{1/2}$ with the above mentioned parameter values was plotted versus the *theoretical superlattice phase* (Fig. 4.4 right, lower x-axis).
Third, the conversion factor c_{VToPh} that minimizes the mean squared error between both parabola were found. It yielded $c_{\mathrm{VToPh}} = 36.82$ and, hence, $1\,\mathrm{V} \hat{=} 1/36.82 \approx 0.027\mathrm{rad}$.[7]

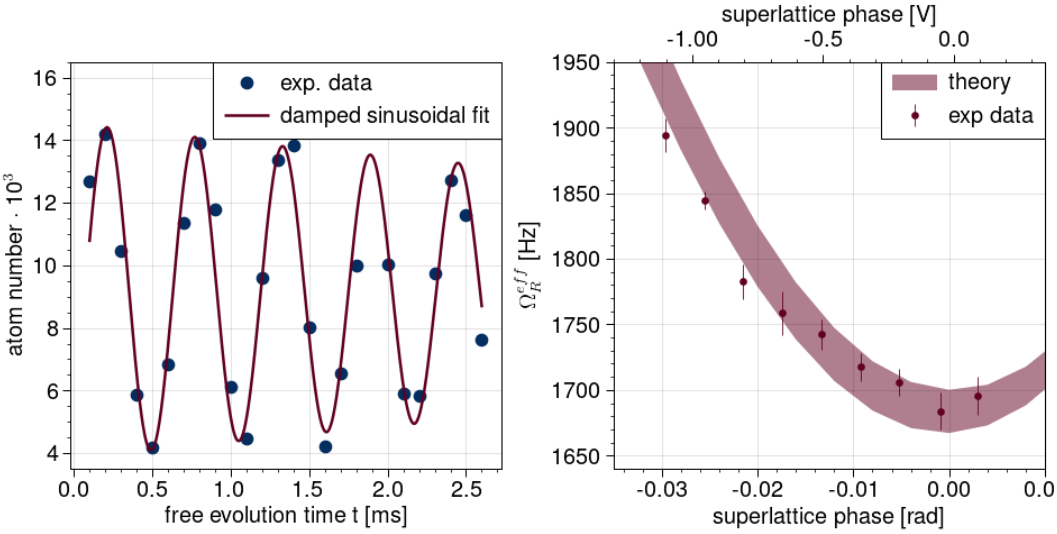

Figure 4.4: Effective Rabi oscillation frequency in the z superlattice. **Left** Bare Rabi oscillations in the symmetric superlattice configuration. **Right** Measurement and theory from the BPPO method of the effective Rabi oscillation frequency.

This conversion factor was used to compare the measured data to theoretical expected effective Rabi frequencies from the BPPO method using two bands (Fig. 4.4 right, shaded region). The y-error of the data points is given by the uncertainty of the sinusoidal fit of the bare Rabi oscillations. The data points are shifted such that the angular point of the parabola is at zero Volt. The theory band originate from the uncertainties in the z532 and z1064 lattice depths determined by parametric heating to be $\sigma_{\mathrm{Vlat}} = 0.5\%$ of the total depth (Sec. 4.1.1) as well as from the uncertainty of the symmetry point and Δ determined by the angular point and curvature of the parabola. The theory coincided

---

[7] Note that the phase difference between the symmetric and antisymmetric superlattice configuration is $\pi/4 \approx 0.785$.

with the data points within the errorbars. The data points for phases further away from the symmetry point, however, stick to the lower edge of the theory band. A phase shift of the superlattice phase during the Rabi oscillation measurement might be caused by an error in the determination of the conversion factor c_{VToPh}. The upper bound for the error of the conversion factor was estimated to be 5%.

4.1.4 Superlattice phase stability

The phase stability of the vertical z superlattice could be inferred from the Rabi oscillation measurement (Fig. 4.4 right). Here, the measured effective Rabi frequency coincided with the theoretical predictions from the BPPO method for all phases. Thus, for the time of the measurement which was about four hours the superlattice phase did not fluctuated more than $0.004 - 0.005\,\mathrm{rad}$ which is approximately the width of the theory band.

4.1.5 Calibration of the Hubbard tunnelling parameter t

Rabi oscillations as induced and measured with the experimental sequence (Sec. 4.1.3) take place when a system undergoes periodic transitions between two states. From this measurement the tunnelling amplitude t in the Hubbard Hamiltonian Eq. 2.1 can be deduced. It describes the transition strength between the two states $|L, 0\rangle$ and $|0, R\rangle$ where a particle occupies either the left or right well of the double well. Taking into account that the Rabi oscillation cycle is defined as the forth and back transition between the two involved states while tunnelling describes only the transition in forward direction, t could be inferred from the Rabi oscillation measurement as $\mathrm{t}^{\mathrm{eff}} = \Omega_{\mathrm{R}}^{\mathrm{eff}}/2$. Here, $\mathrm{t}^{\mathrm{eff}}$ includes the detuning Δ between the two wells.

As shown in Sec. 4.1.3 the effective Rabi frequency and, hence, the effective tunnelling amplitude as a function of the superlattice phase matched the theoretical predictions from the BPPO method. The dependence of the effective tunnelling amplitude on the double well depth and double well barrier height was subsequently experimentally tested and compared to the theoretical predictions (Fig. 4.5). The data were taken for two z1064 lattice depths of $V_{z1064} = 120$ and $210\,\mathrm{E}_{\mathrm{rec}}$ and three different z532 lattice depths, respectively. The phase was set to the symmetric superlattice configuration. Again, the y error yielded from the uncertainty of the damped sinusoidal fit to the oscillations. The theory band yielded from the uncertainty in the two lattice depths of the z532 and z1064 lattice in parametric heating and the uncertainty in the symmetry point.

4.1.6 Second plane emptying

In the Rabi oscillation measurement, it was required to empty (evaporate) each second plane in the vertical stack of two-dimensional lattice planes before detection (Fig. 3.15). Thus, the oscillatory behaviour of the atom number in all not-emptied planes (sites) without explicitly resolving these planes (sites) can be observed.[8]

---

[8] Here, the term "sites" relates to the double well with two sites. This is the point of view of a single connection between the two planes in vertical direction. Actually, there are many of these double well which together form the "plane".

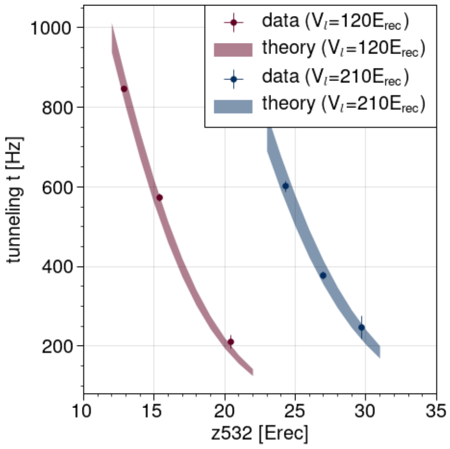

Figure 4.5: Tunnelling frequencies at the symmetry point of the vertical z superlattice. Data points are deduced from Rabi oscillation measurements. Theoretical predictions are made using non-interacting Wannier functions from the BPPO method. The broadened theory bands originate from the uncertainty of the z532 and z1064 lattice depths as well as the one of the symmetry point.

Experimentally, second plane emptying was achieved in several steps. First, the in-plane lattice was ramped to $60\,\mathrm{E_{rec}}$ and the z532 lattice to $120\,\mathrm{E_{rec}}$ to suppress tunnelling in all directions. Thus, the atomic distribution was frozen for tomography, singles/doubles or spin up/spin down discrimination and imaging. In this configuration each plane of the vertical lattice was usually filled. For second plane emptying, the z1064 lattice was ramped up additionally after freezing and before tomography to $28\,\mathrm{E_{rec}}$ using the small Mephisto (Sec. 3.6). Thus, the z superlattice was prepared in its antisymmetric configuration.[9] In turn, two filled adjacent planes in the z532 lattice were again coupled into a double well in the superlattice. At the same time tunnelling within and between the double wells was negligible due to the double well's antisymmetric configuration. In this setting, the red-detuned in-plane lattice was ramped down to $30\,\mathrm{E_{rec}}$ and the blue-detuned z532 lattice was diminished to $0\,\mathrm{E_{rec}}$. Thus, atoms in the upper well of the antisymmetric double well were pushed into the continuum of the underlying potential from the Gaussian lattice laser beams. Contrarily, atoms in the lower well occupied the ground state of the single wells after diminishing the z532 lattice to $0\,\mathrm{E_{rec}}$. In order to pull the atoms in the continuum out of the trap, a magnetic field gradient in z direction was switched on using the fast Feshbach coils.[10] Due to the gravity, the atoms finally left the trap.

The second plane emptying, however, exhibited a spin dependency. That means that one spin component could leave the trap already at smaller applied vertical magnetic field gradients than the other spin component. For the Rabi oscillation measurement this was

---

[9] The small Mephisto laser light frequency was adjusted such that the superlattice phase of the resulting z superlattice was antisymmetric.

[10] Here, a gradient of $7\,\mathrm{G/cm}$ in the opposite direction compensated gravity.

not hindering since a spin polarised gas was used there. When creating the bilayer system, however, second plane evaporation was switched off and the tomography signal had to be optimized to minimize detection noise from neighbouring planes.

4.1.7 Calibration of the Hubbard interaction strength U

After calibrating the Hubbard tunnelling amplitude $t_\perp$ (Fig. 4.5), the on-site interaction strength U (Eq. 2.21) in the vertical superlattice was calibrated. Therefore, measured interaction strengths in isolated double wells along the z direction were compared to theoretical predictions.
On the experimental side, a $|-9/2, -7/2\rangle$ spin mixture was first loaded into the two-dimensional in-plane lattice whose depth was set to $60\,\mathrm{E_{rec}}$. At this time step, the z532 lattice with a depth of $120\,\mathrm{E_{rec}}$ suppressed vertical tunnelling to neighbouring planes. Then, the z1064 lattice was ramped up within 50 ms to either $150\,\mathrm{E_{rec}}$ or $200\,\mathrm{E_{rec}}$ while the z532 lattice was simultaneously decreased to $17, 25$ or $34\,\mathrm{E_{rec}}$. The phase of the resulting superlattice was set to 0.135 rad. As in the bilayer experimental control sequence (Sec. 4.2.4), the magnetic field was subsequently ramped from initially 207 G to 195 G. In order to not loose atoms when crossing the $|-9/2, -7/2\rangle$ Feshbach resonance at 202 G, the spin mixture was swapped to $|-9/2, -5/2\rangle$ just before the magnetic field ramp. Then, at 195 G, radio frequency spectroscopy was employed (Sec. 3.5.4) to measure the interaction strength U in the respective superlattice configuration. In fact, only a relative interaction strength difference $\Delta U = U_{95} - U_{97}$ could be measured by radio frequency spectroscopy when transferring atoms on doubly occupied lattice sites from a $|\downarrow, \uparrow\rangle = |-9/2, -5/2\rangle$ to $|-9/2, -7/2\rangle$ mixture.
For the evaluation, the atom number in the $|m_F = -7/2\rangle$ state served as spectroscopy signal. The latter exhibited two peaks (Fig. 4.6 right upper). One peak arose if atoms on singly occupied lattice sites in the $|m_F = -5/2\rangle$ state were transferred into the $|m_F = -7/2\rangle$ state (right peak). The corresponding frequency is thereby determined by the Zeeman splitting at 195 G between the two involved states. The other peak signalled that the atom in the $|m_F = -5/2\rangle$ state on a doubly occupied site was transferred to the $|m_F = -7/2\rangle$ state (left peak). The radio frequency of the doubles peak is shifted with respect to the transfer frequency for atoms on singly occupied sites just by the relative interaction strength $\Delta U = U_{95} - U_{97}$. In order to determine ΔU accurately, both peaks were each fitted by a Gaussian envelop and the distance between the two Gaussian functions was determined.

The measured relative interaction strength ΔU decreases with increasing short lattice depth V_{z532} for the two considered long lattice depths V_{z1064} (Fig. 4.6 left). This behaviour is expected since, qualitatively speaking, an increasing V_{z532} compresses the Wannier functions more and more. Thus, at 195 G where $U_{97} > U_{95}$, the Wannier functions for $|-9/2, -7/2\rangle$ are more compressed as the ones for $|-9/2, -5/2\rangle$ and, hence, the relative interaction strength increases in its absolute value (Fig. 4.6 left). The dependence on the long lattice depth is rather small. Counter-intuitively, for stronger V_{z532}, the relative interaction strength $|\Delta U|$ at $V_{z1064} = 200\,\mathrm{E_{rec}}$ lies below $|\Delta U|$ in the case $V_{z1064} = 150\,\mathrm{E_{rec}}$.

The measured interaction strengths were compared to theoretical predictions. In a first

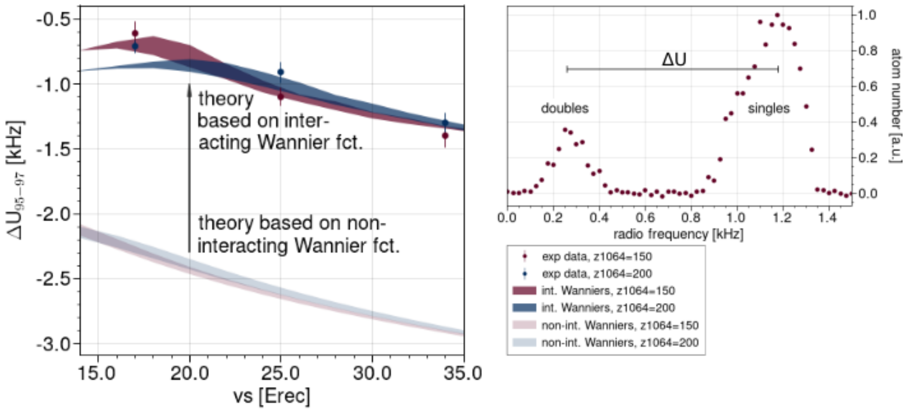

Figure 4.6: Relative interaction strength ΔU in the z superlattice. Left The relative interaction strength was measured via radio frequency spectroscopy in isolated double wells along the z direction. The theoretical relative interaction strength was calculated using non-interacting Wannier functions. Due to the strong repulsively interacting fermions in the isolated double well, however, non-interacting Wannier functions were inappropriate to predict the measured ΔU. A formalism to compute interacting Wannier functions was therefore developed in this thesis (Sec. 2.2.4). Computing ΔU with these interacting Wannier functions leads to a match of theory with data within the errorbars. **Right** Spectroscopy signal of doubles and singles. The frequency spacing of both peaks yields ΔU.

run, non-interacting Wannier functions from the BPPO method were used (Sec. 2.2.2) to deduce the relative interaction strength ΔU following Eq. 2.21 (Fig. 4.6 left, weakly shaded bands). The discrepancy between the theory and the experimental data is rather large. This can be attributed to the strong repulsive interactions at 195 G. Thus, non-interacting Wannier functions are inappropriate to infer ΔU in the lattice. Instead, interacting Wannier functions were employed to infer ΔU. As exemplified in the theory, the interacting Wannier functions are whose which have minimum total energy (Fig. 4.7 left, also cf. Fig. 2.11). Furthermore, since the relative interaction strength $\Delta U = U_{95} - U_{97}$ was measured, interacting Wannier functions for a spin mixture of $|\downarrow, \uparrow\rangle = |-9/2, -5/2\rangle$ and $|-9/2, -7/2\rangle$ were first separately calculated. At the magnetic field of 195 G, both spin mixtures interact repulsively (cf. Fig. 3.12 right for Feshbach resonances) and, hence, broadened interacting Wannier functions are expected compared to the non-interacting case (Fig. 4.7 center). Then, the relative interactions strength results from the difference of the absolute interaction strengths $U_{95} - U_{97}$ of the respective Wannier function with lowest energy (Fig. 4.7 right, dashed lines).
The $\Delta U = U_{95} - U_{97}$ is subsequently computed for experimentally relevant superlattice configurations and compared to the measured data (Fig. 4.6 left, intensely shaded regions). The theoretical predictions thereby coincides with the experimentally ΔU within the errorbars for both z1064 lattice depth $V_{z1064} = 150\,\mathrm{E_{rec}}$ or $200\,\mathrm{E_{rec}}$.

The developed method for interacting Wannier functions in the course of this thesis thus

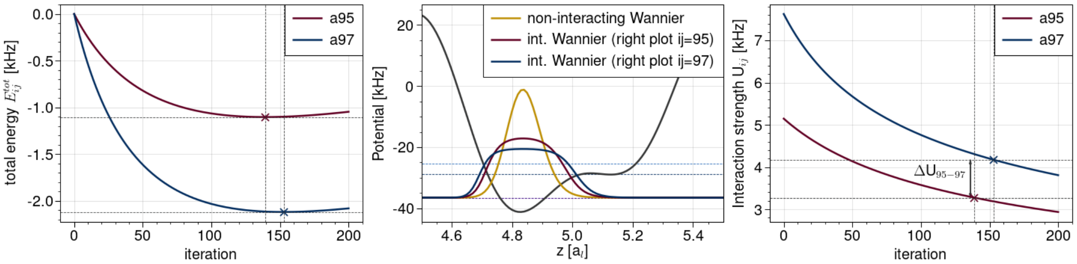

Figure 4.7: **Left** Total energy of the iteratively (x-axis) determined interacting Wannier functions for the two different spin mixtures $|-9/2, -5/2\rangle$ and $|-9/2, -7/2\rangle$. The minimum total energy in both cases is marked with crosses, respectively. **Center** Interacting Wannier functions for $|-9/2, -5/2\rangle$ and $|-9/2, -7/2\rangle$ with minimum total energy. Both are broadened compared to the non-interacting Wannier function as expected for a magnetic field of 195 G. **Right** Interaction term as a function of the iteration for both cases $|-9/2, -5/2\rangle$ and $|-9/2, -7/2\rangle$. The interaction strength at the crosses is the one where the total energy is lowest (left figure). The difference yields $\Delta U = U_{95} - U_{97}$.

allows for a precise prediction of the measured interaction strength in the vertical z superlattice.

4.2 Implementing an analogue quantum simulator for a bilayer Hubbard system

In Sec. 4.1 the superlattice and Hubbard parameter calibration was detailed. In this section, the creation of a bilayer Hubbard system is presented step by step following the main experimental control sequence. Necessary measurements for the characterisation of the interim prepared system are also discussed. The first step deals with the loading of the atomic gas from the Ioffe-Pritchard trap into the dipole trap, where the system was initially adjusted in order to create the bilayer Hubbard system. That comprised the creation of a 50:50 spin mixture, the adjustment of the interactions, evaporative cooling and the loading into the vertical lattice. Thereafter, the creation of the two-dimensional in-plane lattice and its loading with atoms is detailed. This also includes the discussion of the application of the digital mirror device in order to create a band insulator. The splitting of the band insulator into two coupled planes and an analysis of the singles and doubles in these two planes is furthermore explained. The section is completed by a discussion of the compressibility of the bilayer system.

4.2.1 An interacting, 50:50 spin mixtured atomic gas in two dimensions

4.2.1.1 Loading an atomic gas into the dipole trap, setting two-particle interactions and adjusting a balanced population over the two lowest hyperfine states

The atomic gas in the Ioffe-Pritchard trap (Sec. 3.1.2) was transferred to the horizontal dipole trap (DTh) (Sec. 3.1.3) by ramping up the DTh power within 600 ms and subsequently ramping down the current through the Ioffe bars in 800 ms (Fig. 4.8). The initial y and z trap frequency in the DTh after the ramp were $(\omega_y, \omega_z) = (142, 1982\,\mathrm{Hz})$. In the x-direction the atoms were only weakly confined (see Fig. 3.3 and Fig. 3.10 for the laboratory coordinates). The Rayleigh range of the DTh was $z_{\mathrm{R}}^{\mathrm{DTh}}(y, z) = (60, 0.5\,\mathrm{mm})$. At this time step, the atoms occupied all positive m_F states in the lowest hyperfine manifold $|F = 9/2, m_F > 0\rangle$. This was necessary in order to trap them in the magnetic field minimum in the center of the Ioffe-Pritchard trap. In quantum simulators with cold, neutral atoms, however, these m_F states are commonly exploited to simulate the spins in a fermionic ensemble. In order to follow this idea, the atoms were therefore transferred into the two lowest m_F states, i.e. $|F = 9/2, m_F = -9/2\rangle$ and $|F = 9/2, m_F = -7/2\rangle$ (Fig. 3.4). Thus, simulating the spins $|{\downarrow}\rangle$ and $|{\uparrow}\rangle$, respectively. For a better experimental control in preparing this two component spin mixture, all atoms were transferred into the lowest $|F = 9/2, m_F = -9/2\rangle$ hyperfine state at first instance yielding a "polarized" gas. This was achieved by sweeping the residual magnetic field from the pinch and offset coils of the Ioffe-Prichard trap over the hyperfine resonances while a fixed radio frequency was shone onto the atoms. Then, the current through the slow Feshbach coils was ramped up to around 240 G within 500 ms (Sec. 3.4.2) and the current through the offset and Pinch coils of the Ioffe trap was simultaneously diminished to zero. Ramping up the magnetic "Feshbach field" with the slow Feshbach coils adiabatically changed the quantisation axis from the lab x-axis to the lab z-axis (Fig. 3.3). Subsequently, two Landau-Zener sweeps were used to adjust the desired spin balance with 50% of the atoms in the $|F = 9/2, m_F = -9/2\rangle$ and 50% in the $|F = 9/2, m_F = -7/2\rangle$ hyperfine state.[11] The two Landau-Zener sweeps were optimized according to the sweep rate and the number of sweeps.[12] The sweep rate of each sweep determined the probability for a non-adiabatic transition between the two eigenstates of the underlying two level system in the rotating frame and, hence, the balance of the two bare states.[13] Experimentally, the rate was optimized by scanning the sweep width with a constant sweep time of 2 ms (Fig. 4.9 left). Furthermore, due to the two employed sweeps, the dependence was quadratic (Fig. 4.9 left, red curve). In contrast, for a single sweep, the dependence would have been linear (blue curve). The stability of this spin balancing between several experimental realisations could be improved using two sweeps due to a vanishing slope at the maximum of the parabola.[14] The dependence on the number of pulses is mathematically illustrated in [153]. A spin mixing ratio of $N_{-9/2}/N_{-7/2} = 0.995(10)$ was achieved.

The dimple dipole trap (DTdimple) (Fig. 3.7) was ramped up within 100 ms next (Fig. 4.8). This confined the atoms in the direction of the rather long Rayleigh range of the

---

[11] A two component spin mixture also enabled to include interactions in the quantum simulation of the electron gas by means of Feshbach resonances (Sec. 3.4.1). The Feshbach resonance for the two lowest energy states $|F = 9/2, m_F = -9/2\rangle$ and $|F = 9/2, m_F = -7/2\rangle$ is depicted in Fig. 3.12 right.

[12] A balance spin mixture is also required for efficient evaporative cooling in the dipole trap since the prepared polarized gas in the $|F = 9/2, m_F = -9/2\rangle$ hyperfine state did not thermalise due to Pauli blocking.

[13] A too high sweep rate led to more non-adiabatic transitions which resulted in an overpopulation of the ground state while a too small sweep rate led to an adiabatic transfer from the polarized gas in the $|F = 9/2, m_F = -9/2\rangle$ state to a polarized gas in the $|F = 9/2, m_F = -7/2\rangle$ state[86].

[14] Three pulses, however, which caused a cubic dependence with a saddle point could not experimentally improve the stability.

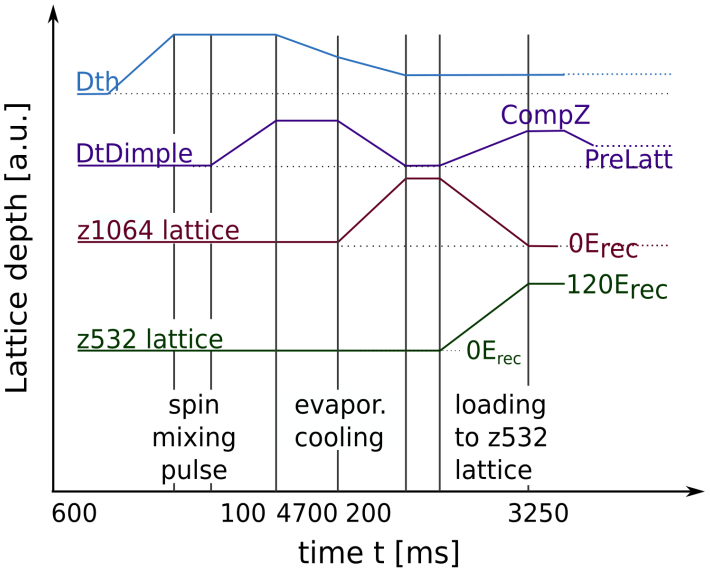

Figure 4.8: Experimental sequence for loading and evaporatively cooling the atomic gas in a dipole trap and subsequently loading it into a one dimensional vertical optical lattice. Two spin mixing pulses were used to obtain a 50:50 spin mixture. The occupation of only each second plane of the vertical z532 lattice was achieved by first loading the atoms in the vertical z1064 lattice with lattice constant $a_{\mathrm{z1064}} = 2a_{\mathrm{z532}}$ and subsequently transfer them into the vertical z532 lattice (cf. Fig. 4.10).

DTh along the x-axis.

4.2.1.2 Evaporatively cooling the 50:50 spin mixed atomic gas in the dipole trap and measuring the atom number and temperature

The balanced two spin component atomic gas was cooled by slowly lowering the power of both dipole beams within 4.7 s and, thus, evaporatively cool the atoms at attractive interactions at a magnetic field of 204 G (Fig. 4.8). The final trap frequencies in the dipole trap after evaporative cooling were $(\nu_x, \nu_y, \nu_z) = (27.4, 35, 339)$Hz. In order to extract the atom number and temperature of the cooled atomic gas, absorption imaging was performed at first instance employing the y-camera (Sec. 3.2.2 and Fig. 3.10). Due to the limited resolution of this camera, however, in-situ imaging of the atom cloud in the dipole trap was not possible. The atoms were therefore released from the trap by switching off the dipole beams and could expand during a time of flight for 10 ms. Then, absorption imaging was performed (Sec. 3.2) and the so-obtained images were fit by the theory of an harmonically trapped, ideal Fermi gas. In this case, the temperature of the gas is given by [86][51]

$$\frac{T}{T_F} = (6\mathrm{Li}(-Z))^{-1/3} \tag{4.6}$$

and the atom number by

$$\mathrm{N} = -\left(\frac{\mathrm{k_B}T}{\hbar\bar{\omega}}\right)^3 \mathrm{Li}_3(-Z). \tag{4.7}$$

Here, $T_F = E_F/k_\mathrm{B}$ is the Fermi temperature which is connected to the Fermi energy E_F by the Boltzmann constant $\mathrm{k_B}$. Furthermore, Z, Li and $\bar{\omega} = (\omega_x\omega_y\omega_z)^{1/3}$ are the fugacity as a fit parameter, the polylogarithmic function and the averaged trap frequency, respectively. The Fermi energy is provided by $E_F = (6N)^{1/3}\hbar\bar{\omega}$. Typically, 60(5)k atoms at temperatures of around $T/T_F = 0.09(1)$ remained in the dipole trap after the evaporative cooling process.

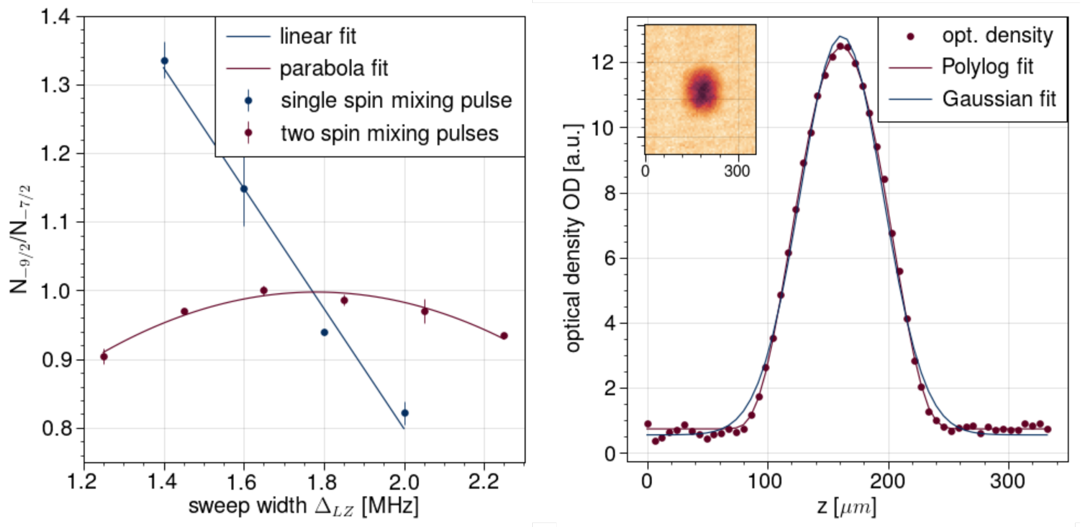

Figure 4.9: Loading and evaporatively cooling a 50:50 spin mixed atomic gas in a dipole trap. Left Ratio between the population of the two lowest hyperfine states $\mathrm{N}_{-9/2}/\mathrm{N}_{-7/2}$ as a function of the sweep width of the first spin mixing sweep. The sweep duration was fixed to 2 ms. The parabola (red curve) resulted from two subsequent Landau Zener sweeps where as the linear curve from only a single spin mixing sweep (blue curve). Using two sweeps resulted in a vanishing slope at the ratio close to one. This, in turn, guaranteed a more stable ratio among different experimental realisations. **Right** Summed optical density from absorption imaging for thermometry of the atomic gas in the dipole trap. The density was fitted employing the theory of the harmonically trapped ideal Fermi gas and the atom number and temperature was extracted. The blue curve is a Gaussian fit to the data showing that the atomic distribution was in a quantum regime were the tails of the Gaussian fit did not well describe the distribution.

4.2.1.3 Loading the 50:50 spin mixed atomic gas in every second layer of the vertical z532 lattice

While the power of the dipole trap was further reduced, the z1064 lattice was ramped up within 200 ms (Fig. 4.8). Thus, by continuing the evaporation, the atoms were adiabatically loaded from the dipole trap into the one dimensional vertical z1064 lattice with lattice constant $a_{\mathrm{z1064}} \approx 2\,\mu\mathrm{m}$. Here, only five neighboured lattice sites (also referred to as "atom planes"[15]) of the z1064 lattice were in total populated with atoms (Fig. 4.10, cf. V_{z1064} and the data points). This was due to the strong confinement of the atoms in the vertical direction in the DTh dipole trap before. After the loading of the z1064 lattice, the atoms were transferred from the z1064 into the vertical z532 lattice by ramping up the latter in 3.25 s and simultaneously diminishing the z1064 lattice to zero (Fig. 4.8). This transfer enabled to populate only every second plane in the vertical z532 lattice (Fig. 4.10, cf. V_{z532} and the data points) since $a_{\mathrm{z532}} = a_{\mathrm{z1064}}/2$. During the up- and down-ramp of both individual lattices the phase of the resulting superlattice was hold in antisymmetric configuration using the small Mephisto (Fig. 3.6).[16][17]

The magnetic field gradient present during tomography which is how the data were taken in Fig. 4.10 (Sec. 3.5.3) could be extracted by matching the data with the simulated lattice (Fig. 4.10). Therefore, the radio frequency of the slicing pulse (Eq. 3.9) was first translated into the corresponding magnetic field value (Fig. 3.4). Then, the magnetic field value at a given point in space z was translated into a distance z in micrometer. With this, it yielded $\nabla B = 3.2994\,\mathrm{mG\mu m^{-1}}$ which matched the calibration in [38].
Furthermore, the atom number and temperature of the atomic gas that populated every second plane could be optimised by adjusting the power of the dimple dipole trap. Concretely, the dimple dipole power during the ramp up of the repulsive z532 lattice (Fig. 4.8) determined the atom number while the dimple dipole power after the z532 ramp governed the evaporative cooling process in the z532 lattice and, hence, the temperature of the gas in the vertical lattice.

4.2.2 Loading the gas in a two-dimensional, in-plane optical lattice

4.2.2.1 A two-dimensional optical lattice from two retro-reflected Gaussian laser beams

In the theory section ideal lattices were considered. The experimental realisation of a lattice structure employing retro-reflected Gaussian laser beams, however, required to take two additional aspects into account.
On the one hand, the retro reflection of the beam in order to create a standing wave exhibited losses. Thus, the forward and reflected beam had different powers which led to a running wave component besides the periodic structure. This running wave component effectively caused an offset R in the lattice potential [105]

---

[15] In the vertical lattice, atoms formed two-dimensional layers within each of the vertical lattice sites

[16] The data from Fig. 4.10 were taken by first loading the z1064 and subsequently the z532 lattice as described above. They represent one spin state measured with tomography (Sec. 3.5.3).

[17] Populating only every second site improved the detection of the atoms residing on this site by reducing the signal from atoms on neighbouring sites during tomography.

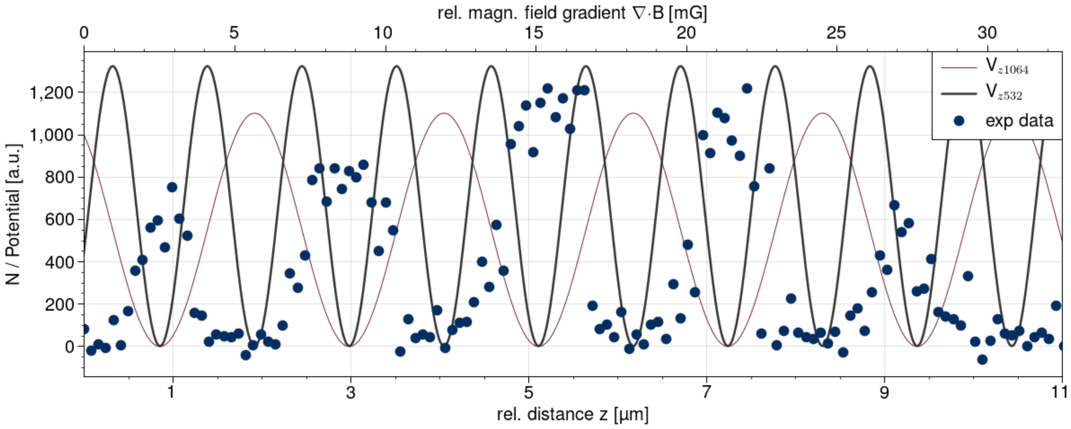

Figure 4.10: Populating each second lattice site of the vertical z532 lattice with atoms. Converting the tomography pulse frequency (Sec. 3.5.3) to the corresponding magnetic field value and the latter to the real space coordinate z, the upper and lower axis can be related to each other. This allows for a validation of the magnetic field gradient during tomography since the detected planes and the wells of the lattice should coincide.

$$V_{\mathrm{lat}}^{\mathrm{off}} = \mp s\left(R + \cos^2(k_{x/y} z)\right) \qquad R = \frac{(1 \pm \sqrt{\gamma})^2}{4\sqrt{\gamma}}. \tag{4.8}$$

Here, γ is the factor by which the power of the reflected lattice beam is reduced compared to the forward beam due to transmission and reflection losses of the optical components in the retro beam path. For both in-plane lattices $\gamma \approx 0.8$. The upper/lower sign are related to the case of a red-/blue detuned lattice with respect to the main optical transition. Moreover, s is the depth of the lattice in units of the recoil energy.

On the other hand, the radial profile of the Gaussian laser beam led to a decreasing lattice depth away from the beam axis and, thus, to a variation of the ground state energy in the periodic potential as a function of the radial distance. Taking both effects into account yielded the actual lattice potential caused by a single retro-reflected Gaussian laser beam with an imbalanced power between the forward and reflected beam [105]

$$V_{\mathrm{lat}}^{\mathrm{exp}} = V_{\mathrm{lat}}^{\mathrm{off}} + V_{\mathrm{lat}}^{\mathrm{ge}} = -(\pm sR + \sqrt{s})\exp\left[-2\left(\frac{\mathrm{x}\cdot\sin\left(\Theta_{\mathrm{lat}}^{\mathrm{x}}\right) + \mathrm{y}\cdot\cos\left(\Theta_{\mathrm{lat}}^{\mathrm{y}}\right)}{\mathrm{w}}\right)^2\right]. \tag{4.9}$$

Here, w is the waist of the Gaussian lattice laser beam and $\Theta_{\mathrm{lat}}^{\mathrm{i}}$ describes the angle between the beam axis i and the i-th lab coordinate (cf. Fig. 3.10). The determination of both parameters was required to precisely know the lattice potential and is therefore discussed in the following.

Inferring the Gaussian laser beam waist at the location of the trapped atomic cloud from a measurement of the trap frequency

The waist w of the Gaussian lattice laser beam at the location of the atomic cloud which goes into the exponent in Eq. 4.9 was inferred from a measurement of the trapping frequency [104]. Therefore, a spin-polarized gas was initially loaded into the x- or y-lattice depending on which trap frequency was measured. The respective lattice depth was set to $6\,\mathrm{E_{rec}}$ in both cases and, hence, the motion of the atomic cloud was predominately restricted to the radial direction of the respective lattice laser beam (Fig. 3.10). Contrarily, in the longitudinal direction of the beam, a lattice formed by retro-reflection so that for short time scales the motion along this direction was suppressed. Subsequently, a magnetic field gradient was applied to displace the atoms in radial direction away from the beam axis. This gradient was abruptly switched off after 110 ms which led to an oscillatory behaviour of the atomic cloud's center of mass in radial direction over time (Fig. 4.11 left). Absorption imaging was used to image the atomic gas in the trap. Furthermore, for small displacements away from the beam axis, the radial Gaussian profile of the lattice laser beam was approximated by a harmonic potential V_{har} and, hence, the waist of the Gaussian lattice laser beam was inferred from the measured trapping frequency ω_{trp} by the relation

$$\mathrm{w} = \sqrt{\frac{2V_{\mathrm{har}}}{m\omega_{\mathrm{trp}}^2}}. \tag{4.10}$$

Here, m is the mass of a particle in the trap. Using a small number of atoms in the atomic cloud ensured to stay in the harmonic approximation of the Gaussian profile.

After fitting the oscillations and extracting the frequency for the x- and y-lattice respectively, typical trap frequencies were about $\omega_{\mathrm{trp}}^{\mathrm{x}} = 19.1(3)\,\mathrm{Hz}$ and $\omega_{\mathrm{trp}}^{\mathrm{y}} = 26.7(3)\,\mathrm{Hz}$. The inferred beam waists were hence about $w_{\mathrm{x1064}}^{\mathrm{y}} = 169(1)\,\mu\mathrm{m}$ and $w_{\mathrm{y1064}}^{\mathrm{x}} = 161(1)\,\mu\mathrm{m}$. Here, w_{x1064}^{y} is the waist of the x1064 lattice laser beam at the location of the atoms in y-direction.

Inferring the angles of the Gaussian lattice laser beams with respect to the lab coordinate system from a density density correlation measurement

Without single site resolution in z imaging, the angles $\Theta_{\mathrm{lat}}^{\mathrm{x/y}}$ between the x- and y-lattice laser beams and the lab frame could not inferred from a simple in-situ image. Therefore, they were determined by an autocorrelation analysis of the measured density after releasing the atoms from the lattice, letting them expand for a time of flight and perform absorption imaging to record the density[38][1][149].

Experimentally, starting with atoms loaded into a three dimensional lattice with lattice vectors $\vec{a} = i \cdot a_{\mathrm{x1064}} + j \cdot a_{\mathrm{y1064}} + k \cdot a_{\mathrm{z532}}$, where a_n is the lattice constant in the respective direction and i, j, k are integer numbers, the motion of the atoms in the lattice was frozen after thermalisation by setting the lattice depths to $V_{\mathrm{x1064}} = V_{\mathrm{y1064}} = 60\,\mathrm{E_{rec}}$ and $V_{\mathrm{z532}} = 120\,\mathrm{E_{rec}}$. The in-plane lattice was then abruptly switched off by switching off the acoustic optical modulators of the x- and y-lattice power control (Fig. 3.9 and 3.6).

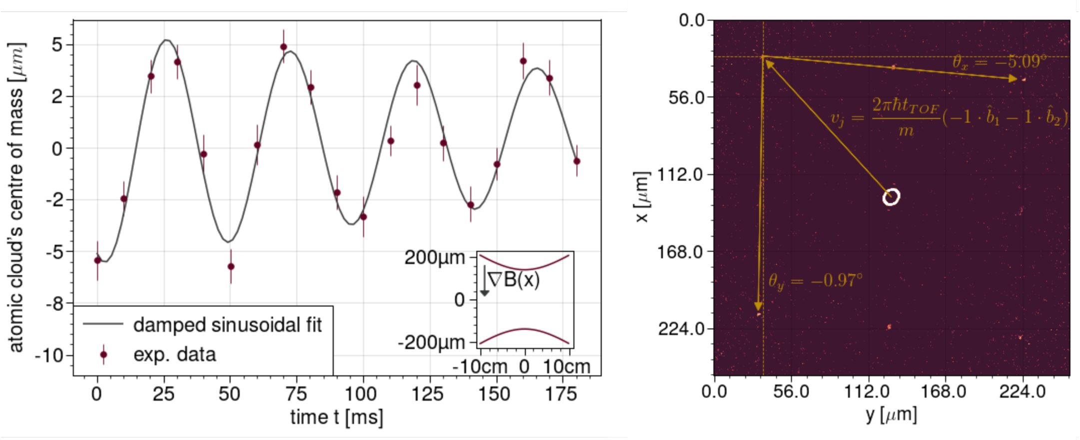

Figure 4.11: Left Trap frequency measurement. The oscillating center of mass of the atomic cloud is plotted against the oscillation time. A damped sinusoidal fit was used to extract the trapping frequency from which the beam waist could be inferred (Eq. 4.10). **Right** Density-density correlation measurement. From the detected dips (yellow points) in the autocorrelation function, the lattice angles Θ^{i}_{lat} could be inferred. Moreover, the magnification of the z-imaging system could be deduced (Sec. 3.5).

This projected the atoms in the lattice onto free space. After a time of flight, the atoms were then absorption imaged. The z532 lattice was lowered but kept on a lower constant value during time of flight of $V_{z532} = 10\,\mathrm{E_{rec}}$. This ensured that the atoms predominantly spread within their initial plane and stayed within the depth of focus of the z-camera.

Theoretically, the autocorrelation function (Fig. 4.11 right) is defined as $C(x, y, t_{\text{TOF}}) = \hat{\rho}(x, t_{\text{TOF}})\hat{\rho}(y, t_{\text{TOF}})$ where $\hat{\rho}(x, t_{\text{TOF}})$ is the density operator at position x after a time of flight t_{TOF}. Employing the Wiener-Khinchin theorem, the autocorrelation function is related to the inverse Fourier transform of the spectrum of the density and could therefore be computed by $C(x, y, t_{\text{TOF}}) = \mathcal{F}^{-1}[|\mathcal{F}(\rho)|^2]$. Here, ρ is the measured density from absorption imaging after time of flight. The so-obtained autocorrelation function exhibits dips at integer multiples of the reciprocal lattice vector $\vec{b}$ of the lattice vectors $\vec{a}_{x1064/y1064/z532}$ (Fig. 4.11 right). The dips are positioned at [38]

$$\vec{v}_{dip} = \frac{2\pi\hbar t_{\text{TOF}}}{m}(i \cdot b_x + j \cdot b_y + k \cdot b_z) \tag{4.11}$$

$$= \frac{2\pi\hbar t_{\text{TOF}}}{m}\left(i \cdot \frac{a_y \times a_z}{a_x \cdot (a_y \times a_z)} + j \cdot \frac{a_z \times a_x}{a_y \cdot (a_z \times a_x)} + k \cdot \frac{a_x \times a_y}{a_z \cdot (a_x \times a_y)}\right) \tag{4.12}$$

Again, i, j, k are integers. Furthermore, the time of flight t_{TOF} enters linearly in Eq. 4.12 and, thus, the dips in the autocorrelation function spread linearly in time (Fig. 4.11 right). Besides, due to the finite resolution of the z-camera the measured autocorrelation function was convolved with the point spread function of the imaging system. This, however, just reduced the dip height but preserved the dip position. The convolved autocorrelation function reads [38]

$$C^{\mathrm{cor}}(x, y, t_{\mathrm{TOF}}) = \frac{\mathcal{F}^{-1}[|\mathcal{F}(\rho)|^2]}{\mathcal{F}^{-1}[|\mathcal{F}(\overline{\rho})|^2]}, \tag{4.13}$$

where $\overline{\rho}$ is the averaged density over the different experimental realisations. By determining the dip positions, the angles $\Theta_{\mathrm{lat}}^{\mathrm{x/y}}$ between the x- and y-lattice laser beams and the lab frame was inferred (see (Fig. 4.11 right)). It yielded $\Theta_{\mathrm{lat}}^{\mathrm{x}} = -5.33(27)^\circ$ and $\Theta_{\mathrm{lat}}^{\mathrm{y}} = -0.91(11)^\circ$ respectively. The two-dimensional lattice is thus slightly twisted compared to a rectangular lattice.

Using both results, i.e. the determined waists w_{x1064}^{y}, w_{y1064}^{x}, $\mathrm{w}_{z1064/z532}^{x}$ from a trap frequency measurement and the lattice angles from the density-density correlation analysis, $\Theta_{\mathrm{lat}}^{\mathrm{x/y}}$, the real lattice potential caused by the retro-reflected Gaussian lattice laser beams was computed using Eq. 4.9. The potential of the individual beams thereby added up to form the total underlying potential (Fig. 4.12 right).[18] Thus, in fact, in a cold atom analogue quantum simulator with optical lattices, the system is not homogeneous. The parameter μ in the Hubbard model (Eq. 2.1) can account for this.

4.2.2.2 Loading the atomic gas into the two-dimensional, in-plane lattice

The x- and y-lattice were ramped up simultaneously to $6\,\mathrm{E}_{\mathrm{rec}}$ within 500 ms to adiabatically load the two-dimensional atomic gases in each second, vertical z532 lattice plane into the two-dimensional in-plane lattice (Fig. 4.12 left). In this shallow lattice the atoms could efficiently redistribute [13] (cf. Fig. 2.6, for band structure). After loading the atomic cloud into the in-plane lattice, the cloud's typical diameter was about $60-100\,\mu\mathrm{m}$. This corresponded to roughly 8.000 occupied lattice sites for a lattice with lattice constant $a_{\mathrm{x1064}} = a_{\mathrm{y1064}} = 532\,\mathrm{nm}$. The diameter of the atomic cloud was thus roughly half of the x and y Gaussian laser beam waists with $w_{\mathrm{x1064}}^{y} = 169\,\mu\mathrm{m}$ and $w_{\mathrm{y1064}}^{x} = 161\,\mu\mathrm{m}$. As a consequence, the variation of the underlying potential led to a variation of the atomic density. The latter increased towards the trap center where the potential was minimum. Theoretically, this density variation could be inferred from the underlying potential $V_{\mathrm{lat}}^{\mathrm{exp}}(r)$ using the local density approximation [86]. Partitioning the potential in small regions and fixing the local Fermi energy to be $E_F(r) = E_F^0 - V_{\mathrm{lat}}^{\mathrm{exp}}(r)$, the local atomic density resulted directly from the local underlying potential (Fig. 4.13 left (right), doubles (singles), compare to Fig. 4.12 right). Here, E_F^0 is the Fermi energy in the trap center.

The in-plane lattice depth was usually set to $6\,\mathrm{E}_{\mathrm{rec}}$ and the z532 lattice to $120\,\mathrm{E}_{\mathrm{rec}}$. After adiabatic loading into the lattice, the atomic motion was frozen by increasing the in-plane lattice to $60\,\mathrm{E}_{\mathrm{rec}}$. The discrimination of singly and doubly occupation was subsequently achieved using the singles/doubles detection sequence (Sec. 3.15).

---

[18] The figure 4.12 right is not true to scale since in reality the periodic structure on top of the underlying potential had a much smaller period.

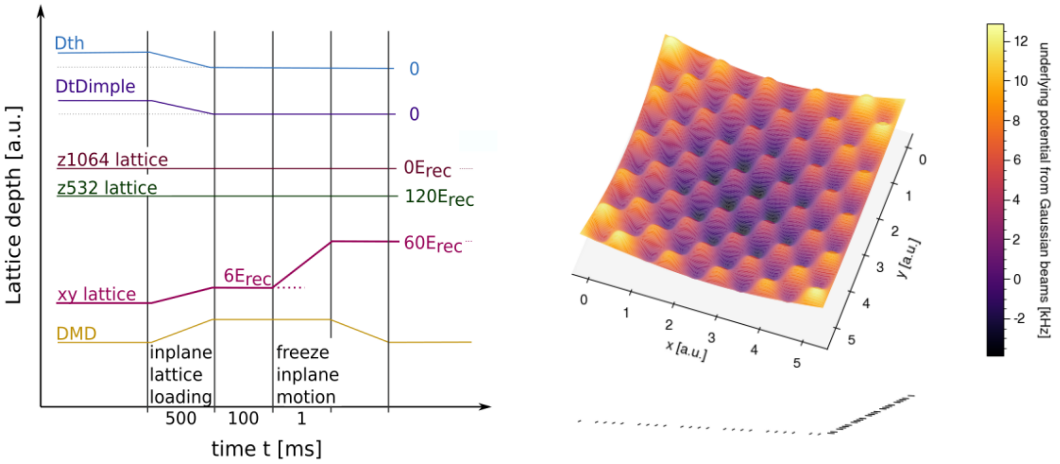

Figure 4.12: Left Main experimental sequence (part 2) in order to create the bilayer Hubbard system. **Right** A real optical lattice with underlying potential due to the Gaussian lattice laser beams (not true to scale).

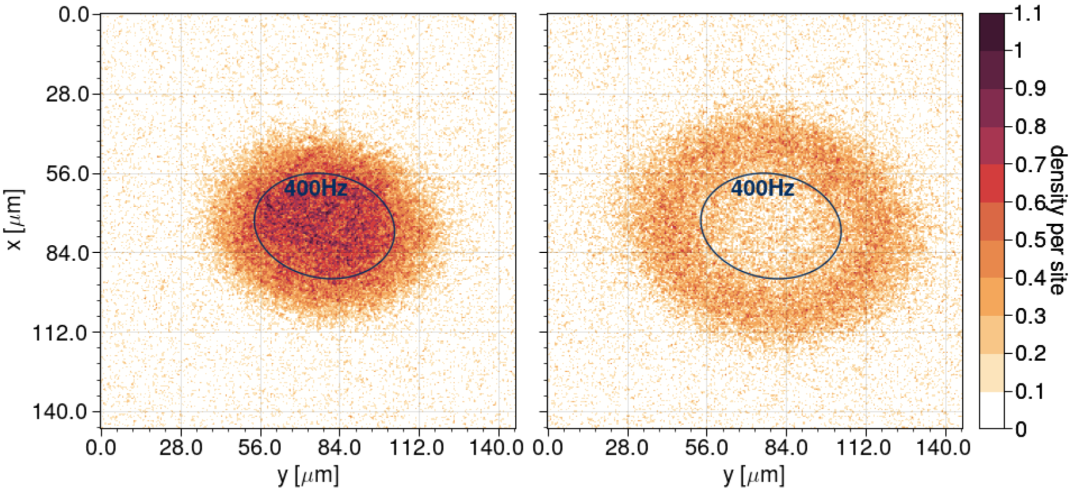

Figure 4.13: In-situ absorption image of doubly (left) and singly (right) occupied lattice sites in a single plane of the two-dimensional, in-plane lattice using tomography and rf spectroscopy (Fig. 3.15). While doubles predominately form in the trap center at minimum potential the singles exhibit a peak density at half-filling. The 400 Hz line is the iso-potential line of underlying potential due to the Gaussian lattice laser beams.

4.2.2.3 Inferring the temperature of the atomic cloud in the in-plane lattice and overall detection efficiencies from the equation of state

In general, the equation of state (EoS) determines the occupation as a function of the chemical potential. Furthermore, the EoS depends on the temperature. Thus, by fitting the theoretical EoS to a measured EoS yielded from the distribution of the atoms in the two-dimensional in-plane lattice (Fig. 4.13), the temperature of the atoms can be extracted. In cold atom experiments, the equation of state was first measured in [74] and in two dimensions in [40].

Non-interacting fermions

For a non-interacting Fermi gas, the EoS[19] is given by the Fermi-Dirac statistics $f_{\mathrm{FD}} = 1/(\exp[(\epsilon - \mu)/(\mathrm{k_B}T)] + 1)$. Furthermore, for uncorrelated fermions with two internal spin states $|\uparrow\rangle$ and $|\downarrow\rangle$ the expectation value factorises $\langle n_\uparrow n_\downarrow\rangle = \langle n_\uparrow\rangle\langle n_\downarrow\rangle$ and if the system is spin balanced, it holds $\langle n_\uparrow\rangle = \langle n_\downarrow\rangle = n/2$. Thus, the number of doubly occupied sites in a non-interacting, spin balanced atomic cloud on a lattice as a function of the chemical potential can be computed by [38]

$$n_{\mathrm{D}} = \langle n_\uparrow n_\downarrow\rangle = \langle n_\uparrow\rangle^2. \tag{4.14}$$

Moreover, for the total number density which is directly yielded from the Fermi-Dirac statistics, it holds $n = (n_{\mathrm{S}} + n_{\mathrm{D}})$, where n_{S} is the number of singles. Thus, n_{S} can be inferred from the total density and the number of doubly occupied sites. In turn, the equation of state for the ideal Fermi gas, i.e. n, n_{D} and n_{S} as a function of the chemical potential μ can be deduced (Fig. 4.14 left, shaded bands). While the number of doubles continuously increase with increasing chemical potential towards the trap center, the number of singles exhibits a maximum at a vanishing chemical potential $\mu = 0$. At this point, the number of spin up/down singly occupied, doubly occupied and empty sites is equal, $n_{\mathrm{S},\uparrow} = n_{\mathrm{S},\downarrow} = n_{\mathrm{D}} = n_{\mathrm{empty}} = 1/4$. The lattice is hence half-filled at $\mu = 0$ with one fermion per lattice site in average. Furthermore, for an evaporatively cooled Fermi gas with Fermi temperature of $T_F \approx 4\,\mathrm{kHz}$ and a typical ratio of $T/T_F = 0.1$ (cf. Sec. 4.2.1.2), the temperature is about $20 - 30\,\mathrm{nK}$. The distribution of singly occupied sites widen symmetrically around half-filling for higher temperatures (Fig. 4.14 left). At the same time the distribution of the doubles flattens. Thus, the band insulator regime in which most of the lattice sites are occupied by two fermions moves to higher chemical potentials for increasing temperature.

Experimentally, the EoS was obtained from the imaged density distributions of doubles and singles (Fig. 4.13) by radially averaging them respectively and plotting them against the local chemical potential $\mu(r)$ (Fig. 4.14 left (data points)). Here, the local chemical potential was inferred from the underlying Gaussian potential of the lattice laser beams given by Eq. 4.9 employing again the local density approximation $\mu_{\mathrm{loc}}(r) = \mu_0 - V_{\mathrm{lat}}^{\mathrm{exp}}$. The measured EoS, however, had to be scaled by the detection efficiencies for singles and doubles $\eta_{\mathrm{S/D}}$ (Fig. 4.14 left) in order to match the predictions

$$n_{\mathrm{S/D}}^{\mathrm{meas}} = \eta_{\mathrm{S/D}} \cdot n_{\mathrm{S/D}}^{\mathrm{theo}}. \tag{4.15}$$

Here, the detection efficiency for singly occupied sites η_{S} could be straightforwardly computed knowing that at half-filling the singles density should be maximum and reach

---

[19] The equation of state for a non-interacting Fermi gas was needed for the Master's project of Janek Fleper during this thesis

$n_{\mathrm{S}}^{\text{half-fill}} = 0.25$. Using η_{S} to match the maximum of the theoretical distribution with the maximum of the data, the temperature could subsequently deduced by matching the width of the theoretical curve to the measured singles distribution width. Having determined the temperature from the singles distribution and knowing that the temperature of the doubles had to be the same as for the singles, the shape of the doubles curve was fixed and the detection efficiency of the doubles η_{D} could be computed matching again the theoretical doubles distribution to the measured one. Typically detection efficiencies were $\eta_{\mathrm{S}} \approx 0.8$ and $\eta_{\mathrm{D}} \approx 0.5$. The latter value originated because only one atom on a doubly occupied site were detected (cf. Fig. 3.15).
The fitting of the theoretically predicted EoS to the measured EoS thus enabled to measure the temperature of the atomic cloud in the two-dimensional lattice as well as to deduce the detection efficiencies $\eta_{\mathrm{S/D}}$.

Interacting fermions
In the discussion of the equation of state for non-interacting fermions the dependence of the singles and doubles distribution on the temperature was elucidated and the role of detection efficiencies $\eta_{\mathrm{S/D}}$ were discussed. During the loading of the atomic cloud into the two-dimensional lattice in the main experimental sequence for the creation of the bilayer Hubbard system, however, attractive on-site interactions of $U \approx -0.4\,\mathrm{t}$ for a $|-9/2, -7/2\rangle$ spin mixture at a magnetic field of $B = 207\,\mathrm{G}$ were realised. The attractive interactions were required for efficient thermalisation in the lattice. The doubles and singles distributions were again recorded from a single plane via tomography, singles/doubles discrimination and absorption imaging and radially averaged (Fig. 4.14 right, data points). In order to extract the temperature and detection efficiencies of this weakly interacting fermionic gas, Determined quantum Monte Carlo (DQMC) theory for the theoretically predicted EoS were employed and fit to the experimental data (Fig. 4.14 right). This was implemented in [38][105]. Interactions changed the distributions as follows: For increasing attractive interactions the slope of the doubles distribution around half-filling increases. Thus, the metallic region shrinks while the band insulating regime widen. The singles distribution becomes flatter for increasing attractive interactions showing the ongoing disappearance of singly occupied sites at large attractive interactions. At increasing repulsive interactions the effects are inverted.

Typical temperatures of $T/t = 1.7$ in units of the tunnelling element t were achieved (Fig. 4.14 right, here $T/t = 1.9$). The determined detection efficiencies were needed to precisely determine the singles and doubles densities in the bilayer Hubbard system.

4.2.3 Producing a Hubbard band insulator in the two-dimensional lattice

The analogue quantum simulator for the bilayer Hubbard system was meant to be implemented by splitting a monolayer into two coupled layers. The splitting process thereby should be performed by ramping up the barrier in a z superlattice configuration from zero to a finite value. A large mono-layered band insulator region with a maximised fraction of doubly occupied sites was desired before splitting in order to obtain a large area, bilayer

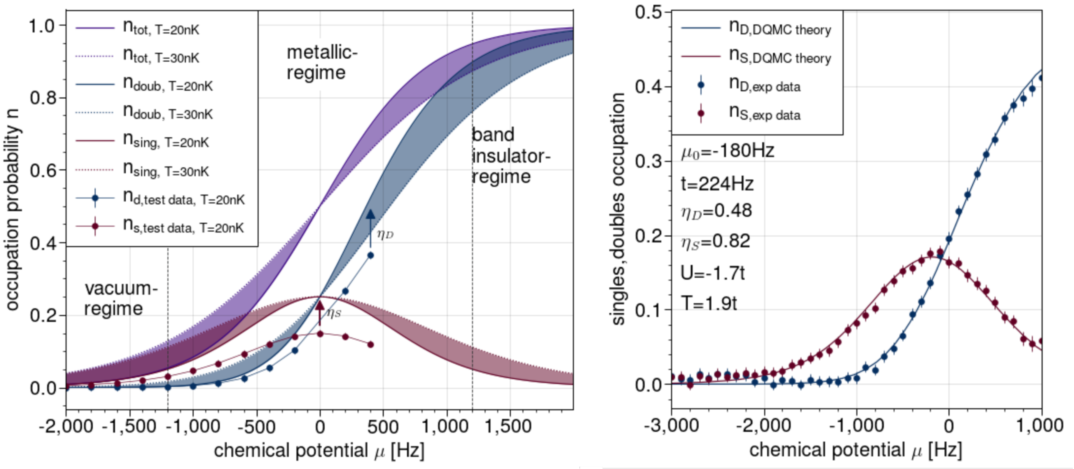

Figure 4.14: Left Equation of state of the ideal Fermi gas in a two-dimensional lattice. Doubly (blue curve) and singly (red curve) occupied sites as a function of the chemical potential μ. At large negative μ a vacuum state with filling close to zero is present. For increasing μ the system enters first a metallic and then a band insulating regime. All these states coexist beside each other in the two-dimensional atomic gas in the in-plane lattice with underlying Gaussian potential (Fig. 4.13). Additionally, the effect of the scaling factors between the measured and theoretical curves for singles (η_S) and doubles (η_D) are emphasised. **Right** Equation of state for interacting particles. The theory was taken from DQMC calculations yielding the ensemble properties of the atomic gas in the two-dimensional lattice.

system close to half-filling, i.e. with one particle per site in average.

Experimental realisation of the band insulator

The digital mirror device (DMD) and DMD laser (Sec. 3.6)[20] was employed in order to produce the large area band insulator with filling close to one. This approach pursued the concept of entropy cooling in [13]. A similar approach is described in [34]. The DMD shaped the DMD laser beam such that the latter compensated the underlying Gaussian potential from the lattice laser beams and created a two level potential at the location of the atoms (Fig. 4.16 right, inset, red line). The inner region had a low potential level and served as a low entropy region. The size of this region was 500 Hz where 500 Hz is the iso-potential line of the underlying Gaussian lattice laser potential without DMD. The corresponding diameter of this region in real space was roughly 30 µm. The size of the inner region was optimised such that the doubles fraction remained high across the entire inner region. In contrast, the outer region with high potential level served as entropy reservoir. The size of the outer region was set to 3500 Hz. At this size, the power of the Gaussian DMD laser beam was still sufficient to compensate the lattice laser potential.

---

[20] DMD laser: For a short and clear discussion, the blue-detuned Gaussian laser beam shown on the DMD and shaped by the latter for the purpose of shaping the underlying potential at the location of the atoms is denoted as DMD laser in this section.

By the redistribution of the atom across the two regions, entropy flowed from the inner to the outer region and a large, low-entropy band insulator formed in the inner.

The DMD laser power was ramped up simultaneously to the ramp up of the in-plane lattice in order to produce the band insulator (Fig. 4.12). The DMD ramp was the only additional step compared to Sec. 4.2.2.2 where atoms were loaded into the two-dimensional lattice. Hence, from the beginning of the ramp on, the atoms were exposed to the underlying two step potential rather than to the underlying Gaussian potential. The ramp of the DMD laser was set to an exponential with negative coefficient. In contrast, the in-plane lattice ramp was sinusoidal. This led to a higher doubles fraction in the inner region due to a delayed increase between the two level. After the 500 ms ramp up and an additional 100 ms time for further thermalisation, the atomic motion was frozen by ramping up the in-plane lattice to 60 $\mathrm{E_{rec}}$ within 1 ms. This scheme produced a high quality band insulator with large doubles and low singles fraction (Fig. 4.15). An average filling of $n = 0.96(2)$ with an average singles density of $n_s = 0.1(2)$ was obtained. In order to compute the filling and the densities, the detection efficiencies for doubly and singly occupied lattice sites were determined as described in the last section *without* DMD. The number of atoms in the band insulator were roughly $N = 8100(200)$. The shape of the band insulator was elliptic mostly due to the elliptic shape of the z532 lattice laser beam.
Furthermore, in the region of the potential step at 500 Hz, the fraction of singly occupied sites increased (Fig. 4.15 right). Therefore, the further evaluation and characterisation of the band insulator was performed only up to 400 Hz (Fig. 4.15, blue line).

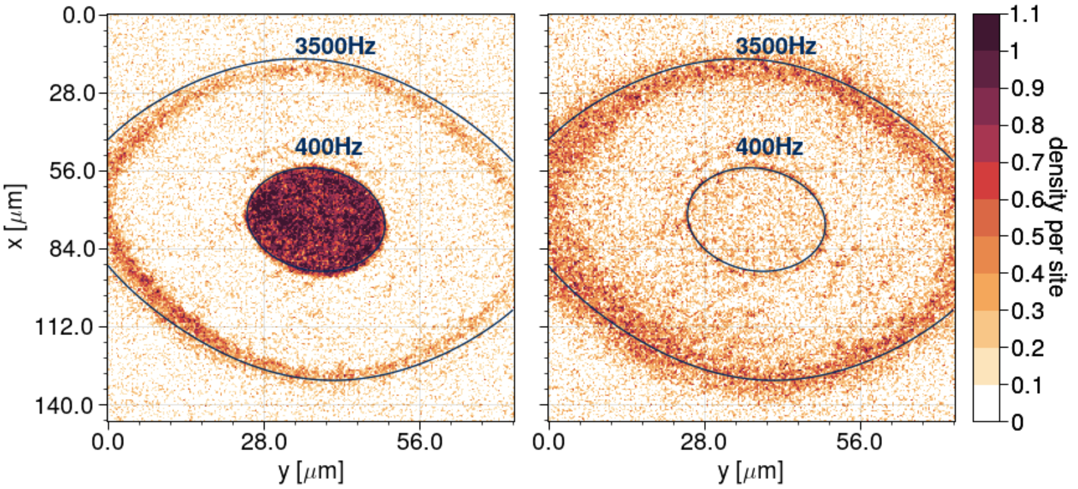

Figure 4.15: Doubly (left) and singly (right) occupied lattice sites in the two step potential (Fig. 4.16 right, inset). The doubles fraction in the inner 400 Hz region is close to one and strongly increased compared to the lattice loading without DMD (Fig. 4.13, same scale in both figures!). Thus, splitting this band insulator region into two coupled planes in a bilayer system led to a filling close to $n = 1/2$, i.e. one particle per lattice site in the bilayer in average.

Characterisation of the band insulator

The temperature was no longer a well defined characteristic of the band insulator since the equation of state could not be fit to the distribution (Fig. 4.15). The single site entropy and singles density were therefore employed in order to characterise the band insulator. The single site entropy was computed as in [36]

$$s = -\mathrm{k_B}\sum_i p_i \log(p_i) \tag{4.16}$$

where, p_i is the probability of the respective state i with $i = \{\uparrow\downarrow, \uparrow, \downarrow, 0\}$ and $\mathrm{k_B}$ is Boltzmann's constant. Furthermore, the probabilities could be directly deduced from the measured densities for singles (n_S) and doubles (n_D) $p_{\uparrow\downarrow} = n_\mathrm{D}$, $p_\uparrow = p_\downarrow = n_\mathrm{S}$ (spin balanced case) and $p_0 = 1 - 2n_\mathrm{S} - n_\mathrm{D}$ [37][36].

Both, the entropy per site s and the singles density n_S did not vary drastically over the band insulator region within the errorbars (Fig. 4.16 left). More concrete, for the site entropy, it yielded values of $s = 0.054\,\mathrm{k_B}$ and for the singles density of 12% to 15%. In the evaluation, averaging for too small radii $r < 50\,\mathrm{Hz}$ became inappropriate due to a small number of lattice sites within this region. Moreover, the entropy per site and the singles density were measured as a function of the DMD laser power (Fig. 4.16 right). Increasing the latter compared to the needed compensation power led to an overcompensation in the center of the trap as well as to an outer region whose potential increased towards the border of the inner region forming a "wall" (Fig. 4.16 right, inset, blue dotted line). The resulting site entropy as well as the singles density monotonically increased for higher DMD powers, i.e. for overcompensation. A reason for that could be that the entropy flow was interrupted by the raising "wall" at the border of the inner region during thermalisation. This, in turn, would led to more singly occupied sites in the inner region and, hence, to an increase of the site entropy. The compensation power was $P_\mathrm{DMD} = 5\mathrm{a.u.}$ (Fig. 4.16 right).

Finally, the stability of the band insulator in time was investigated (Fig. 4.17 left). A linear increase of the entropy per site and of the singles density was observed in time. This corresponded to a heating rate of $\Delta s = 0.093(1)\mathrm{k_B}/s$. Light assisted collisions by the DMD laser light were one reason for this high heating rate when comparing it to [34]. Such collisions could be reduced when changing the frequency of the DMD laser (Fig. 4.17 right[21]). At around 729 nm and 732 nm a decreased number of doubles was measured while the singles number slightly increase. The DMD light was finally set to around 727 nm to minimize the heating rate of the atoms in the trap.

The compensation of the potential in the inner region went along with potential disorder. Dust and other impurities on the optical elements in the path of the DMD laser beam led to interferences in the atom plane and, thus, to non-negligible variations of the compensated potential. The DMD disorder was characterised in the Master's thesis of Janek Fleper.

---

[21] Here, the trapped atoms were hold in the superlattice configuration for 400 ms while they were exposed to the DMD light

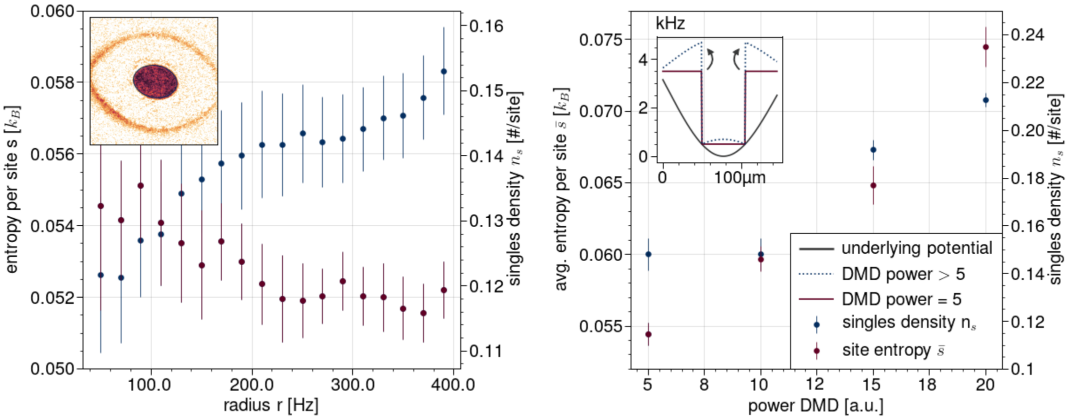

Figure 4.16: **Left** Entropy per site s and singles density n_S in the band insulator as a function of the radius away from the trap center. The radius is provided in units of Hertz as in the underlying potenial. Both quantities were relatively independent from the trap radius which yielded a high quality band insulator across the whole region. **Right** Entropy per site s and singles density n_S in the band insulator as a function of the compensation power of the DMD. Both quantities increases when overcompensating of the trapping potential (see inset).

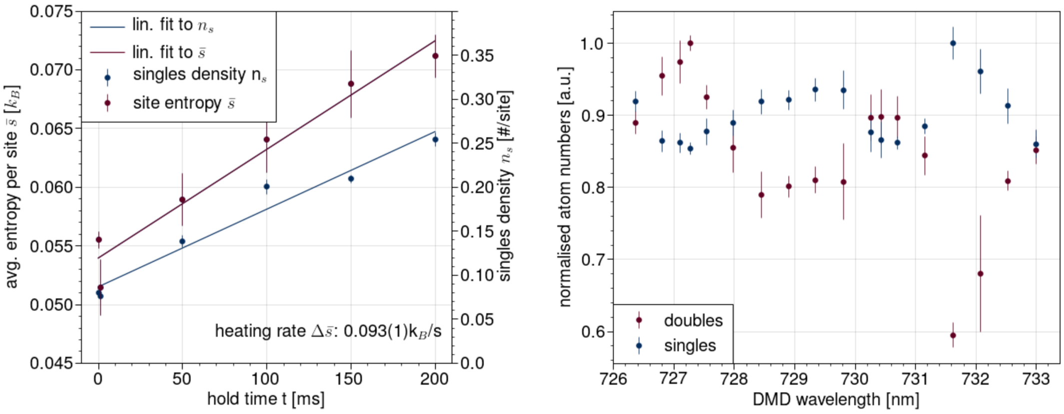

Figure 4.17: **Left** Entropy per site s and singles density n_S in the band insulator as a function of the holding time in the band insulator. This yielded a heating rate of $\Delta s = 0.093(1)\mathrm{k_B}/s$. The heating rate can be reduced by changing the DMD wavelength and, thus, avoid light assisted collisions (right figure). **Right** Singles and doubles in the band insulator as a function of the DMD wave length. At certain wavelength undesired light assisted collisions becomes stronger and doubles are lost.

4.2.4 Splitting the Hubbard band insulator to obtain a quantum simulator for a coupled bilayer Hubbard system

So far, the band insulator was prepared in the vertical z532 lattice (Fig. 4.12 left). With the intention to split the band insulator (Fig. 4.15) in order to initialise the bilayer Hubbard system by ramping up the z532 lattice in a symmetric superlattice configuration, the atoms were first reload into the vertical z1064 lattice (Fig. 4.20 left). A lattice depth of 120 $\mathrm{E_{rec}}$ was chosen for the z1064 lattice. The ramp time was set to 100 ms. The z532 lattice was diminished to zero simultaneously to the ramp up of the z1064 lattice. The reload process was performed in a frozen in-plane lattice at 60 $\mathrm{E_{rec}}$. The in-plane lattice was decreased to 6 $\mathrm{E_{rec}}$ thereafter. At this lattice depth the tunnelling rate in the monochromatic, two-dimensional, in-plane lattice was 224 Hz. Two additional lattice depths of $s_{\mathrm{xy}} = 5, 7\,\mathrm{E_{rec}}$ were employed for spin correlations measurements (Sec. 4.3.3). This varied the in-plane tunnelling rate between $t_{\mathrm{xy}} = 174 - 290\,\mathrm{Hz}$. The DMD was ramped up simultaneously to the ramp down of the in-plane lattice. An additional "wall" around the inner region in this second DMD pattern prevented a backflow of entropy from the reservoir to the inner (Fig. 4.18 left). The size of the inner and outer region was the same as in the loading pattern of the band insulator, i.e. 500 Hz and 3500 Hz. The barrier height was set to $h_{\mathrm{wall}} = 8000\,\mathrm{Hz}$ and its width to $w_{\mathrm{wall}} = 500\,\mathrm{Hz}$. The barrier shape was optimized in order to minimize the amount of doubles breaking into two singles on different sites in the border area of the inner region (Fig. 4.18 left, shaded regions). This effect was visible when the in-plane lattice depth was decreased and in-plane tunnelling has been starting while diffusion of the atoms away from the band insulator region was not inhibited by a strong repulsive DMD potential at the same time. The slope of the barrier in the inner region was hereby restricted due to the point spread function of the

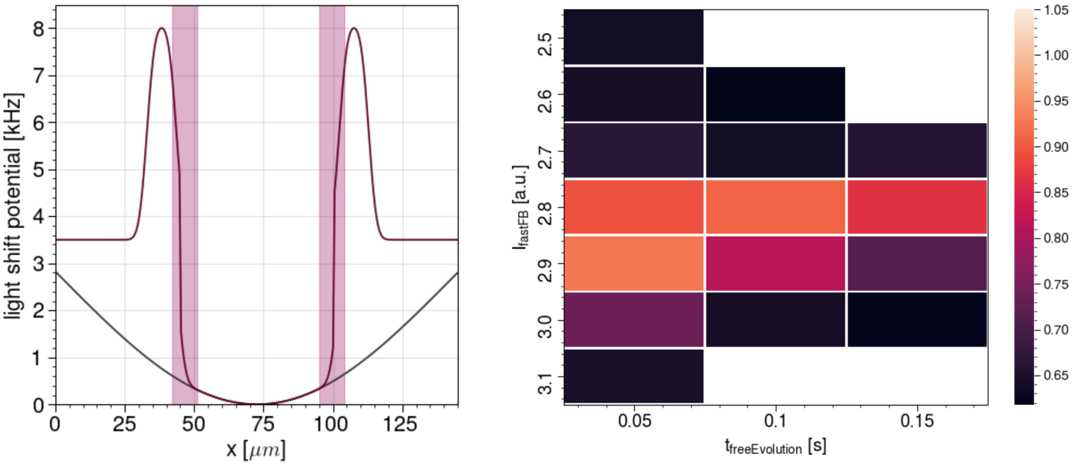

Figure 4.18: Left Second DMD potential with walls. The walls prevent the backflow from entropy into the low entropy center region. The slope of the walls to the inner was limited by the point spread function of the optical path. **Right** Contrast $M = \mathrm{maxOD}(n_{-9/2} - n_{-7/2}) - \mathrm{minOD}(n_{-9/2} - n_{-7/2})$ of the spin wave image (Fig. 4.19). For a vanishing vertical magnetic field gradient $I = 2.8$a.u., the contrast remained high in time since the relative phase (see text) between atoms in different two-dimensional planes was stable. Dephasing at a finite vertical gradient across different planes contrarily led to a washing out of the spin spiral and, hence, the contrast for larger free evolution times, e.g. at $i = 2.9$a.u..

DMD laser path. A slope to about 1 kHz/site could be reached (Fig. 4.18 left). The inner region up to 500 Hz was not compensated with DMD light during the second pattern. The band insulator was hence exposed to the underlying Gaussian potential of the lattice laser beams. Furthermore, a smaller inner region of 450 Hz in the second DMD pattern was tried out following the idea to compress the band insulator after initial loading and, hence, enhance the doubles fraction. This, however, did not show the desired effect.

While the DMD laser was ramped up and the in-plane lattice ramped down to 6 $\mathrm{E_{rec}}$, the superlattice phase was ramped to the desired configuration (Fig. 4.20 left). Since the vertical z532 lattice was switched off at this time and the atoms were confined in the monochromatic, vertical z1064 lattice rather than in the superlattice, they were not exposed to the phase change. The superlattice phase could be set in a range of around $\phi_{sl} = 0.18\,\mathrm{rad}$.

Adjusting the magnetic field and interaction strength during splitting
So far, the atoms were exposed to a magnetic field of 207 G which led to small attractive on-site interactions of $U = -0.4\,\mathrm{t_{xy}}$. This field was generated by the slow Feshbach coils (Fig. 3.3). The attractive interactions were required for efficient loading of the band insulator and thermalisation. For the splitting of the band insulator into two coupled planes, however, and creating a Mott insulator with mostly singly occupied sites in the bilayer system, strong repulsive on-site interactions were required before the splitting process (Fig. 2.2). Such strong repulsion was accessible in a potassium $|m_F = -9/2, -7/2\rangle$ spin mixture at a magnetic field of around 195 G. Similar interaction strengths were also used in [40]. A change in the magnetic field from 207 G to 195 G, however, made it necessary to occasionally swap from the initial $|m_F = -9/2, -7/2\rangle$ to a $|m_F = -9/2, -5/2\rangle$ hyperfine spin mixture. Otherwise, high loss rates would have been occurred due to too high interactions when crossing the $|m_F = -9/2, -7/2\rangle$ Feshbach resonance at 202 G (Fig. 3.12 right). Therefore, a first radio frequency sweep swapped the internal hyperfine state of the $|m_F = -7/2\rangle$ population to the $|m_F = -5/2\rangle$ hyperfine state. The magnetic field was subsequently decreased to 190 G within 1.1 ms. For this fast change of the magnetic field, the fast Feshbach coils were employed due to their small inductance [57]. A second radio frequency sweep then swapped back the population from the $|m_F = -5/2\rangle$ to the $|m_F = -7/2\rangle$ state. Finally, the magnetic field was adjusted at 195 G with the help of the slow Feshbach coils.

Cancellation of residual magnetic field gradients
Residual, in-plane as well as vertical magnetic field gradients during pre-splitting/splitting (Fig.4.20 left/right) were cancelled using the modified Ramsey technique [153][48] (Fig. 4.24).

The residual vertical gradient was mainly evoked by the slow Feshbach coils. The fast Feshbach coils in Anti-Helmholtz configuration were employed to cancel this vertical gradient (Fig. 3.3). An H-bridge enabled to switch the sign of the fast Feshbach gradient and, hence, producing a gradient of same strength but opposite direction to any residual field gradient from the slow Feshbach coils. In order to find the compensating gradient with the Fast Feshbach coils, the offset coils were first used to evoke a small in-plane magnetic field gradient. A $\pi/2$-pulse then transferred the atoms residing in the two lowest hyperfine states $|m_F = -9/2\rangle$ and $|m_F = -7/2\rangle$ into the equatorial plane of the Bloch sphere. Subsequently, the current through the fast Feshbach coils and, thus, the gradient strength was scanned and the atoms were exposed to the resulting vertical gradient $\nabla B_{\text{slow}} - \nabla B_{\text{fast}}$ for a varying free evolution time. A second $\pi/2$-pulse finally transferred the atoms back to the $|m_F = -9/2\rangle$ and $|m_F = -7/2\rangle$ hyperfine states according to their current phase on the Bloch sphere (Fig. 4.24). After freezing the in-plane lattice, both hyperfine states were imaged using the detection scheme in Sec. 3.17. Then, the contrast $\text{M}_{\text{sp}} = \text{maxOD}(n_{-9/2} - n_{-7/2}) - \text{minOD}(n_{-9/2} - n_{-7/2})$ was computed.[22] This revealed spin waves (Fig. 4.19) since the in-plane gradient from the offset coils evoked that the atoms accumulated a different amount of phase during the free evolution time depending on the local gradient strength (Fig. 4.24).

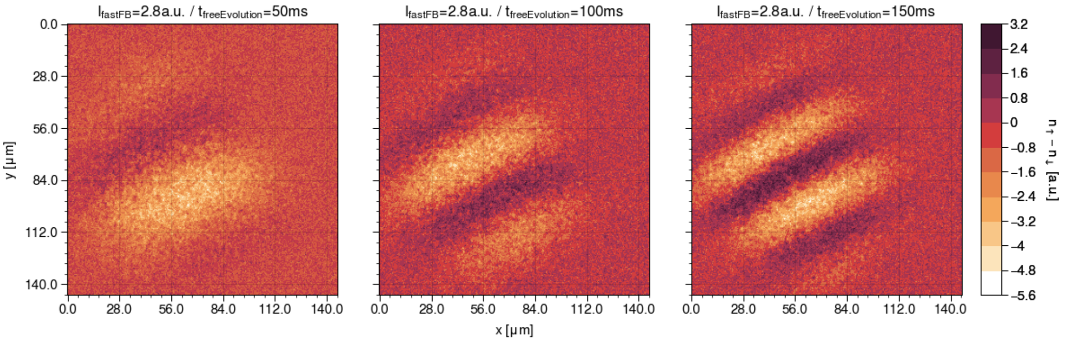

Figure 4.19: Spin waves for three different free evolution times $t_{\text{freeEvol}} = 50, 100, 150\,\text{ms}$ with increasing spin wave vector $\vec{k}$ (from left to right).

The spin wave vector $\vec{k}$ increased with longer evolution times (Fig. 4.19).[23] More important for gradient cancellation, however, was the fact that the spin wave remained visible for all times only for a vanishing vertical magnetic field gradient. For a non-negligible vertical gradient the atoms across different, two-dimensional planes accumulated a different amount of phase which led to a washing-out of the contrast. The contrast was therefore evaluated for different fast Feshbach currents and times (Fig. 4.18 right). The current at which the contrast remained highest for all times then signalled a vanishing, vertical magnetic field gradient [153][24]. The upper limit for the remaining vertical gradient was $3.5\,\mu\text{G}\mu\text{m}^{-1}$.

The residual, in-plane gradient was cancelled by scanning the current through the offset coils. At vanishing in-plane gradient, the spin wave $\vec{k}$-vector had zero length for all times.

The bilayer quantum simulator

Having established a magnetic field of 195 G to induce strong repulsive interactions with negligible residual magnetic field gradients, the vertical z532 lattice was ramped up adi-

---

[22] OD denotes here the optical density.

[23] The absolute value of the spin wave $\vec{k}$-vector increases up to the π-point where it gets Bragg-reflected at the edge of the two-dimensional Brioullin zone (Fig. 4.25).

[24] Fig. 4.19 corresponds to the time evolution at vanishing vertical gradient, i.e. $I = 2.8 a.u.$.

abatically to split the band insulator into two coupled layers (Fig. 4.20 right). The sinusoidal ramp of the z532 lattice was divided into two parts. Each took 35 ms. First, it was ramped to $9\,\mathrm{E_{rec}}$ and subsequently continued to a desired value. For the spin correlation measurements these values ranged from $13\,\mathrm{E_{rec}}$ to $28\,\mathrm{E_{rec}}$. The z1064 lattice depth was set to $120\,\mathrm{E_{rec}}$. This yielded vertical tunnelling rates between $t_{\perp} = 35 - 830\,\mathrm{Hz}$. With an in-plane tunnelling rate of $t_{\mathrm{xy}} = 174\,\mathrm{Hz}$ at $7\,\mathrm{E_{rec}}$ tunnelling ratios of $t_{\perp}/t_{\mathrm{xy}} = 0.2 - 4.75$ could hence be adjusted in the bilayer quantum simulator. Furthermore, with an interaction strength of $U = 0.9\,\mathrm{kHz}$ (Fig. 4.22 right) in a $V_{\mathrm{z1064}} = 120\,\mathrm{E_{rec}}$, $V_{z532} = 13\,\mathrm{E_{rec}}$ superlattice configuration, $U/t_{\mathrm{xy}} = 5.2$. This led to a super exchange energy of $4t^2/U = 135\,\mathrm{Hz}$ (Fig. 2.3).

After the splitting (Fig. 4.20 right) the in-plane motion in the bilayered quantum simulator was frozen within 0.1 ms by ramping up the in-plane lattice to $60\,\mathrm{E_{rec}}$. The coupling of the two planes was subsequently suppressed by ramping the z532 lattice to $120\,\mathrm{E_{rec}}$ also within 0.1 ms. This effectively produced two independent planes. The z1064 lattice as well as the DMD power were finally diminished to zero. The quantum simulator was hence frozen in all directions and the equilibrated bi-layered Hubbard system could be studied in terms of singly and doubly occupation as well as in terms of correlations between both spin species.

4.2.5 The underlying potential across the quantum simulator

The employed bi-chromatic lattice in the quantum simulator for the bilayer system implied important consequences for the underlying potential. The potential from a single Gaussian laser beams was discussed in Sec. 4.2.2.1. The potential from two superimposed Gaussian laser beams for a bi chromatic lattice differed from this theoretical description. Especially, in the monochromatic case, the inserted lattice depth s in recoil energies in Eq. 4.9 yielded the actual lattice depth (Fig. 2.5 left). In contrast, in a bi-chromatic lattice with different lattice constants where a red- and a blue detuned lattice were superimposed, the effective lattice depth of the superlattice did not correspond to the simple sum of both monochromatic lattice depths (Fig. 2.5 center). Furthermore, this effective lattice depth depended on the superlattice phase ϕ (Fig. 2.5 right). For example, for atoms loaded into the lower well of a double well, the ground state energy decreases closer to the anti-symmetric lattice configuration while the maximum of the superlattice potential is nearly independent from the superlattice phase. The effective lattice depth therefore increases for phases closer to the antisymmetric configuration. This phase effect as well as the effective lattice depth in a bi-chromatic lattice had to be taken into account when computing the underlying potential in a bi-chromatic lattice.
In order to do so, the running wave contribution (Eq. 4.8) which is $\propto sR$ and the contribution from a varying ground state energy which is $\propto \sqrt{s}$ (Eq. 4.9) were separately computed. Therefore, either $s_{\mathrm{z532/z1064}}$ or $\sqrt{s_{\mathrm{z532/z1064}}}$ with their corresponding anti-confining pre-factors R and the superlattice phase ϕ were inserted into the one dimensional superlattice potential (Eq. 2.8). This yielded the effective lattice depth for each contribution. Here, the superlattice phase away from the antisymmetry point induced an offset of the superlattice potential compared to the antisymmetry case. This offset was added to the

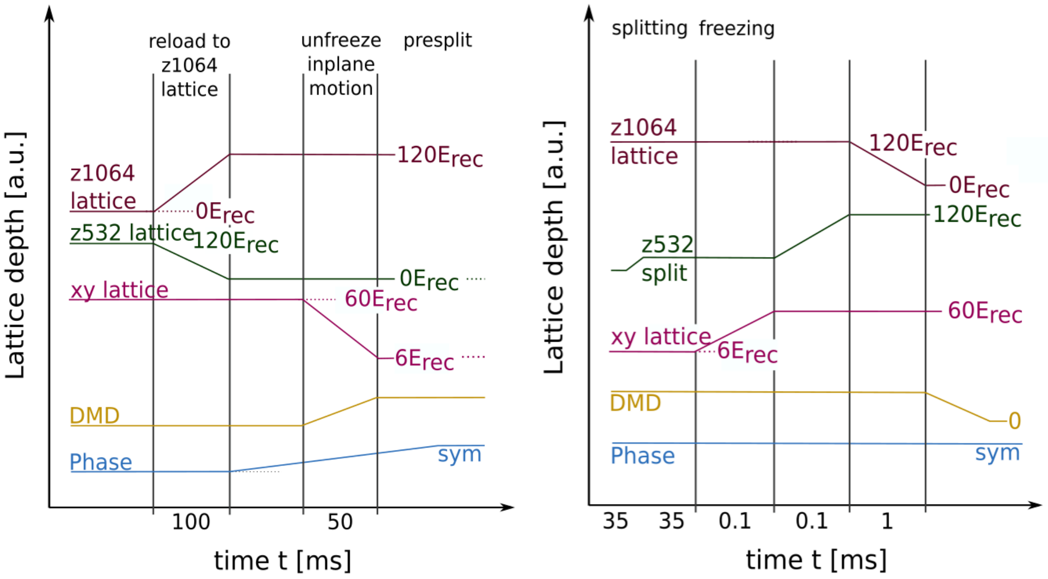

Figure 4.20: Left Main experimental sequence in order to create the bilayer Hubbard system (part 3). The atoms were reloaded from the vertical z532 to the z1064 lattice in a deep in-plane lattice at 60 $\mathrm{E}_{\mathrm{rec}}$. The superlattice phase was prepared while the z532 lattice was switched off. **Right** Main experimental sequence in order to create the bilayer Hubbard system (part 4). The z532 lattice was finally ramped up in the symmetric configuration and split the band insulator into two coupled layers (the bilayer Hubbard system) (Fig. 2.4 left). The motion was subsequently frozen in all directions by ramping up the lattice depths. This allowed for detection of either singles/doubles (Fig. 3.15) or spin up/spin down (Fig. 3.17).

effective potential depth accounting for the phase depending lattice depth (cf. Fig. 2.5 right). The overall depth was then multiplied with the Gaussian envelop of the respective contribution and both contributions were summed as in Eq. 4.9 in order to obtain the underlying potential in a bi-chromatic superlattice.
Furthermore, the above explained procedure to compute the underlying potential of the superlattice required one simplification: In Eq. 4.9 the beam waist determined the shape of the Gaussian envelop. In a bi-chromatic superlattice, however, there are the two beams waists from the z532 and z1064 lattice. For the running wave contribution, the anti-confining prefactor $R_{z532} = 0$ and, thus, there, the beam waist from the z1064 lattice determined the shape of the Gaussian envelop. Contrarily, in the ground state energy variation term, the dominating contribution came from the z532 lattice and its waist entered the Gaussian envelop. This simplification led to an error of maximum 0.8% in the underlying potential if the new bi-chromatic potential simulation at the best matching phase was compared to the theory of two, monochromatic lattices with independent waists where the phase could not be adjusted.

The described approach for the theoretical calculation of the underlying potential in a bi-chromatic lattice was verified with experimental data. Usually, the theoretical calculations are employed in order to compare measured trap frequencies with predictions. From this in turn, the lattice laser beam waists corresponding to the trap frequencies can be inferred (Eq. 4.10). However, these waists were known from the monochromatic theory for each single lattice laser beam. Thus, the simulation of the underlying potential in a bi-chromatic lattice could be proofed by comparing measured trap frequencies in the *superlattice* with theoretical expected trap frequencies from the newly developed simulation for bi-chromatic lattices using the known waists of each single beam. Since for the vertical z superlattice trap frequency data were not available, trap frequency data of the horizontal x superlattice were compared to a corresponding simulation of the x superlattice (Fig. 4.21 left). The x1064 lattice depth was here set to 16 $\mathrm{E}_{\mathrm{rec}}$ while the x532 lattice depth was varied. The theory bands results from the uncertainty of the lattice laser beam waists ±1 µm (cf. paragraph below Eq. 4.10). The errorbars of the experimental data are to small for the large y scale in the plot. For the two intermediate phases the theory coincides with the experimental data. For phases lower than $\phi = 1/3 \cdot \pi/4$, however, there is a discrepancy. One reason for that is the afore mentioned simplification of the theory using only the waist of one of the two beams.

The translation from the x superlattice to the z superlattice potential was achieved by including only a single additional term. This took into account the different lattice constants and therefore the different effective lattice depths of the z lattices compared to the x lattices. All other parameters like the anti-confining prefactor R were simply exchanged. The simulation of the potential in the z superlattice is therefore straightforwardly translated from the x superlattice and, having proofed the simulation of the x superlattice with experimental data, a possible systematic error for the z superlattice is avoided.

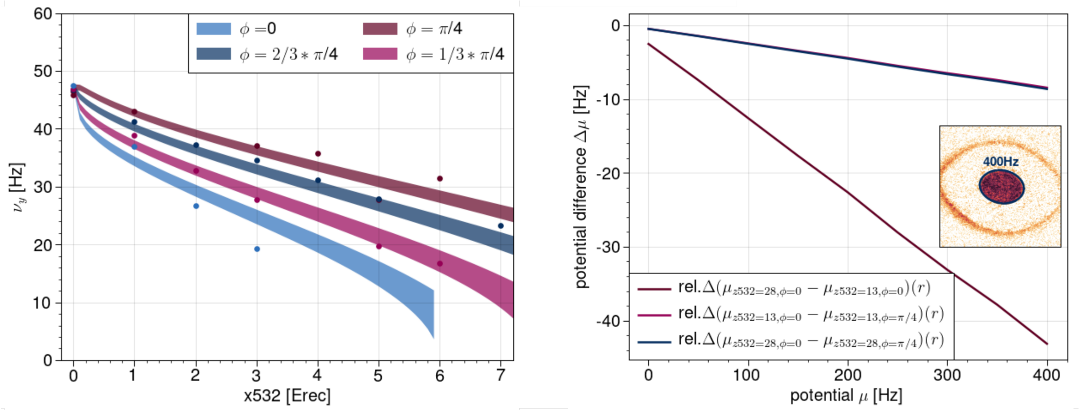

Figure 4.21: Left Trap frequency measurement in the *horizontal x* superlattice. Using these data, the correct calculation of the superlattice potential can be verified. **Right** Relative potential differences between relevant lattice configuration in the bilayer system as a function of (effectively) the distance from the center of the trap (see Fig. 4.15). For example the difference between the two underlying potentials resulting from $V_{z532} = 13\,\mathrm{E}_{\mathrm{rec}}$ or $V_{z532} = 28\,\mathrm{E}_{\mathrm{rec}}$ is small compared to the size of the bilayer system.

With the newly developed theory for the underlying potential in a superlattice configuration in hands, the corresponding DMD potential could be calculated in order to compensate the underlying potential in the inner region of the bilayer quantum simulator for all different superlattice configurations (Fig. 4.18 left). For spin correlation measurements, however, where e.g. the z532 lattice depth during splitting was varied in the range $13 - 28\,\mathrm{E_{rec}}$, the center was not compensated. This reduced the negative effect of disorder in the compensated potential induced by the DMD light. The simulation of the potential in the z superlattice was therefore used in order to determine the change in the underlying potential for these different superlattice configurations and, thus, enabling to value the error made without compensation and possible improvements (Fig. 4.21 right). The relevant measure here is the relative change between two underlying potentials since an overall energy offset between both has no physical effect. In other words, the minimum of two potentials, e.g. resulting from lattice depths of $z532 = 13\,\mathrm{E_{rec}}$ and $28\,\mathrm{E_{rec}}$, can first separately be set to zero and both potentials can be subtracted from each other thereafter to obtain the relative change.

It yielded a linear increase of the absolute, relative difference up to 40 Hz at a radius of 400 Hz for the two superlattice configurations with $\phi = 0$ and $z532 = 13\,\mathrm{E_{rec}}$ or $28\,\mathrm{E_{rec}}$ (Fig. 4.21 right, dark red line). This increase corresponds roughly to 1 Hz/site which suggests that the effect of the change of the underlying potential for different z532 lattice depths is minor. The effect is even smaller for a change in the superlattice phase (Fig. 4.21 right, blue and pink line). As in the case of different z532 lattice depths, the absolute potential bias here increases linearly with radius.

In conclusion, the relative change between different underlying potentials might be minor. Avoiding potential disorder due to interferences from the DMD by simply not compensating the inner region with the DMD might therefore be advantageous.

4.2.6 Singly and doubly occupancies in both planes of the bilayer system

In the last section, the splitting process of the Hubbard band insulator into a coupled bilayer Hubbard system close to half-filling was detailed. In order to qualitatively and quantitatively validate the bilayer quantum simulator, singles and doubles densities in both planes depending on the superlattice phase were experimentally measured and compared with theoretical predictions from a simulation of one and two fermions in a double well.

The theoretical treatment of one particle in a tilted double well is governed by the Hamiltonian

$$\mathrm{H}^{\mathrm{DW}}_{\mathrm{1part}} = \begin{pmatrix} -\Delta & t \\ t & \Delta \end{pmatrix} \tag{4.17}$$

Here, t describes the tunnelling matrix element between both wells and 2Δ defines the difference between the two potential minima of both sites in the double well (Eq. 4.3). The two eigenstates of the system $|U\rangle$ and $|L\rangle$ describe the particle being in the upper or lower well of the double well. Since the double well is aligned vertically along the z direction in the experiment (Fig. 4.22 left, insets) the notation “upper” and “lower” well does not relate to the energy of the corresponding well but rather to the position in z direction.

Thus, for negative detuning, e.g. the upper well has a lower ground state energy than the lower well (Fig. 4.22 left, left inset). The expected occupation probabilities of the upper/lower well by a single particle in the double well is more probable if the occupied well has a lower energy (Fig. 4.22 left, gray solid/dashed line). Both probabilities, which usually approximate one for large, absolute detuning $|\Delta|$ were multiplied by the singles density in the band insulator, i.e. $n_s = 0.1(2)$ (cf. Fig. 4.15). This is reasonable since for large $|\Delta|$, the probability to find a single particle in a double well after splitting the band insulator was expected to just correspond to this singles density in the band insulator. This assumed that in-plane tunnelling between different double wells was suppressed after splitting.
The theoretical treatment of *two* fermions with different spins in a tilted double well follows Eq. 4.2. It has the four basis states $|\uparrow\downarrow, 0\rangle$, $|\uparrow, \downarrow\rangle$, $|\downarrow, \uparrow\rangle$ and $|0, \uparrow\downarrow\rangle$. They describe the occupation of the upper and lower well, $|U, L\rangle$, by the two spins $\uparrow, \downarrow$. Here, the first and last state describe two fermions occupying both either the upper or lower well which gives rise to double occupation (Fig. 4.22 left, light blue line). This probability decreases strongly towards the symmetric configuration of the double well where, for repulsive interactions, it becomes favourable for the two fermions to split and occupy different sites. The probability for two fermions occupying both the *lower* well as a function of detuning is obtained by mirroring the probability to occupy the upper well at $\Delta = 0\,\text{Hz}$. Furthermore, the probability for the $|\downarrow, \uparrow\rangle$ state as a function of the detuning is symmetric around $\Delta = 0\,\text{Hz}$ (Fig. 4.22 left, pink, dashdotted line). The sum of this curve and its mirrored distribution (pink, dotted) describes the probability of singly occupation in either the upper or the lower plane as a function of the detuning (Fig. 4.22 left, pink, solid line).

However, the data exhibit a further subtlety which had to be taken into account when matching the theory to them (Fig. 4.22 right). In the band insulator, the singles density is $n_\text{S} = 0.1$. Thus, splitting the band insulator while suppressing the in-plane tunnelling led to 10% double wells which were occupied by only a single particle. These singles are referred to as "single singles" in the following. The single singles preferentially occupy the energetically lower lying well. For negative detuning, this is the upper well while for positive detuning it is the lower well (Fig. 4.22 left, insets). Measuring singles in the lower well for negative detuning thus leads to a measurement of less singles because all single singles preferentially occupy the upper well. Hence, these double wells are measured as empty which would not be the case if all double wells were filled with two particles instead. Hence, the probability for singles in each plane (pink, solid line) needs to be subtracted by the probability of a single particle in the double well residing in the upper well (gray solid line). This yields a slightly diminished probability to detect singles (Fig. 4.22 left). Moreover, in order to fit the theory to the data, all curves are scaled by their corresponding detection efficiency (Eq. 4.15). In addition, the measured singles densities are reduced by the factor $1 - 2n_\text{S}$ which is due to those double wells which are empty from the beginning on as well as those in which only a single particle is located (cf. Fig. 4.22 left to right).

For the theory it requires to set the tunnelling amplitude t, the on-site interaction strength U and the scaling between the offset lock control voltage and the double well detuning parameter Δ. All three parameters were independently calibrated before. Thus, using

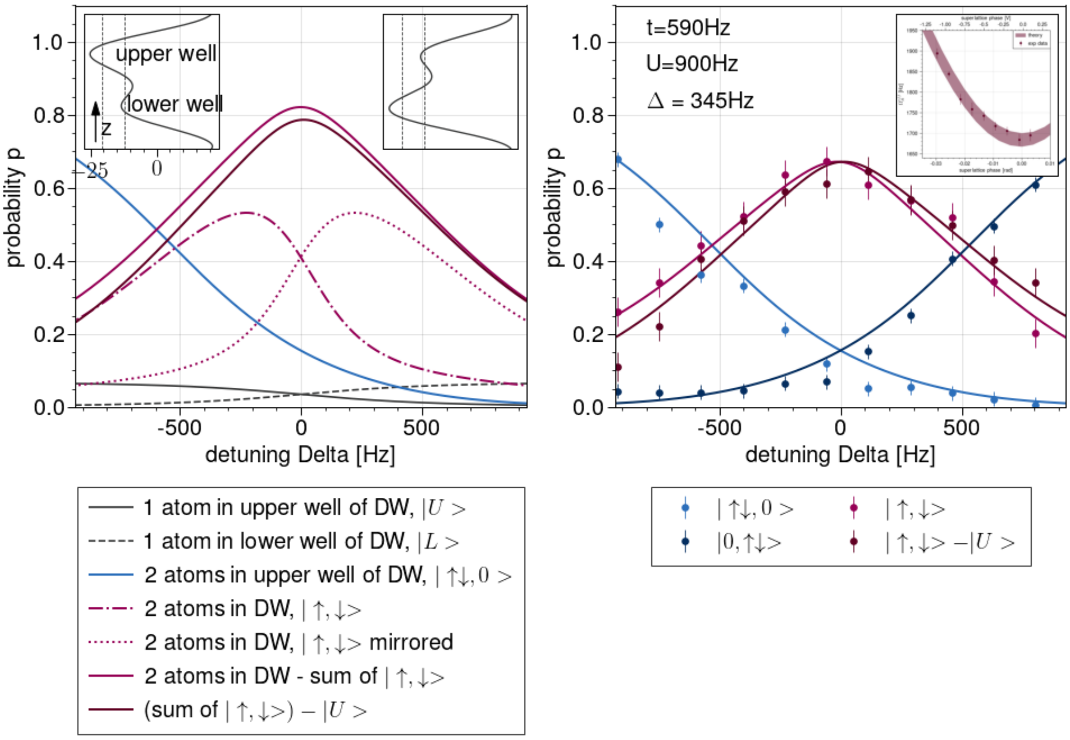

Figure 4.22: Left Theoretically expected singly (solid, pink curve) and doubly (blue curve) occupancies in a double well as a function of the detuning Δ (see text for further explanation). **Right** Measured data (from a single run) and the corresponding composited theoretically expected singly and doubly occupations in many separated double wells as a function of the detuning. This measurement independently validated the calibration measurements of t, U and Δ in chapter4.1. Error bars are taken from an equivalent measurement with five averages. Because of the simultaneous fit of the theory to singles and doubles in both planes, however, the error bars are estimated to be small.

these calibrated parameters, the singles/doubles measurement in both planes is also a double check for these calibrations. The superlattice configuration in this measurement was set to $V_{z1064} = 120\,\mathrm{E_{rec}}$ and $V_{z532} = 15\,\mathrm{E_{rec}}$. Hence, the tunnelling amplitude is $t = 582\,\mathrm{Hz}$ employing the two-band band projection operator method. The tunnelling calibration via Rabi oscillations is in accordance to this value (Fig. 4.5). The double well fit here verifies this value within the errorbars (Fig. 4.22 right). Furthermore, the calibration of the superlattice phase yielded $\Delta = 384(6)\,\mathrm{Hz}$ (Fig. 4.4 right). The Δ from the double well fit, however, resulted in $\Delta = 345\,\mathrm{Hz}$. For the latter value, the theoretical curve in the calibration coincided with the data within the error bars in contrast to the afore determined $\Delta = 384(6)\,\mathrm{Hz}$ (cf. Fig. 4.22 right, inset with Fig. 4.4 right). Thus, the true scaling between the superlattice phase and the offset lock control voltage was rather about $\Delta = 345(6)\,\mathrm{Hz}$. Finally, the interaction strength $U = 900\,\mathrm{Hz}$ coincides with DQMC

calculations and the measurement (Fig.4.29 left).
In conclusion, the implemented bilayer Hubbard system is therefore highly controllable having calibrated and verified all parameters in two independent measurements.

4.2.7 Determinant quantum Monte Carlo simulations

Throughout this thesis many experimentally determined properties of the bilayer Hubbard system were counter-checked with Determinant quantum Monte Carlo (DQMC) simulations. Therefore, the quantum simulation toolbox QUEST was employed [26]. This toolbox was written in FORTRAN. The simulated bilayer Hubbard system had usually a size of 8×8. The interaction strength, tunnelling amplitude, temperature and chemical potential were varied in such simulations.

4.2.8 Compressibility of the bilayer Hubbard system

The isothermal compressibility of the bilayer Hubbard system was measured in order to study the bilayer system's insulating nature. The compressibility of a monolayer Hubbard system was experimentally studied with cold atoms in [40][49]. The isothermal compressibility is defined as

$$\kappa = \frac{1}{n^2}\frac{\partial n}{\partial \mu}. \tag{4.18}$$

In order to measure κ in the bilayer Hubbard system, an in-plane magnetic field gradient was applied. The small offset coils (Fig. 3.3) were used for this purpose. The gradient strength was $|\nabla B| = 24.8\,\mu\mathrm{G}/\mu\mathrm{m}$. It was ramped up during splitting in 70 ms (Fig. 4.20 right) and hold thereafter for 1 s in the thermalised bilayer system. The in-plane lattice was set to $7\,\mathrm{E_{rec}}$ during this time. Singles and doubles in one of the two coupled planes were subsequently imaged in a frozen lattice employing the singles/doubles detection scheme (Fig. 3.15). Then, the total density was deduced from this (Fig. 4.23 left). Moreover, the magnetic field gradient across the planes induced an in-plane varying chemical potential μ ranging between $[-1.5\,\mathrm{t}, 1.5\,\mathrm{t}]$ in the considered region (Fig. 4.23 left). The latter was inferred using the local density approximation. By plotting the so-obtained averaged total density along the iso-potential lines as a function of the chemical potential, the slope determined the compressibility κ (Fig. 4.23 center). This was performed for different ratios $t_\perp/t$ and the measured compressibility was compared to Determinant Quantum Monte Carlo predictions (Fig.4.23 right). The data points (blue) thereby coincided within the errorbars with the theoretically expected compressibility in the bilayer Hubbard system (red points). The errorbars in the DQMC simulation originated from a temperature range between $\mathrm{k_B}T = 1.0 - 1.4\,\mathrm{t}$.

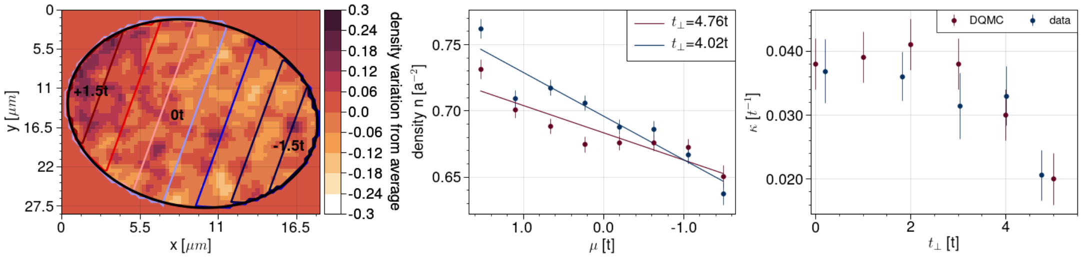

Figure 4.23: Left Image of the total density n in one of the two coupled planes in the bilayer system when a magnetic field gradient is applied. The local chemical potential can be computed employing the local density approximation (coloured iso-potential lines). **Center** The averaged density along the iso-potential lines as a function of the chemical potential. The slopes $\partial n/\partial\mu$ are computed from a linear fit. Exemplarily, the data for the tunnelling ratio $t_\perp/t = 4.02, 4.76$ are shown. **Right**. The compressibility in the bilayer Hubbard system deduced from the calculated slopes $\partial n/\partial\mu$ for all measured ratios $t_\perp/t$. The data coincides within the errorbars with the theoretically expected compressibility from a DQMC simulation.

4.3 Spin correlations in the bilayer system

In chapter 4.2, the implementation of the bilayer Hubbard system in the experimental setup (Sec. 3) was detailed. In this section, spin correlation measurements on the bilayer Hubbard system are discussed and the results are compared to theoretical predictions (Fig. 2.4, phase diagram). This enables to measure the cross over from an anti-ferromagnetically ordered Mott insulating state to a band insulating state with singlet bounds across the two layers.

4.3.1 Intralayer spin correlations

4.3.1.1 Introduction

Intralayer spin correlations in the bilayer Hubbard system are quantified throughout this thesis in terms of the spin structure factor [26]

$$S(q) = \frac{1}{N}\sum_{i,j} e^{-i\vec{q}\,\vec{r}_{i,j}} C^z_{i,j} \tag{4.19}$$

at $\vec{q} = 0$ and $\vec{q} = (\pi, \pi)$. In general, the spin structure factor is the Fourier transform of the spin correlator $C^z_{i,j} = \langle \hat{S}^z \hat{S}^z_j\rangle - \langle \hat{S}^z_i\rangle\langle \hat{S}^z_j\rangle$. Here, each correlator $C^z_{i,j}$ correlates the z component of the spin operator $\hat{S}^z_i$ on lattice site i to the z component of spin operator $\hat{S}^z_j$ on-site j. Furthermore, in a spin balanced system with $n_{S,\uparrow} = n_{S,\downarrow}$, the correlator simplifies to $C^z_{i,j} = \langle \hat{S}^z_i \hat{S}^z_j\rangle$ because the z component on each individual lattice site i averages to zero.[25] The spin structure factor at $\vec{q} = 0$ is referred to as *uniform*

---

[25] Throughout this thesis, spin correlation measurements were performed in spin balanced systems.

or static structure factor. The spin structure factor at $\vec{q} = (\pi, \pi)$ is called *staggered* structure factor. The uniform structure factor, *uniformly* weights all correlators $C^z_{i,j}$ with $e^{-i \cdot 0 \cdot \vec{r}_{i,j}} = 1$ independent from the distance $d_{i,j}$ between the sites i and j. In contrast, for $\vec{q} = (\pi, \pi)$, the prefactor $e^{-i\vec{q}\vec{r}_{i,j}}$ alternates in a *staggered* fashion as $(-1)^{d_{i,j}}$ between lattice sites. By explicitly writing out the sum in Eq. 4.19 for antiferromagnetic correlations and the case $\vec{q} = 0$ further insight can be gained [47]

$$S_{\vec{q}=0} = +|C_{0,0}| - 4|C_{0,1}| + 4|C_{1,1}| - ... \tag{4.20}$$

The first term on the right hand side $C_{0,0}$ describes on-site correlations. This term is also referred to as “local moment” and can be related to the singles density in an homogenous, spin balanced system [154]

$$C_{0,0} = \frac{\langle n_{S,i,\uparrow}\rangle + \langle n_{S,i,\downarrow}\rangle}{4}. \tag{4.21}$$

The second term on the right hand side in Eq. 4.20 amounts the nearest neighbour correlations. The prefactor accounts for the *four* nearest neighbours of each lattice site on a two-dimensional square lattice. Importantly, this term has a negative sign for antiferromagnetic correlations and therefore reduces the static structure factor compared to the local moment (Eq. 4.20). Contrarily, the third term has again a positive sign and, thus, increases the uniform structure factor. It takes into account the correlations between site i and its four *next* nearest neighbours on a two-dimensional square lattice. Since nearest neighbour correlations are commonly larger than next nearest neighbour correlations and the following terms in Eq. 4.20, nearest neighbour correlations in the two-dimensional Hubbard system can be detected by observing a reduced uniform structure factor with respect to the local moment.

The staggered structure factor in contrast to the uniform structure factor exhibits only positive signs for antiferromagnetic correlations

$$S_{q=\pi} = +|C_{0,0}| + 4|C_{0,1}| + 4|C_{1,1}| + ... \tag{4.22}$$

Thus, in the presence of antiferromagnetic spin correlations it lies above the local moment. Furthermore, for only nearest neighbour correlations the uniform and staggered structure factor are equally distanced from the local moment in opposite direction, i.e. while the uniform structure factor lies below the local moment, the staggered structure factor lies above it. An unequal offset between both structure factors and the local moment respectively is therefore an indication for correlations beyond nearest neighbours since then $|C_{1,1}|$ adds positively in both structure factors, compare Eq. 4.20 with 4.22.

In the measurements throughout this thesis, spin correlations in the bilayer Hubbard system were detected by taking absorption images of both spin components in one of the two layers (Fig. 3.17) and in-situ z-imaging (Sec. 3.2.1). This imaging setup does not allow to resolve the occupation of a single lattice site. Rather, the point spread function has a FWHM of 2.6 µm (Sec. 3.2.1) which corresponds to about five lattice sites in the in-plane lattice. The calculation of the uniform structure factor Eq. 4.20 from the measured spin up/down densities was therefore hindered. In fact, each correlator resulted from the measured singles density deconvolved with the imaging point spread function (PSF) [26]

$$C^{\mathrm{z,meas}}_{\mathrm{r,r+d}} = \sum_{i,j} \mathrm{PSF}(r - r_i)\mathrm{PSF}(r + d - r_j) C^{\mathrm{z,actual}}_{i,j}. \tag{4.23}$$

Here, d is the distance between the correlated spins at two positions r and $r + d$ in the absorption image. By integrating the correlations over a distance d which is large compared to the PSF, the measured, integrated uniform structure factor however differs from the actual, integrated uniform structure factor only by a prefactor

$$S^{\mathrm{actual}}_{q=0} = s^2_{px} a^2_l \cdot S^{\mathrm{meas}}_{q=0}. \tag{4.24}$$

Here, s_{px} is the pixel size of the CCD z-camera (Sec. 3.2.1) and a_l is the lattice constant. Thus, even without single site resolution the integrated true uniform structure factor can be deduced by multiplying a scaling factor to the measured integrated uniform structure factor.

In contrast, the staggered structure factor (Eq. 4.22) can only be measured in our setup by a manipulation of the local spin orientations before imaging. A modified Ramsey type sequence for the manipulation was therefore implemented [153][152]. The staggered structure factor is widely used to quantify antiferromagnetic spin correlations in condensed matter systems.

4.3.1.2 Modified Ramsey sequence

The modified Ramsey sequence was embedded into the main experimental sequence to flip the spins in the frozen lattice before detection (Fig. 3.17) in a staggered fashion $(-1)^{i+j}$. Here, i and j are integers indicating the i-th and j-th lattice site in x- and y-direction of the two-dimensional lattice, respectively. Thus, potential antiferromagnetic correlations are unwound to ferromagnetic correlations which enabled the measurement of the staggered structure factor (Eq. 4.24). So, by switching on/off the modified Ramsey sequence part in the main experimental control sequence, the staggered/uniform structure factor could be measured independently.

The modified Ramsey sequence consists of three building blocks (Fig. 4.24): A first $\pi/2$ pulse, a free evolution time t_{freeEvol} in which the atoms in the two-dimensional lattice were exposed to a magnetic field with an in-plane gradient and a second $\pi/2$ pulse. For the calibration of each of the three steps, a spin polarised atomic Fermi gas on a two-dimensional lattice was initially prepared (Fig. 4.24 left, lower row). Thus, for calibration of the modified Ramsey sequence, the three steps were performed in the order as specified above. In the main experiment sequence, however, the modified Ramsey sequence was meant to detect expected antiferromagnetic correlations in the bilayer Hubbard system[26]

---

[26] At low enough temperatures antiferromagnetic correlations are expected, see phase diagram of the monolayer Hubbard model for repulsive interactions (Fig. 2.2).

by unwinding the anti-ferromagnet (Fig. 4.24 right, lower corner) to a ferromagnet (left, lower corner) and, hence, the order of the steps was effectively inverted.

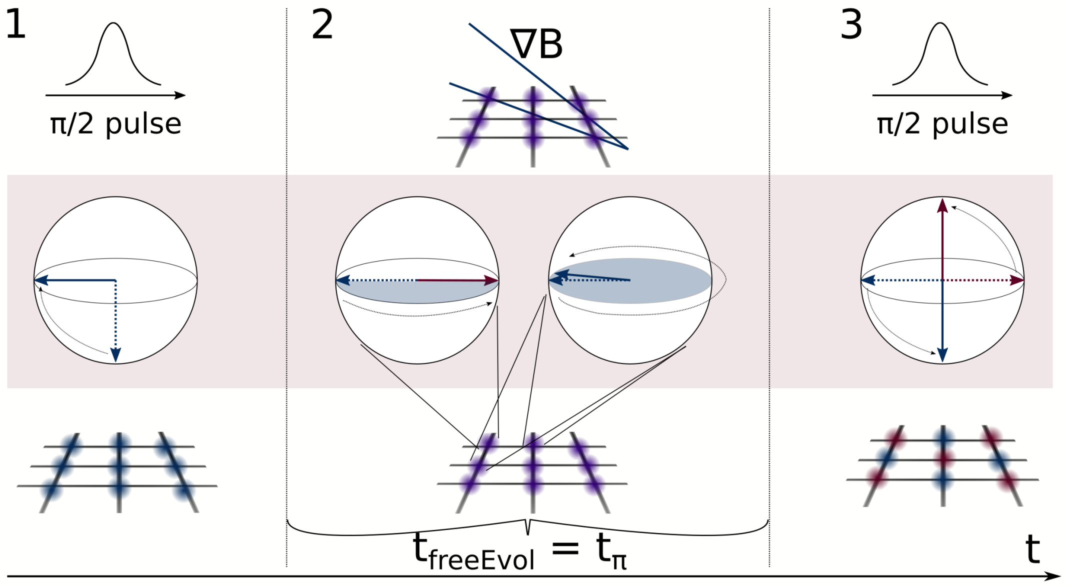

Figure 4.24: Modified Ramsey sequence in three steps. First column a first $\pi/2$ pulse transfers atoms from the lower hyperfine state into a superposition state. **Second column** during a free evolution time t_{freeEvol}, the atoms in the two-dimensional lattice are exposed to a magnetic in-plane gradient along the lattice diagonal and, thus, rotate in the equatorial plane according to the local field strength. **Third column** a second $\pi/2$ pulse mapped the spins back into the measurement z basis depending on their current phase. Starting with a ferromagnet, then, if t_{freeEvol} is chosen such that atoms on adjacent sites acquire a phase difference of π (as shown in the center figure), the second $\pi/2$ pulse produces an anti-ferromagnet. Vice versa, an anti-ferromagnet is unwound to a ferromagnet. The latter effect is employed to measure the staggered structure factor.

For the calibration of the first $\pi/2$ pulse, a spin polarised gas in the lower $|\downarrow\rangle = |m_F = -9/2\rangle$ state was initially loaded into a three dimensional lattice. The first $\pi/2$ pulse then transferred the atoms from this state into a superposition state $|\psi\rangle = 1/\sqrt{2}(|\uparrow\rangle + |\downarrow\rangle)$ on the equatorial plane (Fig. 4.24 first column) where $|\uparrow\rangle = |m_F = -7/2\rangle$. This pulse had a shape of [153]

$$A_{\pi/2}(t) = A^0_{\pi/2} e^{-4\ln 2 \frac{(t-t_0)^2}{\sigma^2_{\pi/2}}} . \tag{4.25}$$

The FWHM of the pulse was $\sigma_{\pi/2} = 50\,\mu\mathrm{s}$. The amplitude $A^0_{\pi/2}$ was calibrated such that half of the atoms were transferred from the initial $|m_F = -9/2\rangle$ state to the $|m_F = -7/2\rangle$ state.[27] The $\pi/2$ pulse frequency was scanned over the transition resonance at which the

---

[27] A scan of the amplitude resulted in a $\sin^2(\Omega_R t)$ dependence of the population of the initial $|m_F = -9/2\rangle$

transfer was maximum (Fig. 4.25 left).
The second $\pi/2$ pulse was subsequently calibrated by switching off the first one and following the same procedure as for the latter.
As a final step the magnetic field was adjusted. Having transferred all atoms into the superposition state with the first $\pi/2$ pulse (Fig. 4.24 left) a magnetic field with an in-plane gradient was applied across the two-dimensional lattice for a free evolution time t_{freeEvol}. During this time, the magnetic moments on each site rotated in the equatorial plane according to the local magnetic field strength. The gradient direction was adjusted such that it coincided with one lattice diagonal (Fig. 4.24 center). The gradient strength was calibrated such that the magnetic moments on adjacent lattice sites accumulated a relative phase difference of π during the free evolution time t_{freeEvol} (Fig. 4.25 right). This special point in time is called the π point. In order to find it, t_{freeEvol} was first varied from zero up to the 2π point at around $t_{\text{freeEvol}} = 0.25\,\text{s}$. At this point, adjacent lattice sites accumulated a relative phase difference of 2π. Thus, the magnetic moments were aligned relative to each other as initially at $t_{\text{freeEvol}} = 0$. A second $\pi/2$ pulse after $t_{\text{freeEvol}} = 0.25\,\text{s}$ therefore again revealed the spin polarised gas (Fig. 4.24 left). However, for all other times $t_{\text{freeEvol}} \in (0, 2\pi)$, the initial spin polarised gas is transduced to a spin wave by the modified Ramsey sequence (Fig. 4.25 right, insets). Here, the spin wave is visible in the contrast $\mathrm{M}_{\text{sp}} = (n_\uparrow - n_\downarrow)/(n_\uparrow + n_\downarrow)$ between the spin up and spin down densities and characterised by the wave vector $\vec{k}_{sp}$ (cf. Fig. 4.19). The latter was extracted from a two-dimensional Fourier transformation to the contrast.
For small free evolution times t_{freeEvol} or close to the 2π point, the arising spin wave has a long wave length and, hence, the amplitude of the corresponding wave vector is small (Fig. 4.25 right). For times t_{freeEvol} in between, the extracted amplitudes of the wave vector $\vec{k}_{sp}$ first linearly increase up to the π-point and then linearly decrease again (Fig. 4.25 right). The amplitude of $\vec{k}_{sp}$ first increased for small times and, after the π point, decreased again. The $\vec{k}_{sp}$ for times close to the π point could not be resolved in the contrast images due to the limiting imaging resolution. Thus, the length of $\vec{k}_{sp}$ was interpolated for times around the π point and the latter was inferred from the intersection of the two linear interpolations (Fig. 4.25 right)[28]. Thus, the time at which spins on adjacent lattice sites acquired a phase difference of π was determined.

A digital laser intensity control (DLIC) unit was employed in order to generate both short $\pi/2$ pulses. Furthermore, the SU(2) symmetry of our experimental implementation of the Hubbard model was verified for the modified Ramsey sequence by switching on/off the first $\pi/2$ pulse of the modified Ramsey sequence and observing the same amount of spin

---

state and of the transferred population to the $|m_F = -7/2\rangle$ state, where Ω_R is the Rabi frequency. The amplitude $A_{\pi/2}(t)$ was obtained by taking the amplitude where an equal amount of spin up and spin down atoms were measured. More details can be found in [153].

[28] The description of the $\vec{k}_{sp}$ is commonly done in reciprocal space. Starting at $t_{\text{freeEvol}} = 0$ the length of $|\vec{k}_{sp}| = 0$. Then, for increasing t_{freeEvol} $|\vec{k}_{sp}|$ increases while at the π point it just reaches one corner of the first Brioullin zone. For even larger t_{freeEvol}, $\vec{k}_{sp}$ is Bragg-reflected at the edge and decreases again to the center of the first Brioullin zone. It hits the center, however, only if the magnetic field gradient is well aligned along the diagonal of the two-dimensional lattice. Otherwise it passes the center and gets again Bragg reflected as soon as it reaches an edge of the first Brioullin zone.

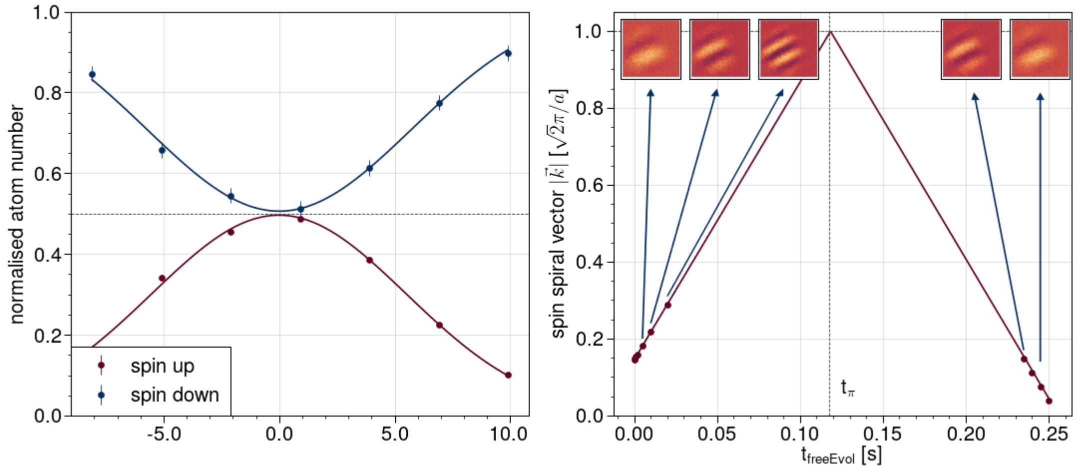

Figure 4.25: Calibration of the modified Ramsey sequence. **Left** Measured and normalised spin up and spin down densities as a function of the $\pi/2$ pulse frequency. At resonance and at the correct amplitude, half of the atoms in the lower $|m_F = -9/2\rangle$ state is transferred to the $|m_F = -7/2\rangle$ state. **Right** Calibration of the free evolution time t_{freeEvol}. For small t_{freeEvol} the spin wave vector is short. It increases towards the π point before it decreases again to zero towards the 2π point. The spin wave for t_{freeEvol} close to the π point cannot be resolved without single site resolution. Therefore, linear interpolation is exploited to find the time $t_{\mathrm{freeEvol}} = t_\pi$ at which atoms on adjacent sites acquire a phase difference of π (referred to as π point). The insets illustrates a possible spin wave.

correlations in both cases.
In conclusion, with the modified Ramsey sequence, the lack of single site resolution of the z-imaging setup could be circumvented by interpolating to the π point and the uniform *and* staggered structure factor could hence be computed for spin correlation analysis (Sec. 4.3.1).

4.3.1.3 Intralayer correlations as function of $t_\perp/t$

The uniform (blue) and staggered[29] (red) spin structure factor was measured in the bilayer Hubbard system for different ratios between the inter- and intra-layer tunnelling $t_\perp/t$ (Fig. 4.26 left). Additionally, the local moment (Eq. 4.21) was determined. DQMC calculations of the respective quantities were performed on a homogenous lattice with 8×8 lattice sites per layer for a filling of $n = 0.4$, a temperature $\mathrm{k_B}T = 1.0 - 1.4\,\mathrm{t}$ and interaction strengths between $U = 2 - 8\,\mathrm{t}$ (Fig. 4.26 left, shaded regions).
A smooth crossover from an anti ferromagnetically ordered state for small $t_\perp/t$ to a band insulating state with vanishing intra-layer anti-ferromagnetic spin correlations at high $t_\perp/t$ is expected to occur in a bilayer Hubbard system around $t_\perp/t \approx 3$ at $U = 8t$ (Fig.

---

[29] Here, the modified Ramsey sequence was switched on for the measurement of the staggered structure factor (Fig. 4.24).

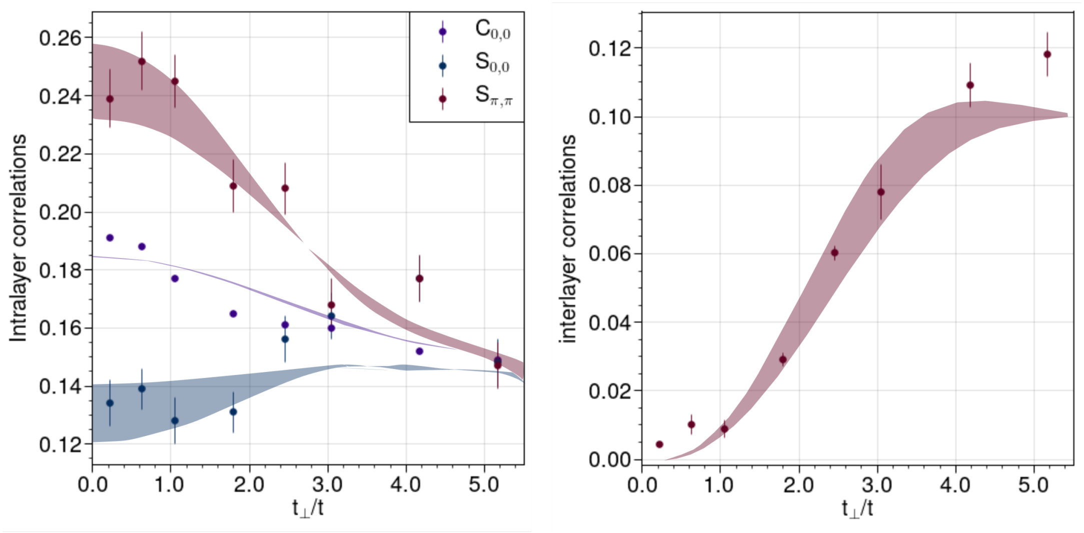

Figure 4.26: Spin correlations in the bilayer system. Left Uniform structure factor, staggered structure factor and local moment in one of the two layers as a function of $t_\perp/t$. Both, the uniform and staggered structure factor are equally spaced from the local moment at low $t_\perp/t$ showing nearest neighbour antiferromagnetic spin correlations. For large $t_\perp/t$, both approach the local moment indicating vanishing off-site correlations. Shaded regions are from Determinant Quantum Monte Carlo calculations for $k_B T = 1.0-1.4\,t$, $U = 2-8\,t$ and $n = 0.4$. **Right** Interlayer antiferromagnetic spin correlations as a function of $t_\perp/t$. They increase with $t_\perp/t$ indicating the formation of singlet bonds across the two planes.

2.4 right). At small $t_\perp/t$, the uniform and staggered structure factor are equally spaced around the local moment (Fig. 4.26 left). This indicates intra-layer nearest neighbour antiferromagnetic spin correlations (Sec. 4.3.1.1). In contrast, for $t_\perp/t \approx 5$, both, the uniform and staggered structure factor approach the local moment which implies that antiferromagnetic order within the two-dimensional layers vanishes. Theoretically, this can be seen by Eq. 4.20 and Eq. 4.22 that are only equal to the local moment if all higher order correlations are zero. In conclusion, the intra-layer nearest neighbour antiferromagnetic spin correlations smoothly diminish by increasing the interlayer tunnelling with respect to the intra-layer tunnelling amplitude (Fig. 4.26 left).

Furthermore, the local moment decreases smoothly with increasing ratio $t_\perp/t$. This is due to an increasing effect of quantum disorder, namely an increasing band width compared to the interaction strength U [135].

4.3.2 Interlayer spin correlations

At high $t_\perp/t$, a band insulating state is predicted with interlayer antiferromagnetic spin correlations (Fig. 2.4 right). The detection of these correlations in the experimentally realised bilayer Hubbard system based on the measurement of singlet triplet oscillations (STO) in the vertical double wells of the bilayer system. In fact, the STO measurement allows to quantify the excess of singlets compared to the triplet states which are present in the double wells. This, in turn, quantifies the amount of spin correlations. The latter are proportional to the excess singlets. In contrast, for an equal number of singlets and each of the triplet states $|t_0\rangle$, $|t_+\rangle$ and $|t_-\rangle$, it was shown in [154] that antiferromagnetic correlations are not present in the system. A similar detection scheme for antiferromagnetic correlations was employed in [65].

Singlet triplet oscillations

In general, oscillations between the singlet state $|s\rangle = 1/\sqrt{2}(|\uparrow,\downarrow\rangle - |\downarrow,\uparrow\rangle)$ and the triplet state $|t_0\rangle = 1/\sqrt{2}(|\uparrow,\downarrow\rangle + |\downarrow,\uparrow\rangle)$ in a double well can be evoked by inducing a spin dependent energy difference between the two wells of the double well. Then, the two states $|\uparrow,\downarrow\rangle$ and $|\downarrow,\uparrow\rangle$ have different energies. In turn, they accumulate a different amount of phase when evolving in time and the singlet state can go over into a triplet state and vice versa. In the experiment, an energy difference between the two wells of the vertical double well was accomplished by applying a magnetic field gradient ∇_zB parallel to the double well. The time evolution of an initial singlet state $|\psi(t)\rangle$ in the double well then reads [154]

$$|\psi(t)\rangle = \frac{1}{\sqrt{2}} \left(e^{-i(\Delta E_\uparrow - \Delta E_\downarrow)t/(2\hbar)} |\uparrow,\downarrow\rangle - e^{i(\Delta E_\uparrow - \Delta E_\downarrow)t/(2\hbar)} |\downarrow,\uparrow\rangle \right) \tag{4.26}$$

with $\Delta \mathrm{E}_\uparrow \propto \nabla_z \mathrm{B}$. Here it becomes visible that, if the accumulated phase amounts to $(\Delta \mathrm{E}_\uparrow - \Delta \mathrm{E}_\downarrow)t/\hbar = n \cdot \pi$ with n mod 2=1, the singlet state goes over into a triplet state and vice versa. Hence, during a free evolution, a periodic oscillation between the singlet and $|t_0\rangle$ triplet state is induced.

The vertical magnetic field gradient ∇_zB was induced across the bilayer Hubbard system. Before the atomic motion in the system was frozen by ramping the in-plane lattice to 30 $\mathrm{E}_{\mathrm{rec}}$ within 500 µs and subsequently the vertical z532 lattice to 36 $\mathrm{E}_{\mathrm{rec}}$ within 100 µs. The fast Feshbach coils were then employed to generate the vertical magnetic gradient. The current through the coils were ramped up within 1 ms, hold for 20 ms and subsequently ramped down again within 1 ms. Instead of varying the time t (Eq. 4.26) to evoke STO, the magnetic field gradient strength was varied during the 20 ms holding time. This reduced noise from magnetic field fluctuations. After ramping down the magnetic gradient, the induced STO were made visible by merging the frozen double wells into single wells (Fig. 4.27 left). Doing so, a singlet state which is present in a double well before merging, is mapped onto a doubly occupancy of the lowest energy level in the single well (Fig. 4.27 left, upper row). In contrast, a triplet state which is present in the double well before merging is mapped onto a state with one atom in the ground and one in a higher lying vibrational state of the single well (Fig. 4.27 left, lower row). The occupation of a higher lying level is necessary in order to preserve the antisymmetry of the overall fermionic wave function. With singles doubles spectroscopy, the two outcomes after merging (detection of a double or a single in the ground band) could be distinguished employing the interaction shift. Thus, from the measured number of doubles, the amount of singlets with antiferromagnetic order before merging could be inferred.

For small $t_\perp/t$, inter-plane spin correlations are not expected to occur and, thus, excess singlets should not be present. This coincides with the measured oscillation amplitude of

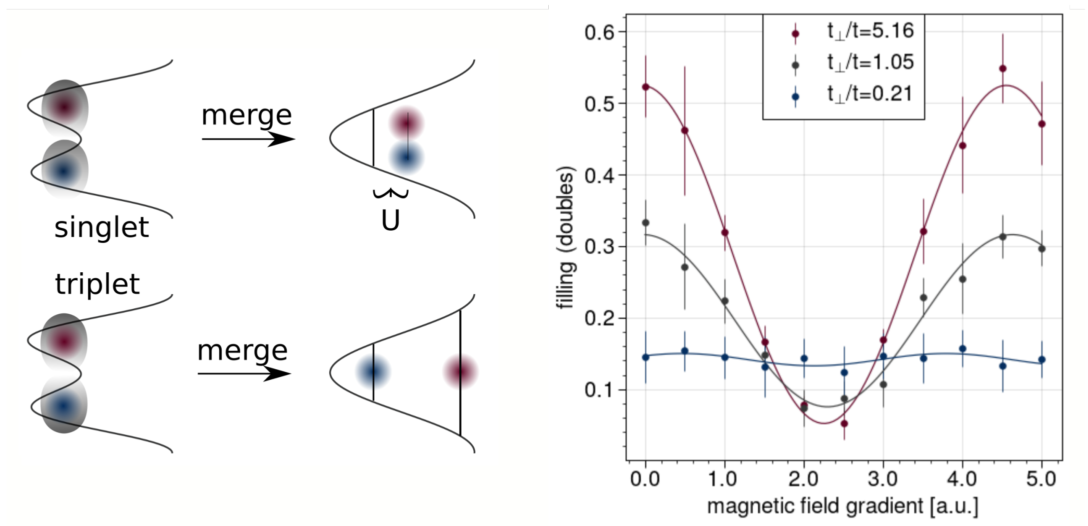

Figure 4.27: Left Detection scheme for interlayer correlations. When merging a double well into a single well by diminishing the short vertical z532 lattice to zero, singlet bonds merge into the ground state of the single site. This is the doubly occupation of the lowest energy level (upper row). In contrast, the triplet state merge such than one atom ends up in a excited vibrational state to maintain the antisymmetry of the wave function (lower row). Thus, the number of doubly occupied sites is a measure for anti-ferromagnetically ordered singlet states before merging and, hence, quantifies inter-plane spin correlations. **Right** Singlet-triplet oscillations (STO). With increasing ratio $t_\perp/t$, the number of singlets across the two planes exceeds more and more the number of triplet states and the amplitude of STO increases.

doubles when scanning the magnetic field gradient strength (Fig. 4.27 right, blue line). In contrast, for large $t_\perp/t$, the number of excess singlets across the two planes is high and, hence, the number of doubles after merging shows oscillations with high amplitude when varying the magnetic gradient strength (Fig. 4.27 right, red line).

Interlayer correlator

The interlayer spin correlations can be deduced from the measured number of doubles. The maximum number of measured doubles during the oscillation (Fig. 4.27 right) corresponds to the number of singlet states. Contrarily, the minimum number of measured doubles corresponds to the number of $|t_0\rangle$ triplet state. The transverse spin correlator can be deduced from the measured number of singlet and triplet states by [65]

$$-\langle \hat{S}_i^x \hat{S}_{i+1}^x \rangle - \langle \hat{S}_i^y \hat{S}_{i+1}^y \rangle = \frac{n_S - n_T}{2} \tag{4.27}$$

Furthermore, since the state is SU(2) symmetric, i.e. $\langle \hat{S}_i^l \hat{S}_j^l \rangle$ is equal for $l = x, y, z$, the spin correlator in the z basis can be written as

$$C^z_{\text{inter}} = -\frac{n_S - n_T}{4}. \tag{4.28}$$

A rigorous derivation of Eq. 4.28 is provided in [154]. In order to determine n_S and n_T in Eq. 4.28 from the data more reliable, a *sinusoidal*-function to the oscillation of the number of doubles were performed for each $t_\perp/t$ and the amplitude was extracted (Fig. 4.27 right). The resulting interlayer correlations (Eq. 4.28) increases with increasing ratio $t_\perp/t$ which is in accordance with the theoretical predictions (Fig. 2.4 right). At very low $t_\perp/t$, the measured inter-plane correlations are slightly higher than expected from the theory. Here, the fit to the oscillations becomes inappropriate and a smaller amplitude is likewise possible within the errorbars (Fig. 4.27 right). For the highest $t_\perp/t$, the measured correlations are slightly higher than expected from the DQMC theory.

The comparison of intra- and inter-layer correlations emphasises the cross over between the intra-layer nearest neighbour spin correlations at small $t_\perp/t$ and the anti ferromagnetic correlations across the two planes for high $t_\perp/t$ (Fig. 4.26 left and right).

4.3.3 Spin correlations for varying ratios U/t

The theoretically expected phase diagram for a bilayer Hubbard system shows that, depending on the ratio U/t, a smooth cross over from intra-layer correlations at small $t_\perp/t$ to interlayer correlations (band insulating phase) at large $t_\perp/t$ exists (Fig. 2.4 right). In order to experimentally observe this cross over for varying ratios U/t, the intra-plane tunnelling amplitude t was varied between 174 Hz − 290 Hz by changing the in-plane lattice depth between $5 - 7\,\mathrm{E}_{\text{rec}}$. Furthermore, the cross over was quantified by the spin correlation ratio

$$R_{\text{corr}} = \frac{C^z_{\text{intra}}}{C^z_{\text{intra}} + C^z_{\text{inter}}}. \tag{4.29}$$

Here, $C^z_{\text{intra}} = 2(S_\pi - C_{0,0})$ quantifies the intra-layer correlations by subtracting the local moment from the staggered spin structure factor and taking a factor of two for the two planes into account (cf. Sec. 4.3.1). For pure intra-layer correlations at low $t_\perp/t$, the ratio R_{corr} approaches one, while for pure interlayer correlations at high $t_\perp/t$ it vanishes. At around $t_\perp/t \approx 2.5$, the ratio becomes 1/2, $R_{\text{corr}} \approx 0.5$, which indicates the smooth cross over from an anti-ferromagnetically ordered state for smaller $t_\perp/t$ to a band insulating state at higher $t_\perp/t$ (Fig. 4.28, dark gray points). The error on R_{corr} was rather large, reaching up to 17%.

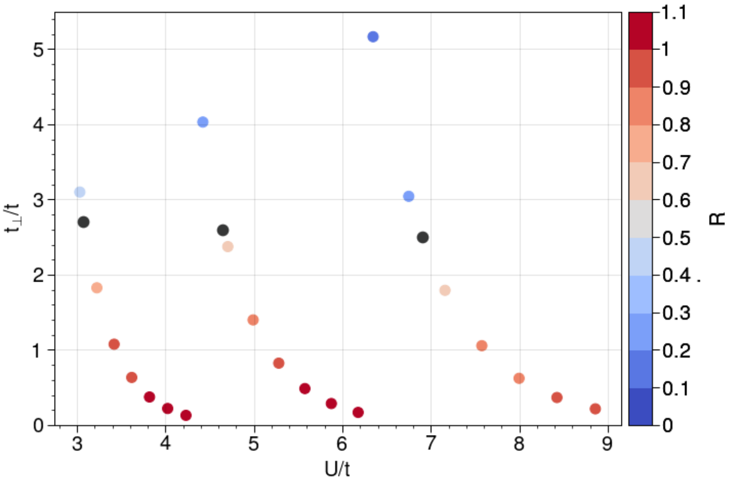

Figure 4.28: Experimentally measured parts of the bilayer Hubbard phase diagram (cf. Fig. 2.4 right). The ratio between intra- and inter-plane correlations was defined to indicate the smooth cross over.

4.4 Thermodynamics in the bilayer Hubbard system considered as monolayer Hubbard system with reservoir

4.4.1 A bilayer as a monolayer Hubbard system with reservoir

The bilayer Hubbard system can be considered as a monolayer Hubbard system with reservoir. In this sense, the chemical potential in the monolayer Hubbard system is tuned by changing the potential difference between the two layers. Technically, this is achieved by varying the phase of the vertical superlattice with the offset lock control voltage $\mathrm{V}^{\mathrm{ctr}}_{\mathrm{zlock}}$. In Sec. 4.2.6, singles and doubles in both layers were measured as a function of $\mathrm{V}^{\mathrm{ctr}}_{\mathrm{zlock}}$ to test the behaviour of the bilayer system (Fig. 4.22). Here, predictions from a simulation of a double well was compared to the data. This double-checked the calibration of the Hubbard parameters. Namely, 1. the tunnelling amplitude (Fig. 4.5) which yielded $t_\perp = 590\,\mathrm{Hz}$ for a $V_{z1064} = 120\,\mathrm{E}_{\mathrm{rec}}$, $V_{z532} = 15\,\mathrm{E}_{\mathrm{rec}}$ lattice configuration, 2. the superlattice phase (Fig. 4.4) which yielded $\Delta = 345\,\mathrm{Hz}$ and 3. the interaction strength with 900 Hz. Thus, this data set shows the expected behaviour and is therefore appropriate to deduce and probe thermodynamics, entropies and density fluctuations in the bilayer Hubbard system regarded as a monolayer Hubbard system with reservoir.

4.4.2 Equation of state, compressibility and the bilayer system temperature

The equation of state in a two-dimensional lattice system describes the number of singly and doubly occupied lattice sites as a function of the chemical potential (cf. Fig. 4.14). Thus, usually, by employing the local density approximation, the equation of state can be determined from a single absorption-image of singles and doubles in a two-dimensional optical lattice with underlying Gaussian potential [40]. In contrast, the equation of state is also directly provided by a measurement of singles and doubles in one (or both) of the two planes of the bilayer system as a function of the superlattice phase without local density approximation (Fig. 4.29 left). This effectively tunes the chemical potential in each individual plane. The sign of the potential, however, is inverted in both planes, i.e. $\mu_{\text{plane1}} = -\mu_{\text{plane2}}$. Hence, the singles/doubles distribution of the second plane can be simply mirrored at the symmetry point of the superlattice (Fig. 4.29 left, round and square data points).

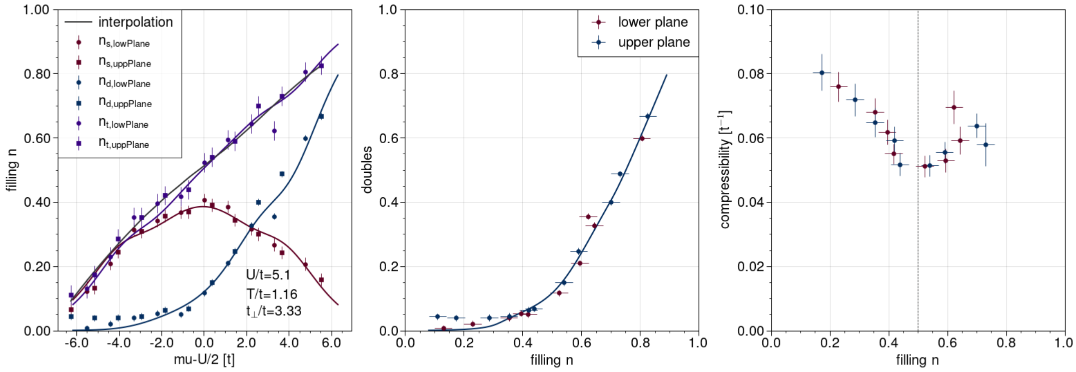

Figure 4.29: Left Equation of state given by the measured number of singles and doubles in each of the two planes of the bilayer Hubbard system as a function of the z superlattice phase. By fitting the data with DQMC theory, the temperature in each layer could be extracted. Since the temperature is an intensive property, the temperature of the whole bilayer Hubbard system could be determined this way. The errorbars in this measurement yielded from an equivalent measurement with five averages and amount to $n_{\text{D,err}} = \pm 0.01$ and $n_{\text{S,err}} = \pm 0.02$. **Center** Number of doubles as a function of the filling. **Right** Compressibility as a function of the filling. It exhibits a dip around half filling indicating the reduced compressibility in the Mott regime. In the pure monolayer Hubbard model, the doubles and compressibility as a function of the filling was measured in [40].

The obtained distribution was fitted with Determinant quantum Monte Carlo (DQMC) theory. Here, the tunnelling amplitude in the $7\,\text{E}_{\text{rec}}$ in-plane lattice was set to $t = 174\,\text{Hz}$. It yielded a temperature of $T = 1.16\,\text{t}$ in the bilayer Hubbard system. This lies in the temperature range which was independently inferred from spin correlation thermometry (Fig.4.26). There, DQMC data were calculated for temperatures $T = 1.0\,\text{t} - 1.4\,\text{t}$. Hence, this measurement can confirm the temperature range and specify it to be $T = 1.16\,\text{t}$.

Furthermore, in each of the two planes, the number of doubles as a function of the filling is expected to increase at half filling if the interactions are repulsive. Below half filling, due to the repulsion, it is energetically favourable to avoid doubly occupation which, however, is not possible any more above half filling (Fig. 4.29 center).

The avoiding of doubly occupancies goes along with a decreased compressibility $\kappa = \partial n/\partial \mu$ around half filling (Fig. 4.29 right). There, it costs energy to produce doubles by further increasing the chemical potential. To compute the compressibility, the numerical differentiation in each data point was obtained by first interpolating the total density data and subsequently calculate the slope in each data point x_i by $(y_{i+1} - y_{i-1})/(x_{i+1} - x_{i-1})$. The y error originates from a calculation of the standard deviation between the so-obtained numerical differentiation and of the left and right numerical derivative, i.e. the slope between neighboured data points $(y_{i+1} - y_i)/(x_{i+1} - x_i)$. The compressibility in the bilayer Hubbard system close to half-filling was also measured applying an in-plane magnetic field gradient (Sec. 4.23). Both measurements coincide with DQMC data at half-filling within the errorbars (Fig. 4.30 c). In a pure monolayer Hubbard model, the compressibility was determined in [40].

The ratio $t_\perp/t$

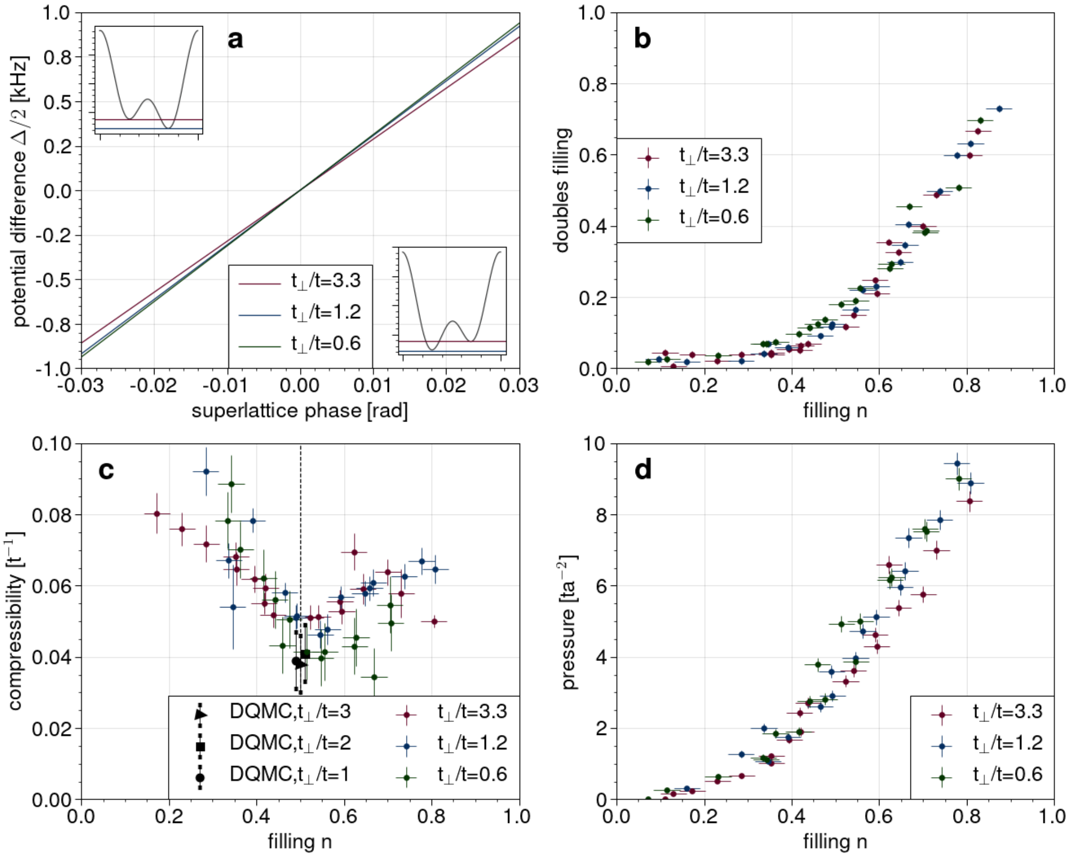

Figure 4.30: **a** The spacing between the lower and upper energy level in the double well Δ depends on the superlattice phase. However, this Δ depends on the lattice configuration and, so, on the ratios $t_\perp/t = 0.6, 1.2, 3.3$. **b** Doubles as a function of the filling, **c** compressibility and **d** pressure for all three ratios $t_\perp/t$. $t_\perp/t = 3.3$ was analysed before (Fig. 4.29).

The bilayer Hubbard system extends the monolayer Hubbard system by the coupling between two planes. This coupling is governed by the inter-plane tunnelling amplitude $t_\perp$

(Eq. 2.6). The affect of $t_\perp$ onto the equation of state if the bilayer Hubbard system is considered as monolayer Hubbard system with reservoir is studied.

In fact, a variation of $t_\perp$ results in a different change of the potential difference between the two planes Δ if Δ is varied (Fig. 4.30 a). More concrete, for an increasing short lattice depth and, thus, decreasing ratios $t_\perp/t$, the potential difference Δ increases faster for small superlattice phases. This difference, however, is small. For example, in a superlattice configuration with $V_{1064} = 120\,\mathrm{E}_{\mathrm{rec}}$ at a superlattice phase of 0.03 rad, the difference in $\Delta/2$ in the case of $t_\perp/t = 0.6$ and $t_\perp/t = 3.3$ is only 6% (Fig. 4.30 a). It is therefore expected that the equation of state does not show a strong dependence on $t_\perp/t$. In order to test this, the three cases $t_\perp/t = 0.6, 1.2, 3.3$ were studied. The case $t_\perp/t = 3.3$ was already analysed before (Fig. 4.29). In the two other cases, the doubles as a function of the filling (Fig. 4.30 b), the compressibility (Fig. 4.30 c) and the pressure (Fig. 4.30 d) show a similar behaviour and a clear difference is not visible within the errorbars. It can further be noted, that in all three cases, the compressibility at the half-filling point matches the predictions from DQMC calculations (Fig. 4.30 c, half-filling at vertical dashed line).

4.4.3 Local and thermodynamic density fluctuations

Besides the compressibility, the local and thermodynamic density fluctuations were analysed for varying superlattice phases. The data set with $t_\perp/t = 3.3$ was used. For a pure monolayer Hubbard model, both quantities were determined in [46]. There, the local density approximation was required which is not the case in the following analysis.

The local (on-site) density fluctuations $\delta n^2/n = \langle \hat{n}_i^2 \rangle - \langle \hat{n}_i \rangle^2$ were deduced from the measured singles and doubles. Using the anti-commutation relations and the fact that the system is spin-balanced, i.e. $\langle \hat{n}_{i,\uparrow} \rangle = \langle \hat{n}_{i,\downarrow} \rangle$, they are given by [46]

$$\delta n^2 = 2 \cdot \langle \hat{n}_{i,\uparrow} \rangle - 4 \cdot \langle \hat{n}_{i,\uparrow} \rangle^2 + 2 \cdot \langle \hat{n}_{i,\uparrow} \hat{n}_{i,\downarrow} \rangle. \tag{4.30}$$

Evaluating the data, the local density fluctuations decrease with increasing total density up to half-filling and then remain nearly constant close to zero (Fig. 4.31 left). For comparison, the local density fluctuations of a non-interacting Fermi gas as a function of the filling follow a binomial distribution for each spin state $\delta n^2/n = 1 - n/2$ (Fig. 4.31 left, dashed line). Here, sites are occupied by zero, one or two fermions with different spins due to Pauli's exclusion principle. In contrast, for an infinite strong repulsively interacting Fermi gas, doubly occupancies are suppressed and, hence, up to half-filling, the local density fluctuations as a function of the filling are described by $\delta n^2/n = 1 - n$ (Fig. 4.31 left, solid line). This means, that either zero or one fermion occupies a site. Beyond half-filling, it yields $\delta n^2/n = 3 - n - 2/n$ from Eq. 4.30 and $\langle \hat{n}_{i,\uparrow} \hat{n}_{i,\downarrow} \rangle = n - 1$. The measured data for $t_\perp/t = 3.3$ with $U = 900\,\mathrm{Hz}\,(\hat{=}5.17\,\mathrm{t})$ are close to the infinite interacting case up to half filling (Fig. 4.31 left). Beyond half-filling, the data do not show the expected behaviour of an re-increase of the local density fluctuations in the metallic state.

The *thermodynamic* density fluctuations $\delta N^2/N$ follow from the measured compressibility κ and density n [46]

$$\frac{\delta N^2}{N} = \frac{\kappa \mathrm{k_B} T}{n} = S_{\mathrm{den}}(q=0). \tag{4.31}$$

Here, the temperature of the gas is set to $T = 1.16\,\mathrm{t}$ which was inferred from the equation of state (Fig. 4.29 left). Furthermore, the thermodynamic density fluctuations are described by the density structure factor at zero momentum $S_{\mathrm{den}}(q=0)$. This structure factor decreases monotonically with increasing density n (Fig. 4.31 center).

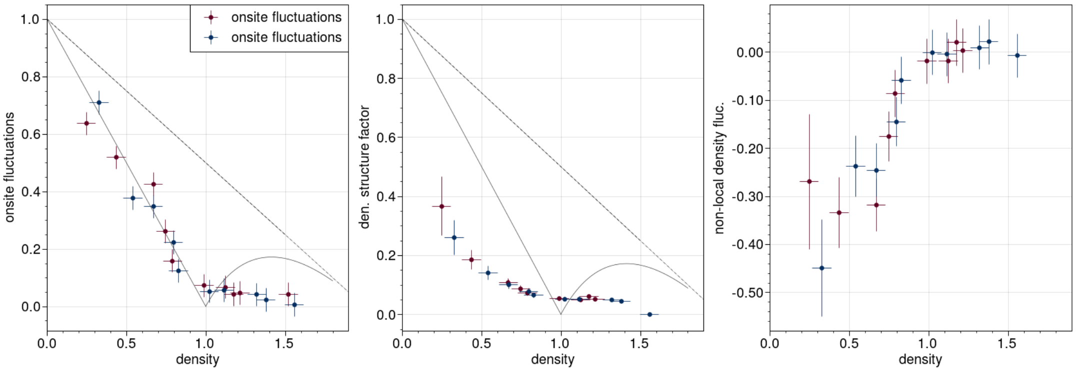

Figure 4.31: Left On-site fluctuation in the upper and lower plane of the bilayer Hubbard system. The gray, dashed (solid) line shows the expected on-site fluctuations for the non-interacting (infinite, repulsively interacting) Fermi gas. The interaction in the bilayer system is $U = 5.1t$. **Center** Density structure factor $S_{\mathrm{den}}(q=0)$ in the upper and lower plane. For better comparison to the measured on-site fluctuations, the gray dashed and solid line are taken from the left plot. **Right** Non-local density fluctuations. The on-site fluctuations (left plot) are higher than $S_{\mathrm{den}}(q=0)$ (center plot) for low fillings. This indicates a suppression of non-local fluctuations around half-filling.

The local (Fig. 4.31 left) and thermodynamic (Fig. 4.31 center) density fluctuations exhibit a discrepancy for low densities n. The *local* fluctuation dissipation theorem which connects the thermodynamic compressibility with the *local* fluctuations is thus violated [46]. This, in turn, suggests non-local (off-site) density correlations. In order to quantify them, the fluctuation dissipation theorem for a lattice system is split into the local δn^2 and non-local contribution of the density fluctuations to the compressibility[46]

$$\kappa = \frac{1}{a^2 \mathrm{k_B} T}\left[\delta n^2 + \sum_{j\neq i} \langle \hat{n}_i \hat{n}_j\rangle - \langle \hat{n}_i\rangle\langle \hat{n}_j\rangle\right]. \tag{4.32}$$

The measured off-site density correlations (Fig. 4.31 right) show a suppression around half filling. This is in accordance with Eq. 4.32, since for a localized state like the Mott insulator around half filling, the expectation value in Eq. 4.32 factorises $\langle \hat{n}_i \hat{n}_j \rangle) = \langle \hat{n}_i \rangle \langle \hat{n}_j \rangle$ and, hence, the contribution from non-local density fluctuations is zero. In contrast, in the metallic state at higher fillings, the non-local density fluctuations are not negligible.

4.4.4 Pressure and entropy

The pressure $p(\mu, T)$ in the bilayer Hubbard system considered as monolayer Hubbard system with reservoir can be deduced from the equation of state (Fig. 4.29 left) by integration [37]

$$p(\mu, T) = \frac{1}{a^2} \int_{-\infty}^{\mu} n(\mu', T) \mathrm{d}\mu'. \tag{4.33}$$

Here, for the numerical integration, the smoothed interpolating function of the total density was used as for the numerical differentiation (Eq. 4.18). Furthermore, the discrete integration was performed by summing over integrands $(n_{i+1} + n_i)/2/(\mu_{i+1} - \mu_i)$ where $i \in [\min_\mu, ..., \max_\mu]$. The error in the pressure results from the uncertainty in the total density. In order to deduce the latter, the uncertainty of singly and doubly occupied sites was first measured to be $n_{\mathrm{s,err}} = \pm 0.02$ and $n_{\mathrm{d,err}} = \pm 0.01$. The uncertainty of the total density then results from the sum $n_{\mathrm{t,err}} = n_{\mathrm{s,err}} + n_{\mathrm{d,err}} = \pm 0.03$. The pressure increases monotonically with density (Fig. 4.32 left). In a pure monolayer Hubbard system, the pressure was determined in [37].

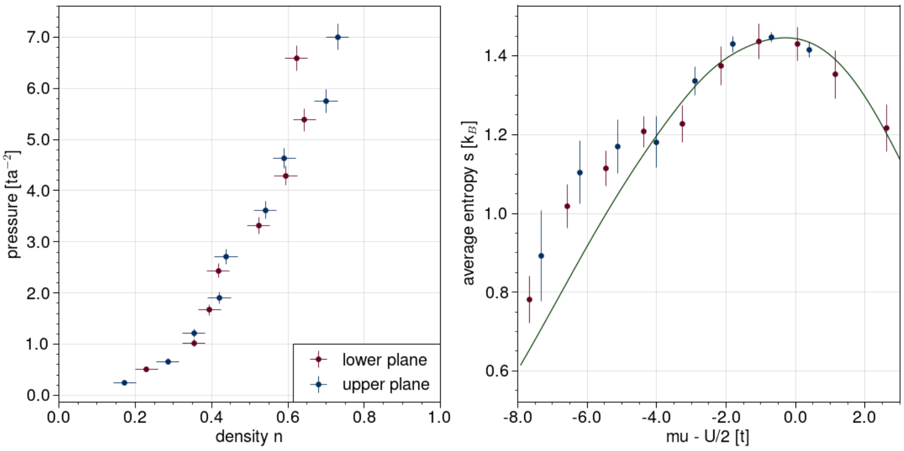

Figure 4.32: Left pressure and **Right** site entropy in the bilayer Hubbard system as a function of the filling for the upper and lower plane

The site entropy s results from the four possible occupation probabilities $\{\uparrow\downarrow, \uparrow, \downarrow, 0\}$ of a single lattice site [37]

$$s = -\mathrm{k_B} \left[p_{\uparrow\downarrow} \ln(p_{\uparrow\downarrow}) + p_{\uparrow} \ln(p_{\uparrow}) + p_{\downarrow} \ln(p_{\downarrow}) + p_0 \ln(p_0)) \right]. \tag{4.34}$$

It can be directly computed from the measured singles and doubles distributions with $n_{\mathrm{D}} = n_{\uparrow\downarrow}$, $n_{\mathrm{S}} = p_{\uparrow} = p_{\downarrow}$ and $n_0 = 1 - 2n_S - n_D$. The entropy increases with increasing chemical potential and exhibits a maximum around half-filling (Fig. 4.32 right). For pure a monolayer Hubbard system, the entropy was determined in [37].

Comment

The thermodynamics, density fluctuations and entropy in the monolayer Hubbard system with reservoir which were discussed throughout this chapter can be further analysed with regard to the ratio $t_{\perp}/t$. This especially includes the comparison of the results to Determinant Quantum Monte Carlo calculations for a bilayer Hubbard system. This is subject of the article in preparation *Thermodynamics, density fluctuations and entropy in a bilayer Hubbard system using cold atoms.*

CHAPTER 5

Outlook

5.1 Bilayer Hubbard model

5.1.1 First-order correlation function in a bilayer Hubbard system

Measuring the equation of state in the bilayer Hubbard system (Sec. 4.4.2) allowed for the determination of the temperature in both planes. This verified the measured temperature via spin correlation thermometry in only one of the two planes. Furthermore, the compressibility κ and the pressure p could be inferred from the equation of state. In a possible next step, the temperature in the implemented bilayer Hubbard system could be varied by smooth modulation of the in-plane lattice. Thus, the thermodynamic entropy in the system

$$s = a^2 \frac{\mathrm{d}p}{\mathrm{d}T}\bigg|_{\mu=const.} \tag{5.1}$$

could be deduced by: 1. determining the equation of state for each temperature, 2. deducing the pressure from it and 3. performing numerical differentiation of the pressure with respect to the temperature at constant chemical potential (Eq. 5.1). In a pure monolayer Hubbard system, the thermodynamic entropy was determined in [46].

In a further step, the thermodynamic entropy could be used with the determined compressibility and pressure to calculate the kinetic energy

$$E_{\mathrm{kin}} = sT + \mu n - pa^2 - Un_{\mathrm{D}}. \tag{5.2}$$

In turn, the kinetic energy on lattice site i is related to the first-order correlation function $G^{(1)}(1) = -1/4E_{\mathrm{kin,i}}$ and, hence, correlations between a single lattice site and its surrounding would be measurable [46]. Moreover, the mutual information determined by the discrepancy between the thermodynamic entropy and the averaged entropy per site (Fig. 4.32 right) can be inferred for the bilayer system. For a monolayer Hubbard system, this was likewise measured in [46].

5.1.2 Particle-hole symmetry and pair correlations in a bilayer system

In addition to the variation of the temperature in the bilayer system, the interaction strength U could be varied employing the Feshbach field. Moreover, a spin imbalance, i.e. a magnetisation, could be introduced. Both together, would enable to check the particle-hole transformation (Sec. 2.1.2.4) in the bilayer Hubbard system if attractive and repulsive interactions were implemented. In a pure monolayer Hubbard system the particle-hole transformation was tested in [58].

The implementation of attractive interactions in the bilayer Hubbard system would also allow for the measurement of the Pauli blocking- and interacting part of the pair correlation function [25]. Employing the fluctuation-dissipation theorem, both parts are connected to the static density structure factor by

$$\int \left[g^{(2)}_{\uparrow\uparrow}(r) + g^{(2)}_{\uparrow\downarrow}(r) - 2\right] \mathrm{d}^2 r = 2\left(\frac{\kappa T}{n^2} - \frac{1}{n}\right). \tag{5.3}$$

In a pure monolayer Hubbard system both parts of the pair correlation function were measured in [25].

5.2 Implementation of the Rice-Mele model

The Rice-Mele model describes a “dimerized” lattice with a unit cell of two sub-lattice sites A and B (Fig. 5.1 left). These sub-lattice sites are coupled by a tunnelling amplitude t_{in} while neighbouring unit cells are coupled by a tunnelling amplitude t_{out}. The Rice-Mele Hamiltonian reads [128][96]

$$H_{\text{RM}} = -\sum_j \left(t_{\text{in}}\hat{a}_j^\dagger \hat{b}_j + t_{\text{out}}\hat{b}_{j+1}^\dagger \hat{a}_j + \text{h.c.}\right) + \frac{\Delta}{2}\sum_m \left(\hat{a}_j^\dagger \hat{a}_j - \hat{b}_j^\dagger \hat{b}_j\right). \tag{5.4}$$

Here, $\hat{a}_j^\dagger$ ($\hat{a}_j$) is the creation (annihilation) operator of a particle on sub-lattice site A of the j-th lattice site and $\hat{b}_j^\dagger$ ($\hat{b}_j$) on sub-lattice site B of the j-th lattice site, respectively. The hermitian conjugated is abbreviated by h.c.. Δ denotes the offset energy between the sub-lattice sites A and B. For $\Delta = 0$, the Rice-Mele Hamiltonian is equivalent to the Su-Schrieffer-Heeger (SSH) model which is discussed in the following.
The fundamental interest in the SSH model lies in the fact that it exhibits the basic features of topological materials [10]. While in the case $t_{\text{in}} > t_{\text{out}}$ (Fig. 5.1), a topological trivial band insulator state reveals with a winding number of zero, the model exhibits a topological insulating state with winding number equal to one for $t_{\text{in}} < t_{\text{out}}$ [86]. Furthermore,

due to the two different tunnelling amplitudes t_{in} and t_{out}, the band structure possesses an upper and lower energy band $E_q^{\text{upp/low}} = \pm\sqrt{t_{\text{out}}^2 + t_{\text{in}}^2 + 2t_{\text{out}}t_{\text{in}}\cos(qa_l)}$. Here, q is the quasi momentum and a_l is the lattice constant of the long lattice (e.g. 1064 nm).
In cold atom experiments the SSH Hamiltonian was established employing an optical superlattice in [4][96][115].

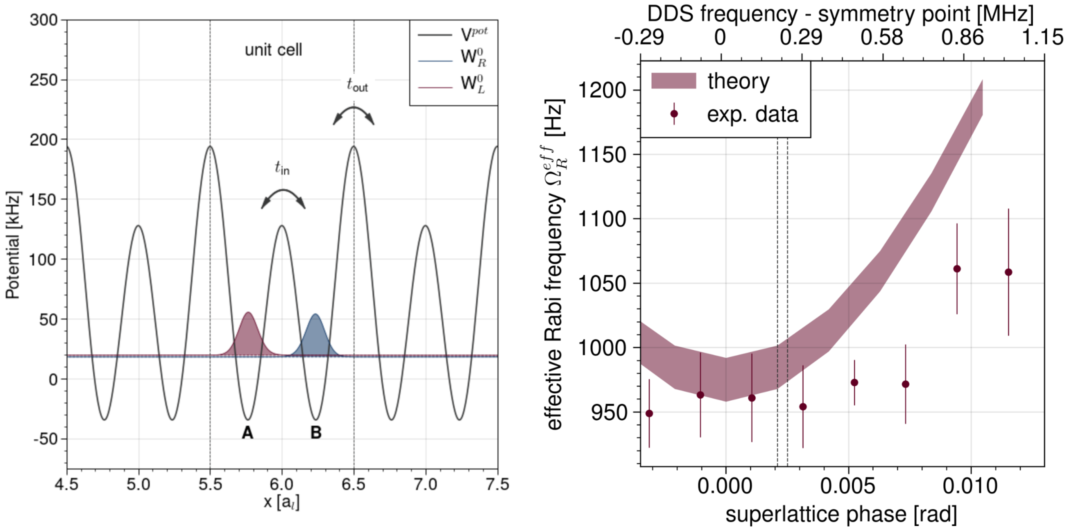

Figure 5.1: Left Su-Schrieffer-Heeger (SSH) model in one spatial dimension. It comprises the two tunnelling amplitudes t_{in} and t_{out} and the on-site interaction U. The model can be realised in cold atom experiments by loading atoms into an optical superlattice. Furthermore, by changing the superlattice phase a tilt between both sites A and B can be adjusted (Fig. 2.5). **Right** Effective Rabi frequency $\Omega_R^{\text{eff}} = 2t^{\text{eff}}$ in isolated double wells of the x superlattice as a function of the x superlattice phase. A similar measurement was performed to calibrate the phase in the vertical z superlattice (Fig. 4.4). Here, for the x superlattice, away from the symmetry point, the measured Rabi oscillation frequencies deviated from the theoretical one obtained by a two-band BPPO calculation. Phase fluctuations during the measurement might be a reason. The vertical dashed lines show the determined symmetry point of the superlattice before and after the oscillation measurement.

In order to realise the SSH model with the experimental setup (Sec. 3) and probe aspects of the model in the future, the in-plane x superlattice was newly set up and calibrated during this thesis (Sec. 3.3.2).[1] The calibration comprised similar methods to the calibration of the vertical z superlattice in order to realise the bilayer system (Sec. 4.1). However, different experimental challenges emerged during the implementation. Main calibration results are briefly provided in the following subsections.

---

[1] The main optics of the superlattice setup already exists [122] but had partly to be exchanged.

5.2.1 Depth-, tunnelling- and interaction strength calibration in the x superlattice

For the complete calibration of the x superlattice, the monochromatic x1064 and x532 lattice, which together formed the x superlattice, were first aligned individually onto the atoms in the dipole trap (Fig. 3.10). Subsequent, the depth of both lattices were independently calibrated by lattice modulation spectroscopy (Sec. 4.1.1). The calibrated lattice lasers were then locked onto each other using the x superlattice offset lock (Sec. 3.11). This resulted in a fixed relative phase between both lattices which could be tuned by tuning the DDS frequency (Fig. 3.11). It yielded a DDS frequency difference of 75 MHz to tune the x superlattice from its symmetric to its antisymmetric configuration.

Tunnelling calibration via Rabi oscillations

The tunnelling amplitude t_{in} of the x superlattice (Fig. 5.1 left) was calibrated via Rabi oscillations as in the case of the z superlattice (cf. Fig. 4.4 right).[2] In order to measure these oscillations, the x1064 lattice depth was set to $15\,\mathrm{E_{rec}}$ and the atoms were initially loaded into this lattice. Then, the x532 lattice was adiabatically ramped up within 35 ms in the antisymmetric superlattice configuration (Fig. 5.2 left). Here, the x532 lattice depth was varied between $11-13\,\mathrm{E_{rec}}$ among different measurements. At these lattice depths, on the one hand, the effective Rabi frequency (Eq. 4.5) was still in a measurable range - even 1 MHz away from the symmetry point.[3][4] On the other hand, tunnelling between unit cells, t_{out} (Fig. 5.1 left), was still sufficient small compared to intra-cell tunnelling t_{in} and could be neglected. After loading the atoms into the antisymmetric superlattice, the Rabi oscillations were induced by non-adiabatically sweeping the superlattice phase within 400 µs from the antisymmetric to the symmetric configuration (Fig. 5.2 second from left). After a free evolution time t_{Rabi} the phase was then swept back non-adiabatically to the antisymmetric configuration such that the left sub-site A in each unit cell was again low and the right sub-site B again up (Fig. 5.2 third from left). By the second non-adiabatic sweep, atoms in the right well were projected onto the excited state in the antisymmetric configuration and atoms in the left well projected onto the ground state. The x1064 lattice was subsequently non-adiabatically ramped up to $40\,\mathrm{E_{rec}}$ (Fig. 5.2 right). This led to a population of the 1^{st} excited energy level by atoms in the resulting antisymmetric superlattice. The first excited band is just below the upper right well in this configuration. Both lattices were finally switched off for band-mapping within 1 ms and the atoms were imaged after time of flight (TOF) of 6 ms. Hence, atoms which occupied the left sub-lattice site A at the end of t_{Rabi} and after the projection the ground state of the antisymmetric superlattice, populated the first Brioullin zone after TOF. In contrast, atoms in the 1^{st} excited energy level after projection populated the second Brioullin zone after TOF. Thus, the site occupation at time t_{Rabi} of the left or right sub-lattice site could be distinguished and Rabi oscillations became measurable.

The theoretical predicted dependence of the Rabi frequency onto the x superlattice phase

---

[2] Compare Sec. 4.1.5 for the tunnelling amplitude calibration of the vertical z superlattice.

[3] Here, the range is limited by the minimum duration of one time step in the experimental control (analogue cards) which is 100 µs. Thus, frequencies much larger than 1 kHz suffered from enough raster.

[4] To the antisymmetric configuration it was 75 MHz.

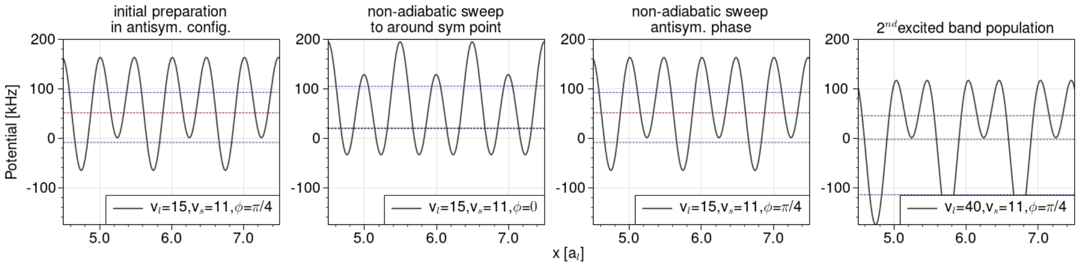

Figure 5.2: Detection scheme for the Rabi oscillation measurement From left to right: 1. Atoms were loaded into the antisymmetric x superlattice with lattice depth x1064=15 E_{rec},x532=11 − 13 E_{rec}. 2. The phase was non-adiabatically swept to around the symmetry point and hold there for the Rabi oscillation time t_{Rabi}. 3. The phase was non-adiabatically swept back to the antisymmetry point. 4. The lattice depth was increased to x1064=40 E_{rec},x532=11 − 13 E_{rec} to populate the 2^{nd} excited band. For sublattice site discrimination between site A and B, lattice modulation was performed.

could so far not be reproduced in the measurement at phases further away from the symmetry point (Fig. 5.1 right). Phase fluctuations and drifts probably disturbed the measurement. In order to quantify these phase drifts, the symmetry point was measured right before and after the Rabi oscillation measurement (Fig. 5.1, vertical dashed lines). The determined drift was less than 5×10^{-4} rad, but the measured symmetry point differed by 1.9×10^{-3} rad from the angular point of the fit which should also give the symmetry point.

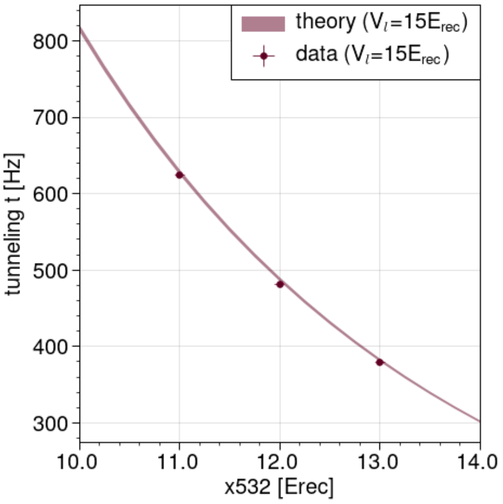

Figure 5.3: Tunnelling amplitude t_{in} (Fig. 5.1 left) as a function of the barrier height (cf. Fig. 2.5 center). The theory bands base on a calculation with non-interacting Wannier functions from the BPPO method. Uncertainties in the lattice depth and phase are taken into account. A similar measurement was performed for the z superlattice (Fig. 4.5).

In contrast, at the symmetry point, the measured Rabi frequency matched the theoretical predictions from a two-band BPPO method calculation for varying x532 lattice depths (Fig. 5.3). The theoretical bands arise due to errorbars in the x1064 lattice depth which was set to ±0.5%, as for the z lattice (Sec. 4.1.1).

X superlattice phase calibration

The superlattice phase was calibrated by slightly modifying the above control sequence to measure Rabi oscillations. Therefore, t_{Rabi} was set to the minimum of $100\,\mu\mathrm{s}$ (Fig. 5.2 second). During this time, atoms started to tunnel for the first time from the initially occupied sublattice site A to B around the symmetry point. By immediately, non-adiabatically ramping back the phase to the antisymmetric case thereafter (Fig. 5.2 third), further tunnelling was suppressed. This led to a population of the second Brioullin zone after TOF only very close to the symmetry point and, hence, a depopulation of the first Brioullin zone there. The integrated atom number in the first Brioullin zone thus exhibited a dip around the symmetry point. Consequently, the minimum of this dip pointed the symmetric superlattice case.

Superlattice phase stability

The superlattice phase of the calibrated x superlattice was subject to phase fluctuations on the order of 1 MHz around the symmetry point although it was actively stabilised against temperature, pressure and humidity by measuring all three quantities in the room and correct the DDS frequency to that effect. Phase drifts on the 15 min time scale could be tracked by the phase calibration method (cf. paragraph before). Since this method required about 10-15 data points to reliably resolve the minimum of the dip in the signal, phase drifts between subsequent experimental cycles on the minute timescale could however not be resolved. An interferometer was set up for this purpose during the writing of this thesis from Janek Fleper. Similar approaches to stabilise an optical superlattice are described in [150].

Interaction strength U calibration

The interaction strength U in the x superlattice was calibrated by radio frequency spectroscopy of atoms in the superlattice and comparing it to predictions. This was also performed for the vertical z superlattice (Sec. 4.1.7). In the x superlattice, the x1064 lattice depth was set to $60\,\mathrm{E_{rec}}$ and the x532 lattice depth to $12\,\mathrm{E_{rec}}$ and $18\,\mathrm{E_{rec}}$ while the superlattice phase was varied from the anti-symmetric configuration to phases close to the symmetry point (0.05 rad) (Fig. 5.4, cf. to Fig. 4.6 left). The measurement of U for phases $< 0.05\,\mathrm{rad}$ had to be treated with caution since the Wannier functions then start to delocalise over the entire double well.

As for the vertical z superlattice, non-interacting and interacting Wannier functions were both separately employed to theoretically predict the relative interaction strength $\Delta U = U_{95} - U_{97}$. The predicted ΔU using non-interacting Wannier functions thereby differ by roughly a factor of two from the data. This corresponds to about 1800 Hz. In contrast, the predicted ΔU using interacting Wannier functions differs only by 200 Hz. By increasing the short lattice depth from $12\,\mathrm{E_{rec}} \to 17\,\mathrm{E_{rec}}$ and $18\,\mathrm{E_{rec}} \to 25\,\mathrm{E_{rec}}$, the predictions for ΔU using interacting Wannier functions even match the data within the errorbars. One reason for that might be that the calibration of the lattice depth of the short lattice is to imprecise. Consequently, the calibrated lattice depth might be higher than assumed. This could probably, however, not explain the whole discrepancy.

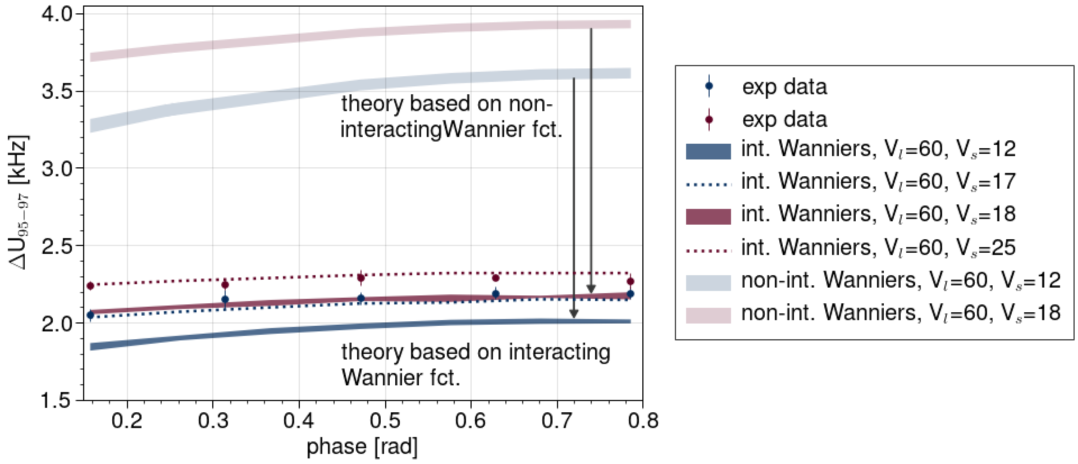

Figure 5.4: Calibration of the interactions strength U in the horizontal x superlattice (Sec. 3.3.2). The superlattice phase was varied and U was measured via SD separation (Sec. 3.5.4). The theoretical calculation was performed with non-interacting and interacting Wannier functions (Fig. 2.12). While the discrepancy between data and predictions from non-interacting Wannier functions is about 1800 Hz, interacting Wannier functions are off from the data by only 200 Hz. The interacting theory even matches data if the short lattice depth is changed from 12 E_{rec} → 17 E_{rec} and from 18 E_{rec} → 25 E_{rec}, respectively. One possible reason might be an improvable calibration method of the short lattice depth which, however, cannot explain the entire 200 Hz.

Site discrimination

In the measurement of Rabi oscillations, site distinction between A and B (Fig. 5.1 left) was achieved using time of flight. This resulted in the population of the first and second Brioullin zone. For future experiments it might be valuable to discriminate between the occupation of the left or right site in the horizontal x superlattice *in-situ*, i.e. while the atoms are trapped in the superlattice. A technique was therefore developed at the end of this thesis.[5] In contrast to the z superlattice, gravity did not pull the atoms out of the confinement of the Gaussian lattice beams. To overcome this limitation in the *horizontal* x superlattice, atoms were first routinely transferred into the upper wells of an antisymmetric superlattice (Fig. 5.2 right). Then, lattice modulation was performed. This transferred the atoms from the 1st excited energy level into the continuum were they got lost. This emptying of sublattice site B had an efficiency of about 85%. In contrast, only 6% of the

---

[5] In the vertical *z superlattice*, the occupation of the upper/lower plane could be distinguished by plane evaporation (Sec. 4.1.6). Here, atoms in the plane with higher offset energy in the antisymmetric z superlattice could not be hold by the underlying potential against gravity and the atoms escaped from the trap as desired and without the need to pull these atoms out of the upper plane.

atoms residing on sublattice site A left the trap due to the lattice modulation.

5.2.2 Outlook: Floquet systems and edge state detection

In the near future, the calibrated x superlattice can be employed to establish a Floquet driven system by means of the periodic modulation of the offset energy Δ between adjacent sublattice sites A and B (Fig. 5.1 left). A similar setup with cold atoms in a superlattice was implemented in [42].

One route to implement a modulation of Δ is to employ an arbitrary function generator (AWG). The latter was set up at the end of this thesis. It provides the driving frequency of about 80 MHz for the acoustic optical modulator (AOM) in the double pass configuration in the x superlattice laser setup (Fig. 3.9). Additionally, it modulates this driving frequency at a desired Floquet frequency in the tens of Kilohertz regime with a Floquet amplitude of up to 2 MHz. The x1064 light's frequency is thus modulated in the AOM at the Floquet frequency by twice the Floquet amplitude. In turn, the relative phase between the x1064 and x532 lattice is modulated[6][7] and, so, the offset energy Δ between adjacent sublattice sites A and B. Floquet systems in cold atom experiments were also studied in [95][64] and theoretically in [60][50].

One route for preparing the atoms in the superlattice for Floquet driving of two atoms in a double well is to create a band insulator first and then split the latter to a Mott insulator. This was likewise done in the vertical z superlattice to create the bilayer Hubbard system (Sec. 4.2.3). There, the vertical z532 lattice was ramped up in the symmetric configuration which split the band insulator into two coupled single-layer Mott insulators. Here, for the x superlattice, the atoms can be first prepared in the x1064 lattice and the x532 lattice is ramped up in the symmetric configuration thereafter to split the single plane band insulator into a single plane Mott insulator with half lattice spacing.

Having prepared a Mott insulator, two further measurements might be performed to test the superlattice and verify the successful implementation of a Floquet system. Preliminarily, both measurements are discussed in the following:

1. To test the superlattice control, the phase is varied around the symmetry point and the number of singles and doubles are detected as a function of the phase. A similar measurement was performed in the z superlattice (Fig. 4.22). This measurement might be appropriate to recheck the phase dependence which could not be satisfactorily reproduce with Rabi oscillations (Fig. 5.1 right).
2. The successful implementation of the Floquet driven system can be tested by measuring singles and doubles as a function of the interaction strength U at the symmetry point of the superlattice (Fig. 5.5 right). Here, for attractive interactions doubles are energetically

---

[6] In this regime, the band width of the electronic lock does not allow for correction of the fast modulation - as desired.

[7] Instead of using the AWG to drive the AOM, a voltage controlled oscillator (VCO) was likewise set up at the end of this thesis. The AWG had the disadvantage that the signal length of the uploaded, arbitrary wave function was limited by the internal storage. This could be circumvented by using the VCO which, however, exhibits long term drifts.

favourable while for repulsive interactions doubles split into two singles. By successfully Floquet driving the system, the tunnelling amplitudes t_{in}, t_{out} are modified compared to the non-driven case and, hence, the distribution of singles and doubles changes between both cases signalling that the Floquet driving works. A similar measurement was performed in [42].

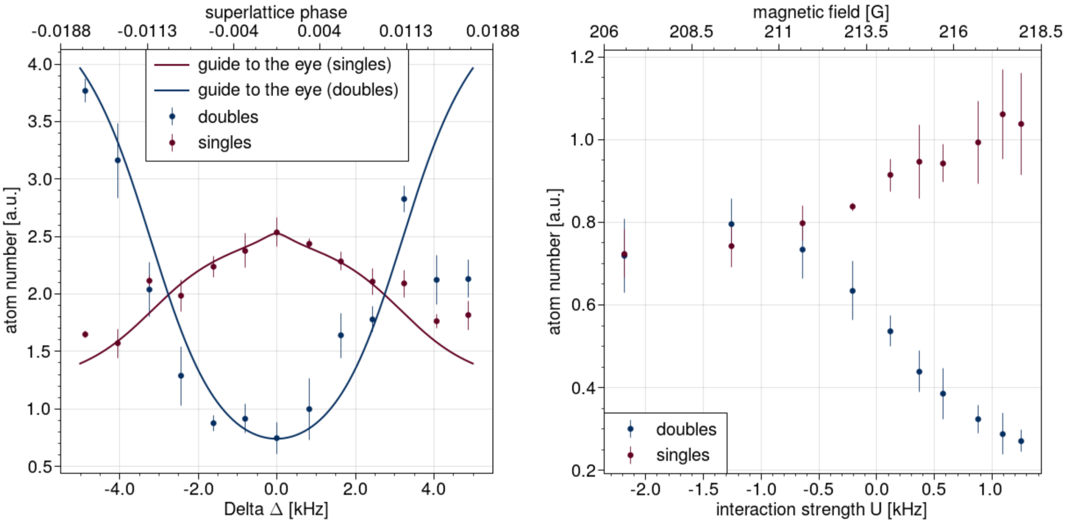

Figure 5.5: Left Singly and doubly occupied lattice sites in the x superlattice as a function of the superlattice phase. In this preliminary result, tomography was not employed and singles and doubles were measured in the total atom cloud across several planes. Therefore, the atom number is given in arbitrary units and the plotted lines are just a guide to the eyes.**Right** Singles and doubles in the symmetric x superlattice as a function of the interaction strength. From attractive to repulsive interactions the two atoms on a doubly occupied site tend to separate into both wells of the double well. This measurement can be used to verify successful Floquet driving (see text).

With the successful implementation of Floquet driving, it becomes possible among other things to control the super exchange interaction and swap its sign [103]. Thus, e.g. a back and forth switching between an antiferromagnet and a ferromagnet could be implemented for system temperatures below the super exchange energy.

Furthermore and beside the implementation of a Floquet system, the x superlattice together with the digital mirror device enables the implementation and detection of edge states [90][68][113]. Such edge states were measured in cold atom experiments in [62][127][91].

Bibliography

[1] Ehud Altman, Eugene Demler, and Mikhail D. Lukin. "Probing many-body states of ultracold atoms via noise correlations". In: *Physical Review A* 70.1 (July 6, 2004), p. 013603.

[2] P W Anderson. "The Resonating Valence Bond State in La2CuO4 and Superconductivity". In: 235 (), p. 4.

[3] P W Anderson et al. "The physics behind high-temperature superconducting cuprates: the plain vanilla version of RVB". In: *Journal of Physics: Condensed Matter* 16.24 (June 23, 2004), R755–R769.

[4] Marcos Atala et al. "Direct Measurement of the Zak phase in Topological Bloch Bands". In: *Nature Physics* 9.12 (Dec. 2013), pp. 795–800. arXiv: `1212.0572[cond-mat,physics:quant-ph]`.

[5] Assa Auerbach. *Interacting electrons and quantum magnetism.* Springer Science & Business Media, 2012.

[6] W S Bakr et al. "Probing the Superfluid–to–Mott Insulator Transition at the Single-Atom Level". In: 329 (2010), p. 5.

[7] Waseem S. Bakr, Jonathon I. Gillen, Amy Peng, Simon Fölling, and Markus Greiner. "A quantum gas microscope for detecting single atoms in a Hubbard-regime optical lattice". In: *Nature* 462.7269 (Nov. 2009), pp. 74–77.

[8] Neven Barišić et al. "Universal sheet resistance and revised phase diagram of the cuprate high-temperature superconductors". In: *Proceedings of the National Academy of Sciences* 110.30 (July 23, 2013), pp. 12235–12240.

[9] Daniel Barredo, Sylvain de Léséleuc, Vincent Lienhard, Thierry Lahaye, and Antoine Browaeys. "An atom-by-atom assembler of defect-free arbitrary two-dimensional atomic arrays". In: *Science* 354.6315 (Nov. 25, 2016), pp. 1021–1023.

[10] Navketan Batra and Goutam Sheet. "Understanding Basic Concepts of Topological Insulators Through Su-Schrieffer-Heeger (SSH) Model". In: *Resonance* 25.6 (June 2020), pp. 765–786. arXiv: `1906.08435[cond-mat]`.

[11] J G Bednorz. "Possible High Tc Superconductivity in the Ba - La- Cu- 0 System". In: (), p. 5.

[12] Andrea Bergschneider. “Strong correlations in few-fermion systems”. PhD thesis. Ruperto-Carola Universität Heidelberg, 2017.

[13] Jean-Sébastien Bernier et al. “Cooling fermionic atoms in optical lattices by shaping the confinement”. In: *Physical Review A* 79.6 (June 3, 2009), p. 061601.

[14] Ulf Bissport. “Dynamical effects and disorder in ultracold bosonic matter”. PhD thesis. Johann Wolfgang Goethe-Universität Frankfurt am Main, 2012.

[15] Eric Black. *Notes on the Pound-Drever-Hall technique.*

[16] Jacob A Blackmore et al. “Ultracold molecules for quantum simulation: rotational coherences in CaF and RbCs”. In: *Quantum Science and Technology* 4.1 (Dec. 5, 2018), p. 014010.

[17] R. Blatt and C. F. Roos. “Quantum simulations with trapped ions”. In: *Nature Physics* 8.4 (Apr. 2012), pp. 277–284.

[18] Immanuel Bloch, Jean Dalibard, and Wilhelm Zwerger. “Many-Body Physics with Ultracold Gases”. In: *Reviews of Modern Physics* 80.3 (July 18, 2008), pp. 885–964. arXiv: `0704.3011`.

[19] Martin Boll et al. “Spin- and density-resolved microscopy of antiferromagnetic correlations in Fermi-Hubbard chains”. In: *Science* 353.6305 (Sept. 16, 2016), pp. 1257–1260.

[20] K. Bouadim, G. G. Batrouni, F. Hébert, and R. T. Scalettar. “Magnetic and transport properties of a coupled Hubbard bilayer with electron and hole doping”. In: *Physical Review B* 77.14 (Apr. 30, 2008), p. 144527.

[21] Peter T. Brown et al. “Observation of canted antiferromagnetism with ultracold fermions in an optical lattice”. In: *Science* 357.6358 (Sept. 29, 2017), pp. 1385–1388. arXiv: `1612.07746`.

[22] Peter T. Brown et al. “Angle-resolved photoemission spectroscopy of a Fermi-Hubbard system”. In: *Nature Physics* 16.1 (Jan. 2020), pp. 26–31. arXiv: `1903.05678`.

[23] Nejat Bulut, Douglas J. Scalapino, and Richard T. Scalettar. “Nodeless d -wave pairing in a two-layer Hubbard model”. In: *Physical Review B* 45.10 (Mar. 1, 1992), pp. 5577–5584.

[24] Thomas Busch and Berthold-Georg Englert. “Two Cold Atoms in a Harmonic Trap”. In: (), p. 11.

[25] C. F. Chan, M. Gall, N. Wurz, and M. Köhl. “Pair correlations in the attractive Hubbard model”. In: *Physical Review Research* 2.2 (May 21, 2020), p. 023210.

[26] Chun Fai Chan. “Quantum simulation of strongly-correlated two-dimensional fermions in optical lattices”. PhD thesis. Rheinischen Friedrich-Wilhelms-Universität Bonn, 2019.

[27] Chingyun Cheng. “Ultracold Fermi Gases in a Bichromatic Optical Superlattice”. In: (2016), p. 145.

[28] Lawrence W Cheuk et al. “Observation of spatial charge and spin correlations in the 2D Fermi-Hubbard model”. In: (), p. 6.

[29] Lawrence W. Cheuk et al. “Quantum-Gas Microscope for Fermionic Atoms”. In: *Physical Review Letters* 114.19 (May 13, 2015), p. 193001.

[30] Lawrence W. Cheuk et al. “Observation of 2D Fermionic Mott Insulators of K 40 with Single-Site Resolution”. In: *Physical Review Letters* 116.23 (June 10, 2016), p. 235301.

[31] C. Chin et al. “Observation of the Pairing Gap in a Strongly Interacting Fermi Gas”. In: *Science* 305.5687 (Aug. 20, 2004), pp. 1128–1130.

[32] Cheng Chin, Rudolf Grimm, Paul Julienne, and Eite Tiesinga. “Feshbach resonances in ultracold gases”. In: *Reviews of Modern Physics* 82.2 (Apr. 29, 2010), pp. 1225–1286.

[33] J. K. Chin et al. “Evidence for superfluidity of ultracold fermions in an optical lattice”. In: *Nature* 443.7114 (Oct. 2006), pp. 961–964.

[34] Christie S. Chiu, Geoffrey Ji, Anton Mazurenko, Daniel Greif, and Markus Greiner. “Quantum State Engineering of a Hubbard System with Ultracold Fermions”. In: *Physical Review Letters* 120.24 (June 14, 2018), p. 243201.

[35] N. R. Claussen et al. “Very-high-precision bound-state spectroscopy near a 85 Rb Feshbach resonance”. In: *Physical Review A* 67.6 (June 20, 2003), p. 060701.

[36] E. Cocchi et al. “Measuring entropy and mutual information in the two-dimensional Hubbard model”. In: *Physical Review X* 7.3 (Aug. 4, 2017), p. 031025. arXiv: `1612.04627`.

[37] E. Cocchi et al. “Measuring Entropy and Short-Range Correlations in the Two-Dimensional Hubbard Model”. In: *Physical Review X* 7.3 (Aug. 4, 2017), p. 031025.

[38] Eugenio Cocchi. “Analogue quantum Simulation of the Two-Dimensional Hubbard Model with Ultracold Fermions”. PhD thesis. University of Cambridge, 2016.

[39] Eugenio Cocchi et al. “Equation of State of the Two-Dimensional Hubbard Model”. In: *PHYSICAL REVIEW LETTERS* (2016), p. 5.

[40] Eugenio Cocchi et al. “Equation of state of the two-dimensional Hubbard model”. In: *Physical Review Letters* 116.17 (Apr. 25, 2016), p. 175301. arXiv: `1512.03431`.

[41] Elbio Dagotto. “Correlated electrons in high-temperature superconductors”. In: *Reviews of Modern Physics* 66.3 (July 1, 1994), pp. 763–840.

[42] Rémi Desbuquois et al. “Controlling the Floquet state population and observing micromotion in a periodically driven two-body quantum system”. In: *Physical Review A* 96.5 (Nov. 1, 2017), p. 053602. arXiv: `1703.07767`.

[43] H Ding, T Takahashi, M Randeria, M R Normant, and T Mochikull. “Spectroscopic evidence for a pseudogap in the normal state of underdoped high-Tc superconductors”. In: 382 (1996), p. 4.

[44] Elizabeth A Donley, Neil R Claussen, Sarah T Thompson, and Carl E Wieman. “Atom–molecule coherence in a Bose–Einstein condensate”. In: 417 (2002), p. 5.

[45] T. Dornheim. “Fermion sign problem in path integral Monte Carlo simulations: Quantum dots, ultracold atoms, and warm dense matter”. In: *Physical Review E* 100.2 (Aug. 22, 2019), p. 023307.

[46] J. H. Drewes et al. “Thermodynamics versus Local Density Fluctuations in the Metal–Mott-Insulator Crossover”. In: *Physical Review Letters* 117.13 (Sept. 20, 2016), p. 135301.

[47] J. H. Drewes et al. “Antiferromagnetic Correlations in Two-Dimensional Fermionic Mott-Insulating and Metallic Phases”. In: *Physical Review Letters* 118.17 (Apr. 25, 2017), p. 170401.

[48] Jan H. Drewes. “Strongly correlated Fermions in optical lattices”. PhD thesis. Rheinischen Friedrich-Wilhelms-Universität Bonn, 2018.

[49] Pedro M. Duarte et al. “Compressibility of a Fermionic Mott Insulator of Ultracold Atoms”. In: *Physical Review Letters* 114.7 (Feb. 20, 2015), p. 070403.

[50] André Eckardt and Egidijus Anisimovas. “High-frequency approximation for periodically driven quantum systems from a Floquet-space perspective”. In: *New Journal of Physics* 17.9 (Sept. 23, 2015), p. 093039.

[51] Michael Feld. “Low temperature phases of interacting fermions in two dimensions”. PhD thesis. University of Cambridge, 2011.

[52] Richard P Feynman. “Simulating physics with computers”. In: (), p. 22.

[53] S Flannigan, L Madail, R G Dias, and A J Daley. “Hubbard models and state preparation in an optical Lieb lattice”. In: *New Journal of Physics* 23.8 (Aug. 1, 2021), p. 083014.

[54] Janek Fleper. “”Long-range disorder in the non-interacting one-dimensional Fermi-Hubbard model””. Master’s thesis. Rheinischen Friedrich-Wilhelms-Universität Bonn, 2020.

[55] C.J. Foot and D.P.C.J. Foot. *Atomic Physics*. Oxford Master Series in Physics. OUP Oxford, 2005.

[56] S. Friebel, C. D’Andrea, J. Walz, M. Weitz, and T. W. Hänsch. “CO 2 -laser optical lattice with cold rubidium atoms”. In: *Physical Review A* 57.1 (Jan. 1, 1998), R20–R23.

[57] Bernd Fröhlich. “A Strongly Interacting Two-Dimensional Fermi Gas”. PhD thesis. University of Cambridge, 2011.

[58] M. Gall, C. F. Chan, N. Wurz, and M. Köhl. “Simulating a Mott insulator using attractive interaction”. In: *Physical Review Letters* 124.1 (Jan. 8, 2020), p. 010403. arXiv: `1907.09045`.

[59] Marcell W. Gall. “Quantum Simulation of the Bilayer Hubbard Model Using Ultracold Atoms”. PhD thesis. Rheinischen Friedrich-Wilhelms-Universität Bonn, 2020.

[60] N. Goldman and J. Dalibard. “Periodically Driven Quantum Systems: Effective Hamiltonians and Engineered Gauge Fields”. In: *Physical Review X* 4.3 (Aug. 18, 2014), p. 031027.

[61] N. Goldman, D. F. Urban, and D. Bercioux. "Topological Phases for Fermionic Cold Atoms on the Lieb Lattice". In: *Physical Review A* 83.6 (June 2, 2011), p. 063601. arXiv: `1101.4500[cond-mat,physics:quant-ph]`.

[62] N. Goldman et al. "Direct imaging of topological edge states in cold-atom systems". In: *Proceedings of the National Academy of Sciences* 110.17 (Apr. 23, 2013), pp. 6736–6741. arXiv: `1212.5093[cond-mat,physics:quant-ph]`.

[63] Michael Golor, Timo Reckling, Laura Classen, Michael M. Scherer, and Stefan Wessel. "Ground-state phase diagram of the half-filled bilayer Hubbard model". In: *Physical Review B* 90.19 (Nov. 18, 2014), p. 195131.

[64] Frederik S. Görg. "Exploring and Floquet-Engineering the Driven Fermi-Hubbard Model with Ultracold Atoms". PhD thesis. ETH Zurich, 2019.

[65] Daniel Greif, Thomas Uehlinger, Gregor Jotzu, Leticia Tarruell, and Tilman Esslinger. "Short-Range Quantum Magnetism of Ultracold Fermions in an Optical Lattice". In: 340 (2013), p. 5.

[66] Daniel Greif et al. "Site-resolved imaging of a fermionic Mott insulator". In: *Science* 351.6276 (Feb. 26, 2016), pp. 953–957.

[67] Markus Greiner, Olaf Mandel, and Tilman Esslinger. "Quantum phase transition from a super¯uid to a Mott insulator in a gas of ultracold atoms". In: 415 (2002), p. 6.

[68] Fabian Grusdt, Michael Höning, and Michael Fleischhauer. "Topological edge states in the one-dimensional super-lattice Bose-Hubbard model". In: *Physical Review Letters* 110.26 (June 25, 2013), p. 260405. arXiv: `1301.7242[cond-mat]`.

[69] Lucia Hackermüller et al. "Anomalous Expansion of Attractively Interacting Fermionic Atoms in an Optical Lattice". In: *Science* 327.5973 (Mar. 26, 2010), pp. 1621–1624.

[70] Elmar Haller et al. "Single-atom imaging of fermions in a quantum-gas microscope". In: *Nature Physics* 11.9 (Sept. 2015), pp. 738–742.

[71] T.W. Hansch and B. Couillaud. "Laser frequency stabilization by polarization spectroscopy of a reflecting reference cavity". In: *Optics Communications* 35.3 (Dec. 1980), pp. 441–444.

[72] Russell A. Hart et al. "Observation of antiferromagnetic correlations in the Hubbard model with ultracold atoms". In: *arXiv:1407.5932 [cond-mat]* (Jan. 31, 2015). arXiv: `1407.5932`.

[73] A. F. Ho, M. A. Cazalilla, and T. Giamarchi. "Quantum simulation of the Hubbard model: The attractive route". In: *Physical Review A* 79.3 (Mar. 19, 2009), p. 033620.

[74] Christian Hofrichter et al. "Direct probing of the Mott crossover in the SU(N) Fermi-Hubbard model". In: *Physical Review X* 6.2 (June 1, 2016), p. 021030. arXiv: `1511.07287`.

[75] W Hofstetter, J I Cirac, P Zoller, E Demler, and M D Lukin. "High-Temperature Superfluidity of Fermionic Atoms in Optical Lattices". In: *PHYSICAL REVIEW LETTERS* 89.22 (2002), p. 4.

[76] J. Hubbard. "Electron Correlations in Narrow Energy Bands. II. The Degenerate Band Case". In: *Proceedings of the Royal Society of London. Series A, Mathematical and Physical Sciences* 277.1369 (1964), pp. 237–259.

[77] Krzysztof Jachymski and Paul S. Julienne. "Analytical model of overlapping Feshbach resonances". In: *Physical Review A* 88.5 (Nov. 6, 2013), p. 052701.

[78] D. Jaksch, C. Bruder, J. I. Cirac, C. W. Gardiner, and P. Zoller. "Cold Bosonic Atoms in Optical Lattices". In: *Physical Review Letters* 81.15 (Oct. 12, 1998), pp. 3108–3111.

[79] S. Jochim et al. "Bose-Einstein Condensation of Molecules". In: *Science* 302.5653 (Dec. 19, 2003), pp. 2101–2103.

[80] S. S. Kancharla and S. Okamoto. "Band insulator to Mott insulator transition in a bilayer Hubbard model". In: *Physical Review B* 75.19 (May 15, 2007), p. 193103. arXiv: `cond-mat/0703728`.

[81] Wolfgang Ketterle, Kendall B. Davis, Michael A. Joffe, Alex Martin, and David E. Pritchard. "High densities of cold atoms in a *dark* spontaneous-force optical trap". In: *Physical Review Letters* 70.15 (Apr. 12, 1993), pp. 2253–2256.

[82] S. Kivelson. "Wannier functions in one-dimensional disordered systems: Application to fractionally charged solitons". In: *Physical Review B* 26.8 (Oct. 15, 1982), pp. 4269–4277.

[83] Nick Klemmer. "Cavity design for high-power frequency doubling". Bachelor's thesis. Rheinischen Friedrich-Wilhelms-Universität Bonn, 2018.

[84] Nick Klemmer. "Ultracold Fermions in an Optical Superlattice". Master's thesis. Rheinischen Friedrich-Wilhelms-Universität Bonn, 2020.

[85] Joannis Koepsell et al. "Robust Bilayer Charge Pumping for Spin- and Density-Resolved Quantum Gas Microscopy". In: *Physical Review Letters* 125.1 (July 2, 2020), p. 010403.

[86] Michael Köhl. *Lecture notes: Atomic, Molecular, and Optical Physics*. 2019.

[87] Michael Köhl, Henning Moritz, Thilo Stöferle, Kenneth Günter, and Tilman Esslinger. "Fermionic atoms in a 3D optical lattice: Observing Fermi-surfaces, dynamics and interactions". In: *arXiv:cond-mat/0410389* (Mar. 9, 2005). arXiv: `cond-mat/0410389`.

[88] C. Kollath, A. Iucci, I. McCulloch, and T. Giamarchi. "Modulation spectroscopy with ultracold fermions in an optical lattice". In: *Physical Review A* 74.4 (Oct. 20, 2006), p. 041604. arXiv: `cond-mat/0608091`.

[89] Mark Kremer, Rashi Sachdeva, Albert Benseny, and Thomas Busch. "Interaction-induced effects on Bose-Hubbard parameters". In: *Physical Review A* 96.6 (Dec. 8, 2017), p. 063611.

[90] Li-Jun Lang, Xiaoming Cai, and Shu Chen. "Edge States and Topological Phases in One-Dimensional Optical Superlattices". In: *Physical Review Letters* 108.22 (May 29, 2012), p. 220401.

[91] Martin Leder et al. "Real-space imaging of a topologically protected edge state with ultracold atoms in an amplitude-chirped optical lattice". In: *Nature Communications* 7.1 (Dec. 2016), p. 13112.

[92] Patrick A. Lee, Naoto Nagaosa, and Xiao-Gang Wen. "Doping a Mott insulator: Physics of high-temperature superconductivity". In: *Reviews of Modern Physics* 78.1 (Jan. 6, 2006), pp. 17–85.

[93] Jinbin Li, Yue Yu, Artem M. Dudarev, and Qian Niu. "Interaction broadening of Wannier functions and Mott transitions in atomic BEC". In: *New Journal of Physics* 8.8 (Aug. 30, 2006), pp. 154–154. arXiv: `cond-mat/0311012`.

[94] Tracy Li et al. "Bloch state tomography using Wilson lines". In: *Science* 352.6289 (May 27, 2016), pp. 1094–1097. arXiv: `1509.02185[cond-mat,physics:quant-ph]`.

[95] H. Lignier et al. "Dynamical Control of Matter-Wave Tunneling in Periodic Potentials". In: *Physical Review Letters* 99.22 (Nov. 27, 2007), p. 220403.

[96] Michael Lohse, Christian Schweizer, Oded Zilberberg, Monika Aidelsburger, and Immanuel Bloch. "A Thouless Quantum Pump with Ultracold Bosonic Atoms in an Optical Superlattice". In: *Nature Physics* 12.4 (Apr. 2016), pp. 350–354. arXiv: `1507.02225`.

[97] Karla Henriette Loida. "Modulation Spectroscopy of Ultracold Atoms in Optical Lattices". In: (), p. 146.

[98] Andrew Peter Mackenzie and Yoshiteru Maeno. "The superconductivity of Sr2RuO4 and the physics of spin-triplet pairing". In: *Rev. Mod. Phys.* 75.2 (2003), p. 56.

[99] Nicola Marzari and David Vanderbilt. "Maximally localized generalized Wannier functions for composite energy bands". In: *Physical Review B* 56.20 (Nov. 15, 1997), pp. 12847–12865.

[100] Namrata Dutta Mazumdar. "Rebuilding a Potassium Quantum Gas Apparatus". In: (), p. 64.

[101] Anton Mazurenko et al. "A cold-atom Fermi–Hubbard antiferromagnet". In: *Nature* 545.7655 (May 2017), pp. 462–466.

[102] Florian Meinert et al. "Observation of many-body dynamics in long-range tunneling after a quantum quench". In: *Science* 344.6189 (June 13, 2014), pp. 1259–1262.

[103] J. H. Mentink, K. Balzer, and M. Eckstein. "Ultrafast and reversible control of the exchange interaction in Mott insulators". In: *Nature Communications* 6.1 (Nov. 2015), p. 6708.

[104] M.-O. Mewes et al. "Collective Excitations of a Bose-Einstein Condensate in a Magnetic Trap". In: *Physical Review Letters* 77.6 (Aug. 5, 1996), pp. 988–991.

[105] Luke A. Miller. "Ultracold Fermions in Two-Dimensional Optical Lattices: Quantum Simulation of the Hubbard Model". PhD thesis. University of Cambridge, 2016.

[106] Andrew. J. Millis. “Optical spectral weights and the physics of correlated electron systems”. In: (2000).

[107] Debayan Mitra et al. “Quantum gas microscopy of an attractive Fermi-Hubbard system”. In: *Nature Physics* 14.2 (Feb. 2018), pp. 173–177. arXiv: `1705.02039`.

[108] Michele Modugno and Giulio Pettini. “Maximally localized Wannier functions for ultracold atoms in one-dimensional double-well periodic potentials”. In: *New Journal of Physics* 14.5 (May 1, 2012), p. 055004.

[109] C Monroe et al. “Quantum Simulation of Spin Models with Trapped Ions”. In: (), p. 20.

[110] A. Moreo and D. J. Scalapino. “Two-dimensional negative- U Hubbard model”. In: *Physical Review Letters* 66.7 (Feb. 18, 1991), pp. 946–948.

[111] N F Mott. “The Basis of the Electron Theory of Metals, with Special Reference to the Transition Metals”. In: *Proceedings of the Physical Society. Section A* 62.7 (July 1, 1949), pp. 416–422.

[112] Markus Müller. “Many-body quantum simulation with rydberg atoms and ions”. PhD thesis. Leopold-Frazens-Universität Innsbruck, 2010.

[113] Shuichi Murakami. “Two-dimensional topological insulators and their edge states”. In: *Journal of Physics: Conference Series* 302 (July 20, 2011), p. 012019.

[114] Simon Murmann et al. “Two Fermions in a Double Well: Exploring a Fundamental Building Block of the Hubbard Model”. In: *PHYSICAL REVIEW LETTERS* (2015), p. 5.

[115] Shuta Nakajima et al. “Topological Thouless Pumping of Ultracold Fermions”. In: *Nature Physics* 12.4 (Apr. 2016), pp. 296–300. arXiv: `1507.02223`.

[116] Satoshi Okamoto and Thomas A. Maier. “Enhanced Superconductivity in Superlattices of High- T c Cuprates”. In: *Physical Review Letters* 101.15 (Oct. 7, 2008), p. 156401.

[117] Ahmed Omran et al. “Microscopic Observation of Pauli Blocking in Degenerate Fermionic Lattice Gases”. In: *Physical Review Letters* 115.26 (Dec. 23, 2015), p. 263001.

[118] Thereza Paiva, Richard Scalettar, Mohit Randeria, and Nandini Trivedi. “Fermions in 2D Optical Lattices: Temperature and Entropy Scales for Observing Antiferromagnetism and Superfluidity”. In: *Physical Review Letters* 104.6 (Feb. 11, 2010), p. 066406.

[119] Ruizhi Pan and Charles W. Clark. “Implementing Majorana fermions in a cold-atom honeycomb lattice with textured pairings”. In: *Physical Review A* 98.3 (Sept. 14, 2018), p. 033604. arXiv: `1802.08804[cond-mat,physics:quant-ph]`.

[120] Maxwell F. Parsons et al. “Site-Resolved Imaging of Fermionic Li 6 in an Optical Lattice”. In: *Physical Review Letters* 114.21 (May 28, 2015), p. 213002.

[121] Eva Pavarini et al., eds. *Quantum materials: experiments and theory: lecture notes of the Autumn School on Correlated Electrons 2016: at Forschungszentrum Jülich, 12-16 September 2016.* Schriften des Forschungszentrums Jülich. Reihe Modeling and Simulation Band 6. Meeting Name: Autumn School on Correlated Electrons. Jülich: Forschungszentrum, Zentralbibliothek, 2016.

[122] D. Pertot et al. "Relaxation dynamics of a Fermi gas in an optical superlattice". In: *Physical Review Letters* 113.17 (Oct. 23, 2014), p. 170403. arXiv: `1407.6037`.

[123] D. S. Petrov, C. Salomon, and G. V. Shlyapnikov. "Diatomic molecules in ultracold Fermi gases - Novel composite bosons". In: *Journal of Physics B: Atomic, Molecular and Optical Physics* 38.9 (May 14, 2005), S645–S660. arXiv: `cond-mat/0502010`.

[124] Frederik Pfeiffer. "Extended PAM in the context of SmB6 and Cold Atoms in optical lattices". Master's thesis. Ludwig-Maximilians-Universität München, 2021.

[125] Antonio Sergio Teixeira Pires. "Theoretical Tools for Spin Models in Magnetic Systems". In: (), p. 17.

[126] Mohit Randeria and Edward Taylor. "BCS-BEC Crossover and the Unitary Fermi Gas". In: *arXiv:1306.5785 [cond-mat, physics:nucl-th]* (Apr. 8, 2014). arXiv: `1306.5785`.

[127] Matthew Reichl and Erich Mueller. "Floquet Edge States with Ultracold Atoms". In: *Physical Review A* 89.6 (June 30, 2014), p. 063628. arXiv: `1404.3217[cond-mat,physics:quant-ph]`.

[128] M. J. Rice and E. J. Mele. "Elementary Excitations of a Linearly Conjugated Diatomic Polymer". In: *Physical Review Letters* 49.19 (Nov. 8, 1982), pp. 1455–1459.

[129] Robert Rüger, Luca F Tocchio, Roser Valentí, and Claudius Gros. "The phase diagram of the square lattice bilayer Hubbard model: a variational Monte Carlo study". In: *New Journal of Physics* 16.3 (Mar. 7, 2014), p. 033010.

[130] Shabnam Safaei, Christian Miniatura, and Benoît Grémaud. "Triangular and honeycomb lattices of cold atoms in optical cavities". In: *Physical Review A* 92.4 (Oct. 8, 2015), p. 043810.

[131] Jun John Sakurai. *Modern quantum mechanics; rev. ed.* Reading, MA: Addison-Wesley, 1994.

[132] A. W. Sandvik and D. J. Scalapino. "Order-disorder transition in a two-layer quantum antiferromagnet". In: *Physical Review Letters* 72.17 (Apr. 25, 1994), pp. 2777–2780.

[133] R. T. Scalettar et al. "Phase diagram of the two-dimensional negative- U Hubbard model". In: *Physical Review Letters* 62.12 (Mar. 20, 1989), pp. 1407–1410.

[134] Richard Scalettar, E. Pavarini, E. Koch, J. van den Brink, and G. Sawatzky. *Quantum Materials: Experiments and Theory.* 2016.

[135] Richard T. Scalettar, Joel W. Cannon, Douglas J. Scalapino, and Robert L. Sugar. "Magnetic and pairing correlations in coupled Hubbard planes". In: *Physical Review B* 50.18 (Nov. 1, 1994), pp. 13419–13427.

[136] U Schneider et al. “Metallic and Insulating Phases of Repulsively Interacting Fermions in a 3D Optical Lattice”. In: 322 (2008), p. 7.

[137] Ulrich Schneider et al. “Fermionic transport in a homogeneous Hubbard model: Out-of-equilibrium dynamics with ultracold atoms”. In: *Nature Physics* 8.3 (Mar. 2012), pp. 213–218. arXiv: `1005.3545`.

[138] U. Schünemann, H. Engler, R. Grimm, M. Weidemüller, and M. Zielonkowski. “Simple scheme for tunable frequency offset locking of two lasers”. In: *Review of Scientific Instruments* 70.1 (Jan. 1999), pp. 242–243.

[139] Jacob F. Sherson et al. “Single-atom-resolved fluorescence imaging of an atomic Mott insulator”. In: *Nature* 467.7311 (Sept. 2010), pp. 68–72.

[140] Jonathan Simon et al. “Quantum simulation of antiferromagnetic spin chains in an optical lattice”. In: *Nature* 472.7343 (Apr. 2011), pp. 307–312.

[141] Benjamin M. Spar, Elmer Guardado-Sanchez, Sungjae Chi, Zoe Z. Yan, and Waseem S. Bakr. “A Fermi-Hubbard Optical Tweezer Array”. In: *arXiv:2110.15398 [cond-mat, physics:physics]* (Oct. 28, 2021). arXiv: `2110.15398`.

[142] J. T. Stewart, J. P. Gaebler, and D. S. Jin. “Using photoemission spectroscopy to probe a strongly interacting Fermi gas”. In: *Nature* 454.7205 (Aug. 7, 2008), pp. 744–747. arXiv: `0805.0026`.

[143] Thilo Stöferle, Henning Moritz, Christian Schori, Michael Köhl, and Tilman Esslinger. “Transition from a Strongly Interacting 1D Superfluid to a Mott Insulator”. In: *Physical Review Letters* 92.13 (Mar. 31, 2004), p. 130403.

[144] Niels Strohmaier et al. “Interaction-Controlled Transport of an Ultracold Fermi Gas”. In: *Physical Review Letters* 99.22 (Nov. 28, 2007), p. 220601.

[145] Kazunori Takada et al. “Superconductivity in two- dimensional CoO2 layers”. In: 422 (2003), p. 3.

[146] Leticia Tarruell and Laurent Sanchez-Palencia. “Quantum simulation of the Hubbard model with ultracold fermions in optical lattices”. In: *Comptes Rendus Physique* 19.6 (Sept. 2018), pp. 365–393.

[147] Andreas Trabesinger. “Quantum simulation”. In: *Nature Physics* 8.4 (Apr. 2012), pp. 263–263.

[148] S. Trotzky et al. “Time-Resolved Observation and Control of Superexchange Interactions with Ultracold Atoms in Optical Lattices”. In: *Science* 319.5861 (Jan. 18, 2008), pp. 295–299.

[149] Thomas Uehlinger. “Engineering artificial graphene with an ultracold Fermi gas”. Artwork Size: 1 Band Medium: application/pdf Pages: 1 Band. PhD thesis. ETH Zurich, 2014.

[150] Paul Michael Uerlings. “Phase stability of an optical superlattice setup for ultracold dysprosium atoms”. In: (), p. 50.

[151] Xiaoling Wu et al. “A concise review of Rydberg atom based quantum computation and quantum simulation”. In: *Chinese Physics B* 30.2 (Feb. 1, 2021), p. 020305. arXiv: `2012.10614[cond-mat,physics:physics,physics:quant-ph]`.

[152] N. Wurz et al. "Coherent Manipulation of Spin Correlations in the Hubbard Model". In: *Physical Review A* 97.5 (May 4, 2018), p. 051602. arXiv: `1709.08231`.

[153] Nicola Wurz. "Imprinting Spin Spirals into an Ultracold Fermi Gas". Master's thesis. Rheinischen Friedrich-Wilhelms-Universität Bonn, 2016.

[154] Nicola Wurz. "Quantum Magnetism in the Two-Dimensional Fermi-Hubbard Model and Beyond". PhD thesis. Rheinischen Friedrich-Wilhelms-Universität Bonn, 2021.

[155] Jin Yang, Liyu Liu, Jirayu Mongkolkiattichai, and Peter Schauss. "Site-resolved imaging of ultracold fermions in a triangular-lattice quantum gas microscope". In: *PRX Quantum* 2.2 (June 21, 2021), p. 020344. arXiv: `2102.11862[cond-mat,physics:physics]`.

[156] Shaoqi Zhu and Biao Wu. "Interaction Effects on Wannier Functions for Bosons in Optical Lattice". In: *Physical Review A* 92.6 (Dec. 30, 2015), p. 063637. arXiv: `1506.08053`.

[157] M. W. Zwierlein et al. "Condensation of Pairs of Fermionic Atoms near a Feshbach Resonance". In: *Physical Review Letters* 92.12 (Mar. 25, 2004), p. 120403.

List of Figures

1.1 Schematic phase diagram for cuprates 4

2.1 Monolayer Hubbard model and a high temperature superconducting material 9
2.2 Schematic phase diagram of the Hubbard model 11
2.3 Hubbard bands and a two level system 12
2.4 Bilayer Hubbard model and its phase diagram 18
2.5 Superlattice potential 19
2.6 Bandstructure in a monochromatic lattice 21
2.7 Bandstructure in a bi-chromatic lattice 23
2.8 Eigenfunctions/-values of the band projected position operator 26
2.9 Wannier functions 27
2.10 Effect of lattice depths on Hubbard parameters and Wannier functions . . . 29
2.11 On-site, interaction and kinetic energy of the ground band Wannier functions 32
2.12 Total energy, attractively and repulsively interacting Wannier functions. . . 32

3.1 Hyperfine structure in potassium 35
3.2 Laser table 36
3.3 Ioffe-Pritchard trap, Feshbach coils, offset coils around the science cell . . . 39
3.4 Zeeman splitting and magnetic evaporation scheme 40
3.5 Optical setups for dipol traps and z-imaging 43
3.6 Laser setup for the vertical z superlattice and the y lattice 47
3.7 Z superlattice setup on the experimental table 48
3.8 Offset lock electronic setup for the z superlattice 49
3.9 Laser setup of the horizontal x superlattice 51
3.10 Optical setup in-plane lattice 52
3.11 Offset lock electronic setup x superlattice 53
3.12 Feshbach resonances 56
3.13 Water cooling circuit 57
3.14 Tomography 60
3.15 Detection scheme for singly and doubly occupied lattice sites 61
3.16 Singles/doubles separation pulse 62
3.17 Detection scheme for “spin-up” and “spin-down” atoms 63
3.18 Optical setup of the DMD laser 64

4.1 Lattice modulation spectroscopy of the z532 lattice 69

4.2 Determination of the symmetry point 71
4.3 Induced Rabi oscillations in isolated double wells 73
4.4 Effective Rabi oscillation frequency in the z superlattice 74
4.5 Tunnelling frequencies at the symmetry point of the vertical superlattice . . 76
4.6 Interaction strength U in the z superlattice 78
4.7 Interacting Wannier functions in the vertical superlattice 79
4.8 Loading and evaporatively cooling the atomic gas in a dipole trap 81
4.9 Loading and evaporatively cooling a 50:50 spin mixed atomic gas in a dipole trap 82
4.10 Populating each second lattice site in the vertical z532 lattice with atoms . 84
4.11 Trap frequencies and density-density correlation 86
4.12 Main experimental sequence (part 2) and illustration of a real optical lattice 88
4.13 In-situ absorption image of doubly and singly occupied lattice sites 88
4.14 Equation of state of the ideal Fermi gas and interacting fermions 91
4.15 Doubly and singly occupied lattice sites in the two step potential 92
4.16 Entropy and singles density in the band insulator 94
4.17 Entropy and singles density in the band insulator (2) 94
4.18 DMD potential with walls and spin wave images 95
4.19 Spin waves 97
4.20 Main experimental sequence (part 3 and 4) 99
4.21 Potential map in the bilayer Hubbard system 100
4.22 Singly and doubly occupations in a double well 103
4.23 Compressibility measured via a magnetic field gradient 105
4.24 Modified Ramsey sequence 108
4.25 Calibration of the modified Ramsey sequence 110
4.26 Spin correlations in the bilayer system 111
4.27 Detection scheme for interlayer correlations 113
4.28 Experimentally measured parts of the bilayer Hubbard phase diagram . . . 115
4.29 Equation of state and thermodynamics in the bilayer system 116
4.30 Thermodynamics in the bilayer system for different ratios $t_\perp/t$ 117
4.31 On-site fluctuation in the bilayer Hubbard system 119
4.32 Pressure and entropy in the bilayer Hubbard system 120

5.1 Su-Schrieffer-Heeger (SSH) model and Effective Rabi frequency in the x superlattice 125
5.2 Detection scheme for the Rabi oscillation measurement 127
5.3 Tunnelling amplitude in the x superlattice 127
5.4 Calibration of the interactions strength in the horizontal x superlattice . . . 129
5.5 Singly and doubly occupied lattice sites in the x superlattice as function of superlattice phase and interaction strength 131